**MTK 22.**

**MŰSZAKI TUDOMÁNYOS KÖZLEMÉNYEK**

**22.**

## TUDOMÁNYOS BIZOTTSÁG/LEKTOROK
## SCIENTIFIC ADVISORY BOARD/PEER REVIEWERS



**ISSN 2393 – 1280**

Erdélyi Múzeum-Egyesület Műszaki Tudományok Szakosztálya
Transylvanian Museum Society – Department of Technical Sciences

# MŰSZAKI TUDOMÁNYOS KÖZLEMÉNYEK

# 22.

**Szerkesztette / Edited by**
**BITAY ENIKŐ – MÁTÉ MÁRTON**

**ERDÉLYI MÚZEUM-EGYESÜLET**
**Kolozsvár**
**2025**

A kötet megjelenését támogatta a Magyar Tudományos Akadémia,
a Bethlen Gábor Alapkezelő Zrt., és az EME Műszaki Tudományok Szakosztálya.

The publication of this volume was supported by the Hungarian Academy of Sciences,
by the Bethlen Gábor Fund, and by the TMS – Department of Engineering Sciences,




Kiadó/Publisher: Erdélyi Múzeum-Egyesület
Felelős kiadó/Responsible Publisher: Biró Annamária
Szerkesztette/Edited by: Bitay Enikő, Máté Márton
Olvasószerkesztő/Proofreader: András Zselyke (magyar), David Speight (English)
Műszaki szerkesztő/DTP: Szilágyi Júlia
Borítóterv/Cover: Könczey Elemér

Nyomdai munkálatok/Printing-work
F&F International Kft. Kiadó és Nyomda, Gyergyószentmiklós
Ügyvezető igazgató/Manager: Ambrus Enikő
Tel./Fax: +40-266-364171

**Online elérhető/Online available at:**

Magyar/Hungarian
https://eme.ro/publication-hu/mtk/mtk-main.htm
DOI: 10.33895/mtk-2024.22

Angol/English
https://eme.ro/publication/mtk/mtk-main.htm
DOI: 10.33894/mtk-2024.22

# TARTALOM

# CONTENT

Műszaki Tudományos Közlemények vol. 22. (2025) 1–9.
DOI: Hungarian: https://doi.org/10.33895/mtk-2025.22.01
English: https://doi.org/10.33894/mtk-2025.22.01

# A CASE STUDY FOR POSSIBLE APPLICATIONS OF ARTIFICIAL INTELLIGENCE TOOLS IN THE DESIGN OF ENGINEERING PROJECTS

Levente BAKOS,[1] István-Csongor BAKOS[2]

[1] *Sapientia Hungarian University of Transylvania, Faculty of Târgu-Mureș, Department of Mechanical Engineering, bakos@ms.sapientia.ro*

[2] *Technical University of Cluj-Napoca, Faculty of Industrial Engineering, Robotics and Production Management, bakosistvancsongor@yahoo.com*

**Abstract**

In our paper we study the potential application of artificial intelligence in the scheduling of engineering projects. We are focusing on a very small slice of project management topic, namely, shaping the major tasks and starting managing risks in the design phase. By design, here, we are not referring to the technological sense of the word, but rather on conceiving the entire technical project. We intend to study the use of AI in the case of engineering projects that are not software-based at all and in which AI is a working tool, not a goal or a constituent element. In our research, we investigated how the best-known Large Language Models respond to the same request. In examining the results, we found that the AI environments made meaningful suggestions, most of them showing in the same time a high degree of similarity. It was also confirmed that the data provided by AI in both scientific and practical contexts should be treated with caution. Still, we prove that AI can be considered a real and powerful, day-to-day tool in project management.

**Keywords***: industrial projects, Artificial Intelligence, Large Language Models.*

## 1. Introduction

The potential use of artificial intelligence, and its expected positive or negative impact in a given field, is a challenging topic among scientists, yet it can be a subject of public debate almost universally. There are probably very few topics that are of interest to everyone, from teenagers and pensioners to worldwide policy-makers, despite being still only at the experimental development stage for scientists. AI (artificial intelligence), as one of the most mediatized scientific achievements of our time, can offer a range of possibilities in both project management and leadership.

In this paper, we explore a very small slice of the project management topic, namely the potential application of AI in the scheduling of certain engineering projects, in particular the management of risks in the design phase. By design, here, we are not referring to the technological sense of the word, but rather conceiving the entire technical project, including, among other things, the supply chain, production management, risk and quality management. We have to note, solutions offered by artificial intelligence (AI) are very common in many segments of technical engineering, especially where there is a software component. These applications of AI in engineering can be very domain-specific, being out of our investigation range. In our research we analysed the possibility of using the most well-known generic platforms, essentially in the conceiving phase of the project, where the whole engineering project is still just a concept, and even the launch of the project is still in question. The design of the production line,

machine purchase, tooling, technology development and other steps will just follow after this phase. For us, AI is just a design tool, not a goal or a constituent element. Although the most common AI applications are fast learners, they are not always reliable for industrial projects. This is partly because even these platforms do not have access to most developments -thus the learning process is limited, and furthermore, these AI solutions may be protected by patents or other rights. The legal framework in the field of AI is still fuzzy, and far from comprehensive and satisfactory [1], Perhaps the biggest step forward is the EU legislation known as the "AI Act", which entered into force on 1 August 2024 [2]. The Regulation 2024/1689 of the European Parliament and of the Council laying down harmonised rules on artificial intelligence basically encourages the use of AI in the EU, primarily for competitiveness reasons, but provides a legal framework that addresses the risks of AI. In art. 4 it states, that “AI is a fast evolving family of technologies that contributes to a wide array of economic, environmental and societal benefits across the entire spectrum of industries and social activities. By improving prediction, optimising operations and resource allocation, and personalising digital solutions available for individuals and organisations, the use of AI can provide key competitive advantages (…), energy, transport and logistics (…), resource and energy efficiency (…)”. Given the industrial areas identified in the list, we thought it worthwhile to research the potential uses of AI in the field of industrial project management. In our analysis, we used either Large Language Model (LLM) [3, 4]) or multimodal type AI platforms with generative functions [5]. We investigated the solutions provided by these platforms in a certain issue that requires planning, design and risk management.

## 2. Planning, scheduling, AI and risk treatment in project management

Project management as a discipline has a well-developed methodology for planning, scheduling and risk management. The PMBOK [6] perhaps one of the best references for practitioners, defines the project as "a time-bound effort to create a unique product, service or outcome." A project is a set of unique (non-standard), not regularly performed set of complex activities done for a well-defined, specific purpose, with fixed deadlines and predefined resource requirements. This definition shows that projects, as a unique series of activities, are characterized by complexity and risks, from the conception of the idea, through the design phase and ultimate implementation [7]. Starting from the very first steps in defining a project, there is a set of variables whose value poses a risk to the success of the project. Explicitly, we are indicating the inherent risks related to the schedule, tasks and the estimation of duration. Practitioners and researchers already identified a plethora of opportunities of AI environments [8, 9, 10]. In risk analysis, AI can proactively identify and prioritize risks and analyse complex risks [11]. AI can also be an important tool for predictive project planning, not only identifying risks but also predicting project outcomes in the light of these risks, and forecasting different scenarios. For example, machine learning algorithms can identify patterns and trends by studying a large amount of data in circumstances that human reasoning is not able to handle [12]. Through machine learning, practitioners are now able to predict project performance. Artificial intelligence offers powerful solutions by analysing vast amounts of data. Using and analysing past data from similar projects, machine learning can predict the expected performance of the current project. This estimation provides support for cost estimation, schedule, feasibility indicators and possible bottlenecks [13]. Machine learning algorithms can revolutionize project management by being able to extract massive amounts of historical project data [14]. They can analyse databases of almost unimaginable size, with cost estimates, timelines, resource allocation, technical and engineering standards, and results from previous projects [15], and can help practitioners almost immediately in the initial phase [16, 17, 18]. The use of an AI environment can expand our project management toolbox, have an impact on human resources, reduce work stress, increase team morale and give the team a greater sense of achievement by solving tasks faster. Data sharing, transparency and other opportunities could be discussed. Artificial intelligence facilitates communication and collabora-

tion within project teams and with external stakeholders [19].

AI can produce real-time reports – by day, week or month – to facilitate data sharing, promote transparency and streamline project implementation. Historical data on resource utilization allows machine learning models to make near-optimal recommendations for the allocation of resources, staff, equipment and budget for the current project. Predicting these problems allows project managers to pro-actively adjust schedules and minimize disruptions [8, 9]. When simulating pro-project scenarios, it is possible for project managers to identify down-potential disruptions. Significantly better-informed scheduling decisions can be made, as machine learning can analyse past project data to identify slippages or bottlenecks in specific processes in similar projects [20].

Obviously, the use of AI is not without risk. The use of AI in project management, as in any other field, can also introduce new risks. The AI environment should support the management in handling risks and should not be a risk in itself [21]. For this reason, AI should be used with due care.

## 3. The best-known generative AI environments and their applications in engineering projects

Based on their very large number of users ChatGPT [22], Google Gemini [23], Microsoft Copilot [24] and Claude [25] are the most popular generative artificial intelligence environments. They are all prompt-based: they operate based on user formulated inquiries and follow some instructions. Behind these environments there are continuously extended databases, developed by major teams, some of them associated with IT giants such as Google and Microsoft. Probably one of the most popular current AI applications is ChatGPT, which is powered by the Open AI platform [26]. Some other environments are much more specialised than ChatGPT, such as Ayanza [27] (best fitted to workflows, better manage and coordinate teams), Stepsize [28] (suitable for technical projects, supply tools for example activity summary in software development), Zapier AI [29] ] (part of a larger group of apps, it focuses mostly on managing workflows integrated into automation projects), Kuki Chatbot [30] (AI-driven chatbot for common questions, designed with entertaining interactions with a virtual assistant, linked with some common brands), Taskade [31] (suited to teams, projects in order to improve planning, track tasks, create best fitting workplace; it uses one of the latest databases of ChatGPT). We have to mention that these applications do not only learn from the users, they need a teaching environment in which the system evolves through different learning models. There are several processes of learning, but most often huge amounts of data are fed during the learning processes. Obviously, in the case of industrial projects the large amount of data often is not available. The learning can be supervised (the system learns from initially labelled data), unsupervised (where the system searches for patterns and learns from them), reinforced (the system learns by reinforcement), semi-supervised (a combination of the previous two, the data is partially labelled and new patterns are formed from it) and transfer-based (refining the already learned, proven model for a new task). At the user level, none of these are of particular importance, and all five of the known learning processes can produce useful results. If we use AI only as a tool, we need to learn at most the instructions and how to achieve results. The quality of the instruction has a major impact on the response and the outcome of the AI.

In spite of the fact that AI models are usually fed by a large database, yet they still cannot solve all problems. Not even the popular chatbots mentioned earlier. The more general the source of the data, the more likely the “support” will not be professionally correct, as the system cannot distinguish between professionally correct and false data. At the same time there is a considerable quality jump between the free version of the AI tool and the services provided with paid subscription. Although the paid version might use the same database, the quality and speed of data processing is better due to better algorithms built into the paid versions. The free versions are tools for gaining users, while the most advanced AI tools will probably never be free of charge. On of the most convincing argument might be the fact the development of artificial intelligence is a time-consuming, and therefore costly, process.

It can take several months, or even years in very specific cases, to create the proper environment.

## 4. Presentation of the experiment

The aim of our experiment is to compare some AI tools that can be used for project planning in engineering projects. We intended to investigate how the most well-known AI applications respond to the same prompt. Furthermore, we searched to what extent they are similar and the solutions provided correspond to real professional requirements. Our plan was to compare the following AI environments: ChatGPT, Copilot, Gemini, Claude, Zapier AI, Taskade, Stepsize, Kuki Chatbot and Ayanza. The comparison was based on a single set of instructions in which we ask the AI platforms to organise a fatigue test of a known car component in the context of a manufacturing project. The search was carried out on 20 November 2024.

We typed the following prompt into the search interface of the AI platforms:" Hi! I would like to perform a cyclic fatigue test using a fatigue machine on the rear suspension spring of a Volkswagen Golf 7 with OEM reference number 1K0511115BD. It is made of SAE 9254 (alloy steel for springs), in compliance with VDA 241-009 standard. The test requirements are as follows: 3 springs to be tested in one day, 50,000 products manufactured per year, testing at 10 Hz and 1 million cycles. Please list what machines I need, what processes I need, a schedule and calculate an approximate budget. The budget cap is € 300 000. The hourly rate for engineers in our company is € 6.5 per hour, for the other staff (technician, administration, project staff, etc.) is € 5 per hour. Please also indicate the brand of the machine. In addition, please identify the main risks involved in the above project"

## 5. Presentation of results

The first result of the experience was that not all the studied apps could handle our request. The ChatGPT, Copilot, Gemini, Claude, Zapier, Taskade and the Stepsize platforms gave reasonable responses, while the Kuki Chatbot and Ayanza failed to provide suitable results for the task. Very politely, Ayanza, responded that next time, if we will ask it for a non-technical task, it will probably be able to help us. If we study those AI environments with reasonable suggestions, we can observe many similarities. The differences are mainly in the time and cost estimations. In **Table 1** we summarize the main data provided by the studied systems. As we show on the tables above, almost all of the fatigue test environments recommended one of the MTS devices, except for the Copilot environment, which clearly recommended a more cost-effective solution. A comparison of the proposed project durations shows that the recommended values vary from an optimistic 1 month (Gemini) to 4 months.

The comparison between the provided schedules is shown on **Figure 1.** Here we can see the differences between the length of the proposed projects. We have used the arithmetic mean of each proposed task in order to make possible the comparison. It is obvious that the apps were not able to calculate an accurate duration of the project. In project management, there is a special literature only estimating durations. There are complex mathematical formulae and algorithms, and also many rules of thumb of practitioners to make a schedule.

Given the relative simplicity of the project, there is obviously no significant difference in the proposed roles and number of project team members. Generally speaking, all the platforms highlighted engineers, technicians and project managers as necessary staff, while the quality engineer was only mentioned by Claude.

**Table 1.** *Comparison of responses from AI platforms*

| | Suggested test equipment | Budget (euró) | Duration (months) | HR needs (persons) |
|---|---|---|---|---|
| **ChatGPT** | Instron 8800, MTS Criterion | 145 000 | 3-4 | 4 |
| **Copilot** | Zwickroell, Admet | 81 400 | 2-3 | 5 |
| **Gemini** | MTS, Shimadzu | 169 000 | 1-2 | 7 |
| **Claude** | Instron Electropuls, MTS Landmark | 177 840 | 3 | 4 |
| **Taskade** | MTS System, Instron | 175 500 | 3-4 | 6 |

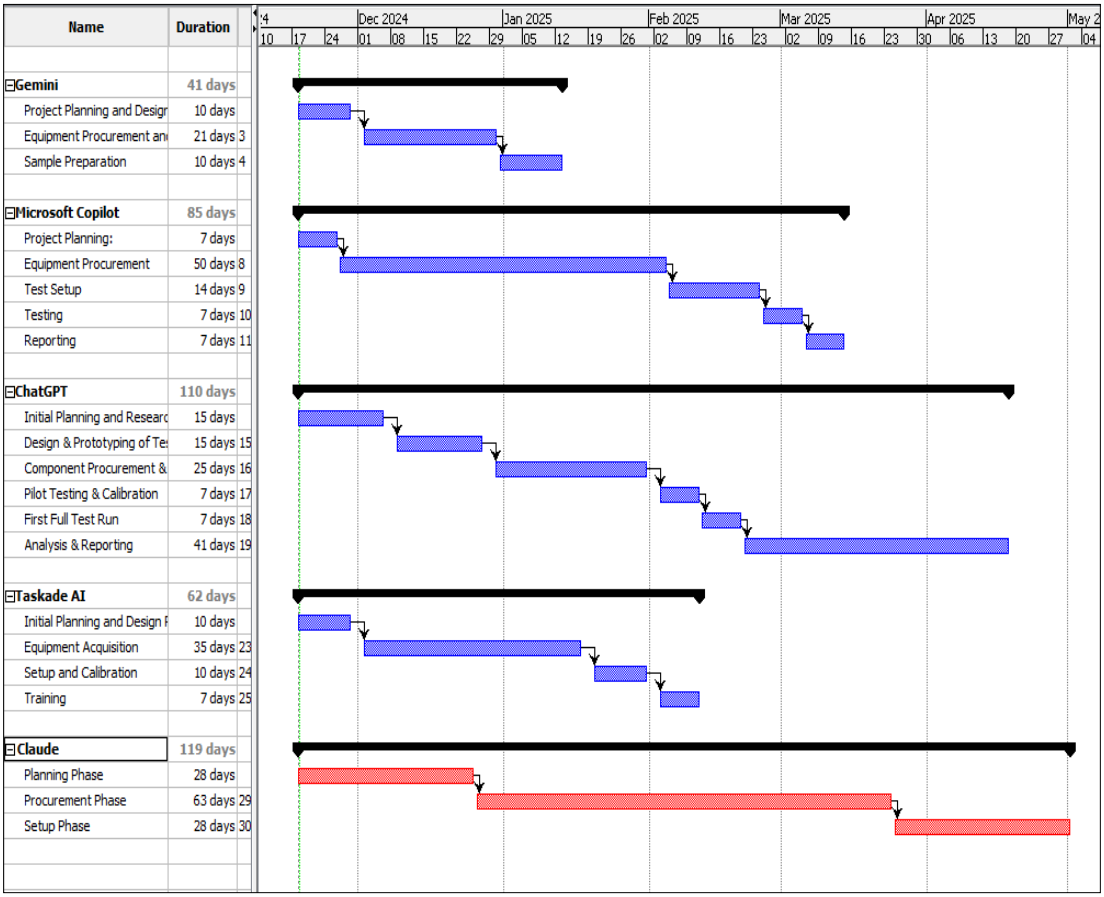


**Fig. 1.** *Comparison of schedules.*

Administrative staffing needs were identified by Copilot, Gemini and ChatGPT. In each case only one person was proposed. Two apps, Gemini and Taskade, suggested the need for more engineers and more technicians. Both platforms proposed 3 engineers and 2 technicians. In reality, it is likely that these roles could be covered on a part-time basis, the proposed values and justifications were used to define a job that clearly covered the tasks, without reference to the human resources already available in the respective areas.

In the introductory part of our paper, we highlighted that although we deal with a small slice of project management, even within this, an important subdomain is the study of AI support in risk identification. Even the single prompt we have formulated gives arguments for the possible use of AI in identifying potential risks.

Based on the responses, we found that the data on risks also show a relatively large variation. However, the responses are in line with the literature background. The simplest answers were from ChatGPT and Copilot. The most detailed response was provided by Taskade. **Table 2** summarises the responses provided by the platforms.

**Table 2.** *Risk results*

| | NR[1] | RP[2] | D[3] |
|---|---|---|---|
| **ChatGPT** | 5 | No | Low |
| **Copilot** | 5 | No | Low |
| **Gemini** | 14 | No | Low |
| **Claude** | 5 | Yes | Medium |
| **Taskade** | 12 | No | High |

[1] *NR= Number of risks identified,* [2]*RP= Risk mitigationproposal ,* [3]*D= Level of detail*

From the table above, we can also see that the Claude environment was beside the identification of certain risk factors, also suggested risk mitigations as well. In terms of the number of risk factors identified, Gemini was the best, it identified 14 risk factors. We noticed all apps showed the evident intention to group certain risks – as happens in practice, in real risk evaluation processes. The reason for grouping, is not only that it provides, although indirectly, suggestions on how to address risks, but also that it makes it possible to assign resources to handle these groups together. Risk management requires often significant human and financial resources. By grouping, an optimization can take place so the risks can be managed more effectively. Only the critical risks should be managed separately.

Our experiment proves that it is advisable to use AI in project planning, even if we have previous experiences gained in similar projects. An inquiry related to risks can be used as a guide or as a checklist during the risk identification process. In such cases, it may be interesting to compare the project manager's own experience with what the solutions indicated by AI. In cases where we do not have any starting point, AI can alert us to risks that are very difficult to think about in the absence of experience. So, for example, in our case, being a completely new task of purchasing fatigue test equipment, the risk factor identified by ChatGPT of springs with possible material defects during the calibration process was a surprise risk factor. It became clear to us that AI can be an important tool for predictive project planning.

The first search was performed on 16 November 2024, but when we repeated the search, we found that the results were different. The data shown in this paper is based on the data generated on 18 November 2024. From a methodological point of view, we might have some concerns due the difficulty in reproducing the experiment for further reference. It is not like the case of a technical measurement experiment or a social study on the same sample. Here, the experiment once repeated will never deliver exactly the same results. Nevertheless, interesting findings can be made and conclusions can be drawn. At the same time, since we have recorded the responses to the prompts during our experiment, it will be possible, in a way, to do longitudinal research in the future to analyse the evolution of AI platforms. With scientific rigour, we can try to analyse the evolution of each platform over time based on a single prompt. Further interesting analyses can be made by asking the question firstly in English, a very common language in the field of AI, and later in a less common language. We used the Hungarian language, being the mother tongue of the authors and a language with a difficult and unusual vocabulary and grammar. Hungarian is relatively less spoken worldwide, but still a fair amount of tech data is available. It is not the subject of this paper, but there are obvious differences between the Hungarian and English answers provided by the studied apps. The data presented in this paper shows only the responses in English.

The fact that for a given prompt, even within a few minutes of each other, we get different results in some details, even on the same platform, only reinforces the well-known fact that data provided by AI in both scientific and practical contexts should be treated with due caution. This applies primarily to the Large Language Model based AI, and is largely not true for specific AI applications developed for medical, engineering or other domains (e.g. diagnostics based on image processing).

## 6. Conclusions

During our case-study presented here, we have attempted to show, through a relatively simple example, that artificial intelligence can now be a tool in project management. It can support the planning and scheduling of new and unfamiliar technical projects, and, as well, in the cases we might have previous experience. We experienced, that AI has been able to propose a technically accurate schedules, identify key activities, calculate durations and costs. It was able to identify important tasks and the right sequence of these operations. Unfortunately, partially due to simplicity of this project, the AI did not propose parallel operations. Under normal circumstances a project manager will try decrease the overall duration by creating parallel tasks. However, the estimates duration and costs can provide useful data for project planning, even if the data are clearly not accurate as expected. Note that the

case study presented – in order to be able to compare the results – is based on a single question (prompt). This single prompt provided useful, interesting data to the project managers. Under real circumstances, there are no restrictions to have a conversation between the platforms and the project design team. In fact, there are tools available, some of them platform-dependent, to refine the first results. In fact, the simplest tool available in each case is to have conversation and improve the results based on received answers. If the prompt did not provide satisfactory answers, there is always the possibility for improvement through further inquiries. In our experiment, for comparability reasons, we had to forego this possibility and condense everything into a single prompt. We just asked for support primarily to identify tasks and estimate their duration, conceive schedules, identify resources. Furthermore we were interested about the availability of each resource. The provision of data on timetables has proved relatively useful. We have seen that AI can provide significant help, right from the planning phase, in identifying and managing the risks that may arise during the project. Simulations highlight potential areas of vulnerability and allow adjustments to be made. This may obviously lead to a better use of resources during the execution of the project, increasing the likelihood of project success. Although only a limited number of specific answers related to risks were obtained, the few risk factors identified could form the basis for identifying specific risk groups, or a more detailed and precise list could be drawn up after further questions might been asked.

As conclusion we may state, that as artificial intelligence develops, new opportunities in the field of project management are also emerging, shaping an already dynamic field. The vast amount of data analysed by AI can shed light, recognise patterns and correlations, and by looking at data from countless previous projects, it can provide the project manager with previously unimaginable analyses. Through machine learning, AI can therefore take data-driven decision making to a new level and become an indispensable tool for pro-active planning of complex projects.

However, we have also seen evidence that, beyond the indisputable benefits listed, the reliability of the data is questionable, and that it is not currently possible to rely solely on AI for risk analysis, nor even for scheduling and cost planning. The provided results may differ depending on which AI environment was queried. We can posit, using the data provided by AI is risky and may in itself generate new risks. Still, artificial intelligence offers opportunities that were not previously possible. Identifying and mitigating risks has traditionally relied on human expertise and experience. A fundamental characteristic of any project is its innate relatively high risk. Projects are unique, and therefore must handle a novel situation through a complex set of activities. Therefore, success depends on the ability to navigate the sea of potential risks. This is where artificial intelligence may offer assistance and sometimes solutions. As an overall conclusion we can state that AI, used with care, can support project design activities and may reduce the risk of failure. The presence of artificial intelligence in project management is no longer an experiment, but a real, powerful, day-to-day tool that is difficult to avoid.

Our paper has examined a very small slice of project management, so the conclusions drawn here are obviously not representative. Our intention was to demonstrate that AI and large language models can be used to schedule certain engineering projects. Since we recorded the responses to the prompts during our experiment, a longitudinal study will allow us to analyse the evolution of AI platforms. Thus, we can try to examine the evolution of each platform over time, based on a single prompt with scientific objectivity. We are confident, that the relatively short time between the date of our experiments and the date of publishing the present article, already gives to the reader, and to the authors, the opportunity compare the development of the studied platforms.

## References

[1] Rodrigues R.: *Legal and Human Rights Issues of AI: Gaps, Challenges and Vulnerabilities*. Journal of Responsible Technology, 4. (2020) 100005. https://doi.org/10.1016/j.jrt.2020.100005

[2] (EU) 2024/1689 rendelet: A mesterséges intelligenciára vonatkozó harmonizált szabályok megállapításáról szóló rendelet, Európai Unió, 2024. https://eur-lex.europa.eu/legal-content/HU/TXT/?uri=CELEX:32024R1689

[3] Hadi M.U., Al-Tashi Q., Qureshi R., et al.: *Large Language Models: A Comprehensive Survey of Its Applications, Challenges, Limitations, and Future Prospects.* TechRxiv. (2024). https://doi.org/10.36227/techrxiv.23589741.v6

[4] Russell S., Norvig P.: *Artificial Intelligence: A Modern Approach*. 2. ed. Pearson Education, 2020.

[5] Suzuki M., Matsuo Y.: *A Survey of Multimodal Deep Generative Models*. Advanced Robotics, 36/5–6. (2022) 261–278. https://doi.org/10.1080/01691864.2022.2035253

[6] Projektmenedzsment útmutató. 6. kiadás. Akadémiai Kiadó, 2020. ISBN: 978 963 454 501 9

[7] Royer P. S.: *Risk Management: The Undiscovered Dimension of Project Management*. Project Management Journal, 31(1), (2000) 6–13. https://doi.org/10.1177/875697280003100103

[8] Taboada I., Daneshpajouh A., Toledo N., de Vass T.: *Artificial Intelligence Enabled Project Management: A Systematic Literature Review*. Applied Sciences, 13/8. (2023) 5014. https://doi.org/10.3390/app13085014

[9] Bellam S.: *Robotics vs Machine Learning vs Artificial Intelligence: Identifying the Right Tools for the Right Problems*. Credit & Financial Management Review, 24/2. (2018) 1–10.

[10] Wang Q.: *How to Apply AI Technology in Project Management*. PM World Journal, 8/3. (2019).

[11] Shen Q.: *AI-Driven Financial Risk Management Systems: Enhancing Predictive Capabilities and Operational Efficiency.* Applied and Computational Engineering, 69. (2024) 134–139. https://doi.org/10.54254/2755-2721/69/20241494

[12] Warin T., Stojkov A.: *Machine Learning in Finance: A Metadata-Based Systematic Review of the Literature.* Journal of Risk and Financial Management. 14. (2021) 302. https://doi.org/10.3390/jrfm14070302

[13] Subramaniyan M., Skoogh A., Bokrantz J., Sheikh M. A., Thürer M., Chang Q.: *Artificial Intelligence for Throughput Bottleneck Analysis – State-of-the-art and Future Directions.* Journal of Manufacturing Systems, 60. (2021) 734–751. https://doi.org/10.1016/j.jmsy.2021.07.021

[14] Pan Y., Zhang L.: *Roles of Artificial Intelligence in Construction Engineering and Management: A Critical Review and Future Trends*. Automation in Construction, 122. (2021) 103517. https://doi.org/10.1016/j.autcon.2020.103517

[15] Santos J. I., Pereda M., Ahedo V., Galán J. M.: *Explainable Machine Learning for Project Management Control.* Computers & Industrial Engineering, 180. (2023) 109261. https://doi.org/10.1016/j.cie.2023.109261

[16] Moussa A., Ezzeldin M., El-Dakhakhni W.: *Predicting and Managing Risk Interactions and Systemic Risks in Infrastructure Projects Using Machine Learning*, Automation in Construction, 168. (2024) 105836. https://doi.org/10.1016/j.autcon.2024.105836

[17] Odejide O. A., Edunjobi T. E: *AI In Project Management: Exploring Theoretical Models for Decision-Making and Risk Management*. Engineering Science & Technology Journal, 5/3. (2024) 1072–85. https://doi.org/10.51594/estj.v5i3.959

[18] Prasetyo M. L., Peranginangin R. A., Martinovic N., Ichsan M., Wicaksono H.: *Artificial Intelligence in Open Innovation Project Management: A Systematic Literature Review on Technologies.* Applications, and Integration Requirements, Journal of Open Innovation: Technology, Market, and Complexity, 11/1. (2025) 100445. https://doi.org/10.1016/j.joitmc.2024.100445

[19] Simón C., Revilla E., Sáenz M. J.: *Integrating AI in Organizations for Value Creation through Human-AI Teaming: A Dynamic-Capabilities Approach*. Journal of Business Research, 182. (2024) 114783. https://doi.org/10.1016/j.jbusres.2024.114783

[20] Patel N: *Practical Project Management for Engineers.* Artech House Publishers, 2023

[21] Ehrlinger F., Ehrlinger L., Ehrlinger L., Geist V., Ramler R., Sobiezky F., Zellinger W., Brunner D., Kumar M., Moser B: *AI System Engineering—Key Challenges and Lessons Learned.* Machine Learning and Knowledge Extraction, 3/1. (2021) 56–83. https://doi.org/10.3390/make3010004

[22] OpenAI, ChatGPT chatbot, 2025. (accessed on: 2025. jan. 2.) https://chatgpt.com

[23] Google, Gemini AI assistant, 2025. (accessed on: 2025. jan. 2.) https://gemini.google.com/app

[24] Microsoft, Copilot AI, 2025. (accessed on: 2025. jan. 2.) https://copilot.microsoft.com

[25] Anthropic, Claude AI, 2025. (accessed on: 2025. jan. 2.) https://claude.ai

[26] OpenAI, About OpenAI, 2025. (accessed on: 2025. jan. 2.) https://openai.com/about/

[27] Ayanza, Ayanza AI Assistant, 2025. (accessed on: 2025. jan. 2.)
https://ayanza.com

[28] Stepsize, GenAI, 2025. (accessed on: 2025. jan. 2. https://www.stepsize.com)

[29] Zapier, Zapier AI chatbot, 2025. (accessed on: 2025. jan. 2.)
https://zapier.com/ai/chatbot

[30] ICONIQ+Pandorabots, Kuki AI, 2025. (accessed on: 2025. jan. 2.)
https://www.kuki.ai

[31] Taskade, Taskade AI, 2025. (accessed on: 2025. jan. 2.)
https://www.taskade.com

Műszaki Tudományos Közlemények vol. 22. (2025) 10–16.
DOI: Hungarian: https://doi.org/10.33895/mtk-2025.22.02
English: https://doi.org/10.33894/mtk-2025.22.02

# DESIGN OF A BRAKE AND BRAKE ASSIST SYSTEM FOR AN ELECTRIC RACE CAR

Bálint BORBÉLY,[1] Attila SZÁNTÓ,[2] Szabolcs Sándor DIÓS,[3] Géza HUSI[4]

[1] *Debrecen University, Faculty of Engineering, Department of Vehicles Engineering, Debrecen, Hungary, borbelybalint26@gmail.com*

[2] *Debrecen University, Faculty of Engineering, Department of Basic Technical Studies, Debrecen, Hungary, szanto.attila@eng.unideb.hu*

[3] *Debrecen University, Faculty of Informatics, Debrecen, Hungary, dios.szabolcs@eng.unideb.hu*

[4] *Debrecen University, Faculty of Engineering, Department of Vehicles Engineering, Debrecen, Hungary, husigeza@eng.unideb.hu*

**Abstract**

The project investigates the conversion of a Toyota MR2 W10 passenger car. The aim was to replace the car's original braking system with a more modern one, so that the car's braking system could cope with more demanding conditions than planned in competition. The design took into account the stresses on the braking system and the adhesion and friction coefficients.

**Keywords**: *prototype electric race car, brake system, brake assist system, design.*

## 1. Introduction

DEAC Motorsport has been competing in the Slalom Championship organised by the MNASZ for more than 4 years. During this time we have won several races in several categories.

In the future we would like to compete in other categories with vehicles of our own design. As part of this, we have started the modification of a Toyota MR2 at the University of Debrecen, Faculty of Engineering.

The project consists of several parts, the current study is on the braking system. The vehicle is represented in **Figure 1**.

First, we looked at the original brake system. The front disc is 252 mm in diameter and has a floating caliper. According to the factory data, the braking distance from 100km/h to a stop is 44 metres. This is 32-35 metres for today's cars with ABS.

## 2. Modification of the vehicle braking system

The force on the disc of the original brake system is calculated as follows, depending on the factory values:

– Hydraulic pressure ($P$): 80 bar
– Piston diameter ($d$): 51 mm
– Coefficient of friction ($\mu$): 0,3
– Number of pimps ($n$): 1
– Effective radius of brake disc ($r$): 0,12 m **[2]**.

Pumping surface calculation **[3]**:

$$A = \pi d^2/4 \quad (1)$$

The force exerted by the brake lining:

$$F_r = P \cdot A \cdot n \quad (2)$$

**Fig. 1.** *Toyota MR2* **[1]**

The force on the brake disc is given by the force exerted by the brake pad multiplied by the coefficient of friction:

$$F_f = \mu \cdot F_r \quad (3)$$

Torque applied by the braking force on the brake disc:

$$M = F_f \cdot r \quad (4)$$

The same principle is used to determine the braking force of the new braking system to be installed.

We had several options for the design of the Toyota MR2 braking system. One is to design a new one from scratch, the other is to transfer it from an existing vehicle. As the University owns several vehicles, the braking system will be transferred from an Opel Vectra C car. However, it should be noted that this modification will also change the behaviour of the vehicle.

The EBC Orangestuff brake pad will probably be the biggest change, as it has a coefficient of friction of 0.5, which can rise to over 0.6 under load. The other changes are the brake disc diameter, which increases to 285 mm, and the brake piston size, which increases to 57 mm.

The force on the disc of a modified brake system can be calculated using the formulae described above [2].

Basic values of the modified braking system:
– Hydraulic pressure ($P$): 80 bar
– Piston diameter ($d$): 57 mm
– Coefficient of friction ($\mu$): 0.5
– Number of pimps ($n$): 1
– Effective radius of brake disc ($r$): 0.135m.

The next step was to modify the caliper to accommodate the new caliper stirrup. The wheel bearing's splitter circle is 4×100, which means that there are 4 holes on a 100 mm diameter circle. The brake disc to be installed has a 5×110 pitch circle, therefore a pitch circle modifier (Figure 2) must be placed between the brake disc and the wheel bearing.

To facilitate scaling, we created a pattern splitter modifier in Solid Edge [5], and printed it from STL format using a 3D printer.

For 3D printing, we used a machine with FDM (Fused Deposition Modelling) technolog [6] Since it is a vehicle part, ABS+ industrial plastic was chosen as the pattern splitter modifier. It is important to point out that 3D print (Figure 3) is only a "sample" and not a final component to be incorporated.

In order to mount the brake caliper unit on the stub, an adapter has to be made. With the factory caliper clamp, only the smaller brake pads could be used, which would not grip the full extent of the brake disc, and the caliper would also have less force to exert.

The Vectra C caliper, on the other hand, has a larger piston diameter and the brake pads have almost double the area of the Toyota MR2 brake. However, with the increase in disc diameter and the change in pitch, the factory rims will not be compatible with the car, so 5×110 or possibly 5×112 rims can be fitted, and 5×112 rims require the use of conical wheels. The holes for the 2 mounting bolts on the caliper bracket almost match the holes on the wheel studs, but there is a slight difference. The distance between the holes on the wheel hub is 130 mm, while the distance between the holes on the stirrup is 125 mm.

**Fig. 2.** *The pitch circle modifier.* [4]

**Fig. 3.** *3D printed pattern splitter.*

The holes are the same size, with 12 mm diameter holes in both the stub and the stirrup, but threads are only in the stirrup, with a thread pitch of 1.25 mm (**Figure 4**).

The first brake pad chosen was the EBC DP41414R „Yellowstuff" **[7]** racing brake pad. This brake pad is designed for track use, mainly for slalom and mountain racing (**Figure 5**).

Generally, the brake pad of choice has a friction coefficient of 0.6, is above 800 degrees Celsius and is fail-safe. EBC brake pads are typically free of health-damaging material **[7]**.

The handbrake in this case is a bowden cable, so it can be operated with a custom-made bowden cable that can be folded in the car. It is important that the cables are the same length, so that the two calipers apply the same amount of brake on both sides of the handbrake at the same time. The car's handbrake lever has a sensor in it, which was designed so that if the handbrake was applied with the ignition on and the engine running, it activated an indicator light on the instrument panel to show that the handbrake was applied.

This will also be provided with a circuit breaker after the electric motor has been installed, which breaks the connection between the "throttle" and the motor controller. This means that when the handbrake is applied, the accelerator pedal will not transmit a signal to the motor controller, thus protecting the motor and the rest of the drive train. There will also be an indicator light in the dashboard that will illuminate when the handbrake is applied, as the car is currently just an empty body with no dashboard.

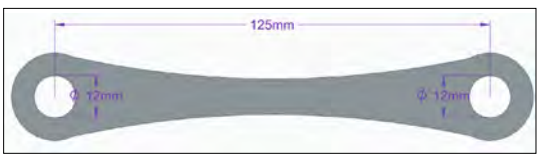


**Fig. 4.** *Distance between holes on the console.*

## 3. Brake „Line-lock"system

The brake line lock system, or "line-lock system", is used to lock the front or rear brake circuit so that the circuit does not receive the hydraulic pressure and only the open circuit will apply the braking force when the brake pedal is depressed (**Figure 6**).

The universal kits can be installed one brake hose at a time and operate on a 12V system **[8]**.

When locked, the indicator light illuminates to indicate to the driver that the brake circuit is not in use. The car will be fitted with 2 sets of rear brakes. The end will be connected to a cap-switch, so that the entire rear brake system can be locked at the push of a button.

This is necessary because the car will run on racing tyres, whose operating range is temperature dependent. The sudden rise in surface temperature is achieved by a process known as rubber burnout. During a burnout, the driven wheels, in this case the rear and rear wheels, spin while the car is held stationary with the brakes on. In the absence of a brake hose locking system, the rear brake would also be applied, providing both propulsion and deceleration, which would put a heavy load on both the drivetrain and the brake. If the car is fitted with this system, the rear brake can be locked before the tyre is burnt and only the front brake will engage during the warm-up, allowing the car to remain stationary and reducing the load on the driveline as there will be no braking force on the rear axle.

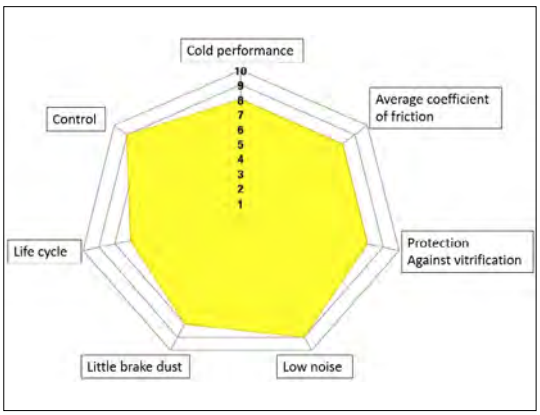


**Fig. 5.** *EBC DP91414 performance chart* **[7]**

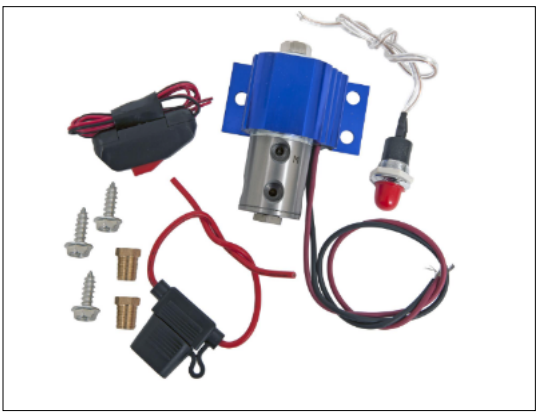

**Fig. 6.** *Brake „Line-lock" system kit* **[8]**

## 4. Electric vacuum pump brake assist

The car is equipped with brake assist, so that comfortable and powerful braking can be achieved with the factory system, but due to the lack of an internal combustion engine (as the brake assist in this version is supplied from the intake manifold) it is inoperable in its current state.

We first looked into the brake assist solutions used in today's electric cars. There are several solutions used by car manufacturers, in lower-end cars a conventional vacuum brake booster is used and an electric vacuum pump supplies the brake booster with the necessary vacuum of around 0.8-1 bar [9] (Figure 7).

This solution is also applicable here, as the car has a 12V electrical system. These pumps can be operated in 2 ways, with regulation and with control (Figure 8).

Fig. 7. *Electric vacuum pump.* [9]

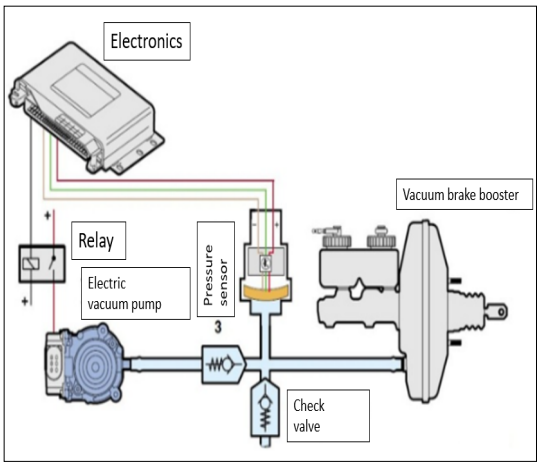


Fig. 8. *Electric vacuum pump circuit.* [10]

## 5. Vehicle validation by simulation measurement

Since vehicle redesign is a multi-step process and several developments take place in parallel, a virtual model had to be created for the preliminary vehicle test (Figure 9).

For this purpose Automation [11] developed by Camshaft Software and BeamNG.Drive [12] were used. Both programs are widely used for testing engines and vehicles.

First, in Automation, the original and modified brakes were adjusted to give the calculated brake force. All tests were simulated at 8:52 a.m. in sunny weather with no wind. The ambient air temperature is set to 25°C. Gravity acceleration: 9.81m/s$^2$. The asphalt of the track used for the tests and simulation has a coefficient of friction of 0.98 and a coefficient of sliding friction of 0.7.

***Factory brake simulation:***

First, we took the factory brake data. The red solid line indicates the front brake force, while the blue line indicates the rear brake force. On the left is the brake force in N and below is the vehicle's speed.

The weight of the car in this case is 1090kg with 252mm diameter discs at the front and 240mm diameter discs at the rear. The dashed lines show the grip limit for the tyres. All factors are included in these values, including downforce and even centre of gravity drift (Figure 10).

The following figure shows the braking time. The left side shows the speed of the vehicle, while

Fig. 9. *Toyota MR2 BeamNG.Drive.*

the bottom side shows the time elapsed since the brake pedal was depressed (Figure 11).

The car will stop from its top speed in almost 7 seconds, and its stop from 100-0 km/h will be 44 metres. The tyre is 185/55R15 street rubber.

***Electric Toyota MR2 with modified brakes:***

The next step was to enter the data of the car being developed. As it will be fitted with fibreglass batteries and the internal combustion engine will be replaced by an electric motor and a battery, there will be a change in both centre of gravity and weight.

This reduces the weight of the car to 958 kg. A modified brake caliper is also fitted, so the diameter of the brake discs is now 285 mm at the front and 278 mm at the rear.

The red solid line (Figure 12) indicates front brake force, while the blue line indicates rear brake force. On the left is the braking force in N and below is the vehicle speed.

The dashed lines also indicate the grip limit of the rubber, which has also increased since the tyres have been replaced with 305/30ZR15 semi-slick tyres, the size we like to use in races.

From the Automation program, you can directly transfer the finished models to BeamNG.Drive, where you can use the designed cars on the road. So we continued in this program and tested the credibility of the data provided by Automation on the asphalt road.

The test consisted of 4 races and the best time counted. One race consisted of accelerating to 100 km/h and then braking completely. This was followed by the same from 150 km/h. In addition, the temperature of the brake discs was monitored continuously.

First the measurement was done with the factory data.

The brake disc temperature was imported into an Excel spreadsheet with a sample of 1 second (Table 1. and 2.).

**Table 1.** *Braking from 100km/h for the first time*

| Temperature | Rear brake | Front brake |
|---|---|---|
| Surface | 118 °C | 137 °C |
| Internal | 108 °C | 130 °C |

**Table 2.** *Braking from 100 km/h for the fourth time*

| Temperature | Rear brake | Front brake |
|---|---|---|
| Surface | 208 °C | 243 °C |
| Internal | 186 °C | 226 °C |

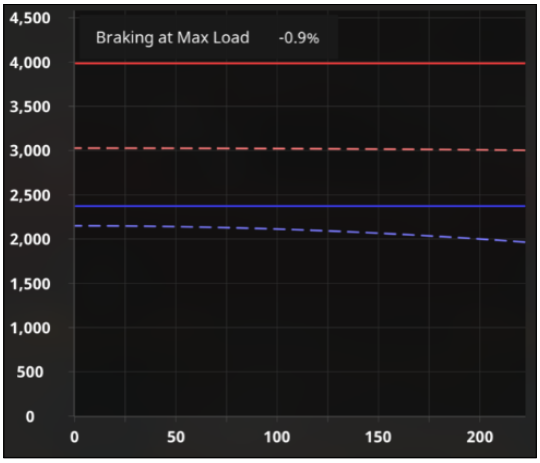


**Fig. 10.** *Simulated factory brake performance.*

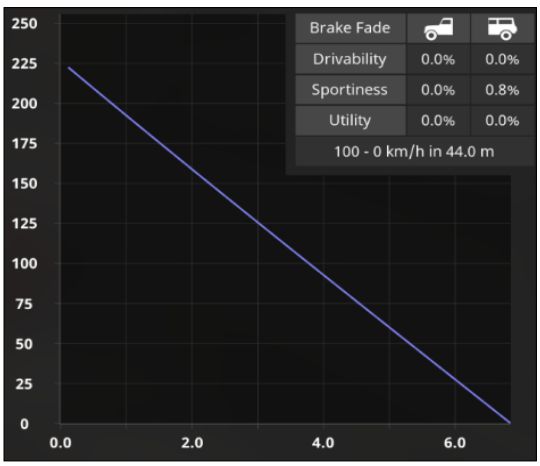


**Fig. 11.** *Gactory braking distance.*

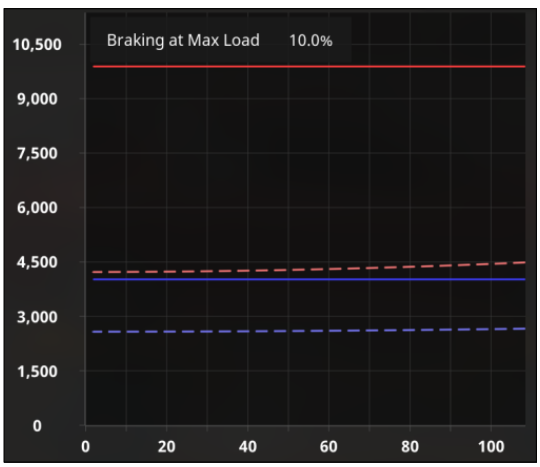


**Fig. 12.** *Simulated performance of modified brake.*

Afterwards, the braking data with the modified brakes were examined (**Table 3.** and **4.**).

**Table 3.** *Braking from 100km/h for the first time*

| Temperature | Rear brake | Front brake |
|---|---|---|
| Surface | 143 °C | 218 °C |
| Internal | 144 °C | 208 °C |

**Table 4.** *Braking from 100 km/h for the fourth time*

| Temperature | Rear brake | Front brake |
|---|---|---|
| Surface | 119 °C | 292 °C |
| Internal | 119 °C | 278 °C |

As you can see, the rear brake doesn't heat up much, the centre of gravity is too far forward, and the braking of the electric motor makes it easier for the rear brake to do its job, plus it also recovers energy. This can be controlled very well with the iBooster.

## 6. Digital infrastructure & developments

The University of Debrecen, Faculty of Technology has made significant developments in recent years, and thanks to the new infrastructure, developments have been launched in a number of directions. In the Vehicle Manufacturing Laboratory, the renovation of old machine units with AI functions has started **[13]**. Furthermore, just as we have applied digital models to the vehicle crank in our project, Digital-Twin models have been used in education to facilitate teaching **[14, 15]**. And machine learning techniques **[16]** have been used to sort and sort other parts **[17]**, ], which is also important for vehicle manufacturing and development. For composite materials, there are also advances that can contribute to better body manufacturing **[18]**. In the context of vehicle modelling, the collection and processing of telemetric data **[19]** is of particular importance, and with this in mind we have started to build our own Linux distribution-based server **[20]**. In the future, this will allow us to design further vehicle simulation models **[21]**. Furthermore with our 3D printing **[22]** capability, we also have the ability to launch aircraft-related projects **[23]**.

## 7. Conclusion

The braking system should be considered a top priority when it comes to track days, especially if the car will be used exclusively on a race track. It's no use having a high endurance if you can't stop the car and drive it steadily. After all, it is rapid deceleration that you want to experience before every corner, not sudden stops. Thanks to the increased braking force and the semi-slick tyres, the braking distance has been reduced from 44 metres to 29 metres from 100km/h to a stop, according to simulation data. The higher the speed from which the braking is performed, the greater the improvement. Once the parts designed in Solid Edge have been produced and the parts mentioned in the project have been sourced, the construction and modification of the car will begin, together with the other students and DEAC Motorsport team members.

Our aim is to have a finished car for the first race and to test our work so far. The simulation-based validation showed how important it is to have a simulation environment in advance where we can test a braking system developed directly for racing on the basis of recorded data. It is estimated that at higher temperatures, the stopping distance did not deteriorate and the low temperature difference between the internal and friction surfaces shows how good the heat transfer and heat conduction properties of the disc are.

Of course, there is still room for improvement on the vehicle, the ones just outlined are just one of the many.

**Acknowledgements**

We would like to express our sincere gratitude to Timotei Erdei, lecturer at the Department of Vehicles Engineering and head of the Vehicle Engineering Laboratory. Also to the University of Debrecen, Faculty of Engineering.

„SUPPORTED BY THE EKÖP-24-4 UNIVERSITY RESEARCH SCHOLARSHIP PROGRAM OF THE MINISTRY FOR CULTURE AND INNOVATION FROM THE SOURCE OF THE NATIONAL RESEARCH, DEVELOPMENT AND INNOVATION FUND.”

## References

[1] Klug L.: *Visszatérhet a Toyota MR2, ráadásul már nem elektromosként beszélnek róla.* 2023. https://speedzone.hu/visszaterhet-a-toyota-mr2-egyelore-csak-japanban/

[2] MR2-Gen2-UK-launch-pack-1990 [Online] https://media.toyota.co.uk/wp-content/uploads/sites/5/pdf/MR2-Gen2-UK-launch-pack-1990.pdf

[3] Kádár L., Varga F., Kőfalusi P.: *Közúti járműrendszerek szerkezettana.* 2014 [Online]. https://mogi.bme.hu/TAMOP/kozuti_jarmurendszerek_szerkezettana/index.html

[4] Osztókör módosítók adatai általánosan; [Online]: https://www.ebay.com/b/Wheel-Spacers-Adapters-Hub-Centric-Rings-for-Mini-Cooper/122154/bn_7063932216

[5] Goanta A. M., Haraga G.: (2017). *Aspects of Modelling Classical or Synchronous Modelling with Solid Edge ST 9*. MATEC Web of Conferences, 112. (2017) 06024. https://doi.org/10.1051/matecconf/201711206024
[6] Templom T., Erdei T. I., Molnár Zs., Shaw E., Husi G.: *Designing a Delta Tripod Based Robot Fused Deposition Modelling 3 Dimensional Printer Using an Open-Source Arduino Development Platform*; MATEC Web of Conferences, 184. (2018) 02013. https://doi.org/10.1051/matecconf/201818402013
[7] EBC Féktárcs – fékbetét [Online]; https://ebcbrakes.hu/auto-fekbetet-fektarcsa-fekcso/opel-fekalkatreszek/opel-vectra/opel-vectra-1-8-2002-2004-12449
[8] Line-lock rendszer leírás és adatai [Online] https://www.emag.hu/tovbmup-fekzar-elektromos-vezerles-rozsdamentes-acel-kek-sa34749/pd/DQYGSSYBM/
[9] Vákuumszivattyú adatai és paraméterei [Online] https://www.emag.hu/elektromos-vakuumszivattyu-univerzalis-kompatibilitas-12v-a-szerelveny-tartozeka-4-huvelyk-6151045565567/pd/DQJ05JYBM/
[10] Közúti járműrendszerek szerkezettana [Online]: https://www.mogi.bme.hu/TAMOP
[11] Automation - The Car Company Tycoon, Engine and Vehicle Simulator [Online] https://www.automationgame.com/
[12] A. Gambi, M. Mueller, G. Fraser: *AsFault: Testing Self-Driving Car Software Using Search-Based Procedural Content Generation.* 2019 IEEE/ACM 41st International Conference on Software Engineering: Companion Proceedings (ICSE-Companion), Montreal, QC, Canada, 2019, 27–30. https://doi.org/10.1109/ICSE-Companion.2019.00030
[13] Kapusi T. P., Erdei T. I., Husi G., Hajdu A.: *Application of Deep Learning in the Deployment of an Industrial SCARA Machine for Real-Time Object Detection.* Robotics 2022, 11, 69. https://doi.org/10.3390/robotics11040069
[14] Erdei T. I., Krakó R., Husi G.: *Design of a Digital Twin Training Centre for an Industrial Robot Arm*. Appl. Sci. 2022, 12, 8862. https://doi.org/10.3390/app12178862
[15] Erdei T. I., Nusser D. P., Husi G.: *Cyber-Physical Recreation of Six DOF Industrial Robot Arm*. International Review of Applied Sciences and Engineering, 15/2. (2024) 147–160. https://doi.org/10.1556/1848.2023.00660
[16] Chowdhury R. S., Islam M. A., Yusuf D. H. B. M., Amin M. Bin, Hassan M. S., Barua S., Abdullah M.: *Implications of Artificial Intelligence (AI) and Machine Learning-Based Fintech for the Financial Assets Related Traditional Investment Theories.* Journal of Infrastructure, Policy and Development, 8/12. (2024) 7415. https://doi.org/10.24294/jipd.v8i12.7415
[17] Erdei T. I., Kapusi T. P., Hajdu A., Husi G.: *Image-to-Image Translation-Based Deep Learning Application for Object Identification in Industrial Robot Systems*. Robotics, 13. (2024) 88. https://doi.org/10.3390/robotics13060088
[18] Alamry A., Islam M. S., Hamdan S., Anwar M., Abdullah M.: *Enhancing the Performance of Hybrid Bio-Composites Reinforced with Natural Fibers by Using Coupling Agents*. Materials Research Express, 12/3. (2025). https://doi.org/10.1088/2053-1591/ad92f4
[19] Dave G. S., Pandhare A. P., Kulkarni A. P., Khankal D. V., Abdullah M. *Experimental Investigation of Centrifugal Pump Machine and Its Faults through Different Type of DAQ System and Selecting One Based on Statistical Approach.* Cogent Engineering, 11/1. (2024) https://doi.org/10.1080/23311916.2024.2417683
[20] Szántó A., Ádámkó É., Juhász G., Sziki G. Á.: *Simultaneous Measurement of the Moment of Inertia and Braking Torque of Electric Motors Applying Additional Inertia*. Measurement, 204. (2022) 112135. https://doi.org/10.1016/j.measurement.2022.112135
[21] Sziki G. Á., Szántó A., Kiss J., Juhász G., Ádámkó É.: *Measurement System for the Experimental Study and Testing of Electric Motors at the Faculty of Engineering, University of Debrecen*. Appl. Sci. 12. (2022) 10095. https://doi.org/10.3390/app121910095
[22] Masuk A., Diós S. S., Dinya T., Szántó A., Husi G.: *Labor Developments and Methods for Supporting Education in the Cyber-Physical and Intelligent Robot Systems Laboratory.* Műszaki Tudományos Közlemények, 20. (2024) 36–41. https://doi.org/10.33894/mtk-2024.20.07
[23] Masuk A., Géza H.: *Uses of Aero Graphene and CNT in Modern Aircraft.* AIP Conference Proceedings, 2941/1. (2023). 020029. https://doi.org/10.1063/5.0181354

Műszaki Tudományos Közlemények vol. 22. (2025) 17–22.
DOI: Hungarian: https://doi.org/10.33895/mtk-2025.22.03
English: https://doi.org/10.33894/mtk-2025.22.03

# THE RELATIONSHIP BETWEEN AI AND CNC TECHNOLOGY

István György BURAI,[1] György CZIFRA[2]

[1] *Óbuda University, Bánki Donát Faculty Of Mechanica and Safety Engineering, Institute of Mechanical Engineering and Technology, Budapest, Hungary, burai.istvan@bgk.uni-obuda.hu*

[2] *Óbuda University, Bánki Donát Faculty Of Mechanica and Safety Engineering, Institute of Mechanical Engineering and Technology, Budapest, Hungary, czifra.györgy@bgk.uni-obuda.hu*

**Abstract**

Our research focuses on the applicability of artificial intelligence (AI) in the education of CNC programming. In this article, we present the current application areas of AI, focusing on its role in CNC technology. We define what the term artificial intelligence entails and briefly review its application areas. The acronym CNC is interpreted, and we summarize the history of CNC. We examine the potential of artificial intelligence, which we use to support CNC technology, and we present the application of AI in the context of Industry 4.0.

**Keywords***: arificial inteligence, CNC, Industry 4.0.*

## 1. Introduction

Artificial intelligence (AI) is a set of computer algorithms that can mimic human intelligence in performing various tasks. Such activities include learning, problem solving, planning, natural language processing or image recognition. Artificial intelligence can reason and make decisions based on available data without human intervention [1].

Given the current state of development of artificial intelligence, one type is available, called Artificial Narrow Intelligence (ANI), also known as narrow or narrow AI. This type can only perform a specific task, which it can perform more efficiently than a human. It is the highest level of AI currently available. Examples include self-driving vehicles, facial recognition systems, digital personal assistants, language processing AI (Copilot, ChatGPT, Gemini, etc.), or for example a chess game [2].

The next stage of development is Artificial General Intelligence (AGI), which would not only specialise in a single task, but would be able to do complex thinking, learning and adapting in multiple environments. Such a system could understand problems and find creative solutions in a human-like way. AGI is still experimental and its development is a major goal of AI research.

The highest theoretical type is Artificial Super Intelligence (ASI), which would far surpass human intelligence not only in computational capacity, but also in reasoning, decision-making, and even emotional and social intelligence. The functioning of ASI would fundamentally change social and economic systems, but would also raise significant ethical questions. This type of capability exists today on a purely theoretical level, but is an important part of the future AI discourse [3]. Below are listed the technological solutions known to date for this capability:

Machine Learning is an artificial intelligence-based technology that allows computer systems to learn and evolve automatically by processing experience and data, without the need to explicitly program each step. Algorithms recognise patterns in data sets and can use them to make predictions, decisions or classifications. The three main types of machine learning are supervised learning, where the model learns with known input-output pairs. Unsupervised learning, which can discover hidden structures and clustering, and reinforcement learning, where the system develops its decision strategies based on rewards and punishments. Today, machine learning is widely used in applications such as recommender systems (Netflix, Spotify), financial forecasting, health diagnostics, fraud detection and self-driving vehicles.

Deep Learning is a special branch of machine learning that uses deep neural networks. These networks learn from large amounts of data and can perform complex tasks. Examples include image recognition and natural language processing. A special feature of deep learning is that it uses multilayer neural networks that can generate hierarchical representations of data. This allows the system to interpret information at progressively more abstract levels. Deep learning techniques have led to significant advances in machine vision, speech recognition and natural language processing. For example, Convolutional Neural Networks (CNNs) are excellent for image recognition tasks, while Long Short-Term Memory (LSTM) networks are efficient for processing sequential data such as text [4].

Deep learning and computer vision play a key role in the development of self-driving cars. Such systems use convolutional neural networks (CNNs) to process data collected by cameras and sensors. These networks can recognise and interpret the environment, such as road signs, pedestrians, other vehicles and road conditions. Self-driving cars continuously learn and adapt to different traffic situations, increasing safety and efficiency. The use of deep learning and computer vision allows cars to navigate autonomously, avoid obstacles and drive safely without human intervention. Uber and Tesla, for example, have made significant advances in this area and are continuously developing their self-driving technologies [5].

Natural Language Processing (NLP) is a branch of AI that focuses on understanding and generating human language. Applications of NLP include autocorrect and spell-check functions that help correct spelling mistakes and clarify text. In addition, NLP is used for sentiment analysis, which allows the detection and analysis of the emotional content of texts, for example in social media posts or customer reviews. NLP can also be used in question-answering systems that automatically answer users' questions, such as customer service chatbots. In addition, NLP technology is used for text translation, allowing automatic translation between different languages, for example in Google Translate. Other applications of NLP include speech recognition, which enables the conversion of spoken language into text, for example in Siri and Alexa virtual assistants. Some popular NLP software solutions [6]:

- spaCy is a Python-based library that supports more than 72 languages and enables efficient text processing;
- MonkeyLearn is a Machine Learning platform that enables text analysis and data visualization;
- Stanford CoreNLP is a Java-based NLP tool that produces linguistic annotations from text and supports multiple languages;
- IBM Watson is a comprehensive enterprise text analysis solution that can perform a variety of NLP tasks.

Computer Vision allows computers to interpret images and videos. Applications of computer vision include face recognition, object recognition and self-driving cars.

Facial recognition systems can identify and authenticate people by their faces. For example, FaceID technology on Apple devices allows users to unlock their devices using their face. Face recognition is also used in security systems, for example to identify passengers at airports [2, 7].

Object recognition systems can identify and categorise different objects in images. For example, the YOLO (You Only Look Once) algorithm provides high-performance object recognition in real-time applications such as security cameras and industrial automation. In Amazon Go stores, object recognition helps to power automated checkout systems, where customers can simply pick items from the shelves and the system automatically invoices them [8]. Some popular software solutions for computer vision [9]:

- OpenCV is an open source machine learning and computer vision library that contains over 2500 algorithms for various tasks such as face recognition, object identification and tracking moving objects;
- TensorFlow is an open-source machine learning framework widely used in computer vision projects such as image classification and object recognition;
- YOLO is a high-performance object recognition algorithm designed for real-time applications and is widely used in security systems and industrial automation.

Action Planning is the process by which intelligent systems can sense their environment, make decisions and act. Robots are used in various industries and in healthcare. Industrial robots use action planning to optimise manufacturing processes, for example in automotive manufacturing, where robots can sense the position of parts, make decisions about assembly sequences

and perform assembly operations with precision [10]. Healthcare robots use action planning in surgical procedures, such as the Da Vinci surgical system, which can sense the patient's anatomical structures, make decisions about the most optimal cutting paths, and perform surgical interventions with precision [11]. In logistics networks, action planning helps optimize the delivery of shipments, for example, drones can sense their environment, make decisions about the most optimal routes, and deliver packages safely [12]. Agricultural robots use action planning to care for plants, for example, robots can sense the condition of plants, make decisions about the amount of nutrients and water needed, and perform care operations with precision [13].

Artificial intelligence is currently being applied in many areas. The aim is to harness the benefits of AI to improve quality of life, increase problem solving efficiency and support innovation. Here are some areas where AI has been used (**Figure 1**).

This research aims to explore and investigate the potential of artificial intelligence to support CNC technology. The adaptation of AI to some area of CNC technology involves several steps and aspects. The idea of adaptation raises a number of questions. Does AI have solutions that can positively impact CNC technology? Another big question is whether there is an area of CNC technology that can be supported by AI? The first step in this long process is to examine the subjects of adaptation and to identify the key areas and tasks for the application of AI.

## 2. CNC technology

The letters CNC stands for Computer Numerical Control. Manufacturing equipment in which the necessary movements are performed by motor(s) (stepper, servo) without human intervention. The operation of the motor or motors is controlled by a computer, which is called control of the machine tool.

CNC technology is used in the field of machining, in manufacturing processes such as turning, milling, drilling, grinding, where the material removal process is controlled by a computer using programming codes. The computer numerical control machine is the mainstay of modern manufacturing, dating back to the 1940s when the first NC machines appeared.

After the Second World War, the Cold War period focused on the importance of arms production, which called for an increase in the efficiency and productivity of production. In the late 1940s, in 1949, John T. Parsons, an early pioneer in computer science, developed the first concept of numerical control while working on an Air Force research project at the Massachusetts Institute of Technology (MIT).

At MIT's Laboratory of Servomechanisms, an experimental milling machine was built that could be used to produce helicopter blades and stiffer shells for aircraft using motorised shafts. In the 1940s and 1950s, early Numerical Control machines still used a punched tape to input instructions, a common tool for telecommunications and

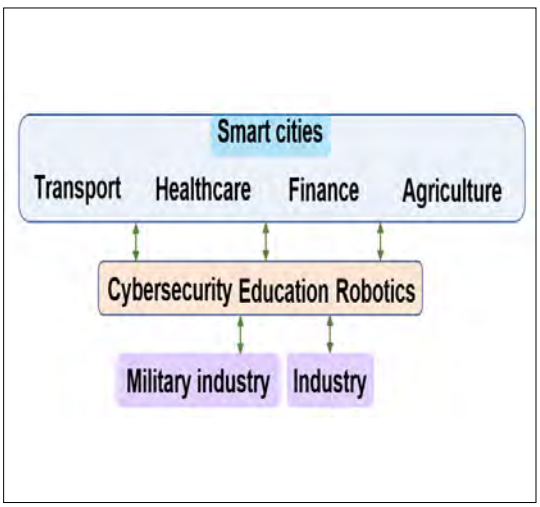


**Fig. 1.** *Areas of use of AI.*

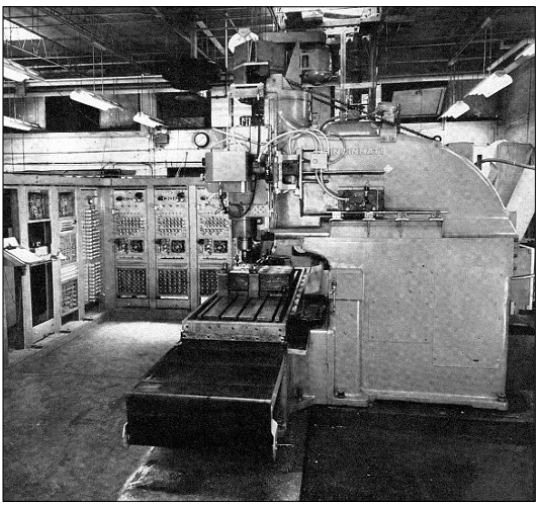

**Fig. 2.** *The first NC milling machine (Cincinnati Milacron Hydrotel).*

data storage at the time. This technology was later replaced by analogue computing.

In 1952, Richard Kegg, in collaboration with MIT, created the first NC milling machine (**Figure 2**), which became known as the Cincinnati Milacron Hydrotel. At this time, NC technology was limited primarily to machining centers.

The 1960s and 1970s saw the emergence of digital technologies, which significantly automated and made manufacturing processes more efficient.

In the 1970s, the use of Computer Aided Design (CAD) and Computer Aided Manufacturing (CAM) brought great advances in CNC machining.

Since the 1990s, CAD and CAM systems have become an integral part of CNC technology, enabling even more precise and flexible manufacturing solutions **[14]**.

## 3. The CNC technology and the AI

The development of machine tools and the associated CNC technology is unique. The result of this evolution is faster, more accurate and reliable part production. Machines with 5-8-10 axes (e.g. turning centre, machining centre) available today enable increasingly complex part production. The current state of CNC technology shows significant advances in intelligent manufacturing systems, especially in the context of Industry 4.0.

Digital twin technology in the CNC industry is based on the creation of exact digital replicas of physical entities such as machine tools, tools, workpieces and manufacturing processes that are synchronised with their physical counterparts through real-time data link. The combination of IoT devices, advanced sensors, data analysis algorithms and simulation tools enables continuous data collection, analysis and real-time monitoring of system health.

The sensors record real-time data on the state of physical systems, such as temperature, pressure or vibration, which is transmitted to central data processing systems via computer networks such as WiFi or industrial Ethernet. Here, cloud computing ensures secure data storage and processing, providing real-time insight into the operation of systems.

Digital twins not only monitor the current state, but can also simulate the behaviour of systems. They can use physics-based simulations to visualise possible changes in processes, such as a machine malfunction or component wear. Artificial intelligence (AI) and data analysis algorithms can detect anomalies, predict failures and suggest maintenance or optimisation actions. The most striking feature of the digital twin is its two-way communication: this technology not only receives data, but also provides feedback, for example with automatic system adjustments or decision-support suggestions. This reduces downtime due to failures while increasing the operational efficiency of the assets.

Using Augmented Reality (AR), digital twins offer visual interfaces that make it easier to quickly identify and deal with errors. For example, a maintenance engineer can monitor the current status of machines with AR glasses. Cyber security, such as data encryption and access control, ensures data protection and authenticity.

The technological innovations of the digital twins will bring new levels of efficiency, sustainability and resilience to industrial operations, contributing to the objectives of Industry 4.0 and reducing environmental impacts **[15]**.

Artificial intelligence is used in many areas of CNC technology, typically to optimise and increase the efficiency of manufacturing processes. Some solutions for the application of AI:

- Tool wear prediction;
- Machining parameter optimisation;
- Predictive maintenance;
- Surface quality prediction;
- Toolpath optimisation.

Tool wear prediction: AI helps predict tool wear in CNC machines, which can increase tool life and improve machining efficiency.

Machining parameter optimisation: AI systems optimise machining parameters such as cutting speed and depth of cut to improve surface quality and reduce energy consumption.

Predictive maintenance: MI enables predictive maintenance of CNC machines, which helps to anticipate machine service needs and minimise downtime.

Surface quality prediction: AI techniques, in particular machine learning and deep learning models, can predict the surface quality of machined parts, which can improve the accuracy and reliability of manufacturing processes.

Toolpath optimisation: AI algorithms can optimise toolpaths, reducing programming time and minimising tool positioning errors. For example, Autodesk Fusion 360 CAM software uses AI to increase the efficiency of CNC programming **[4]**.

## 4. Conclusions

CNC technology is one of the fastest growing players in the industry. Its most active expansion has been in the field of component manufacturing (turning, milling, drilling, grinding) and continues today. The use of manually operated machining centres is now limited to special cases and has been replaced by CNC-controlled production machines. One reason for this is the incredibly rapid change in computer technology. With the advent of artificial intelligence (AI), we can delegate tasks to AI that can make the manufacturing process more efficient, more accurate, safer and improve maintenance planning.

An examination of the current relationship between AI and CNC confirmed the importance of research supporting the collaboration between AI and CNC technology. The involvement of artificial intelligence to support CNC programming is a key element in AI-related research. In addition to existing roles, new potential applications can be formulated to further enhance manufacturing efficiency at any stage of the production process. AI, as a technological assistant, can suggest several alternatives for the manufacturing process of a product and can also enable the creation of flexible part machining codes at the manual CNC programming level.

This research aims to apply artificial intelligence in the field of CNC technology in secondary and university education. The aim of using AI solutions is to increase the quality and efficiency of education, in a way that the application of new technology does not involve extra work and is as safe as possible. The integration of AI in education is a long and complex process, the first task of which will be to identify the characteristics of the related fields (AI, education, CNC) and their adaptation and interaction effects. To do this, I will carry out a SWOT analysis for the three domains. Then, I will treat the three areas as a single entity according to my research objective and investigate their viability through another SWOT analysis. Depending on the results obtained, I will identify the strategically important tasks.

In the context of AI, it is necessary to examine what technologies and applications are currently available, where and in what form AI is used in CNC technology and education. In its current form, is it suitable for the task at hand and to what extent can it solve it? The potential for developing the AI system should be explored. The running environment, software solution, operating principle and learning methodology of the AI should be defined. It is important to explore how available AI systems (e.g. ChatGPT, Gemini, Copilot, etc.) can be integrated into an existing, well-functioning user environment, such as Moodle.

Overall, the involvement of AI in supporting CNC programming is a key element in AI-related research. In addition to existing roles, new potential uses can be formulated to further enhance manufacturing efficiency at any stage of the production process. As a process assistant, AI can suggest several alternatives for the manufacturing process of a product and can also enable the generation and control of flexible part machining program code. This calls for the formulation and research of the role of AI in education and the educational methods related to the development of AI.

## References


[1] Russell S., Norvig P.: *Artificial Intelligence – a Modern Approach.* Series in Artificial Intelligence, Prentice Hall, Englewood Cliffs, NJ, 2009.

[2] Goodfellow I., Bengio Y., Courville A.: *Deep Learning*. Genet Program Evolvable Mach, 19. (2018) 305–307. https://doi.org/10.1007/s10710-017-9314-z

[3] Bostrom N.: *Superintelligence*: *Paths, Dangers, Strategies*. Oxford University Press, 2014.

[4] LeCun Y., Bengio Y., Hinton G.: *Deep Learning*. Nature, 521. (2015) 436–444.

[5] Khurana D., Koli A., Khatter K.: *Natural Language Processing: State of the Art, Current Trends and Challenges*. Multimedia Tools and Applications, 82. (2023) 3713–3744. https://doi.org/10.1007/s11042-022-13428-4

[6] Kuei-Hu Chang: *Natural Language Processing: Recent Development and Applications*. Department of Management Sciences R.O.C. Military Academy, 2002. https://doi.org/10.3390/app132011395

[7] Lynn T.: *Computer Vision Applications.* (2025). https://blog.roboflow.com/computer-vision-applications/ (accessed on: 2025. 04. 09.)

[8] Lynn T.: *Computer Vision Examples.* (2025). https://blog.roboflow.com/computer-vision-examples/ (accessed on: 2025. 04. 09.)

[9] Gao M., Zou G., Li Y., Guo X.: *Recent Advances in Computer Vision: Technologies and Applications.* Electronics, 13 (2024) 2734. https://doi.org/10.3390/electronics13142734

[10] Singh G. & Pidadi P., Malwad D.: *A Review on Applications of Computer Vision*. (2023). https://doi,org/10.1007/978-3-031-27409-1_42.

[11] Gao J, Yang Y, Lin P, Park DS.: *Computer Vision in Healthcare Applications*. Journal of Healthcare Engineering, 2018 Mar 4; 2018:5157020. https://doi.org/10.1155/2018/5157020.

[12] Jalal A. M., Toso E. A. V., Morabito R.: *Integrated Approaches for Logistics Network Planning: a Systematic Literature Review*. International Journal of Production Research, 60/18. (2021) 5697–5725. https://doi.org/10.1080/00207543.2021.1963875

[13] Jiachen Yang, Jingfei Ni, Yang Li, Jiabao Wen Desheng Chen: *The Intelligent Path Planning System of Agricultural Robot Via Reinforcement Learning*. Sensors, 22/12. (2022) 4316. https://doi.org/10.3390/s22124316

[14] Noah Harrison: *CNC History: The Origination and Evolution of CNC Machining*, 2021. https://www.rapiddirect.com/blog/cnc-history/ (accessed on: 2025. 02. 28.).

[15] Daraba D., Pop F., Daraba C.: *Digital Twin Used in Real-Time Monitoring of Operations Performed on CNC Technological Equipment*. Applied Sciences, 14/22. (2024) 10088. https://doi.org/10.3390/app142210088

[16] Kusiak A.: *Smart Manufacturing.* International Journal of Production Research, 56/1–2. (2017). 508–517. https://doi.org/10.1080/00207543.2017.1351644

[17] Teti R., Jemielniak K., O'Donnell G., Dornfeld D.: *Advanced Monitoring of Machining Operations*. CIRP Annals, 59/2. (2010) 717–739. https://doi.org/10.1016/j.cirp.2010.05.010

Műszaki Tudományos Közlemények vol. 22. (2025) 23–26.
DOI: Hungarian: https://doi.org/10.33895/mtk-2025.22.04
English: https://doi.org/10.33894/mtk-2025.22.04

# EQUIPMENT FOR MEASURING CONICAL PARTS

Gergely DAMÓ,[1] László JAKAB-FARKAS,[2] Erzsébet EGYED-FALUVÉGI[3]

*Sapientia Hungarian University of Tranylvania, Faculty of Technical and Human Sciences, Department of Mechanical Engineering. Târgu Mureș, Romania*

[1] *gergelydamo@gmail.com*

[2] *jflaci@ms.sapientia.ro*

[3] *faluvegi.erzsebet@ms.sapientia.ro*

**Abstract**

Tapered components play numerous roles in the devices we use daily and those that surround us, sometimes performing special or even indispensable functions. The aim of this paper is to design and implement a measuring device suitable for determining the taper and taper angle of pin-type tapered components. The basic concept of the measuring instrument is inspired by the sine ruler, while effective measurement is ensured by the displacement of a digital gauge along two perpendicular axes. The data processing is performed by an Arduino microcontroller, which displays the results on an LCD screen. We measured a workpiece with a known taper. The measurement accuracy was verified using hypothesis testing.

**Keywords***: rate of taper, taper angle, sine block.*

## 1. Introduction

In modern manufacturing, precision is essential. Parts must be within certain dimensions, known as tolerances, which are specified by the designer and recorded in the technical documentation. During the manufacturing process, the dimensions of the parts are regularly checked to ensure the required quality. For quality control, universal measuring (e.g., calipers) and/or specialized inspection tools (e.g., gauges) are used.

Tapered parts play a huge role in our daily lives and require special attention and precision in both manufacturing and quality control. This paper deals only with the latter, quality control.

Tapered parts are characterized by their taper, as defined by the international standard ISO 3040-2016. As shown in **Figure 1**, , the taper is the ratio of the difference between two different diameters measured on a length parallel to the taper axis and the length dimension.

The taper is denoted by *C*, which can be written mathematically as:

$$C = \frac{D-d}{L} = 2\mathrm{tg}\frac{\alpha}{2} \qquad (1)$$

The degree of taper can be given as a ratio or in percentage form, and the cone angle can also be interpreted, which is recommended to be specified in degrees.

There are several methods and measuring devices for measuring taper **[3]**, which are discussed in detail in **[2].** The present paper is based on the sine bar, which is an indirect measurement method. It is preferred for its accuracy and simplicity. **Figure 2** illustrates the arrangement of the measuring device during measurement. The sine bar is supplemented with gauge blocks and a dial indicator.

The measured workpiece is placed on the sine bar and raised with the help of gauge blocks until it becomes parallel to the measurement base surface. The parallelism can be checked with a dial gauge. Knowing the distance between the two cylinders of the sine bar and the height of the gauge block, the cone angle of the part can be given by a trigonometric relationship:

$$\sin\alpha = \frac{H}{L} \qquad (2)$$

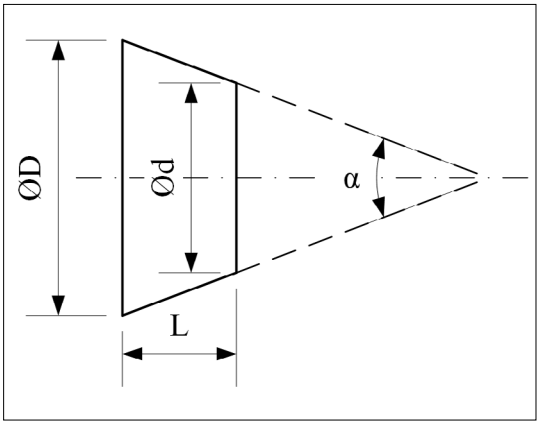


**Fig. 1.** *Interpretation of taper according to ISO 3040-2016.* **[1]**

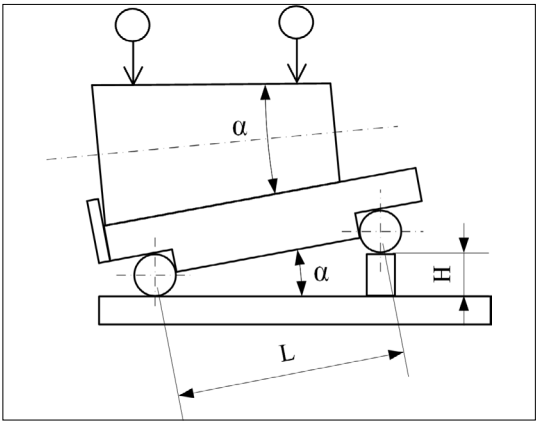


**Fig. 2.** *The sine bar during measurement.* **[2]**

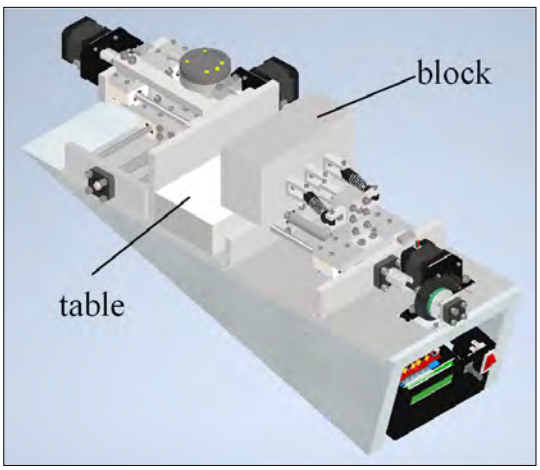


**Fig. 3.** *The 3D model of the designed equipment.*

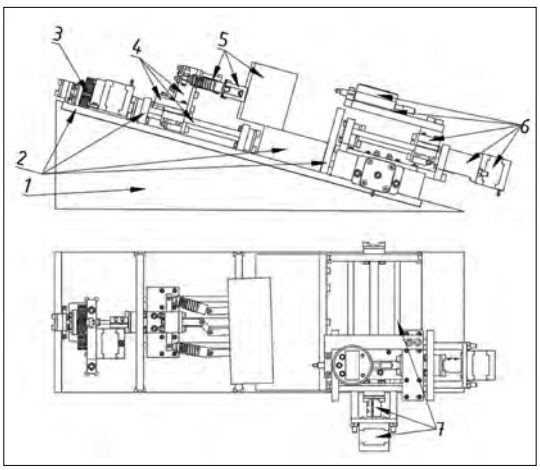


**Fig. 4.** *The construction of the equipment.*

This paper presents the design and construction of a measuring device that provides a fast and simple measurement.

## 2. Overview of the planned system

The main consideration in designing the device (**Figure 3**) is simplicity and accuracy while ensuring a stable and rigid structure.

The whole system is located on a 15° slope. The measured part is placed on the table marked in white, the principle of the sine bar is embodied in the mounting block on the table (**Figure 3**). The effective measurement is done with the help of a digital dial gauge, which taps the workpiece, thus ensuring the principle of the sine bar (**Figure 2**).

The device is divided into 7 units: 1 - the slope, 2 - the base plate and its components, 3 - the sliding clutch unit, 4 - the workpiece fixing unit, 5 - the double articulation unit, 6 - the gauge touch-securing unit, 7 - the gauge positioning unit. The device also includes an LCD display (**Figure 4**), which allows the user to tell how many points to taper the dial gauge, and the taper result is also displayed here.

The movement of the device is controlled by 3 stepper motors, while the associated control and transmission of the measured data is handled by an Arduino Mega and an Arduino Nano. These microcontrollers are located under the slope to be properly protected. The rigidity is provided by metal elements, which increases the accuracy of

the system. The taper gauge can measure pieces up to Φ60 mm in diameter and 160 mm in length.

## 3. The functioning of the measuring system

According to the purpose, the measuring device is used to determine the cone angle of the external tapered rotating surfaces. To do this, the workpiece is placed on the white marked table (**Figure 3**), and the user can select from the menu on the LCD display whether to measure at 4, 5, 6, 10 or 12 points. Before the measurement starts, the probe of the dial gauge is moved to position 0 by the stepping motors. The stepping motor fixes the workpiece by the 4 – fixing unit and the 5 – double articulation unit until the sliding clutch slides. At this point the effective measurement begins, during which the units that move and position the dial gauge are activated.

## 4. Evaluation of the results

### 4.1. A mérendő munkadarab

The measured workpiece is a 3D printed part with the following geometric characteristics (**Figure 1**):

$D = 30$ mm
$d = 10$ mm
$L = 100$ mm
$\alpha/2 = 5.711°$

### 4.2. Determining taper with measuring microscope

The semi-cone angle of the workpiece was measured with a microscope at the Sapientia Hungarian University of Transylvania, Faculty of Technical and Human Sciences – Târgu Mureș.

The resulting semi-cone angle is 5.66°, determined by the direct method. The deviation of the measurement result from the model-determined cone angle value is negligible, 0.05°.

### 4.3. Determination of the taper with the implemented measuring equipment

During the measurement with the measuring device, the system stores the measured points, from which it interpolates a line. The microcontroller calculates the line's axis using the method of the least squares, which is in fact the semi-cone angle of the measured part. From the menu, 4, 5, 6, 10 and 12 measuring points were selected in order and 3 measurements were taken with each of them, summarized in **Table 1**.

**Table 1.** *Summary of the results*

| Num. of pts. | 4 | 5 | 6 | 10 | 12 |
|---|---|---|---|---|---|
| Results [°] | 5.06 | 5.35 | 5.61 | 5.65 | 5.7 |
| | 5.14 | 5.33 | 5.6 | 5.66 | 5.71 |
| | 5.03 | 5.32 | 5.6 | 5.64 | 5.7 |
| Average [°] | 5.07 | 5.33 | 5.6 | 5.65 | 5.7 |
| Deviation * [°] | 0.22 | 0.11 | 0.07 | 0.09 | 0.07 |
| α | 0.05 | | | | |
| $t_{crit}$ | 4.302653 | | | | |
| t | −5.091 | −5.8418 | −2.69087 | −1.1501 | −0.16818 |
| Decision | H1 | H1 | H0 | H0 | H0 |

**the standard deviation values are rounded*

To verify the results of the system, we also used a hypothesis test. It was checked that the deviation of the measurement results from the expected value of 5.71° was negligible at the 0.05 level. The null hypothesis: the average is equal to the expected value; the counter hypothesis: the mean is different from the expected value.

For this we use a t-test, the results of which are also shown in **Table 1**.

The range of acceptance is (-4.3; 4.3). Based on the actual t values, it can be concluded that the average from 4 and 5 touches is significantly different from the expected value of 5.71°, thus the counter hypothesis holds, while the average for 6, 10 and 12 touches does not differ significantly from the expected value.

**Figure 5** illustrates the averages of the measurements.

A value of $R^2 = 0.69$ indicates a strong relationship between the averages and the number of touches.

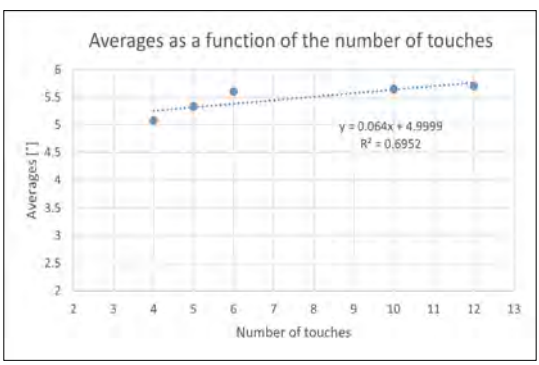


**Fig. 5.** *The averages as a function of the number of touches*

## 5. Conclusions

In conclusion, the designed and realized laboratory equipment shows a close and directly proportional relationship between the number of touch points and the accuracy of measurement (**Figure 5**).

Furthermore, a minimum of 6 probing operations is required to obtain a measurement result with an acceptable accuracy at the specified level.

It should also be noted that at 12 touch points the deviation becomes very small.

## References

[1] ISO 3040:2016 – Geometrical Product Specification (GPS) – Dimensioning and Tolerancing - Cones

[2] Aparin G. A., Gorogyeckij I. E.: *Tűrések és műszaki mérések*. 2. kiadás. Nehézipari Könyvkiadó, Budapest, 1954. 146–161.

[3] Curtis M., Farago F.: *Handbook of Dimensional Measurement.* Industrial Press, Norwalk (CT), 2014.

Műszaki Tudományos Közlemények vol. 22. (2025) 27–31.
DOI: Hungarian: https://doi.org/10.33895/mtk-2025.22.05
English: https://doi.org/10.33894/mtk-2025.22.05

# IMPLEMENTATION OF AN INTERIOR-POINT ALGORITHM BASED ON A KERNEL FUNCTION FOR WEIGHTED LINEAR COMPLEMENTARITY PROBLEMS

Zsolt DARVAY,[1,2] Edina MÁTHÉ[1,2]

[1] *Babeș-Bolyai University, Faculty of Mathematics and Computer Science, Cluj-Napoca, Romania, zsolt.darvay@ubbcluj.ro*

[2] *Transylvanian Museum Society, Department of Mathematics and Computer Science*

**Abstract**

We consider the solution of weighted linear complementarity problems using interior-point algorithms, where the search directions are determined by a specific kernel function. To achieve a more efficient implementation, we modify the theoretically well-performing algorithm. The resulting methods are analyzed using a code written in the Python programming language. We present numerical results for problems whose solutions, based on previous theoretical findings, would require a very high number of iterations.

**Keywords**: *interior-point algorithm, kernel function, weighted linear complementarity problem, search direction, Newton's method.*

## 1. Introduction

The concept of the weighted linear complementarity problem (WLCP) was introduced by Potra [1] in 2012. The WLCP can be defined as follows. Find a pair of vectors $(x, s) \in \mathbb{R}^n \times \mathbb{R}^n$ such that:

$$\begin{aligned} -Mx + s &= q, \\ xs &= w, \\ x,s &\geq 0, \end{aligned} \qquad (1)$$

where $q \in \mathbb{R}^n$ is a given vector, $w \geq 0$ is a given weight vector, and $M \in \mathbb{R}^{n\times n}$ is a given matrix. The WLCP is actually an extension of the linear complementarity problem (LCP), since the special case where all components of the weight vector are zero results in an LCP. The application areas of the WLCP are broad. In particular, the linear complementarity problem arises in the study of mechanical interactions, such as obstacle problems or structural design problems [2]. Moreover, the WLCP is useful in systems where variables or conditions have varying degrees of importance. It is frequently applied in economic modeling, for example in the case of Fisher's market equilibrium problem [1].

To ensure the solvability of the problem described in system (1), the matrix $M$ must satisfy certain conditions. We analyze a variant of these conditions in which the matrix $M$ satisfies the $P^*(\kappa)$ property. A matrix $M$ is called a $P^*(\kappa)$-matrix if there exists a nonnegative real number $\kappa$ such that the following inequality holds for all vectors $x \in \mathbb{R}^n$:

$$(1+4\kappa)\sum_{i\in I_+} x_i(Mx)_i + \sum_{i\in I_-} x_i(Mx)_i \geq 0,$$

where $I = \{1, 2, ..., n\}$,
$I_+ = \{i \in I : x_i(Mx)_i \geq 0\}$ and
$I_- = \{i \in I : x_i(Mx)_i < 0\}$.

To solve this problem, we use an interior-point algorithm. Before proceeding, we introduce some notations. Let $\mathbb{R}^n_+$ denote the set of nonnegative real $n$-dimensional vectors, and $\mathbb{R}^n_{++}$ the set of positive ones. We define $\mathcal{F}$ as the set of feasible solutions, and $\mathcal{F}^0$ as the set of strictly feasible pairs:

$$\mathcal{F} := \{(x,s) \in \mathbb{R}^n_+ \times \mathbb{R}^n_+ : -Mx + s = q\},$$
$$\mathcal{F}^0 := \{(x,s) \in \mathbb{R}^n_{++} \times \mathbb{R}^n_{++} : -Mx + s = q\}.$$

Furthermore, for a given $(x^0, s^0) \in \mathcal{F}^0$, we define the weighted central path, which depends on a parameter $t \in [0,1]$. For this purpose, we introduce the following notation:

$$w(t) = (1-t)w + tx^0s^0. \qquad (2)$$

If we replace the weight vector in system (1) with the expression of $w(t)$ given above, we obtain a solvable system that determines the weighted central path:

$$\begin{aligned} -Mx + s &= q, \\ xs &= w(t), \\ x,s &\geq 0. \end{aligned} \tag{3}$$

If $M$ is a $P^*(\kappa)$-matrix and $\mathcal{F}^0 \neq \emptyset$, then the previously defined parameterized system of equations has a unique solution $(x(t), s(t))$ for each parameter $t \in [0,1]$. The set of these solutions gives the weighted central path assigned to the problem.

If we apply Newton's method to the system of equations (3), we get the following system:

$$\begin{aligned} -M\Delta x + \Delta s &= 0, \\ s\Delta x + x\Delta s &= w(t) - xs, \end{aligned} \tag{4}$$

from which the search directions can be determined.

Next, we introduce the variance vector $v = \sqrt{\frac{xs}{w(t)}}$, which can be used to define a proximity measure to the weighted central path.

To solve the problem, we will use the method of kernel-based interior-point algorithms. A function $\psi$ is called a kernel function if it satisfies the following conditions:

$\psi: \mathbb{R}_{++} \to \mathbb{R}_+$ is twice continuously differentiable, $\psi(1) = \psi'(1) = 0$ and $\psi''(t) > 0$ for all $t > 0$. For a given kernel function, the associated barrier function $\Psi: \mathbb{R}^n_{++} \to \mathbb{R}_+$ can be defined as follows:

$$\Psi(v) = \sum_{i=1}^{n} \psi(v_i).$$

The system of search directions can be specified using kernel functions:

$$\begin{aligned} -M\Delta x + \Delta s &= 0, \\ s\Delta x + x\Delta s &= -w(t)v\nabla\Psi(v). \end{aligned} \tag{5}$$

It can be shown that using the logarithmic kernel function $\psi(t) = \frac{t^2-1}{2} - \log(t)$ in system (5) yields the original system of equations (4), which is obtained by applying Newton's method. In what follows, we use the kernel function

$$\psi(t) = \frac{t^2-1}{2} + \frac{t^{-1}-1}{2} - \frac{t-1}{2}$$

to compute the search directions. A detailed theoretical analysis of this kernel function is provided in the paper of Chi, Wang, and Lesaja [3].

## 2. Theoretical algorithm

We present the theoretical algorithm introduced in [3] and then discuss the modifications made for the implementation. Some steps of the algorithm are given by separate functions. To determine the search directions, we substitute the kernel function $\psi$ into the expression on the right-hand side of the system (5), solve the resulting system and return the computed directions. This is done with the following function:

**function** ***searchDirection*** $(x, s, t)$
**begin**
  Solve the system of equations (5).
  **return** $(\Delta x, \Delta s)$;
**end**.

To perform the full-Newton step, we add the search directions to the current iterates:

**function** ***fullNewtonStep*** $(x, s, \Delta x, \Delta s)$
**begin**
  **return** $(x, s) + (\Delta x, \Delta s)$;
**end**.

The parameter defining the weighted central path is updated using the following function:

**function** ***updateUsingTheta*** $(t, \theta)$
**begin**
  **return** $(1 - \theta)t$;
**end**.

Based on these functions, the theoretical algorithm is presented as follows.

**Algorithm 1.** (Chi, Wang és Lesaja [3])

Assume that for the pair of vectors $(x^0, s^0) \in \mathcal{F}^0$ we have $x^0 s^0 \geq w$.

Let $\varepsilon > 0$ be the accuracy parameter.

Let $\theta = \bar{\theta}_{min}$ be the barrier update parameter, where

$$\bar{\theta}_{min} = \frac{\gamma}{3\gamma + (18\bar{\kappa} + 10)\beta},$$

$$\bar{\kappa} = \frac{(1 + 4\kappa)max(x^0 s^0)}{4\,min(w)} - 0.25.$$

$\gamma = min(w)$, $\beta = \|x^0 s^0 - w\|$.

Let $\tau > 0$ be the threshold parameter.

Let $t^0 = 1$, such that $\delta(x^0, s^0; t^0) \leq \tau$, where

$$\delta(x, s; t) = \left\| v\left(\frac{\Delta x}{x} + \frac{\Delta s}{s}\right) \right\| = \left\| \frac{e}{2} + \frac{e}{2v^2} - v \right\|.$$

$x = x^0$, $s = s^0$, $t = t^0$;

**while** $\|xs - w\| > \varepsilon$ **do**
**begin**
  $(\Delta x, \Delta s) =$ ***searchDirection*** $(x, s, t)$;
  $(x, s) =$ ***fullNewtonStep*** $(x, s, \Delta x, \Delta s)$;
  $t =$ ***updateUsingTheta*** $(t, \theta)$;
**end**.

To implement it efficiently, we made several modifications to Algorithm 1.

## 3. Modified algorithm

Since it is possible during the steps of the algorithm to reach an infeasible point, we introduce the residual vector

$r_q = -Mx + s - q$.

Instead of system (5) we determine the search directions using the following modified system:

$$\begin{aligned} -M\Delta x + \Delta s &= -r_q, \\ s\Delta x + x\Delta s &= -w(t)v\nabla\Psi(v). \end{aligned} \qquad (6)$$

The function assigned to system (6) is the following:

**function** ***modifiedSearchDirection***$(x, s, t)$
**begin**
  $r_q = -Mx + s - q$;
  Solve the system of equations (6).
  **return** $(\Delta x, \Delta s)$;
**end**.

Instead of moving to the next point with a full-Newton step, we calculate the maximum step-size to the boundary in a variable $\alpha$, and then reduce it by a factor $\rho \in (0, 1)$:

**function** ***NewtonStep***$(x, s, \Delta x, \Delta s, \rho)$
**begin**
  $\alpha_x = min\left\{\frac{-x_i}{\Delta x_i} \middle| \Delta x_i < 0\right\}$;
  $\alpha_s = min\left\{\frac{-s_i}{\Delta s_i} \middle| \Delta s_i < 0\right\}$;
  $\alpha = min\{\alpha_x, \alpha_s\}$;
  **return** $(x, s) + \rho\alpha(\Delta x, \Delta s)$;
**end**.

We implemented two methods to reduce the parameter $t$. The first is the same as the version given in the theoretical algorithm, which uses $\theta$ to reduce the value of $t$:

**function** ***updateParameter***$(t, \theta, x, s, \zeta)$
**begin**
  **return** ***updateUsingTheta*** $(t, \theta)$;
**end**.

The second variant updates the parameter $t$ using the method introduced in [4] applying a scaling factor $\zeta \in (0,1]$ :

**function** ***updateParameter***$(t, \theta, x, s, \zeta)$
**begin**
  **return** ***updateUsingZeta***$(x, s, \zeta)$;
**end**
**function** ***updateUsingZeta***$(x, s, \zeta)$
**begin**
  **return** $t = \zeta\left|\frac{x^T s - w^T e}{(x^0)^T s^0 - w^T e}\right|$;
**end**.

Assuming that $x^0 s^0 \neq w$, we obtain that the denominator of the above expression cannot be 0. The modified algorithm is presented below.

**Algorithm 2.** Suppose that for the pair of vectors $(x^0, s^0) \in \mathcal{F}^0$ we have $x^0 s^0 \geq w$, $x^0 s^0 \neq w$.

Let $\varepsilon > 0$ be the accuracy parameter. Furthermore, let $\theta \in (0, 1)$, and $\zeta \in (0, 1]$ be the update parameters.

Let $\rho \in (0, 1)$ be the scaling parameter of the step.
$t^0 = 1$, $x = x^0$, $s = s^0$, $t = t^0$;

**while** $\|xs\text{-}w\| > \varepsilon$ **do**
**begin**
  $(\Delta x, \Delta s) =$ ***modifiedSearchDirection***$(x, s, t)$;
  $(x, s) =$ ***NewtonStep***$(x, s, \Delta x, \Delta s, \rho)$;
  $t =$ ***updateParameter***$(t, \theta, x, s, \zeta)$;
**end**.

We present several numerical results obtained using the above algorithm.

## 4. Numerical results

The algorithm presented above was implemented in the Python programming language, using the NumPy library for linear algebra operations. Each time we executed the program we used the matrix proposed by Csizmadia [5]:

$$M = \begin{pmatrix} 1 & 0 & 0 & \dots & 0 \\ -1 & 1 & 0 & \dots & 0 \\ -1 & -1 & 1 & \dots & 0 \\ \vdots & \vdots & \vdots & \ddots & \vdots \\ -1 & -1 & -1 & \dots & 1 \end{pmatrix}.$$

For this matrix, it was proven in [6] that for $n \geq 4$ we have $\kappa = 2^{2n-8} - 0.25$. This matrix plays a significant role in the study of $P^*(\kappa)$-WLCP, as the value of $\kappa$ increases exponentially with the problem size. We also assumed that $q = [0, 1, ..., n-1]^T$. Furthermore, we used the initial values $x^0 = s^0 = e$, where e is the $n$-dimensional all-one vector. Note that in this case, the condition $(x^0, s^0) \in \mathcal{F}^0$ holds.

To satisfy the inequality $x^0 s^0 \geq w$, the values of the weight vector $w$ were chosen as randomly generated positive real numbers less than one. Since we analyzed the algorithm from several perspectives, the elements of $w$ were generated under different constraints. Furthermore, we used the values $\varepsilon = 10^{-6}$, $\rho = 0.9$. As for the parameter θ, we also investigated values greater than the theoretically determined value $\bar{\theta}_{min}$, from the following set:

$\theta \in \{\bar{\theta}_{min}, 10^{-6}, 10^{-5}, 10^{-4}, 10^{-3}, 0.01, 0.02, ..., 0.1, 0.2, ..., 0.9\}$.

We found that, in general, increasing $\theta$ still yields correct results, and the algorithm converges to the solution more quickly. To illustrate this, we consider the number of iterations and CPU times (in seconds) obtained for the Csizmadia ma-

trix of the size $4\times4$. We used a computer with an Intel Core i5-1035G1 processor and 8 GB of RAM, under the Windows 10 operating system, in a Python 3.11.6 environment for the tests (**Table 1**).

The following table presents the minimum number of iterations obtained for different values of $\theta$ as a function of the dimension. It can be observed that the minimum number of iterations increases linearly with the dimension. In the last row we indicated from which value of $\theta$ we get this minimum number of iterations. It can be concluded that in case of higher dimensions, the number of iterations cannot always be reduced by increasing the value of $\theta$ (**Table 2**).

Further results were obtained with the implementation in which the parameter $t$ is reduced using a scalar $\zeta$. With this method, we achieved similar results in terms of the number of iterations of Algorithm 2 (**Figure 1**).

In case of $n=10$, $\zeta=0.1$, **Figure 2** is intended to show how the categorization of the weight vector into different intervals affects the values of s in the solution. It is known that if the weight vector is zero, then we get back in the vector $s$ the increasing natural numbers represented by the vector $q$. When the values of $w$ fall into an interval close to zero, the values of $s$ approximate those of $q$. If we select an interval for the values of the weight vector, the elements of which are farther from zero, then the values of $s$ will also shift accordingly.

**Table 1.** *The number of iterations obtained for different values of θ.*

| Θ | Iteration | CPU |
|---|---|---|
| 0.1 | 139 | 0.0156 |
| 0.01 | 1445 | 0.0625 |
| $10^{-3}$ | 14498 | 0.7031 |
| $10^{-4}$ | 145029 | 6.8281 |
| $10^{-5}$ | 1450342 | 107.3906 |
| $10^{-6}$ | 14503470 | 1035.1250 |
| $\bar{\theta}_{min}=3.86\cdot10^{-7}$ | 37573477 | 3006.2031 |

**Table 2.** *Minimum iteration number as a function of the dimension, where D denotes the dimension, and I the minimum number of iterations.*

| **D** | 20 | 30 | 40 | 50 | 100 | 200 | 300 | 400 | 500 |
|---|---|---|---|---|---|---|---|---|---|
| **I** | 18 | 22 | 26 | 29 | 48 | 84 | 121 | 158 | 195 |
| **Θ** | 0.7 | 0.6 | 0.5 | 0.5 | 0.3 | 0.2 | 0.2 | 0.2 | 0.09 |

This trend is also observed in the case of $x$, where the elements of this vector converge to zero as the values of the weight vector are chosen closer to zero (**Figure 3**).

## 5. Conclusions

We modified the kernel function-based interior-point algorithm published by Chi, Wang, and Lesaja **[3]** to efficiently solve the $P^*(\kappa)$-WLCP. We investigated two variants to reduce the parameter that determines the weighted central path. We presented various numerical results using the Python code we developed.

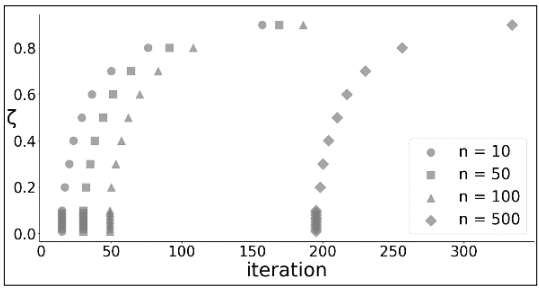


**Fig. 1.** *Number of iterations of the algorithm as a function of the parameter ζ.*

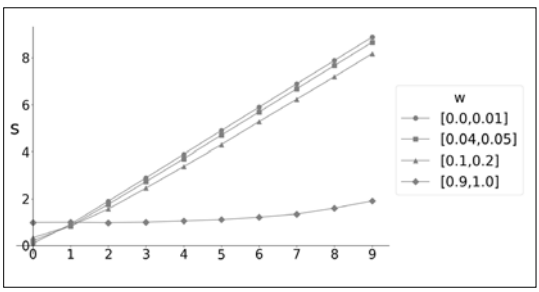


**Fig. 2.** *Values of the vector s as a function of the weight vector.*

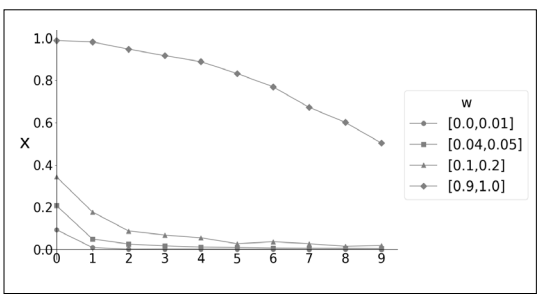


**Fig. 3.** *Values of the vector x as a function of the weight vector.*

**Acknowledgements**

The authors express their gratitude to the Transylvanian Museum Society for the support provided for the research work.

## References

[1] Potra F. A.: *Weighted Complementarity Problems – a New Paradigm for Computing Equilibria*. SIAM Journal on Optimization, 22/4. (2012) 1634–1654. https://doi.org/10.1137/110837310

[2] Ferris M. C., Pang J. S.: Engineering and Economic Applications of Complementarity Problems. SIAM Review, 39/4. (1997) 669–713. https://doi.org/10.1137/S0036144595285963

[3] Chi X., Wang G., Lesaja G.: *Kernel-Based Full-Newton Step Feasible Interior-Point Algorithm for $P^*(\kappa)$-Weighted Linear Complementarity Problem.* Journal of Optimization Theory and Applications, 202/1. (2024) 108–132. https://doi.org/10.1007/s10957-023-02327-9

[4] Darvay Zs., Orbán A.-Sz.: *Implementation of the Full-Newton Step Algorithm for Weighted Linear Complementarity Problems*. Papers on Technical Science, 15. (2021) 15–18. https://doi.org/10.33894/mtk-2021.15.04

[5] de Klerk E., E.-Nagy M.: *On the Complexity of Computing the Handicap of a Sufficient Matrix*. Mathematical Programming, 129. (2011) 383–402. https://doi.org/10.1007/s10107-011-0465-z

[6] E.-Nagy M., Illés T., Povh J., Varga A., Zerovnik J.: *Sufficient Matrices: Properties, Generating and Testing*. Journal of Optimization Theory and Applications, 202/1. (2024) 204–236. https://doi.org/10.1007/s10957-023-02280-7

Műszaki Tudományos Közlemények vol. 22. (2025) 32–39.
DOI: Hungarian: https://doi.org/10.33895/mtk-2025.22.06
English: https://doi.org/10.33894/mtk-2025.22.06

# INFLUENCE OF COOLING AGENT TYPE ON THE DESIGN AND POWER DEMAND OF HEAT PUMPS

János DÓSA,[1] Ovidiu Bogdan TOMUS[2]

[1] *University of Petrosani, Faculty of Mechanical and Electrical Engineering, Department of Mechanical Industrial and Transport Engineering, Petrosani, Romania. iondosa@upet.ro*

[2] *University of Petrosani, Faculty of Mechanical and Electrical Engineering, Department of Mechanical Industrial and Transport Engineering, Petrosani, Romania. bogdantomus@upet.ro*

**Abstract**

The paper presents the comparative exergetic analysis of different heat pump designs from an energy consumption point of view. Heat pumps are usually classified according to the environment from which they extract heat in order to help the consumer in choosing a heat pump type, based on the available heat sources. From the construction point of view, a wide variety of heat pumps have appeared as a result of the various heat sources to be considered, and the refrigerants used. Also, due to the desire to improve their operation, various constructive variants have been developed. Considering that all heat pumps use electricity to operate, their energy consumption for producing the same thermal effect should be a criterion for their choice, along with economic aspects.

**Keywords***: heat pump, exergy analysis, power demand.*

## 1. Introduction

A heat pump is a heat engine designed to extract heat from a lower temperature environment and transfer it to a higher temperature environment. It is used to manage thermal energy, whereby energy rejected in the cooling process and waste heat can be used for heating and hot water production, and ambient heat can be used likewise.

Heat pump technology is a relatively old technology, in fact the energy crisis of the 1970s gave a boost to research in this field.

Today, the EU and the UN have developed common goals for a sustainable future, and one of these goals is affordable and clean energy. In light of this directive, heat pump technology is experiencing a new renaissance, with more and more heat pumps being installed.

With heat pump heating playing a central role in the European Union's green energy transition, more and more companies are installing heat pumps, resulting in different companies adopting unique design solutions.

The aim of this paper is to highlight the different aspects of heat pump operation in terms of exergy efficiency and energy consumption.

## 2. Classification of heat pumps

Heat pumps are usually classified according to the environment from which they extract heat, helping the consumer to choose a particular type of heat pump based on the heat source available [1–8].

According to most sources of information, the main types of heat pumps are:

– Geothermal heat pumps;
– Air-to-water heat pumps;
– Air-to-air heat pumps;
– Water-to-water heat pumps.

Consequently, they are classified according to the heat source, which is understandable since the target audience is the user.

However, heat pumps can also be classified according to the design of the system:

– Monovalent systems, which operate without auxiliary heating, are implemented by drilling geothermal boreholes, installing a flat plate collector, and are built to use thermal and other waste heat, groundwater heat.;
– Bivalent systems, which operate with auxiliary heating and are built using air, surface water heat.

From a structural point of view, a very wide range of heat pumps have been developed due to the different heat sources that have been considered for exploitation and the refrigerants used. In addition, the desire to improve their operation has also led to the emergence of different design variants.

The classification of heat pumps by process and type of operation [9–11] serves the purpose of this paper much better, and can be summarized as follows:

A. Heat pumps with vapour compression cycle:
  A.1. Compression heat pumps:
  – Rotary piston;
  – Rotary compressor;
  – Turbocompressor.
  A.2. Absorption heat pumps:
  – Indirectly heated;
  – Directly heated;
  – Adsorption heat pump;
  – Resorption heat pump;
  – Ejector heat pumps.
B. Gas Compression Heat Pumps:
  – Heat pumps using air as refrigerant;
  – Stirling cycle heat pumps;
  – Vortex tube heat pumps;
  – Vuilleumier cycle heat pumps.
C. Thermoelectric effect heat pumps.

Among the above-mentioned types of heat pumps, one type from each major class will be analyzed: vapour compression cycle, gas cycle and thermoelectric effect heat pumps.

## 3. Design and cycles of heat pumps

### 3.1. The vapour compression heat pumps

Vapour compression heat pumps are perhaps the most widely used type of heat pump. The first of these types uses R12 (ammonia) refrigerant and this refrigerant is still widely used in large refrigeration systems. The Freon family of compounds, the commercial name for halogenated hydrocarbons with excellent properties, is widely used in the refrigeration industry. Freon's chlorine content is highly ozone depleting and CFC refrigerants have been replaced by newer, less polluting refrigerants, hydrochlorofluorocarbons (HCFCs).

Water vapour is a type of refrigerant that is completely neutral from an environmental point of view, so, in the following, we will present vapour compression heat pumps using ammonia and water as refrigerants.

#### 3.1.1. The vapour compression heat pump using ammonia refrigerant

Heat pumps suitable for exploiting low thermal energy sources are the vapour-compression, water-to-water system [10, 11] heat pumps. This type of heat pump (Figures 1 and 2) is suitable for extracting waste heat from water at temperatures below 40 °C and deliver domestic hot water at temperatures up to 50–80 °C.

A mathematical model of such a heat pump was developed in [12] so the thermal characteristics of the heat pump will be calculated based on that model.

#### 3.1.2. Vapour compression heat pump using water as refrigerant

Figure 3 shows a vapour compression heat pump operating with water as refrigerant, while the cycle diagram is shown in Figure 4.

### 3.2. Gas compression heat pump

The basic design of a gas compression heat pump is similar to that of a vapour compression heat pump, as shown in Figure 5, while its cycle is shown in Figure 6.

From a thermodynamic point of view, the vapour compression heat pump (Figure 3) operates according to the Carnot cycle modified for practical applications.

In the expander, isentropic expansion is replaced by an isentropic process in the expansion valve, while in the compressor, isentropic compression occurs, resulting in a temperature Tc higher than the condensation temperature (Figure 4) [10, 11].

The theoretical cycle of a gas compression heat pump (Figure 3) is a Joule cycle [10, 11], in which expansion and compression are achieved by means of turbomachinery.

While the operation of the vapour compression heat pump has been described in several articles due to their widespread use, the gas compression heat pump is not used as often and therefore the literature on it is scarcer.

The basic characteristic of a gas compression heat pump is the compression ratio [10, 11]:

$$\beta_c = \frac{p_2}{p_1} \qquad (1)$$

where $p_2$ is the outlet pressure, $p_1$ is the inlet pressure of the turbocompressor, in bar.

The characteristic parameter of heat pumps is the COP (coefficient of performance), which for gas compression heat pumps can be expressed by the following formula [10, 11]:

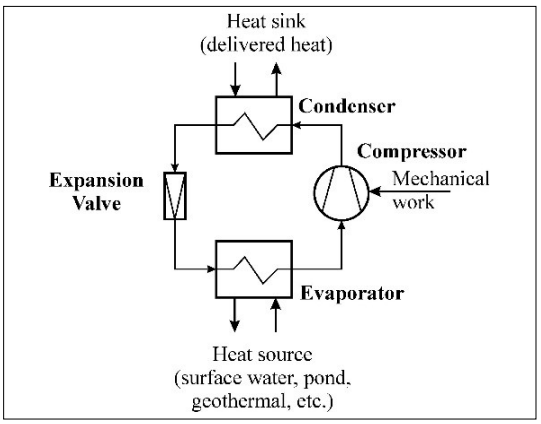


**Fig. 1.** *The vapour compression heat pump using ammonia refrigerant.*

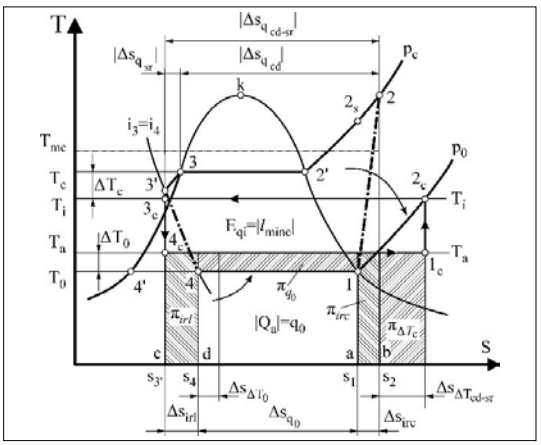


**Fig. 2.** *Cycle of the vapour compression heat pump using ammonia refrigerant.*

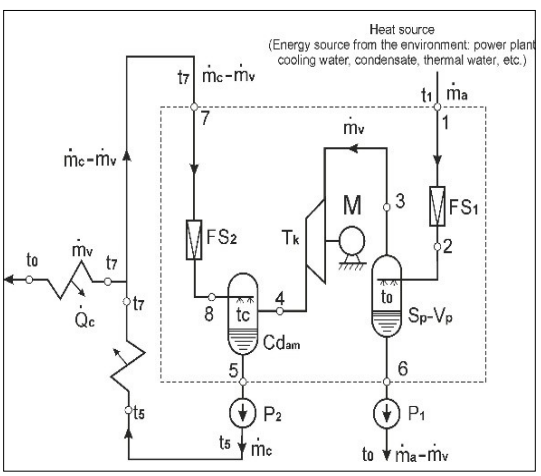


**Fig. 3.** *The vapour compression heat pump using water refrigerant.*

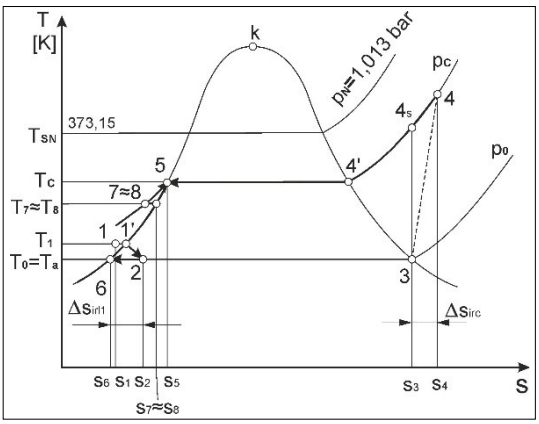


**Fig. 4.** *Cycle of the vapour compression heat pump using water refrigerant.*

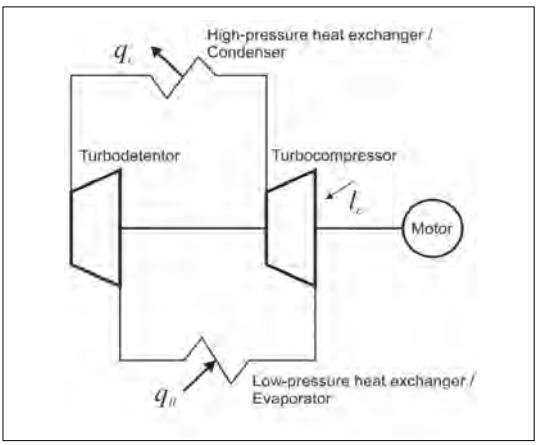


**Fig. 5.** *Gas compression heat pump.*

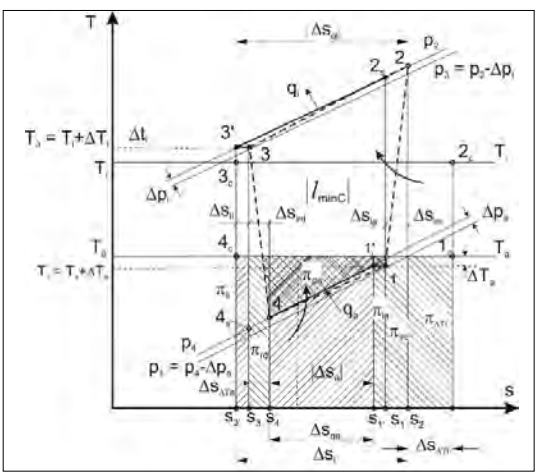


**Fig. 6.** *Cycle of the gas compression heat pump cycle.*

$$\mu_t = \frac{1}{1 - \beta_c^{\frac{1-k}{k}}} \quad (2)$$

where $k$ is the adiabatic coefficient.

Another parameter to compare heat pumps is the exergy efficiency, which can be calculated using the following equation [10, 11]:

$$\eta_E = \frac{|l_{\min C}|}{|l|} \quad (3)$$

where $l_{minC}$ is the specific minimum work of the ideal Carnot cycle in kJ·kg$^{-1}$, while $l$ is the specific work of the actual cycle in kJ·kg$^{-1}$.

Based on the actual cycle of the gas compression heat pump (Figure 6) [10, 11] calculations can be performed to determine characteristic parameters that can be compared with the corresponding characteristics of the heat pumps analyzed.

### 3.3. Thermoelectric heat pump

Figure 7 shows a schematic of a thermoelectric heat pump while Figure 8 presents a schematic of a thermoelectric element [10, 11].

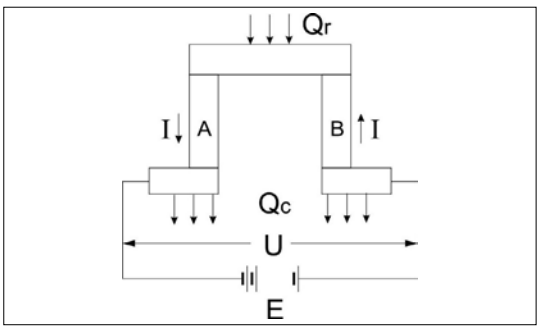


7. ábra. *Termoelektromos hőszivattyú*

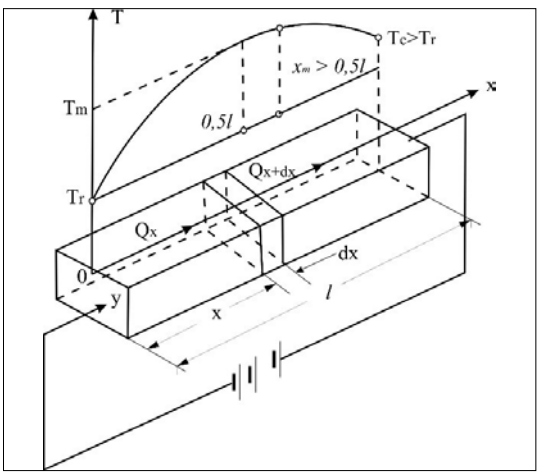


8. ábra. *Termoelektromos elem*

These devices are based on the thermoelectric phenomenon, namely the Seebeck, Peltier and Thomson effects. The phenomenon in which a temperature difference between two different electrical conductors or semiconductors produces a voltage difference between the two materials is known as Seebeck.

When heat is applied to one of two conductors or semiconductors, the heated electrons flow towards the colder one.

The inverse of the Seebeck effect is called the Peltier effect; an electric current flowing through a junction between two materials releases or absorbs heat at the junction in unit time to compensate for the difference in chemical potential between the two materials.

The Thomson effect is the heat evolution or absorption when an electric current passes through a circuit of a single material with a temperature difference along its length.

This heat transfer relies on the common heat generation associated with the electrical resistance to currents in conductors. Note that the Thomson and Peltier effects refer to reversible processes. The Thomson effect is usually ignored in the design of thermoelectric systems.

The mathematical model of a thermoelectric heat pump is fundamentally different from the models of heat pumps presented above and will be described in more detail below.

For a thermoelectric heat pump, based on the schematic drawing of the thermoelectric element shown in Figure 8 the heat flux through the cold point of the element can be calculated using the following equation [10]:

$$Q_r = \alpha \cdot I \cdot T_r - 0.5 \cdot R \cdot I^2 - \Lambda \cdot \Delta T, \text{ (W)} \quad (4)$$

where:

$\alpha$ is the total Seebeck coefficient V·K$^{-1}$-ben;

$R$ is the total electrical resistance in Ω;

$\Lambda$ is the total conductivity of the thermoelectric element in W·K$^{-1}$.

The equations to calculate these elements are:

$$\alpha = |\alpha_A| + |\alpha_B|, \text{ (V/K)} \quad (5)$$

where $\alpha_{A,B}$ – Seebeck coefficient of the A and B components of the thermoelectric element in V·K$^{-1}$.

$$R = \rho_A \cdot \frac{l_A}{A_A} + \rho_B \cdot \frac{l_B}{A_B}, \text{ (Ω)} \quad (6)$$

where:

$\rho_A, \rho_B$ – resistance of the thermoelectric element components A and B in Ω·m;

$l_A$, $l_B$ – length of the thermoelectric element components A and B in m;
$A_A$, $A_B$ – surface area of the thermoelectric element components A and B in m$^2$.

Finally:

$$\Lambda = \lambda_A \cdot \frac{A_A}{l_A} + \lambda_B \cdot \frac{A_B}{l_B}, \text{ (W/K)} \quad (7)$$

where $\lambda_A$, $\lambda_B$ – thermal conductivity of the components of the thermoelectric element A and B in W·m$^{-1}$·K$^{-1}$.

To compute the thermal characteristics of the thermoelectric system, the heat exiting the hot spot of the thermoelectric element must be calculated, starting with the energy balance equation [10]:

$$Q_c = Q_r + P_i, W \quad (8)$$

where: $P_i$ – electrical power required for operation, in W, $Q_r$ – heat flux through the cold spot of the element, in W.

Maximum cooling efficiency of the system:

$$\varepsilon_{fmax} = \frac{Q_r}{P_i} \quad (9)$$

The maximum efficiency of a heat pump, also known as the coefficient of performance (COP):

$$\mu_{max} = \frac{Q_c}{P_i} \quad (10)$$

Exergetic efficiency of cooling:

$$\eta_{Ef} = \frac{m - \frac{T_c}{T_r}}{m + 1} \quad (11)$$

In which $m$ is a parameter that can be calculated:

$$m = \sqrt{1 + Z \cdot \frac{T_c + T_r}{2}}, \quad (12)$$

where $Z$ is the efficiency of the thermoelectric element, calculated by the following equation:

$$Z = \frac{\alpha^2}{\Phi_{min}}, \quad (13)$$

while the value $\Phi_{min}$ is given by equation:

$$\Phi_{min} = \left(\sqrt{\lambda_A \cdot \rho_A} + \sqrt{\lambda_B \cdot \rho_B}\right)^2. \quad (14)$$

The exergy efficiency of a thermoelectric heat pump can be calculated as follows:

$$\eta_{Et} = \frac{m - \frac{T_r}{T_c}}{m + 1} \quad (15)$$

## 4. Thermal characteristics of heat pumps

Heat pump heating is at the heart of the European Union's green energy transition, so it is mostly used in households for heating and hot water. Heat pumps that can be used to harness low heat energy sources are the vapour-compressed, water-to-water system [10, 11]. This type of heat pump is capable of harnessing waste heat from water at temperatures below 40°C to heat domestic hot water to 50-80°C.

The heat pumps described above use electricity to operate. The compressor (Figure 1), and the turbo compressor (Figure 3 and 5) are driven by an electric motor, while the thermoelectric heat pump as the name implies is driven by electricity directly and is therefore fundamentally different from other heat pumps.

As shown in Figures 2, 4. and 6 the implementation of the heat pump's thermodynamic cycle (vapour compression, gas compression, etc.) and the type of refrigerant used strongly influences the design solutions employed. Heat pump designs are very diverse, and if multi-stage solutions were to be analyzed, the design solutions would be even more diverse and time-consuming to list.

The thermal characteristics of the heat pumps are calculated using the following initial data: the required heat input $Q_i$, to cover the demand of a household $Q_i$ = 28 kW; $T_i$ = 65 °C – domestic hot water temperature; $T_a$ – ambient temperature (heat source). The heat source temperature is selected depending on the fact that the heat pump with water vapour cooling medium cannot be operated at a lower heat source temperature, i.e. $T_a$ = 30, 35, 40 °C.

For the vapour compression heat pump, some more data are needed: $\Delta T_c$ = 5 °C – temperature difference for condenser heat transfer (heat transport); $\Delta T_0$ = 5 °C – temperature difference for evaporator heat transfer; $T_{sr}$ = 10 °C – temperature difference for sub-cooling; the refrigerant used is R717 (ammonia).

For the vapour compression heat pump using R717 (ammonia) refrigerant, the results are shown in Table 1, while the results for the heat pump using water refrigerant are shown in Table 2. Also, for the gas compression heat pump, the temperature difference for the condenser heat transfer (heat transfer) and the temperature difference for the evaporator heat transfer is set to $\Delta T_c = \Delta T_0$ = 5 °C.

The results obtained from the gas compression heat pump calculations are shown in **Table 3**.

The thermal characteristics of the thermoelectric heat pump were calculated considering the same heat source temperatures, temperature rises and the required 28 kW of heat dissipation.

In addition, the semiconductor materials used for the construction of the thermoelectric elements, in this case tellurium (A) and bismuth (B), must be selected.

The physical characteristics of the materials for bismuth are: diameter d = 7 mm, length l = 3.2 mm, Seebeck coefficient $\alpha = -0.21 \cdot 10^{-3} V \cdot K^{-1}$, electrical conductivity $\rho = 10^{-5}$ Ω·m; thermal conductivity $\lambda = 1.45\ W \cdot m^{-1} \cdot K^{-1}$. And the physical characteristics of tellurium are: length l = 3.2 mm, Seebeck coefficient $\alpha = 0.23 \cdot 10^{-3}$, $V \cdot K^{-1}$, electrical conductivity $\rho = 10^{-5}$ Ω·m; thermal conductivity $\lambda = 1.45\ W \cdot m^{-1} \cdot K^{-1}$, while the dielectric strength is determined by calculations. For the thermoelectric heat pump, the results are plotted in **Table 4**.

**Table 1.** *Thermal characteristics of the vapour compression heat pump (R717 refrigerant)*

| Thermal characteristic | Value | | |
|---|---|---|---|
| Heat source temperature, $T_a$ [°C] | 30 | 35 | 35 |
| Actual power, $P_e$ [kW] | 5.24 | 4.54 | 4.54 |
| Specific internal energy absorbed as heat, $q_0$ [kJ·kg$^{-1}$] | 996.29 | 999.80 | 999.80 |
| Delivered specific heat, $q_c$ [kJ·kg$^{-1}$] | 1198.23 | 1170.64 | 1170.64 |
| Ideal COP $\mu_C$ | 9.66 | 11.27 | 11.27 |
| Theoretical COP $\mu$ | 5.93 | 6.85 | 6.85 |
| Actual COP $\mu_e$ | 5.34 | 6.17 | 6.17 |
| Exergy efficiency, $\eta_E$ [%] | 61.41 | 60.79 | 60.79 |

**Table 2.** *Thermal characteristics of the vapour compression heat pump using water refrigerant*

| Thermal characteristic | Value | | |
|---|---|---|---|
| Heat source temperature , $T_a$ [°C] | 30 | 35 | 40 |
| Minimum required power, $P_{min}$ [kW] | 3.02 | 2.84 | 2.65 |
| Compressor power, $P_c$ [kW] | 4.86 | 4.86 | 4.86 |
| Pump power , $P_p$ [kW] | 0.11 | 0.06 | 0.04 |
| Total $P_{tot}$ [kW] | 7.99 | 7.76 | 7.55 |
| Exergy loss due to the irreversibility of the compression process, $\pi_{irc}$ [%] | 15.82 | 15.82 | 15.82 |
| Exergy loss in the throttle valve, $\pi_{irl}$ [%] | 3.97 | 7.83 | 11.60 |
| Exergy loss due to irreversibility of heat transfer in the condenser, $\pi_{\Delta Tc}$ [%] | 18.02 | 18.02 | 18.02 |
| Maximum COP $\mu_{max}$ | 9.26 | 9.87 | 10.56 |
| Actual COP $\mu_e$ | 5.07 | 5.13 | 5.15 |
| Exergy efficiency $\eta_E$ [%] | 62.20 | 58.33 | 54.56 |

**Table 3.** *Thermal characteristics of the gas compression heat pump*

| Thermal characteristic | Value | | |
|---|---|---|---|
| Heat source temperature, $T_a$ [°C] | 30 | 35 | 40 |
| Actual power, $P_e$ [kW] | 18.99 | 18.47 | 18.06 |
| Specific work required to operate the actual cycle, $l_e$ [kJ·kg$^{-1}$] | 87.53 | 90.58 | 93.62 |
| Specific heat absorbed in the evaporator, $q_a$ [kJ·kg$^{-1}$] | 44.99 | 50.01 | 55.04 |
| The specific heat delivered by the condenser, $q_i$ [kJ·kg-1] | 129.02 | 136.97 | 144.91 |
| Specific work of the ideal Carnot cycle, $l_{minC}$ [kJ·kg-1] | 13.36 | 12.16 | 10.72 |
| Ideal COP $\mu_C$ | 9.657 | 11.27 | 13.52 |
| Theoretical COP $\mu$ | 1.54 | 1.58 | 1.61 |
| Actual COP $\mu_e$ | 1.47 | 1.51 | 1.55 |
| Exergy efficiency $\eta_E$ [%] | 15.90 | 13.98 | 11.93 |

**Table 4.** Thermal characteristics of the thermoelectrical heat pump

| Thermal characteristic | Value | | |
|---|---|---|---|
| Heat source temperature, $T_a$ [°C] | 30 | 35 | 40 |
| Electrical power required for operation, $P_e$ [kW] | 13.61 | 11.96 | 10.22 |
| Energy extracted as heat from a heat source, $Q_r$ [kW] | 14.39 | 16.04 | 17.78 |
| Ideal COP $\mu_C$ | 9.66 | 11.27 | 13.53 |
| Actual COP $\mu_e$ | 2.06 | 2.34 | 2.74 |
| Exergy efficiency $\eta_E$ [%] | 21.30 | 20.80 | 20.20 |

## 5. Conclusions

Based on the data presented above, the following conclusions can be drawn.

In line with the values reported in the literature, the variation of the thermal characteristics of heat pumps with respect to the heat source temperature is as follows:

- the effective coefficient of performance, (COP) $\mu_e$ increases with increasing heat source temperature;
- the exergy efficiency $\eta_E$ decreases with increasing heat source temperature;
- the electrical power required for operation, $P_e$ decreases with increasing heat source temperature.

The exergy efficiency $\eta_E$ decreases with increasing heat source temperature, by 1.1% for the thermoelectric heat pump, by 3.97% for the gas compression heat pump, by 7.64% for the water vapour refrigerant heat pump and by 2.16% for the vapour compression ammonia refrigerant heat pump.

In order to compare the different types of heat pumps in terms of electricity consumption, a suitable basis for comparison must be found.

A classical heating method is electric resistance heating, which is a good basis for comparison because electric resistance heating has a conversion efficiency of 100% in the sense that all the electrical energy input is converted into heat **[13, 14]**, and at the same time the exergy factor of electrical energy is 1 **[15]**. The exergy factor as defined in the literature **[15]** ] is the ratio between exergy and energy, usually a number between 0 and 1.

**Figure 9** shows the variation of the actual coefficient of performance (COP) $\mu_e$ as a function of heat source temperature. As can be seen, the effective coefficient of performance (COP) $\mu_e$ increases with increasing heat source temperature and from this point of view, the order of efficiency is as follows: the vapour-compressed ammonia refrigerant heat pump, the vapour-compressed water vapour refrigerant heat pump, the thermoelectric heat pump and, lastly, the gas-compressed heat pump. Since all electrical energy is converted into heat, the resistance power factor is set to 1, so all heat pumps perform better than resistance heating in this respect.

**Figure 10** presents the variation of the exergy efficiency $\eta_E$ as a function of the heat source temperature, where it can be seen that the efficiency decreases as the heat source temperature increases and, from this point of view, the order of efficiency is as follows: the vapour-compressed ammonia refrigerant heat pump, the vapour-compressed water vapour refrigerant heat pump , the thermoelectric heat pump and the gas-compressed heat pump in last place, from this point of view the resistance heating performs best since the electric current is essentially pure exergy.

**Figure 11** shows the variation of electrical power required for operation, Pe as a function of heat

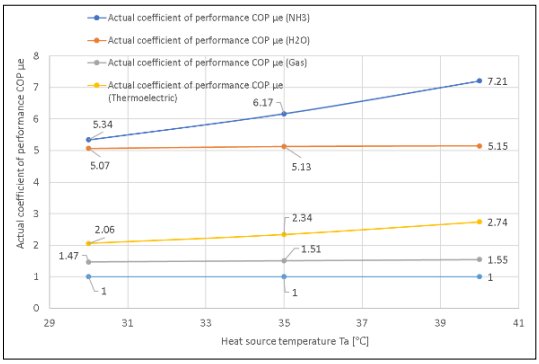


**Fig. 9.** *Actual coefficient of performance, COP*

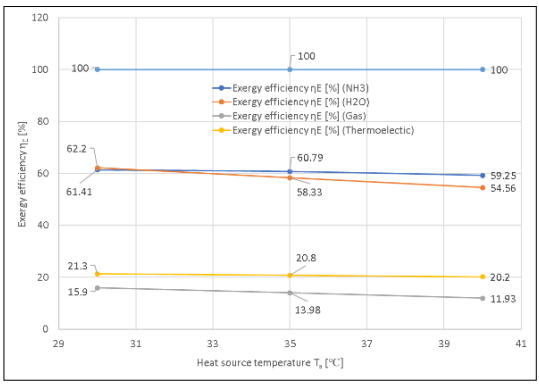


**Fig. 10.** *Exergy efficiency.*

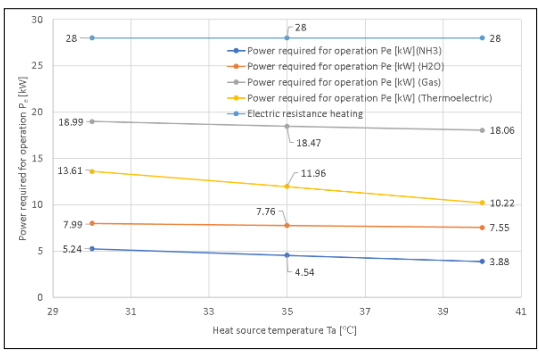


**Fig. 11.** *Power required for operation.*

source temperature, where it can be seen that the power decreases as the heat source temperature increases and, from this point of view, the order of efficiency is as follows: the vapour-compressed ammonia refrigerant heat pump, the vapour-compressed water vapour refrigerant heat pump, the thermoelectric heat pump and the gas-compressed heat pump in last place, from this point of view the resistance heating performs the worst because the exergy factor of the electric current is 1.

Summarizing, the choice of a heat pump for a particular application is more complex than one might think at first glance, and their classification by heat source can only be a starting point in choosing the right heat pump.

The performance required to operate should be an important criterion, as this will affect the operating costs in the long run, but other economic aspects, such as the initial investment, should not be neglected, as they all affect whether the investment will ever pay off.

## References


[1] BOSCH https://www.bosch-homecomfort.com/hu/hu/residential/tudas/hoszivattyu/hoszivattyu-tipusok-melyiket-valasszuk/ (accessed on: 2024. aug. 16.)

[2] ESTÉ-Credit Side Kft. https://rifeng-hoszivattyu.hu/hoszivattyu-tipusok/ (letöltve: 2024. augusztus 16.)

[3] Mitsubishi Electric, ZUBADAN, ecodan. https://www.zubadan.info.hu/tudasbazis/otthoni_felhasznalok/altalanos/A%20h%C5%91szivatty%C3%BA%20t%C3%ADpusai (accessed on: 2024. aug. 16.)

[4] HidroGeo Drilling. https://www.hgd.hu/hu/hoszivattyuk-tipusai (accessed on: 2024. aug. 16.)

[5] Energia Partner https://www.energiapartner.hu/energia/353-a-hoszivattyus-rendszerek-fajtai-jellem zoi-es-letesitese (accessed on: 2024. aug. 16.)

[6] EHPA. https://www.ehpa.org/about-heat-pumps/types-of-heat-pumps/ (accessed on: 2024. aug. 16.)

[7] The Renewable Energy Hub, UK https://www.renewableenergyhub.co.uk/main/heat-pumps-information/the-differe nt-types-of-heat-pumps (accessed on: 2024. aug. 16.)

[8] The News – Air Conditioning, Heating Refrigeration. https://www.achrnews.com/articles/152628-the-9-types-of-heat-pumps (accessed on: 2024. aug. 16.)

[9] Branimir Pavkovic: *Alkalmazott hőszivattyús rendszerek új és felújított épületeknél*. Épületenergetika, HUHR/1001/2.2.1/0009, 2012

[10] Radcenco V. et. al.: *Instalații de pompe de căldură*. Editura Tehnică, București, 1985. 115–367.

[11] Radcenco V. et. al.: *Processes In Refrigeration Equipment*. Didactică si Pedagogică Pulishing House, Bucharest, 1983, 372–390.

[12] Dosa I.: *Efficiency of Heat Recovery from Exhaust Ventilation Air of Underground Mines*. Revista Minelor, 3. (2015).

[13] US Department of Energy. https://www.energy.gov/energysaver/electric-resistance-heating (letöltve: 2024. augusztus 16.)

[14] Dincer I. (Szerk.): *Comprehensive Energy Systems. Vol. 1: Energy Fundamentals*. Elsevier, 2018, 265–339.

[15] Gong M., Wall G.: *Exergy Analysis of the Supply of Energy and Material Resources in the Swedish Society*. Energies, 9. (2016) 707. https://doi.org/10.3390/en9090707

Műszaki Tudományos Közlemények vol. 22. (2025) 40–45.
DOI: Hungarian: https://doi.org/10.33895/mtk-2025.22.07
English: https://doi.org/10.33894/mtk-2025.22.07

# DESIGN OF A TIMER-BRAKE PRESS

Dominik FEHÉR,[1] Sándor RAVAI-NAGY,[2] Ferenc SZIGETI[3]

[1] *University of Nyíregyháza, Institute of Engineering and Agricultural Sciences, Department of Engineering Basics, Physics and Mechanical Engineering Technology. Nyíregyháza, Hungary, feherdomi@gmail.com*

[2] *University of Nyíregyháza, Institute of Engineering and Agricultural Sciences, Department of Engineering Basics, Physics and Mechanical Engineering Technology. Nyíregyháza, Hungary, nagy.sandor@nye.hu*

[3] *University of Nyíregyháza, Institute of Engineering and Agricultural Sciences, Department of Engineering Basics, Physics and Mechanical Engineering Technology. Nyíregyháza, Hungary, szigeti.ferenc@nye.hu*

**Abstract**

The topic of the article is the modification of a mechanical arm press and its installation on the production line. After discussing the necessity of the development, the design process of a key component – the timer locking mechanism – is elaborated. This is followed by an overview of the press mounting and installation requirements, and the solutions as well as the key components of the equipment, such as the toothed part and the locking mechanism. Detailed assembly models are created, and load tests are performed on the components and surfaces supporting the press using both traditional calculations and finite element methods to verify that the designed structure can withstand mechanical loads without significant deformation. Finally, a development opportunity is presented that allows for the automation of not only the timer-brake press but also any other flanging press.

**Keywords**: *press automation, finite element analysis, manufacturing optimization.*

## 1. The project overview

The VW Touareg 536 model is a luxury "Premium SUV" category sport utility vehicle manufactured by Volkswagen. The assembly of the upper leather-covered plastic part of the off-road vehicle's gear shifter (in German, Oberteil, meaning upper part) (**Figure 1**).

The project was initiated due to a customer complaint indicating adhesion issues on the final product. To identify the root causes, laboratory tests were conducted in the facility, which revealed three main sources of error: incorrect fastening, poor manual edge crimping, and insufficient fixation time.

During the manufacturing process, a pre-cut leather piece sprayed with adhesive is applied to the injection-molded plastic component, and the edges held in a fixed position for a sufficient period to allow the adhesive to set properly (**Figure 2**).

The solution to the task required the coordination of the edge tools provided by the German parent company with an appropriate mechanical arm press. To achieve this, an adapter had to be

**Fig. 1.** *Touareg 536 transmission* **[1]**

**Fig. 2.** *„Touareg 536 Oberteil" final product*

designed for the upper tool, as well as a timing brake mechanism to prevent premature release of the press, thereby reducing scrap production. Since parts are also manufactured for right-hand drive vehicles, the installation of two separate presses was necessary. The company places high importance on space utilization, which is why the presses were mounted on a rotating support plate, allowing integration with the existing connecting presses. The sizing, manufacturing technology development, and bearing design of the support plate were also part of the project, ensuring an efficient and ergonomic design.

## 2. Description and Function of Timer-brake Presses

The task of the press is to secure the product for the required duration, applying the necessary force, and then re-flanging the product (**Figure 3**). To understand the operation, it is first necessary to introduce the upper tool and the locking mechanism. The operator places the product into the upper mold, then pushes the lower tool into position on a moving tray. After that, by pulling the lever, the pressing operation is initiated, which is ensured by the press head working against a spiral spring.

The locking mechanism is mounted on a shaft, which rotates together with the press arm against the force of the spiral spring (**Figure 4**). The concept is based on the connection of a toothed curved component and a locking unit, which prevents the premature release of the press. The operation of the system is supported by an inductive sensor, which initiates a countdown after a specified time. At the end of the countdown, a pneumatic actuator releases the lock, allowing the press to be disengaged.

A base plate was designed for the mounting of the locking mechanism and the actuator, ensuring proper positioning and providing enough space for the toothed arc (**Figure 5**). The base plate connects to the cast body of the press at three attachment points, two of which are connected to existing threaded holes, while the third requires the creation of a new hole. During the design of the structure, maintenance possibilities were also considered, and a manual release lever was incorporated, allowing the press to operate even in the absence of compressed air.

The central element of the timer is the ‘ATmega328’ microcontroller, which responds to the signal of an inductive sensor **[3]**. When the toothed part passes in front of it, a 60-second countdown

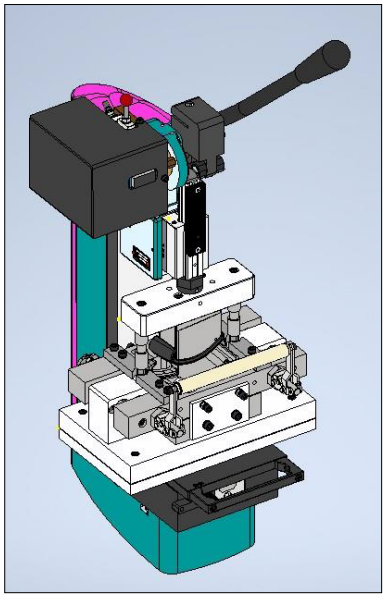

**3. ábra.** *Assembly model of the timer-brake press* **[2]**

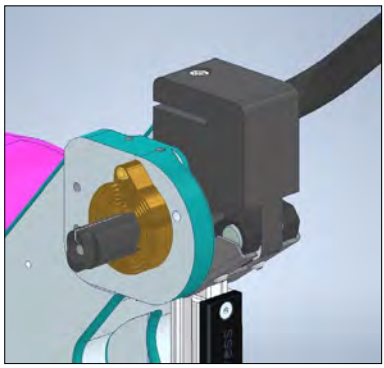

**4. ábra.** *The spiral spring and the shaft stub* **[2]**

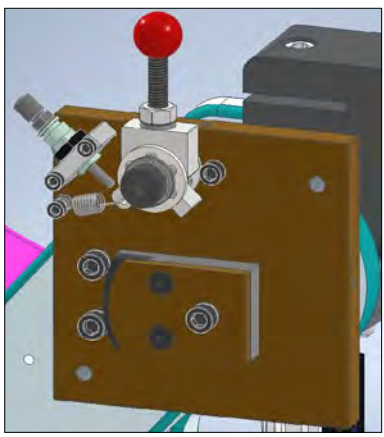

**Fig. 5.** *The locking mechanism, the toothed arc and the work cylinder in assembled condition* **[2]**

starts, which is displayed on a screen. After 5 seconds, a LED changes from green to yellow, and when the time runs out, it turns red, accompanied by an audible signal to alert the operator. At this point, the relay module switches 24V to the electropneumatic valve, which puts pressure on the work cylinder, thus releasing the mechanical lock. After 2 seconds, a new signal is received, indicating that the product should be removed from the tool. If this is not done, the spiral spring slightly lifts the press arm, but the guide pin prevents the full opening. The microcontroller monitors the return movement of the toothed component, so the counter can only reset with the next downward movement.

## 3. Installation of the press on the production line

To install the press into the production line, a rotating plate design is required, onto which two presses and two fastener placement presses will be mounted. During the design process, the loads, material quality, and mounting points had to be considered. Based on the model created with Inventor software, we determined the weight of the presses and the location of the bearings, which is essential for the finite element simulation (**Figure 6**).

When designing the plate, operator accessibility, safe and simple geometry, and aesthetic appearance were important considerations (**Figure 7**). To secure the plate, a spring pin was used, which, when inserted into a hole, prevents rotation. The operator releases it, rotates it 180°, and then the pin secures the plate again.

## 4. Results of the load tests

In the load testing performed using the finite element method, material quality is crucial as it determines the load capacity and rigidity. The company primarily uses aluminum for the shoulder, as it is lightweight, high-strength, and its natural oxide layer provides corrosion protection. Additionally, it is easily machinable, which reduces processing costs. The test showed four main results. The first is the reduced stress (**Figure 8**), which shows the specific load at the location of the highest stress. Its maximum value is 7,72 MPa, which does not approach the critical limit **[5]**.

The second is the equivalent deformation, which shows the total deformation energy of the material. Its value is $4.261 \cdot 10^{-5}$, a dimensionless value, which is negligible (**Figure 9**) **[5]**.

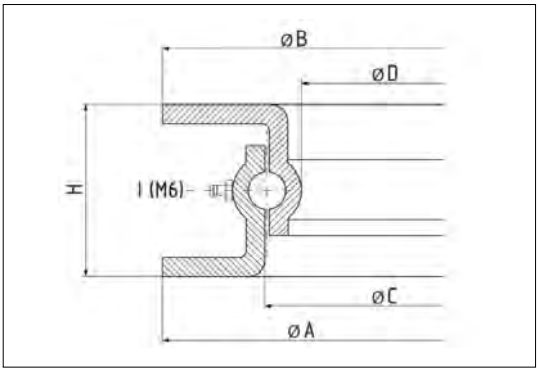


**Fig. 6.** *The key dimensions of the bearing* **[4]**

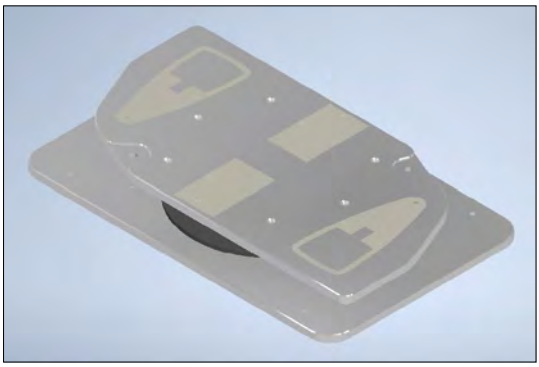

**Fig. 7.** *The rotating plate with the press pressure surfaces* **[2]**

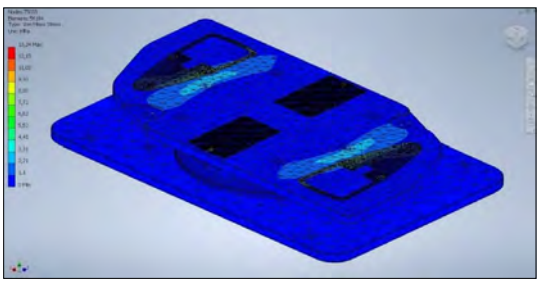

**Fig. 8.** *Illustration of the reduced stress* **[2]**

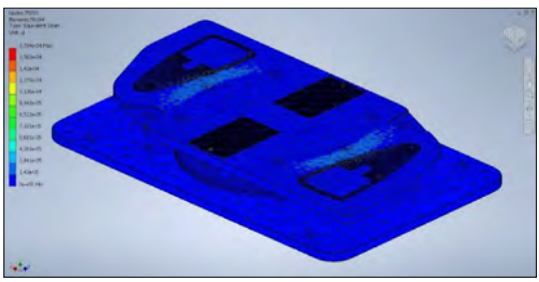

**Fig. 9.** *Value of the equivalent elastic deformation* **[2]**

The third is the examination of deflection, particularly at the two edges of the plate, where the maximum value is 0.04098 mm, which is insignificant (**Figure 10**) **[5]**.

Finally, a small angular rotation of 0.01 degrees was observed at the locations of the two timed presses, which is also negligible. These results confirm that the structure meets the design requirements, is stable, and its performance is adequate. The next step is to request a quote for the bearings and develop the manufacturing technology for the rotating plate and the base plate.

## 5. Computer-aided manufacturing design of the toothed component

The rough and finish machining of the component, as well as the contour milling, were performed using "Inventor CAM" software, while the tooth formation was carried out with the "Edgecam" program. The machining parameters were determined with the help of the "Sandvik Coroplus® Tool Guide". The preform is clamped in a machine vice, and first, the roughing and finishing of side "A" are performed using a 50 mm diameter "CoroMill® 390" face mill. After a 180° rotation, side "B" is machined in the same manner (**Figure 11**) **[6]**.

Next, the shoulder is shaped using a 10 mm Coro-Mill® Dura end mill, followed by machining the groove, drilling the holes, and preparing the thread (**Figure 12**) **[7]**.

For machining the outer contour, the workpiece is secured in a fixture held by a chuck, and the machining is carried out by fitting the STL model from the previous phase for continuity (**Figure 13**).

Finally, the workpiece is secured in a dividing fixture for the machining of the teeth (**Figure 14**), using a 10 mm diameter, 45° chamfering carbide mill (**Figure 15**).

## 6. Press development proposal

Analysis of the production data revealed that the press is efficient, but there is room for further optimization. The operators' workload varies, which increases the cycle time. With automation, non-productive time can be reduced: based on the development, the pneumatic cylinders would perform the pressing with a two-button start, while the operator could focus on other tasks. During the cycle of the modified press, three work cylinders would handle the movement of the tools, a timer would control the process, and a lamp would signal the completion at the end of

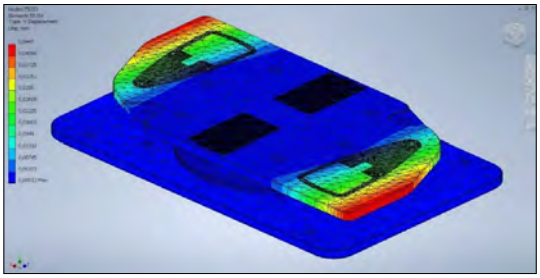

**Fig. 10.** *Lehajlás vizsgálata* **[2]**

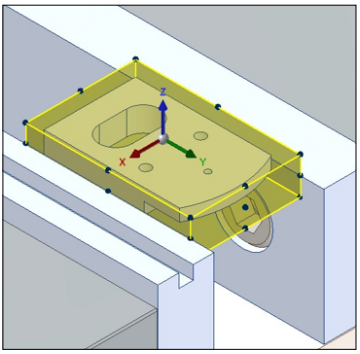


**Fig. 11.** *Fitting the semi-finished part to the workpiece* **[1]**

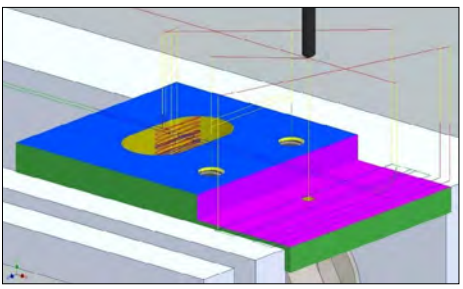

**Fig. 12.** *Shaping of features* **[2]**

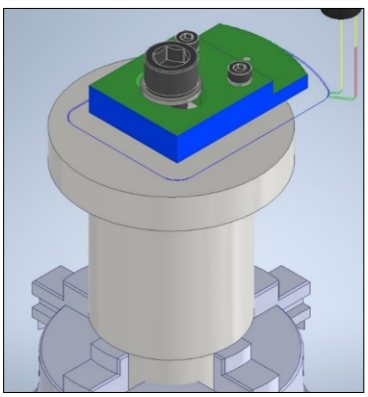

**Fig. 13.** *The device clamped in the chuck with the workpiece* **[2]**

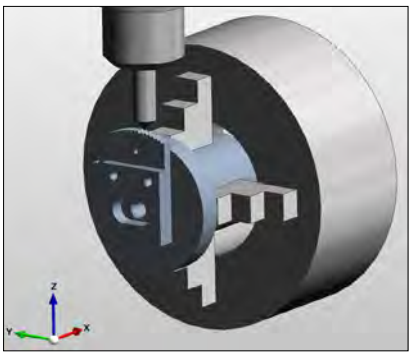

**Fig. 14.** *Machining of the teeth* **[8]**

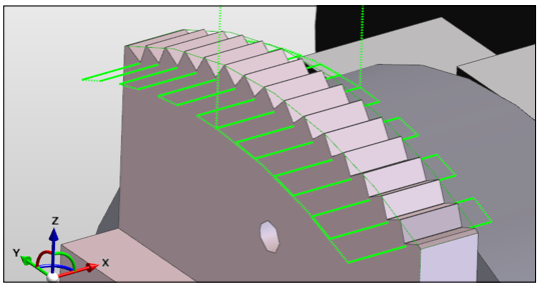

**Fig. 15.** *Toolpath for machining the teeth* **[8]**

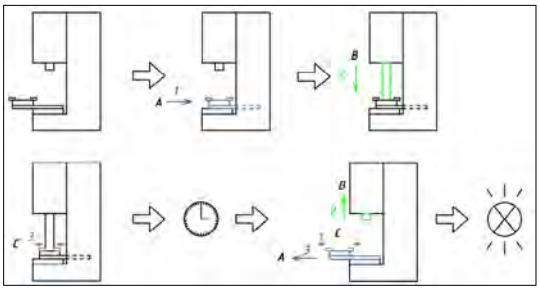

**Fig. 16.** *A complete working cycle of the press* **[3]**

the cycle (**Figure 16**). The automation requires 3 pneumatic work cylinders, 3 5/2 bistable valves, and a PLC.

During the modification, the press locking mechanism and arms are removed. The system uses sequential control, where the progression is conditional. The control process is built using a sequential process diagram that includes the operators and the steps. This is essentially a graphical representation that allows the control of automation systems to be documented and programmed in a logical, understandable way (**Figure 17**) **[9]**.

**Figure 18** provides an insight into the PLC program describing the process, for which a ladder diagram was created. The inputs are labeled as 'X' and the outputs as 'Y' **[9]**.

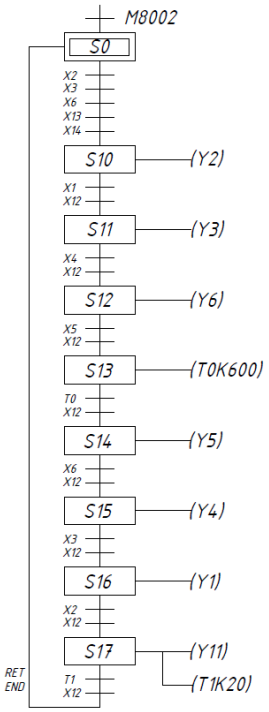


**Fig. 17.** *Sequential process diagram* **[2]**

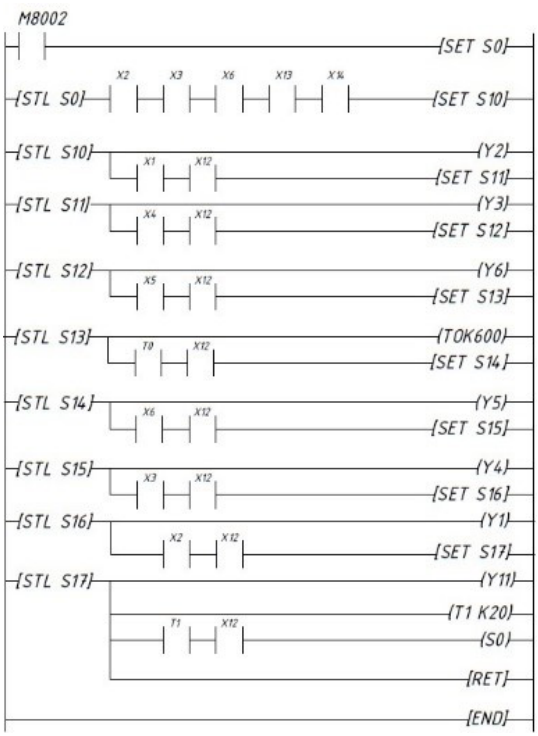


**Fig. 18.** *Ladder diagram* **[2]**

## 7. Conclusion

The load tests conducted using the finite element method during the project confirmed the stability and compliance of the designed structure. During the press installation, attention was given to space utilization, operator accessibility, and safety. During the development, the possibility of automating the press was also considered, aiming to reduce non-productive time and ease the workload of operators. The transformation with pneumatic cylinders and a PLC would enable automated operation, thus accelerating the manufacturing processes. Thanks to automation, production efficiency would increase, while manufacturing costs would decrease. This development is expected to be implemented as production volumes increase. The press with a timer brake ensured the proper product quality, and previous complaints related to delamination were eliminated. The application of the new system reduced scrap production, and with the regulation of the manufacturing processes as described in the article and the commissioning of the timer brake press, customer satisfaction improved.

### Acknowledgments

The research work was supported by the Scientific Council of the University of Nyíregyháza.

### References

[1] New Volkswagen Touareg r line jogdíjmentes képek (accessed on: 2024. 04. 20.). https://www.shutterstock.com/hu/search/new-volkswagen-touareg-r-line?consentChanged=true&page=2

[2] Autodesk Inventor Professional 2024 Build: 153

[3] Introduction to ATmega328 (laccessed on: 2024. 04. 27.) https://www.theengineeringprojects.com/2017/08/introduction-to-atmega328.html

[4] AutoCAD T.53.0.0 AutoCAD LT 2023

[5] Nándori F.–Szirbik S.: Szilárdságtan. Miskolci Egyetem Gépészmérnöki és Informatikai Kar, Miskolc 2008.

[6] CoroMill 390 Versatile Right-Angle Corner Milling Tools with Chamfering Function for Mixed Production. (accessed on: 2024. 06. 11.) https://www.sandvik.coromant.com/hu-hu/tools/milling-tools/shoulder-milling-edging-tools/coromill-390

[7] CoroMill Dura Versatile Solid Carbide End Mills (accessed on: 2024. 06. 11.). https://www.sandvik.coromant.com/hu-hu/tools/milling-tools/solid-carbide-end-mills/coromill-dura/coromill-dura-multimaterial

[8] EDGECAM 2021.0

[9] Ferenczi I.: *PLC programozási alapismeretek*. Nyíregyházi Egyetem, Nyíregyháza, 2018.

Műszaki Tudományos Közlemények vol. 22. (2025) 46–51.
DOI: Hungarian: https://doi.org/10.33895/mtk-2025.22.08
English: https://doi.org/10.33894/mtk-2025.22.08

# PRESENTATION OF A MODULAR SYSTEM FOR DRYING SEWAGE SLUDGE FROM SEAGOING VESSELS

Attila KÁRI-HORVÁTH,[1] Zsolt LANTOS,[2] Gábor KRISTÓF[3]

[1] *Hungarian University of Agricultural Sciences and Life Sciences, Technical Institute, Department of Materials Science and Mechanical Processes. Gödöllő, Hungary, kari-horvath.attila@uni-mate.hu*

[2] *Gyémánt-Pirazol Ltd. Debrecen, Hungary, zsolt.lantos@gyemantpirazol.hu*

[3] *Gyémánt-Pirazol Ltd. Debrecen, Hungary, gabor.kristof@gyemantpirazol.hu*

**Abstract**

Nowadays, people who take a cruise don't realize that they are putting both the environment and human health at risk significantly more than if they had chosen to travel by any other means. The large quantities of fuel burned during the voyage pollute the atmosphere and thus endanger health, and the (hazardous) waste and sewage of all kinds that are generated on board every day cannot be left on board. A ship carrying about 3000 passengers produces on average about 80 $m^3$ of waste water per day! Newer ships are often capable of carrying a minimum of 8,000 passengers, so the amount of waste water they produce is obviously higher. Just look at these huge floating cities of 10-12 stories. The amount of waste generated on board, being far greater, must be managed in an environmentally friendly way in accordance with ever stricter standards. These factors justify that companies in the industry are constantly working to develop new technologies and solutions, not only with the building of new ships, but also the modernization of older ones.

**Keywords***: sewage sludge, waste recovery, MARPOL Convention, modular system.*

## 1. Waste management options

Waste hierarchy is a priority order established by the European Union giving the options for managing waste, from the most favourable to the least favourable. The waste hierarchy system helps to establish a priority order between waste management activities, based on which – with certain exceptions – the best solution is prevention. However, if this is not possible in certain circumstances, then reuse and recycling should be applied to as much waste as possible, and only as a last resort should waste be incinerated or landfilled **[1]**.

It focuses first on prevention and reuse, giving products a “second chance”. This is followed by recycling and composting, and waste incineration, which can generate electricity. Landfilling is the most harmful solution for the environment and our health, but it is also the cheapest **[2]**. Recovery therefore means the use of waste in a way that results in the exchange of raw materials and resources. In this way, waste becomes a marketable, economically advantageous secondary raw material or energy carrier that has a positive social perception and thus contributes significantly to achieving environmental protection goals. There are two main types of recovery, material recovery and energy recovery. The recovery, recycling and regeneration of components should be considered, among other things, as recovery in their material. In international practice, components suitable for energy production are called RDF (Refuse-Derived Fuel) or SRF (Solid Recovered Fuels), i.e. fuel derived from waste or alternative fuel.

## 2. The MARPOL Convention

The **MARPOL 1973/1978 Convention** *(International Convention for the Prevention of Pollution from Ships)* aims to protect the marine environment and prevent pollution from ships. The convention, which is mandatory for all seagoing ships of over 500 GT engaged in international trade, addresses the following potential hazards

and sources of pollution. From our point of view, the provisions of Annex IV are the most important, so we will elaborate on this.

Annex I: Oil pollution prevention regulations
Annex II: Regulations for the prevention of pollution caused by toxic substances in bulk liquid form
Annex III: Requirements for the prevention of pollution caused by packaged dangerous goods transported by sea
Annex IV: Regulations for the prevention of pollution by sewage from ships
Annex V: Regulations for the prevention of pollution caused by household and other wastes generated on board ships
Annex VI: Regulations for the prevention of air pollution from ships

### 2.1. Annex IV.

**Wastewater:**

a) drainage and other waste from any type of toilet, urinal and toilet cistern;
b) drainage from medical premises (pharmacy, patient bay, etc.) through washbasins, washbasins and tumuli located in such premises;
c) discharge from places containing live animals; or
d) other wastewater, if mixed with the above-mentioned sewers.

**Application**

The provisions of this Annex shall apply to:

a) i. new ships of 200 gross tonnage or more;
   ii. new ships of less than 200 gross tonnage and certified to carry more than 10 persons;
   iii. new ships which do not have a measured gross tonnage and are certified to carry more than 10 persons;
b) i. existing ships of 200 gross tonnage and above, 10 years after the entry into force of this Annex;
   ii. new ships of less than 200 gross tonnage and certified to carry more than 10 persons;
   iii. new ships which do not have a measured gross tonnage and are certified to carry more than 10 persons.

## 3. Thermal drying

Drying is basically the phenomenon of removing liquid from a solid by evaporation. Mechanical methods of separating liquid and solid are not considered drying. The principles and phenomena of drying processes are generally independent of the type of energy used. A significant part of the energy consumption during drying is for the evaporation of liquid water (2258 kJ/kg at 101.3 kPa). The solid may contain water in different forms, such as free moisture or bound form, which directly affects the drying rate [3].

The dewatering option is called thermal drying when an external supplemental energy source allows the waste to be heated. Thermal drying requires the input of significant amounts of thermal energy to the wet solids to evaporate the water and to heat the solids and remaining water. Gravity convection or forced air convection drying ovens can provide greater uniformity, temperature control, and rapid drying capability. Oven drying can result in an efficient dehydration process and short drying times, with maximum temperatures of 250–350 °C. [4]

The dewatering option is called thermal drying when an external auxiliary energy source allows the waste to be heated. The drying process is usually used to evaporate the water from the residual solids in the wastewater. In addition to the dryer, the drying system usually consists of material handling and storage equipment, heat generation and transfer equipment, air handling and distribution equipment, emission control equipment, and auxiliary systems. These equipment systems can take many forms. In direct heat dryers, hot air/gas flows through a vessel and comes into direct contact with wet solid particles. The contact between the hot air and the cold wet concentrate allows the transfer of thermal energy, which causes the temperature of the wet material being dried to increase and the water to evaporate. The hot air/gas can be produced by almost any heat source, but is most often produced by a gas or oil-fired furnace. Examples of direct drying equipment include rotary drum dryers (**Figure 1**). [5, 6, 7]

In this type of system, the heat is supplied through a fuel-burning furnace that is fed directly into the dryer drum. The dried material is separated from the hot exhaust gas, screened and processed, and then either returned to the dryer or to storage silos. The exhaust air/gas is cooled and a portion is returned to the dryer. The remaining air/gas is treated in air pollution control equipment and then discharged to the atmosphere. The recirculation of the dryer exhaust gas serves three important functions. First, it increases the overall thermal efficiency of the drying system, second, it minimizes the volume of exhaust gas

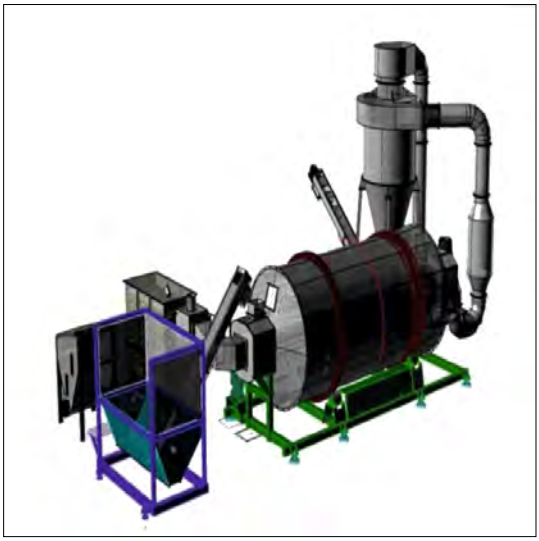

**Fig. 1.** *Schematic diagram of a rotary drum dryer* **[8]**

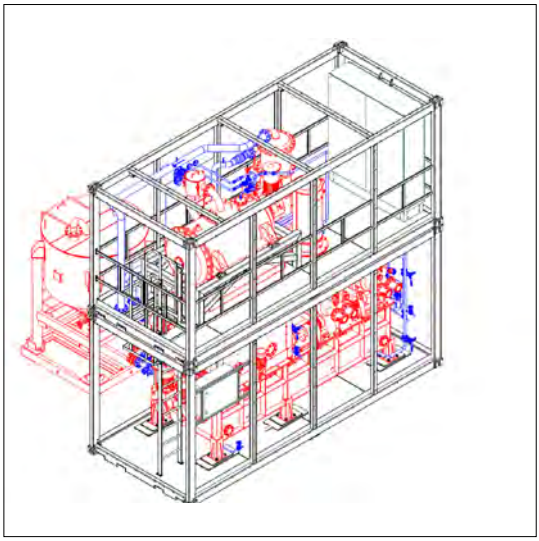

**Fig. 2.** *Schematic diagram of the frame structure.*

that requires air pollution control, and third, it provides a safety role by limiting the oxygen concentration in the system, which reduces the risk of explosions. Air pollution control processes for tumble dryers typically consist of additional particulate removal followed by regenerative thermal oxidation to eliminate odors and volatile organic compounds. **[5, 9, 10]**

Direct drying systems vary considerably in the type of equipment used to process wet and dried biosolids. Even the rotary drum systems shown in **Figure 1** vary considerably in the general layout and equipment used. Another type of direct dryer, which is increasingly used in the United States and Europe, is the belt dryer. This is usually a lower temperature system than the rotary drum system. The heat supply is usually a fuel-burning furnace, but unlike the rotary drum system, the system exchanges heat with a heat transfer fluid, hot water, or flue gas in an air heat exchanger, rather than the furnace being directly immersed in the drying chamber. **[7]**

## 4. The principle of modular design

In the current international competitive shipbuilding market, success is based on offering both competitive prices and short delivery times. This has led to a focus on cost reduction in terms of steel structure, machinery and manufacturing process optimization. However, as the opportunities for further development of steel structure manufacturing and assembly techniques are diminishing, the shipbuilding industry has explored other options to reduce lead times and costs. Recently, modularization has become an incslireasingly popular method for reducing manufacturing costs.**[11]**

Modularity is an approach that divides a system into smaller parts, called modules, that can be independently created and assembled to create a final product. Modular manufacturing is widely used in the automotive, aerospace, and other industries, with proven time and cost savings. **[11]** The characteristics of modular manufacturing, such as the use of assembly lines, high levels of prefabrication, and outsourcing, allow for significant improvements in quality while reducing costs and production lead times. In our case, modularity means that the equipment we designed and built fits into 2 containers (**Figure 2**). The lower unit, Frame I, is an extended-height 20' HC container (H:6060 × SZ:2440 × M:2900 mm), while the upper unit, Frame II, is a 20' HC container with increased height (H:6060 × SZ:2440 × M:2600 mm). The unit is the same size as a standard height 20'DC (L:6060 × W:2440 × H:2600mm) sea container. The units can be lifted using corner elements designed and manufactured to the same design as the factory.

## 5. Implementation process of the drying equipment

Our equipment is a drying device composed of several parts, which has a Pre-dryer part and a Main Dryer part. The former's task is to preheat and pre-dry the material to be treated by apply-

ing it in a thin layer (~80% moisture content). The latter's task is to dry the material to the desired <=20% moisture content. Pre-drying takes place in thin layers applied to the surface of heated cylindrical drums with a combined feeding and crushing, with a total pre-drying surface of approx. 5.7 m2. Main drying takes place in the heated frame with two parallel shafts, heated double-walled individual leaf augers, with a total main dryer heated surface of approx. 25 m2. The capacity of the device is 800 - 1000 kg/h, and its maximum energy requirement is 110 kW/h. According to previous shipboard experience, by treating this (so-called) "sticky phase" in such a way that, thanks to the structural design, it continuously shears the clumping material and shreds it while transporting it.

The frame elements are transported separately, with the necessary mechanical and electrical disassembly and assembly work. In the vertical direction, the upper frame is loaded with its entire weight on the lower one, no other fastening connections (e.g. screw connections) have been created. This is sufficient when installed on land, but additional fastening elements may be required when placed on a ship. Sidewall and roof frame elements with sandwich panel inserts have been manufactured for both frame components, which can be assembled with screw connections and are equipped with their own small lifting lugs to facilitate their movement.

The sandwich panel inserts ensure the preservation of the structure during transport. The upper frame container can be completely paneled during operation, if the internal operating temperature allows this. In the case of the lower container, the long side panels (at least on one side) and the distant short side panels should be removed during operation. In the case of outdoor placement (if necessary), rain shield plates according to the picture below have been designed for the frame structures on one of the long sides. A frame element with a passenger door has been used on the shorter side of the lower container according to **Figure 3**. Access to the frame structure is ensured even with panels installed through this. The upper Frame Structure II. unit can be accessed using the access ladder placed inside the door.

We planned to test the pre-dryer first, so the production of the related components began in parallel with the container frame structures. These were: the silo, the tank with a unique mixer, the shredder-feeder, the filling-preparer, the pre-drying drum, the knife material separator and the oil tanks. In the meantime, the control and the design of the weak and strong current systems were carried out. The tests of the pre-drying unit were carried out while the electrical and control system was already in operation (**Figure 4**).

Everything was designed so that after the pre-drying tests, the dryer could be "slid" into place by lifting the individual components. The installation of the pre-drying tests and the necessary units was ensured by making a "mold" of the main dryer that held the elements designed for the main dryer. The production of the main dryer took place in parallel with the pre-drying tests, where several difficulties had to be addressed:

- Since both screws were designed to be heated from the inside, the deformation caused by welding had to be minimized during the production of the screw blades.
- Due to the unidirectional rotation of the two pulleys, we faced additional alignment challenges
- On the first try, both pulleys were made according to the drawing, but we found that they did not "turn in each other", so one of the pulleys had to be re-manufactured to match the other, made according to the drawing.
- The co-rotation of the gears that turn the pulleys had to be fine-tuned along with their control, which was only possible after many attempts.

**Fig. 3.** *.The frame element of the pedestrian door.*

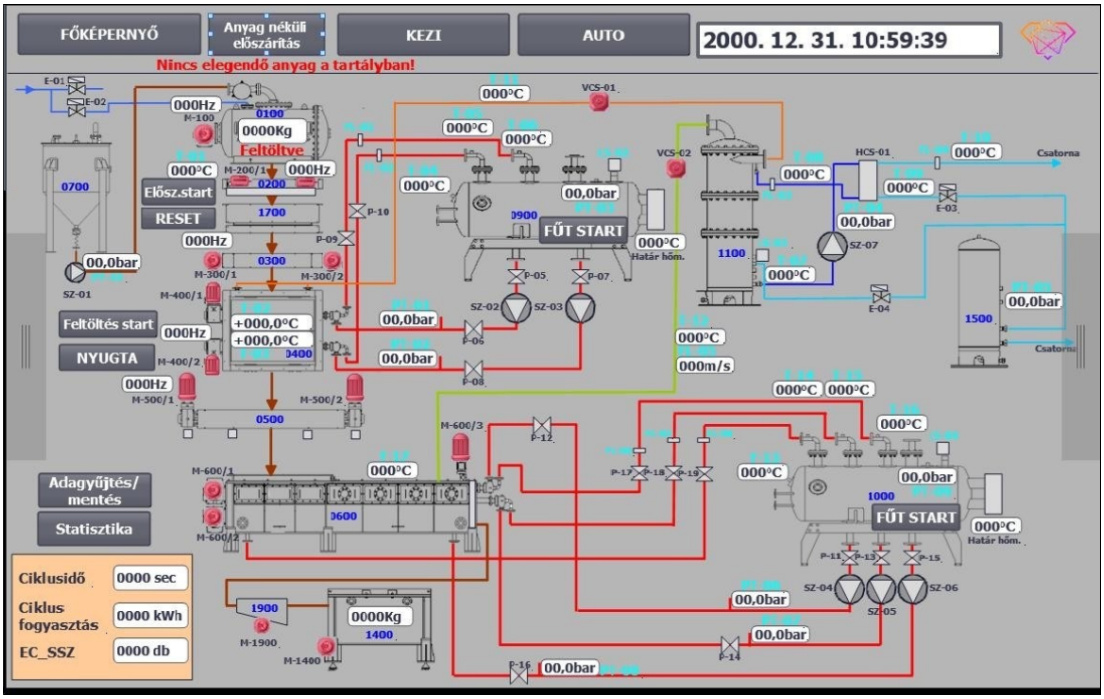


**Fig. 4.** *Schematic diagram of the control system (detail).*

After solving these problems, the production was followed by the mechanical assembly phase, which was implemented as an installation in the frame structure unit, in order to ensure optimal space utilization. In the meantime, the testing of the equipment continued, the commissioning, the licensing process was started, and the documentation for obtaining utility model protection was prepared. Test protocols (notes/records) were prepared for the testing steps, in which the function tests to be performed and tested, as well as mechanical, mechanical and electrical operation tests were precisely defined. The tests ended with good results, the equipment was installed, and its operation has been flawless ever since. The assembled equipment is shown in **Figure 5.**

## 6. Conclusions

The drying process is usually used to evaporate water from the residual solids in the wastewater. In addition to the dryer, the drying system usually consists of material handling and storage equipment, heat generation and transfer equipment, air handling and distribution equipment, emission reduction equipment and auxiliary systems. These equipment systems can take many forms, one of which is the drying equipment designed and manufactured by us, which operates on the Oasis of the Seas ship. Our equipment is a drying equipment composed of several parts, which has a so-called Pre-dryer part and a so-called Main dryer part. The task of the former is to preheat and pre-dry the material to be treated by applying it in a thin layer (~ 80% moisture content). The task of the latter is to dry the material to the desired ~ 20% moisture content.

**Fig. 5.** *The assembled equipment*

## Acknowledgement

Project no. 2019-1.1.1-PIACI-KFI -2019-00320 has been implemented with the support provided by the Ministry of Culture and Innovation of Hungary from the National Research, Development and Innovation Fund, financed under the 2019-1.1.1-PIACI-KFI funding scheme.

## References

[1] Kaszáné Kiss M.: *Hulladékgazdálkodás.* Debreceni Egyetem, 2003.

[2] Szira Z. : *A települési szilárd hulladék keletkezésének összefüggés-vizsgálata, valamint az önkormányzatok által biztosított hulladékkezelési közszolgáltatások elemzése Pest megyében.* PhD-értekezés. Gödöllő: Szent István Egyetem, 2010.

[3] C.L. Hii, S.V. Jangam, S.P. Ong, A.S. Mujumdar: *Solar Drying: Fundamentals*. Applications and Innovations, 2012.

[4] Yuan J, Zhang D, Li Y. , et al.: *Effects of Adding Bulking Agents on IO-stabilization and Drying of Municipal Solid Waste*. Waste Manage., 62. (2017) 52–60.

[5] Water Environment Federation. Residuals and Biosolids Committee Bioenergy Technology Subcommittee. Fact Sheet: Drying of wastewater solids. January 2014. [Internet]

[6] Dhaundiyal A., Toth L. : *Thermo-Economic Assessment of a Bench-Scale Pyrolysis Unit through a Process Simulator*. Biofuels Bioproducts & Biorefining-Biofpr, 17. (2023) 1681–1697.

[7] Virág S., Montvajszki M., Korzenszky: *Termikus hulladékkezelési eljárások*. Szarvas, 2015. TÁMOP-4.2.2.A-11/1/KONV-2012-0015 projekt: Alapkutatás fejlesztés a Szent István Egyetem Pirolízis Technológia Központjában.

[8] https://www.limehungary.hu/dobszaritok/

[9] Lányi K., Molnar E., Vanó I., Korzenszky P.: *Looking Behind The Process of Pyrolysis in Waste Management: Questions on The Composition and Quality of End-Product and Their Answers by Meas of Analytical Chemistry.* Hungarian Agricultural Engineering (2014) 25–28.

[10] Korzenszky P., Lányi K., Simándi P.: *Test Results of a Pyrolysis Pilot Plant in Hungary.* Hungarian Agricultural Engineering, 28. (2015) 48–52.

[11] Eskildsen K.: *Modularization*. Aalborg University Copenhagen, 2011.

Műszaki Tudományos Közlemények vol. 22. (2025) 52–58.
DOI: Hungarian: https://doi.org/10.33895/mtk-2025.22.09
English: https://doi.org/10.33894/mtk-2025.22.09

# WATERCRESS AS A MEDICINAL HERB GROWN IN A HYDROPONIC SYSTEM

Kiss Virág,[1] Izbékiné Szabolcsik Andrea,[2] Bellér Gábor[3]

[1] *University of Debrecen, Department of Environmental Engineering, Debrecen, Hungary, viraglps00@gmail.com*

[2] *University of Debrecen, Department of Environmental Engineering, Debrecen, Hungary. szabolcsikandi@eng.unideb.hu*

[3] *University of Debrecen, Department of Environmental Engineering, Debrecen, Hungary. beller.gabor@eng.unideb.hu*

**Abstract**

In this research, synthetic bathing water was created treated by coagulation and mechanical filtration. The waters were qualified before and after treatment, so that the effectiveness of the treatment could be calculated. The greywater produced during the treatment was circulated in a hydroponic tower next to a tapwater control tower. The watercress grown was analyzed in the towers and their results were compared. The results show that the greywater treatment was effective and the watercresses were comfortable in the synthetic bathing water tower without nutrient solution. They grew larger than their counterparts grown in tapwater, and their average moisture content was also higher. Additionally, the spectrophotometric determination of indole-3-carbinol content was investigated in the plants. However, the obtained spectra were noisy, and the absorbance values were too small for reliable evaluation. Our further aim is to improve the determination of active ingredient using other methods (e.g. solid phase extraction).

**Keywords***: greywater, watercress, hydropony, indole-3-carbinol.*

## 1. Introduction

Nowadays, the treatment and reuse of greywater from households is becoming increasingly common, as water is a limited resource. The reuse of greywater allows for a reduction in household water use, which contributes to reducing water consumption, and therefore it is important to raise awareness of the importance of reusing greywater in households. In addition, it is essential to protect our health, to which the consumption of medicinal herbs makes a major contribution. Watercress is a highly nutritious plant that has a number of beneficial effects on the human body, and indole-3-carbinol, which is thought to have cancer-preventive effects, is also found in it. With the right results, the sustainability of medicinal plant supply to the pharmaceutical and food industries can be enhanced through the cultivation of watercress in hydroponic towers.

## 2. Alternative water source: greywater

In households, two types of wastewater are distinguished based on quality criteria. These are blackwater and greywater. Blackwater is the more polluted fraction of wastewater, which is produced during the flushing of toilets and therefore contains contaminants that pose a serious health risk. Greywater (GW) is the less contaminated fraction of wastewater, which does not contain the blackwater from toilet flushing. It includes used water from bathroom activities, washing dishes and laundry. Greywater can be further subdivided into light and dark greywater fractions based on the degree of contamination. For many water-using activities, such as the self-irrigation of medicinal plants, greywater treatment is necessary, otherwise the plants would take up undesirable pollutants that would enter the food chain. In our research, synthetic

bathing water was treated, which was based on tap water, using coagulation/flocculation chemical methods and mechanical filtration through sand [1, 2].

## 3. Hydroponic cultivation of watercress

Watercress (Nasturtium officinale) is a highly nutritious plant of the cruciferous family (Brassicaceae) that has many beneficial effects on the human body. It is full of vitamins and minerals such as vitamin C, vitamin A, vitamin K, as well as folic acid, calcium and iron. It also has antioxidants such as beta-carotene, lutein and quercetin. Furthermore, it is rich in a compound called glucosinolate, which is converted into indole-3-carbinol when plant cells are broken down (e.g. by chopping or chewing) [3].

By growing watercress in a treated greywater-based hydroponic system, the supply of medicinal plants can be made more sustainable to the pharmaceutical and food industries. By growing up to 600 plants on 7.5 m2 of land up to three times faster and 30% more efficient than conventional methods, and by recycling and reusing the water circulating in the system, 90% less water can be used up than conventional outdoor cultivation [4].

## 4. Material and methods

Based on the previous research results of the Department of Environmental Engineering [2], ], a synthetic bathwater based on tap water was created, and this greywater fraction was treated by coagulation with ferric chloride ($FeCl_3$) (Figure 1) and mechanical filtration through sand. The greywater produced during the treatment was circulated in the hydroponic tower, which was assessed before and after treatment to calculate the effectiveness of the treatment. A tap water control tower was also operated for a better comparison. The irrigation water entering and leaving the towers was also assessed to monitor changes in water quality. Among the water quality parameters, pH, specific conductivity (EC), zeta potential (ZP), turbidity (TURB), biochemical oxygen demand ($BOD_5$), chemical oxygen demand (COD), and total organic carbon (TOC) were investigated.

For pH measurement, a SenTix 41 combined pH electrode was used, for specific electrical conductivity (EC) and zeta potential (ZP), a Zetasizer Nano Z device, for turbidity (TURB), a Turb 555-IR turbidity meter, for biochemical oxygen demand ($BOD_5$), OxiTop IS 12 devices, for chemical oxygen demand (COD), a NANOCOLOR Linus spectrophotometer, and for total organic carbon (TOC), a Shimadzu TOC-VCPN device were applied. Plants were pre-grown for 12 days and placed in hydrobaskets with rockwool cubes in Rotower hydroponic tubes, distributed by Green Drops Farm Ltd. as shown in Figure 2.

The watercresses spent 20 days in the hydroponic system. Each day, pH and EC parameters were measured in both towers. Different plants have different ideal pH requirements, but the optimal range varies between 6.5 and 7.5. The optimal level was maintained by the addition of 24.5% phosphoric acid. Water evaporated or consumed by the plants was replenished every 3 days (tap water was taken from the main water supply and treated greywater was prepared and treated in

**Fig. 1.** *Coagulation-flocculation chemical treatment.*

**Fig. 2.** *Watercress in the hydroponic system.*

advance and stored in a refrigerator). During the analysis of the watercresses, the average plant length, the maximum root length and the moisture content of the bushes in both towers were measured, and the average chlorophyll-a, chlorophyll-b and total carotenoid concentrations were also measured with a Nanocolor Vis spectrophotometer. The concentration of the active ingredient indole-3-carbinol (I3C) in the water sample was determined by UV/VIS spectrophotometry. The concentration of I3C was measured using an Agilent Cary 60 photometer and ethyl acetate and ultrapure water were used as solvents.

## 5. Results and conclusions

In this chapter, the results of the water and plant qualification and I3C determination studies are presented together with their evaluation.

### 5.1. Water quality parameters

As part of our research, synthetic bathwater was prepared and treated four times. Untreated greywater was assessed to evaluate the effectiveness of the treatment. In addition to using tap water as irrigation water in one of the hydroponic towers, it also served as the base for the synthetic greywater, so each time, tap water samples were taken and assessed, along with untreated and treated greywater. The quality parameters of the water types are presented, averaged and supplemented with standard deviations, using tables.

In **Table 1** it can be observed that tap water has the lowest average pH (7.67±0,1), which is basically higher than the typically neutral (7) value of tap water. This indicates that the tap water used in our study is slightly more alkaline. For the treatment of greywater, turbidity (TURB), $BOD_5$, and COD results were evaluated according to Regulation (EU) 2020/741 of the European Parliament and of the Council on minimum requirements for the reuse of water **[5]**, and Directive 91/271/EEC on urban wastewater treatment **[6]** respectively. Measurement of TURB is important in greywater treatment, as high turbidity affects filtration and disinfection processes, as well as reducing the aesthetic quality of the water. According to EU Directive 2020/741 **[5]** TURB should not exceed 5 NTU. The treated greywater had an average TURB value of 0.82±0.78 NTU, which is below the EU 2020/741 turbidity limit. The aim of greywater treatment is to minimize the amount of organic matter. According to EU Directive 2020/741 **[5]** the permitted value of $BOD_5$ for agricultural irrigation is ≤ 10 mg/l. The average $BOD_5$ value of the greywater treated was 4.13±3.64 mg/l which does not exceed this limit. The reduction of COD levels is a key factor in the treatment of greywater. The COD limit value under Directive 91/271/EEC **[6]** is 125 mg/l. The average value of the synthetic bathwater treated during the research was 14.1±4.5 mg/l, thus, this requirement was fulfilled with the applied treatment. Overall, the treated greywater fulfilled the TURB, $BOD_5$ and COD limits, and no significant differences were found compared to the drinking water, thus the treatment procedure can be considered effective. By comparing the parameters of untreated and treated synthetic bathing water, treatment efficiencies were also calculated, as shown in **Table 2.**

Based on the results of treatment efficiency, it can be said that the amount of pollutants was reduced by the treatment process. The treatment of greywater was mainly aimed at reducing TURB, $BOD_5$, COD and TOC, which was achieved by having a treatment efficiency of more than 90% for these parameters.

**Table 1.** *Summary table of results for water types*

| Parameter | Unit of measurement | Tapwater | Untreated greywater | Treated greywater |
|---|---|---|---|---|
| pH | - | 7.67±0.1 | 8.18±0.1 | 8.06±0.1 |
| EC | µS/cm | 7.67±38 | 917±23 | 851±203 |
| ZP | mV | - | -32.57±1.70 | -11.47±2.26 |
| TURB | NTU | 0.29±0.06 | 43.3±6.1 | 0.82±0.78 |
| $BOD_5$ | mg/l | 1.38±0.52 | 137±61 | 4.13±3.64 |
| KOD | mg/l | 8.83±0.72 | 515±170 | 14.1±4.5 |
| TOC | mg/l | 2.74±0.27 | 57.7±5.4 | 3.86±0.94 |

**Table 2.** *The treatment efficiency of the water quality parameters*

| Parameter | Unit of measurement | Treatement efficiency (%) |
|---|---|---|
| pH | - | decreased |
| EC | µS/cm | 7,27 |
| ZP | mV | 64,78 |
| TURB | NTU | 98,11 |
| $BOD_5$ | mg/l | 96,97 |
| KOD | mg/l | 97,27 |
| TOC | mg/l | 93,31 |

### 5.2. Analysis of the irrigation water before and after the hydroponic tower

Treated synthetic bathwater and tap water (used as a control) entering the hydroponic tower were certified. At the end of the trial period the water quality parameters of the tower water were measured again to monitor changes in water quality. Since water was added several times, the average of the water inputs was used as a basis.

In **Table 3,** it can be observed that the pH of the tap water decreased, which can be explained by the addition of phosphoric acid (which was added to maintain the correct pH). Smaller amounts of phosphoric acid were added, which did not cause a drastic drop in pH, so it had to be used more often to maintain the optimal pH. TURB also decreased, but $BOD_5$, COD and TOC increased due to plant activity.

**Table 4** illustrates that the pH and ZP of the treated greywater also decreased, which is also due to the addition of phosphoric acid. More phosphoric acid was added at the beginning of the experiment than to the tap water, which resulted in a much lower pH than the tap water tower from the beginning of the experiment. The lower pH also affects the specific conductance and the nutrient uptake of the plants. The increase in EC is either due to the pH change or to the accumulation of possible organic or inorganic matter that the plants did not take up. The TURB value also decreased here, and $BOD_5$, COD and TOC also increased, again due to the activity of the plants. These suggest that the plants did not take up any residual organic and inorganic matter from the synthetic bathwater. In conclusion, the organic matter content ($BOD_5$, COD and TOC) of the tap water increased more than that of the treated greywater at the end of the experiment. However, turbidity was reduced more in the treated synthetic bathwater than in the tap water.

**Table 3.** *Tap water parameters before and after the hydroponic tower*

| Parameter | Unit of measurement | Tapwater | | Change |
|---|---|---|---|---|
| | | Before | After | |
| pH | - | 7.67±0.11 | 6.82±0.01 | decreased |
| EC | µS/cm | 767±38 | 580±11 | decreased by 24.49% |
| TURB | NTU | 0.29±0.06 | 0.12±0.03 | decreased by 58.62% |
| $BOD_5$ | mg/l | 1.38±0.52 | 4±0 | increased by 189.85% |
| KOD | mg/l | 8.83±0.72 | 22±0 | increased by 149% |
| TOC | mg/l | 2.74±0.27 | 18.03±0.02 | increased by 558% |

**Table 4.** *Treated greywater parameters before and after the hydroponic tower*

| Parameter | Unit of measurement | Treated greywater | | Change |
|---|---|---|---|---|
| | | Before | After | |
| pH | - | 8.06±0.05 | 6.71±0.01 | decreased |
| EC | µS/cm | 851±203 | 1225±34 | increased by 44.03% |
| ZP | mV | -11.47±2.26 | −5.43±2.64 | decreased by 52.66% |
| TURB | NTU | 0.82±0.78 | 0.15±0.03 | decreased by 81.71% |
| $BOD_5$ | mg/l | 4.13±3.64 | 4.50±0.71 | increased by 8.96% |
| KOD | mg/l | 14±4 | 17±1 | increased by 20.74% |
| TOC | mg/l | 3.86±0.94 | 6.50±0.06 | increased by 40.62% |

### 5.3. Analysis of watercresses

During the hydroponic plant cultivation, a total of 20 watercresses were analysed from each tower. In the analysis of the watercresses, the average plant length of each bush in each tower was measured using 3 parallel measurements and the maximum root length was measured using a tape measure. The results obtained were averaged separately for the parameters of the plants grown in the drinking water and in the treated greywater towers.

The average maximum root length of the watercresses grown in the tap water tower was 49±7 cm and that of the watercresses grown in the cultivated greywater tower was 35±8 cm, as illustrated in **Figure 3**. The difference in maximum root length is about 14 cm and the plants grown in drinking water have the longer roots.

The average plant length was 19±3 cm for the tap water plants and 19±6 cm for the treated greywater plants, as illustrated in **Figure 4**.

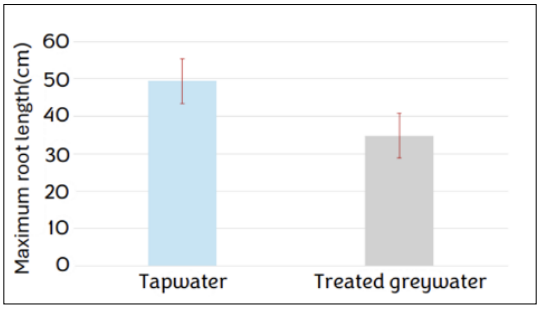


**Fig. 3.** *Comparison of the average maximum root length of the watercresses.*

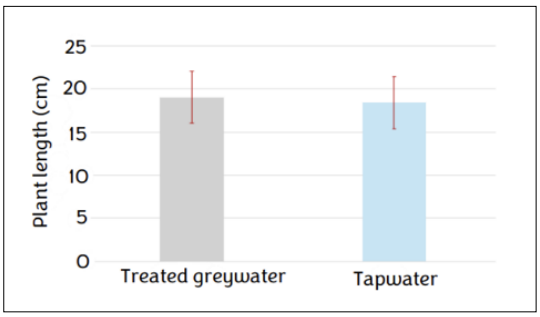


**Fig. 4.** *Comparison of the average plant length of the watercresses.*

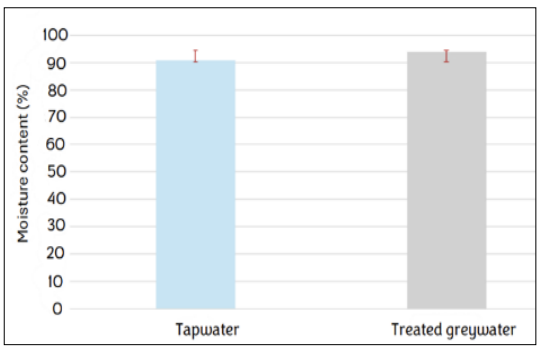


**Fig. 5.** *Average moisture content of the watercresses.*

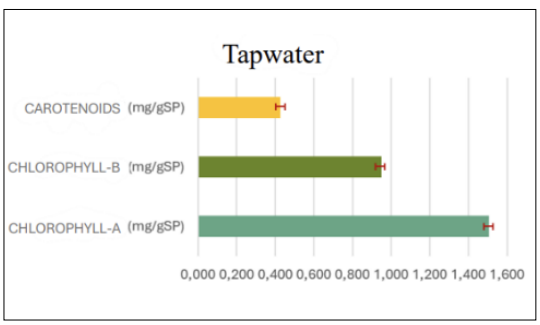


**Fig. 6.** *The average concentration of chlorophyll-a, chlorophyll-b, and carotenoids in the watercresses grown in tap water*

Overall, there is no significant difference in plant length. The wet and dry biomass weights of the watercresses were measured to determine their average moisture content, which is compared in **Figure 5** .

In terms of average moisture content, it can be said that there is not much difference between the plants grown on tap water (90.94±0.02%) and treated greywater (93.84±0.01%), but the average moisture content of the watercresses in the treated synthetic water tower is slightly higher. However, our measurements support the claims in the literature **[7]**, regarding the high moisture content of watercress.

In order to determine the concentration of chlorophyll-a, chlorophyll-b and total carotenoids, pigments from the plants were firstly extracted and then determined spectrophotometrically. From these results, the concentrations of chlorophyll-a, chlorophyll-b and total carotenoids were calculated and averaged. **Figure 6** shows the average results of the watercresses grown on tap water and **Figure 7** shows the average results of the watercresses grown on treated greywater.

The average chlorophyll-a concentration of the tap water reared watercress was 1.50±0.25 mg/gSP, chlorophyll-b concentration 0.95±0.20 mg/gSP, and carotenoids concentration 0.43±0.08 mg/gSP.

The plants grown in the treated greywater had an average concentration of chlorophyll-a of 1.18±0.20 mg/gSP, chlorophyll-b of 0.71±0.12 mg/gSP and carotenoids of 0.32±0.60 mg/gSP. In comparison, the watercresses in the tap water hydroponic tower had a slightly higher average concentration of the pigments compared to the treated greywater tower.

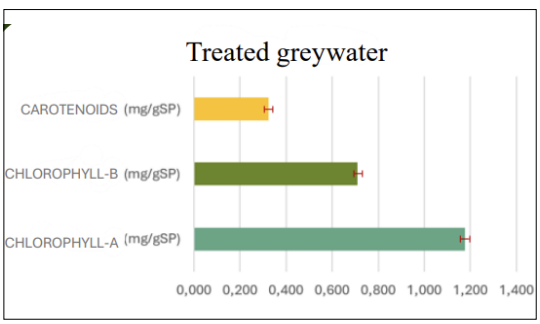


**Fig. 7.** *The average concentration of chlorophyll-a, chlorophyll-b, and carotenoids in the watercresses grown in treated greywater.*

### 5.4. Results of the I3C active ingredient determination analysis

As a preliminary experiment, the spectrum of ethyl acetate in aqueous solution was firstly determined. The absorbance of pure ethyl acetate was too intense, so aqueous solutions were analysed. Using this series of experiments, the molar spectrum (ε) of ethyl acetate in aqueous medium was determined in the wavelength range 190-290 nm, as illustrated in **Figure 8**.

The absorption maximum of ethyl acetate is between 200 nm and 210 nm, with low absorption at longer wavelengths. To determine the molar spectrum of I3C, I3C solid chemical was used. To prepare the calibration series, solid I3C was dissolved in ethyl acetate and diluted with ultrapure water. The molar spectrum of I3C between 225 and 300 nm is illustrated in **Figure 9.**

The calibration series showed that the absorption maximum of I3C was in the range of 250 nm to 300 nm. At these wavelengths, the interfering effect of ethyl acetate is negligible but can be corrected if necessary. For the I3C determination of watercress extracts, 0.5; 1; and 2 g of watercress slurries were weighted and extracted with ethyl acetate and diluted with ultrapure water. Representative spectra are shown in **Figure 10**.

The following conclusions were drawn from the spectra of extracts containing watercress pulp of different masses. The absorbance systematically increased with increasing volume of the extract in the cuvette, but unfortunately the fine structure of I3C (**Figure 9**) is difficult to discern. The measured spectra are noisy and the absorbances are too low for reliable evaluation. An additional method was also tried, but the same conclusions were drawn as for the spectra of watercress extracts. Experiments for the quantification of I3C are planned, both by further development of the spectrophotometric method and by the inclusion of other techniques. In the former case, increasing the cuvette concentration (and thus the absorbance) is a possible approach, but even then the matrix effect can be a problem. As an alternative method, for example, high-performance liquid chromatography (HPLC) is an obvious choice. In the coming period, we intend to further develop the spectrophotometric method for the determination of I3C using solid phase extraction (SPE).

It is important to note that these data were generated using synthetic greywater treated without nutrient solution during the cultivation of watercress in a hydroponic system.

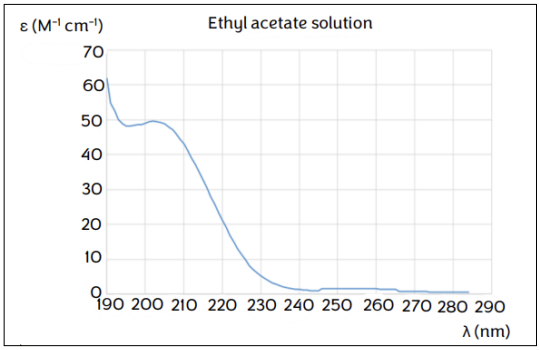


**Fig. 8.** *The spectrum of ethyl acetate.*

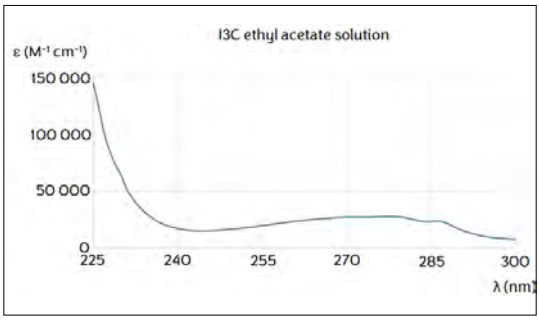


**Fig. 9.** *The spectrum of I3C ethyl acetate solution.*

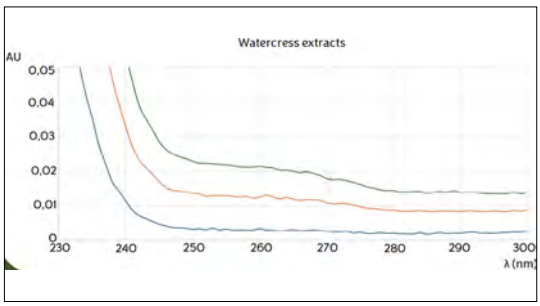


**Fig. 10.** The spectrum of the solution containing 1 g of watercress paste.

## 6. Conclusions

The management of greywater in households and the importance of its reuse were investigated, with a particular focus on the hydroponic cultivation of watercress (Nasturtium offi-cinale), which can make the supply of medicinal plants more sustainable by recycling greywater. Greywater is a type of household wastewater that does not contain black water (wastewater from toilet flushing), the proper treatment of which is a key to prevent plants from picking up unwant-

ed contaminants. In this research, greywater was treated by the coagulation/floculation chemical method and mechanical filtration, and then applied to watercress cultivation in a hydroponic system. The quality parameters of the tap water and treated greywater were continuously measured and the results showed that the treatment of the greywater was successful as it fulfilled the water quality limits (turbidity, $BOD_5$, COD) set by the European Union **[5, 6]**. The growth and biological parameters of the watercresses were also monitored. There was no significant difference in plant length, root length and moisture content between plants grown on tap water and treated greywater, although tap water plants had slightly higher concentrations of chlorophyll-a, chlorophyll-b and carotenoids. The concentration of the active substance indole-3-carbinol (I3C) was determined by UV/VIS spectrometry. However, the measured spectra are noisy and the absorbances are too small for reliable evaluation. In conclusion, the results of this study showed that treated greywater can be effectively used to grow watercress in hydroponic systems, thereby reducing water logging in a sustainable manner, while not significantly affecting the quality parameters of the plants.

## References

[1] Y.-P. V.-A. M. Boyjoo: *A Review of Greywater Characteristic and Treatment Processes*. In: Water Scien. and Techn., 2013, pp. 67, 1403-1424

[2] Andrea Szabolcsik-Izbéki: *The Removal of Pollutants from Synthetic Bathroom Greywater by Coagulation-Flocculation and Filtration as a Fit-for-Purpose Method*. Journal of Environmental Chemical Engineering, 12/1. 2024.

[3] The webpage of Green Drops Farm Kft., *Vízitorma*. (accessed: 2025. 02. 16.) https://rotower.greendropsfarm.com/hu/gyogynoveny-hidroponias-rendszerben/

[4] A Green Drops Farm Kft. honlapja: *Hidropóniás növénytermesztés*. (accessed: 2025. 02. 16.) https://rotower.greendropsfarm.com/hu/blog/

[5] E. U. H. Lapja: *Az Európai Parlament És A Tanács (Eu) 2020/741 Rendelete (2020. május 25.) a víz újrafelhasználására vonatkozó minimumkövetelményekről.* (accessed: 2025. 02. 16.) https://eur-lex.europa.eu/legalcontent/HU/TXT/?uri=CELEX%3A32020R0741

[6] EUR-LEX, *A Tanács irányelve (1991. május 21.) a települési szennyvíz kezeléséről (91/271/EGK), 1991*. (accessed: 2025. 02.16.) https://eur-lex.europa.eu/legalcontent/HU/TXT/?uri=CELEX:31991L0271

[7] Ali Esmail Al-Snafi: *A Review on Nasturtium Officinale: A Potential Medicinal Plant*. IOSR Journal of Pharmacy Series. I., 10/9. (2020) 33–43.

Műszaki Tudományos Közlemények vol. 22. (2025) 59–64.
DOI: Hungarian: https://doi.org/10.33895/mtk-2025.22.10
English: https://doi.org/10.33894/mtk-2025.22.10

# INTERDISCIPLINARY AI RESEARCH METHODOLOGY

Levente KOLCSÁR,[1] László BAKÓ[2]

[1] *Sapientia University, Faculty of Technical and Human Sciences, Department of Electrical Engineering, Târgu Mureş, Romania, kolcsar.levente@ms.sapientia.ro*

[2] *University, Faculty of Technical and Human Sciences, Department of Electrical Engineering, Târgu Mureş, Romania, lbako@ms.sapientia.ro*

**Abstract**

The use of artificial intelligence (AI) in our time is becoming more and more extensive, so it is no question that there is a need for new AI concepts. We have developed our research methodology to accommodate new cognitive science theories, which we present through a concrete example: how Integrated Information Theory (IIT) was born and what it is good for. IIT is one of the main theories of consciousness in cognitive neuroscience and phenomenology. The main pillar of our methodology is the philosophy of science, which puts IIT into context, examines its origin and usability. This serves the purpose of a framework to be able to interpret ideas from the most diverse fields and to rank them according to their engineering applicability, so that we can create new, useful AI toolkits from them.

**Keywords***: AI, research, philosophy of science, IIT.*

## 1. Introduction

In our study, using the philosophy of science methodology, the AI researcher contextualizes theories from the field of cognitive sciences and only then begins working with them. This is necessary because interdisciplinary work requires order and a unified interpretation, which demands a well-defined framework. Through this method, the researcher becomes familiar with the theory itself, its origin, its mathematical description, and its applicability. We define the three main fields that constitute the structure of the methodology:

**α. Philosophy** consists of systematic linguistic and conceptual structures derived from our perceptions of the world. The central questions of philosophy are: What is nature? What is its origin? What is its foundation? Who are we? These ideas manifest not only in our understanding methods but also in our everyday lives.

**β. Science** as we define it, is a branching process that, like philosophy, seeks to understand nature. However, it grounds this understanding in systematic observation and experimentation.

This reveals that the overlap between the two fields occurs during the creation of new scientific theories, as in their earliest phase, devoid of experiments, researchers must rely solely on imagination. This connection, evident both logically and historicall [1], underscores that science originates from philosophy.

**γ. Philosophy of Science** is the branch of philosophy concerned with scientific thinking and methodology. Its primary aim is to systematically guide and refine scientific research and methods, while addressing the challenges of scientific reasoning and human bias. Examples of fields where we deem this discipline critical include: atomic physics, cosmology, biology, cognitive sciences, AI research, psychology, ethics, and the humanities. Conversely, we consider it less pivotal in areas such as: applied sciences, technologies, industry, and any domain where existing theories are applied unchanged.

## 2. Structure of the Methodology

The AI researcher must analyze and document the discovered or newly devised theory across the listed contexts, examining distinct aspects within each. The contexts correspond to the subjects defined by Greek letters (α, β, γ):

I. Historical Context (α, β)
II. Mathematical Description(α,β,γ)

III. Epistemological Context (β, γ)
IV. Ontological Context (α, β, γ)
V. Methodological Context (β, γ)
VI. Scientific Results (β)
VII. AI Applicability (β)
VIII. Axiological Context (α, γ)

For each context, the theory must be scored on a scale of 1–5, depending on its prominence in that context. A score of 1 indicates no relevance, while 5 denotes maximal relevance.

Example: The Integrated Information Theory (IIT) receives a score of 3 in the AI Applicability context. This scoring **Table 1** helps prioritize which theories warrant deeper engagement. The researcher must cite annotated sources in the documentation to ensure usability for future publications.

At the conclusion of the methodology, the theory's general properties are recorded, and a weighted composite score is calculated. The theory's AI applicability is then expressed as a percentage.

## 3. Methodology Example: IIT

We selected a representative theory that originated outside technical disciplines, exhibits strong context I. and II. relevance, and serves as a paradigmatic case for philosophical questions in science.

- Name: Integrated Information Theory (IIT); **[2]**
- Field: Cognitive Neuroscience and Phenomenology;
- Lead Author: Dr. Giulio Tononi (Neuroscientist);
- Theory: The causally integrated information within a network serves as a metric for determining its potential "consciousness". Denoted as Φ, it quantifies the extent to which a network's structure integrates causal information in itself.

**Table 1.** *Score table for IIT*

| Context | Points |
|---|---|
| I. | 5 |
| II. | 5 |
| III. | 3 |
| IV. | 1 |
| V. | 4 |
| VI. | 4 |
| VII. | 3 |
| VIII. | 4 |

### 3.1. Historical Context (I.)

In this context, we examine the pre-theoretical intellectual traditions or scientific procedures that preceded the theory historically, as well as its relationship to classical philosophical movements. While this section can often be omitted, it is recommended for theories with deep historical roots. IIT scores 5 here, as it originates from a longstanding philosophical problem: What is consciousness? Why is it so difficult to explain? Dr. Tononi provides a robust historical and literary overview in his book Phi **[3]**, where he explains how thinkers like Galileo grappled with questions of consciousness.

The "hard problem of consciousness" was famously articulated by philosopher David Chalmers in the modern era **[4]**: How do biological mechanisms give rise to unified, qualitative subjective experience? Why does red appear as "red"? Why is consciousness so specific and qualitative?

From this problem IIT constructed its main axioms. (**Figure 1**)

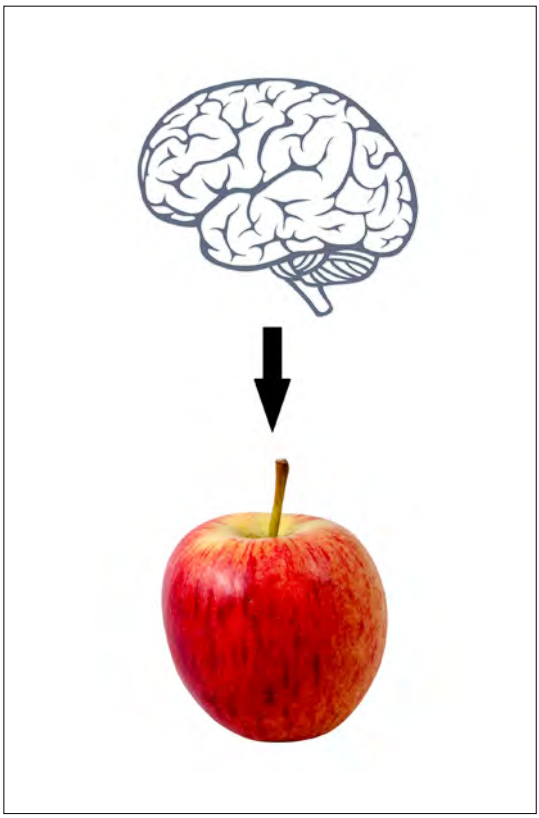

**Fig. 1.** *The "hard problem of consciousness"* **[5]**

### 3.2. Mathematical Description (II.)

In this section, we study the formal mathematical description of the theory, including all axioms, equations, and relationships that form its foundation. Axioms are properties derived from general observations, postulates are theoretical statements of derived regularities, and mathematical expressions formalize these postulates. In this context IIT scores 5 points.

#### 3.2.1. Existence

Axiom: Consciousness exists; therefore, it must possess causal power.

Postulate: The network must exhibit cause-effect power.

Mathematical Expression: Given a stochastic network in a state $x_t$ with transition probability matrix $T$, describing the probabilities of transitions from $x_t$ to $x_{t+1}$. From this we define the network's cause-effect repertoire:

$$P_{cause}(x_{t-1} | x_t)$$
$$P_{effect}(x_{t+1} | x_t) \quad (1)$$

#### 3.2.2. Composition

Axiom: Consciousness is composed of distinguishable phenomenological elements (e.g., sounds, colors, sensations).

Postulate: The network must form a complex of mechanisms (subsets of elements) that collectively constrain the cause-effect repertoire.

Mathematical Expression:

For a fully connected 3-node network:

$$M = \{A, B, C, AB, AC, BC, ABC\} \quad (2)$$

where $M$ is the set of mechanisms. A mechanism qualifies as a complex if its calculated $\Phi > 0$. (Mechanisms include bidirectional connections, e.g. $AB = \{AB, BA\}$)

#### 3.2.3. Information

Axiom: Every conscious experience is specific and distinct from other possible conscious states.

Postulate: The network must exhibit a differentiated causal structure (high informational divergence from randomness).

Mathematical Expression:

$$EI_{cause} = D(P_{cause}, P_{max})$$
$$EI_{effect} = D(P_{effect}, P_{max})$$
$$EI = min(EI_{cause}, EI_{effect}), \quad (3)$$

where:

$EI_{cause}$ – cause information;
$EI_{effect}$ – effect information;
$P_{max}$ – maximum entropy distribution;
$EI$ – effective information;
$D$ – distance metric (e.g., Earth Mover's Distance or Kullback–Leibler Divergence)

#### 3.2.4. Integration

Axiom: Consciousness is unified, not reducible to independent parts.

Postulate: integrated information (Φ) represents the irreducibility of information in a mechanism.

Mathematical term: bipartitions of the network: {{*A*}, {*B*,*C*}}, {{*B*}, {*A*,*C*}}, {{*C*}, {*A*,*B*}}}

$$\Phi = min_{MIP}[D(P_{total}, P_{partitioned})] \quad (4),$$

where:

$\varphi > 0$, if the subsystem is irreducible;
$P_{total}$ – cause-effect repertoire of the network;
$P_{partitioned}$ – cause-effect repertoire of the partitioned network;
$MIP$ – minimum information partition.

#### 3.2.5. Exclusion

Axiom: Consciousness is a specific state in time and space, excluding other states.

Postulate: The network's major complex is the one with maximal Φ.

Mathematical Expression:

$$\Phi_{max} = arg\ max_{m \in M}\{\Phi(m)\} \quad (5)$$

### 3.3. Epistemological Context (III.)

This section evaluates how the theory expands current knowledge and its explanatory power, a critical criterion for applicability. In AI, we aim to implement as many useful properties as possible to develop better problem-solving artificial agents.

Natural Agent (Living Being) → Artificial Agent (AI)

Properties of natural agents are extrapolated to artificial agents. Cognitive science studies the cognitive properties of human beings. IIT quantifies consciousness through the metric Φ. For this section, the theory scores an average of 3 points.

### 3.4. Ontological Context (IV.)

This context examines the ontological framework (e.g., electromagnetism, cells, atoms, or unconventional paradigms) the theory uses in its explanations.

IIT is ontologically independent, akin to Shannon's information theory, meaning it applies to any medium since it focuses on state dynamics rather than the specific processes or elements

constituting those states. For example, IIT can model both neurons and logic gates. This ontological independence is valuable for AI research, as such theories can be adapted to technical domains. IIT scores 1 point here.

### 3.5. Methodological Context (V.)

This section assesses the extent to which the theory aligns with established scientific methodologies:

Deductive Method: 0. Background → 1. Theory → 2. Prediction Method → 3. Testing the Prediction (Measurement) → 4. Validate the Prediction → 5. Accept/Reject the Theory

Inductive Method: 0. Background → 1. Observation (Measurement) → 2. Identify Patterns → 3. Generalize → 3. Theory → 4. Validate the Theory → 5. Accept/Reject the Theory.

IIT follows a deductive methodology. While it has demonstrated neuroscientific results, its computational complexity (NP-hard) for large networks necessitates approximations. Thus, it scores 4 points in this context.

### 3.6. Scientific Results (VI.)

Here, we evaluate how well the theory is validated through observational and experimental methods. A high score reflects robust explanatory power for natural phenomena.

IIT scores 4 points in this context because it has produced predictive results comparable to the Global Workspace Theory of consciousness [6]. Additional achievements in brain research include. [7, 8] (Note: A score of 1 is assigned if no experimental results exist. Findings within the theory's own field suffice for validation.)

### 3.7. AI Applicability (VII.)

For the IIT theory, a public Python library (pyphi) has been developed, freely available under the condition that associated publications are properly cited. [9] This library enables the calculation of Φ for arbitrary n-node stochastic networks. Figure 2 illustrates our example, in which we compute Φ for a network of logic gates.

Python code:

```
#The name of the nodes and it's order:
  node_labels = ('OR','AND','XOR' )
#Initial states vector [n]:
  state = (1, 0, 0)
#Connectivity matrix [n * n]:
  cm = np.array ([[0,1,1],
                  [1,0,1],
                  [1,1,0]])
#Transition probability matrix [2^n * 2^n]:
  tpm = np.array([[1, 0, 0, 0, 0, 0, 0, 0 ],
                  [0, 0, 0, 0, 1, 0, 0, 0 ],
                  [0, 0, 0, 0, 0, 1, 0, 0 ],
                  [0, 1, 0, 0, 0, 0, 0, 0 ],
                  [0, 1, 0, 0, 0, 0, 0, 0 ],
                  [0, 0, 0, 0, 0, 0, 0, 1 ],
                  [0, 0, 0, 0, 0, 1, 0, 0 ],
                  [0, 0, 0, 1, 0, 0, 0, 0 ]])
#Note:
cm connectivity entries can take binary values (0 or 1). In this example, the main diagonal is set to 0 because the network does not include nodes with self-connections.
tpm is a matrix that encodes the probabilities of transitioning from all possible states at t (row indices) to all possible state at t+1
#Generating the network:
  net = pyphi.Network(tpm, cm, node_labels)
#Compute the major complex of the network:
  mct = pyphi.compute.major_complex(net, state)
#Use Φ of the major complex:
  phi_maxt = mc.phi
#Φmaxt = 1.916
```

Currently, we can state that IIT is useful for network analysis to determine the degree of recurrence (feedback loops) in a network, as feedback increases the Φ value. According to the model, the more recurrent pathways a network has, the more integrated it becomes. This property can also be interpreted as dynamic memory, determined not only by the states of nodes but also by

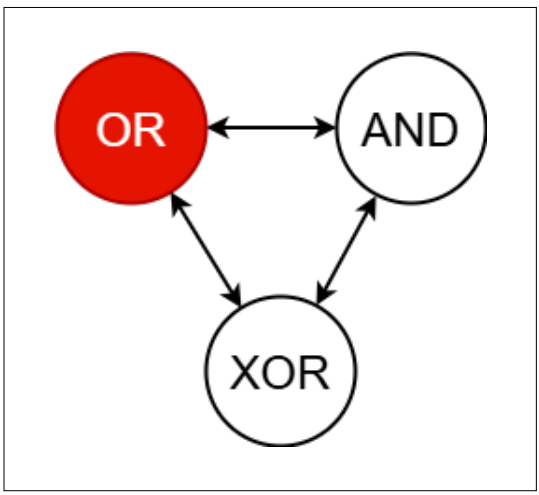


**Fig. 2.** *Example network (red "1", white "0").*

the network's topology. While this is a network analysis tool, we do not yet see direct utility for AI, so we assign a neutral score of 3 for AI applicability. Potential applications include using Φ as a training criterion for networks with variable topologies or, in the future, as a metric for ethical classification of AI systems. This context requires further analysis, as we believe Φ could also be applied to network optimization and sensor fusion problems.

### 3.8. Axiological Context (VIII.)

This section evaluates the theory's relevance to AI ethics. AI ethics is an increasingly critical issue, making this context significant for many models. According to the nonprofit Eleos AI **[10]** two main risks threaten AI evolution:

– Overestimation (attributing human-like properties to AI);
– Underestimation.

IIT scores 4 here, as its Φ metric suggests even logic gates could form a "conscious" AI. However, we remain critical of this claim. While Φ is currently treated as a metric—not a definitive measure—we acknowledge its potential role in understanding consciousness. We intentionally avoid defining consciousness or intelligence, as these remain open questions in neuroscience. For AI, we aim to maintain flexibility to develop new models. IIT posits consciousness as an internal process distinct from intelligence (an output property.

### 3.9. Methodology Summary

At the end of the documentation, we record the general properties of the IIT theory:

– Brain inspired AI? Yes;
– Traditional/Statistical AI? No;
– Top-down model? Only in method;
– Bottom-up model? No;
– Deductive or inductive? Inductive.

Using the context scores (**Table 1**) we calculate a weighted composite score, prioritizing AI applicability (VII.) while heavily weighting mathematical rigor (II.) and scientific results (VI.). Contexts III., IV., V., and VIII. contribute indirectly, while I. (historical) is excluded. Context IV. is inversely weighted, as stronger ontological foundations complicate interdisciplinary adaptation. This weighting requires further refinement.

$$\text{sum} = \text{I.}*0 + \text{II.}*0.5 + \text{III.}*0.25 - \text{IV.}*0.25 + \text{V.}*0.25 + \text{VI.}*0.5 + \text{VII.}*1 + \text{VIII.}*0.1$$

Converted to a percentage using the rule of three:

$$IIT_{rating} = 74\%.$$

## 4. Conclusions

Our methodology is a starting point for deriving practical AI tools from cognitive science theories. While it requires refinement through application to more theories, the goal is to enable analysis of any theory or model, regardless of its cognitive science origin. A repository of such analyses would simplify designing new models by leveraging existing insights and identifying promising applications for implementation.

The representative IIT theory discussed by the methodology requires further analysis on our part in terms of its applicability in AI, which will be a separate task for us in the near future.

## References


[1] Quack M.: *Science and Arts, Philosophy and Science: Why after All? Why Not?*, Helvetica Chimica Acta, 106/4. (2023) 1–3. https://doi.org/10.1002/hlca.202200174

[2] Oizumi M., Albantakis L., Tononi G.: *From the Phenomenology to the Mechanisms of Consciousness: Integrated Information Theory 3.0*. PLOS Computational Biology, 2014, 1–25. https://doi.org/10.1371/journal.pcbi.1003588

[3] G.: *Phi: A Voyage from the Brain to the Soul.* 1. ed. Pantheon Books, New York, 2012, 1–38.

[4] Chalmers D.: *Facing up to the Problem of Consciousness*. Journal of Consciousness Studies, 2/3. (1995) 200–219. https://philpapers.org/rec/CHAFUT

[5] UI Here free samples. https://www.uihere.com/ (2025.02.22)

[6] Cogitate Consortium, Ferrante O., Gorska-Klimowsk U., et al.: *An Adversarial Collaboration to Critically Evaluate Theories of Consciousness.* bioRxiv 2023.06.23.546249, 1–68. https://doi.org/10.1101/2023.06.23.546249

[7] Ferrarelli F., Massimini M., Sarasso S., Casali A., Riedner B.A., Angelini G., Tononi G., Pearce R.A.: *Breakdown in Cortical Effective Connectivity during Midazolam-Induced Loss of Consciousness*. Proc Natl Acad Sci USA. 107/6. (2010) 2681–2686. https://doi.org/10.1073/pnas.0913008107

[8] Casali A.G., Gosseries O.: *A Theoretically Based Index of Consciousness Independent of Sensory Processing and Behavior*. Science Translational Medicine, 5. (2013) 1–12. https://hdl.handle.net/2268/171542

[9] Mayner W.G.P., Marshall W., Albantakis L., Findlay G., Marchman R., Tononi G.: *PyPhi: A Toolbox for Integrated Information Theory.* PLoS Computational Biology, 14/7. (2018) 1–21. https://doi.org/10.1371/journal.pcbi.1006343

[10] Long R., Sebo J., Butlin P., Finlinson K., Fish K., Harding J., Pfau J., Sims T., Birch J., Chalmers D.: *Taking AI Welfare Seriously*. arXiv:2411.00986, (2024) 1–3.
https://doi.org/10.48550/arXiv.2411.00986

Műszaki Tudományos Közlemények vol. 22. (2025) 65–71.
DOI: Hungarian: https://doi.org/10.33895/mtk-2025.22.11
English: https://doi.org/10.33894/mtk-2025.22.11

# FINITE ELEMENT MODELLING OF THE RESTORATION OF WOODEN STRUCTURAL ELEMENTS WITH 3PHV60 TYPE EPOXY RESIN

Péter MÁRTON,[1] Kristóf Renátó VARGA,[2] Gábor KÖLLŐ[3]

[1] *Technical University of Cluj-Napoca, Faculty of Civil Engineering, Cluj-Napoca Romania, marton.peter17@gmail.com*

[2] *Budapest University of Technology and Economics, Faculty of Architecture, Budapest, Hungary, k.r.varga1211@gmail.com*

[3] *Technical University of Cluj-Napoca, Faculty of Civil Engineering, Cluj-Napoca Romania, Gavril.Kollo@cfdp.utcluj.ro*

**Abstract**

This article deals with the issue of repairing wooden structural elements with 3PHV60 type epoxy resin. The primary objective of this paper is to model the effects of cracking. Finite element design software has been used to study this issue and the results obtained have been compared with the results of previously performed destructive tests. The results of the damaged specimens were compared with the results of the resin-restored specimens.

**Keywords***: finite elemet modelling, structural timber, timber repair, epoxy resin, consolidation.*

## 1. Introduction

Nowadays, the rehabilitation of buildings is becoming increasingly important, but the restoration of damaged structural elements of a building poses many challenges. Structural restoration requires a responsible engineering approach, including an economical and environmentally conscious approach. One of the main principles of an economic and environmental approach is restoration/intervention according to the extent of the damage.

The aim of this multi-stage research is to investigate the local restoration of locally damaged timber structural elements with 3PHV60 type epoxy resin. The main question of the research is whether resin can increase the load-bearing capacity and stiffness of damaged timber structural elements.

## 2. Initial situation

The first step of the research was to investigate the mechanical properties of the 3PHV60 resin for the restoration of wooden structural frames, which is the subject of a previously published article - *Determination and comparison of the mechanical properties of epoxy resin type 3PHV60 with C24 structural graded softwood.* [1] To investigate the mechanical properties of the 3PHV60 type epoxy resin used, studies based on fracture tests were carried out. We have supplemented our knowledge with information provided by the manufacturer. After studying the mechanical properties of the resin, the applicability of the resin on wood was investigated. For more information on this issue, see the study entitled *Application of 3PHV60 type epoxy resin for the repair of timber structures.* [2]

## 3. Presentation of the test specimens

The study investigates the effect of cracks in the wooden structural members. To calculate the shear stresses of the elements subjected to bending, Eurocode 5 uses a $\mathbf{k}_{cr}$ coefficient (crack for shear resistance) which takes into account the effect of cracking to calculate the effective section width.

When determining the shear capacity, the element width to be taken into account is calculated by the relation $\mathbf{b}_{ef} = \mathbf{k}_{cr}\mathbf{b}$. For sawn and glued laminated timber, the value of $\mathbf{k}_{cr}$ is 0.67. Based on this value, weakening with a regular geome-

try was applied to 1/3 of the tested cross-section along the entire length of the specimen.

As a starting point, undamaged specimens were tested. Afterwards, we continued with the testing of unilaterally weakened specimens and finally specimens repaired with resin. The results of the tested cases were compared.

For the destructive tests and finite element models, the static model illustrated in **Figures 2–4.** was used, taking into account the requirements of the standard MSZ EN 408:2010+A1:2012 **[3]** .

During the destructive tests, the vertical displacement was measured at midspan and the force F at the moment of fracture. The study entitled *A The Use of Epoxy Resin in the Repair of Cracked Wooden Structural Elements* **[4]** provides a detailed demonstration of the results of the destructive tests.

## 4. Finite element modelling

After destructive tests, the experiments were also modelled by finite element method using ANSYS 2024 R2 software, and the resulting force-displacement diagrams were compared with those obtained in non-destructive tests. For the nonlinear calculation, the wooden specimen was constructed from SOLID45 type elements, assuming a linearly elastic orthotropic material with a material model that is hardening in tension and perfectly ductile in compression. The resin reinforcement was modelled using SOLID185 element type and assuming a linearly elastic isotropic material.

Assuming perfect working together between the two materials, the displacements at the common nodes of the different elements are linked so that they are identical throughout the calculation. Articulated supports were defined at one end of the beam and roller supports at the other end. The loads were placed on the beam at the third points on 40×40 mm rigid load distribution plates with small displacement controlled loads. The elements are composed of 5 mm×5 mm×5 mm finite elements.

In the theoretical model, the elastic moduli, Poisson's ratios and limit stress values of the materials were taken into account based on the results of the destructive tests and data from the literature. The parameters of the wood material model are summarized in **Table 1**.

### 4.1. Intact wood specimens

The force-displacement diagrams obtained from the destructive tests of the undamaged specimens were constructed alongside the diagrams

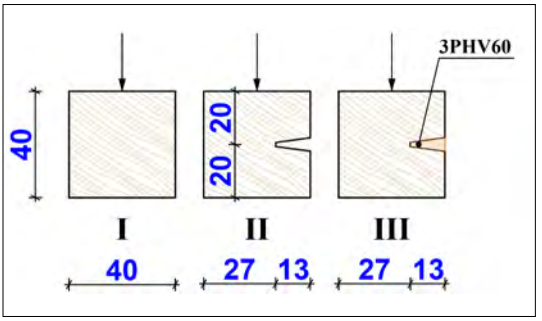


**Fig. 1.** *Cross section of the test specimens examined.*

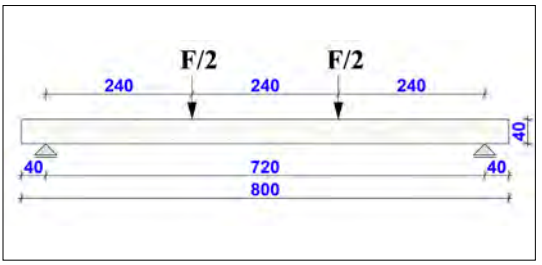


**Fig. 2.** *Experimental configuration used for testing intact wood specimens.*

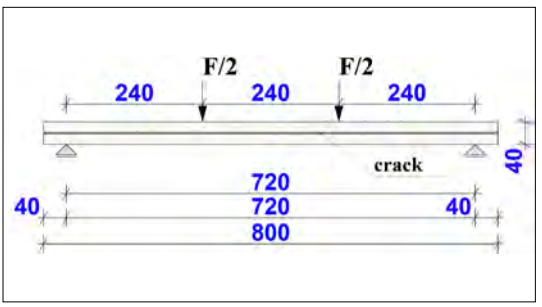


**Fig. 3.** *Static model used for testing wooden specimens cracked on one side.*

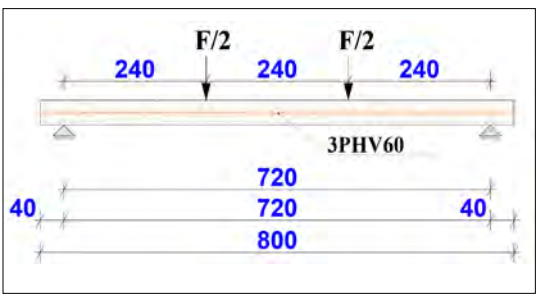


**Fig. 4.** *Static model used in the testing of resin-restored wood specimens.*

**Table 1.** *Mechanical properties of wood used in finite element models*

| Mechanical property | Value |
|---|---|
| Young-modulus (x direction) | 11000 N/mm$^2$ |
| Young-modulus (y direction) | 649 N/mm$^2$ |
| Young-modulus (z direction) | 1408 N/mm$^2$ |
| Poisson's raio (xy direction) | 0.462 |
| Poisson's ratio (xy irány) | 0.255 |
| Poisson's ration (xz direction) | 0.422 |
| Shear modulus (xy) | 1364 N/mm$^2$ |
| Shear modulus (yz) | 110 N/mm$^2$ |
| Shear modulus (xz) | 1320 N/mm$^2$ |
| Yield stress (tension, x direction) | 50 N/mm$^2$ |
| Young-modulus after yield stress (tension, x direction) | 500 N/mm$^2$ |
| Yield stress (tension, y direction) | 5 N/mm$^2$ |
| Young-modulus after yield stress (tension, y direction) | 100 N/mm$^2$ |
| Yield stress (tension, z direction) | 5 N/mm$^2$ |
| Young-modulus after yield stress (tension, z direction) | 100 N/mm$^2$ |
| Yield stress (compression, x direction) | 30 N/mm$^2$ |
| Young-modulus after yield stress (compression, x direction) | 0 N/mm$^2$ |
| Yield stress (compression, y direction) | 50 N/mm$^2$ |
| Young-modulus after yield stress (compression, y direction) | 0 N/mm$^2$ |
| Yield stress (compression, z direction) | 50 N/mm$^2$ |
| Young-modulus after yield stress (compression, z direction) | 0 N/mm$^2$ |

obtained in the finite element model, so that the correctness of the model could be checked **Figure 5** illustrates the destructive and finite element (ANSYS) force-displacement diagrams of undamaged specimens. The dashed line indicates the force-displacement function of the theoretical model. The vertical displacements measured in the theoretical model at the moment of failure are illustrated in **Figure 6**. **Figure 7** shows the evolution of the normal stresses and **Figure 8** the evolution of the shear stresses.

In the finite element model, the Young's modulus of the resin in all directions is 650 N/mm$^2$ and the Poisson's ratio is 0.3.

In the destructive test, the average of F breaking forces was 5569 N and the average of vertical displacements at mid-span was 28.26 mm. In the theoretical model, the breaking force was 5106 N and the vertical displacement at mid-span was 23.86 mm.

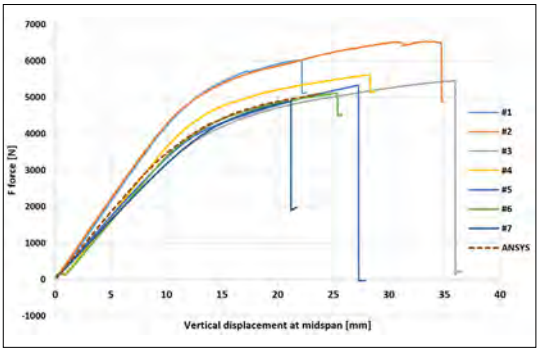


**Fig. 5.** *Force-displacement diagram of undamaged test specimens.*

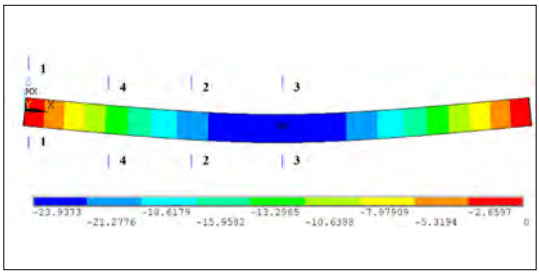

**Fig. 6.** *Displacement diagram of undamaged specimens in ANSYS finite element software.*

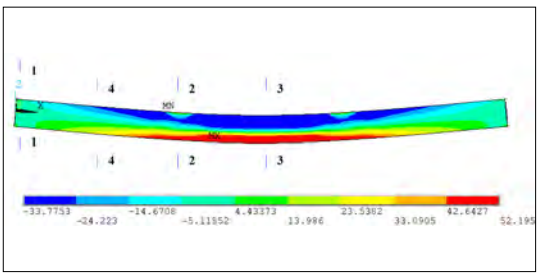

**Fig. 7.** *Normal stress diagram of undamaged specimens in ANSYS finite element software.*

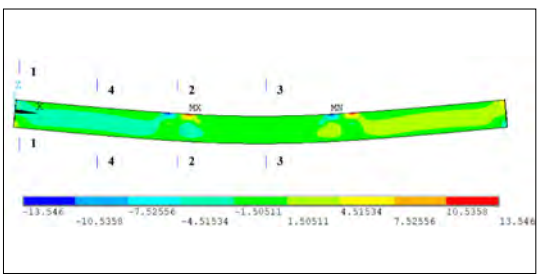

**Fig. 8.** *Shear stress diagram of undamaged specimens in ANSYS finite element software*

### 4.2. Test specimens cracked on one side

After destructive testing, a finite element method was also used to investigate an element with a simulated crack on one side of the element at the neutral axis. **Figure 9** shows the specimen meshed with the finite element software. **Figure 10.** shows the force-displacement diagram of the finite element model and the force-displacement diagrams of the destructive test. **Figure 11** shows the vertical displacements of the cracked element in mm. **Figure 12** shows the distribution of normal stresses of the cracked element in N/mm$^2$. **Figure 13** shows the shear stresses of the cracked element in N/mm$^2$.

The force-displacement diagram of the element modelled with the finite element software matches well with the diagrams of the fractured specimens.

The average value of the breaking forces obtained in the destructive tests was 5363 N and the average value of the displacements measured at midspan was 29.33 mm. The breaking force obtained by the finite element method was 5018 N, with a displacement of 23.43 mm.

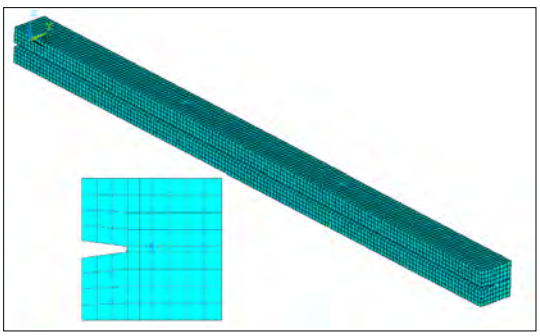

**Fig. 9.** *Finite element model of a specimen cracked on one side.*

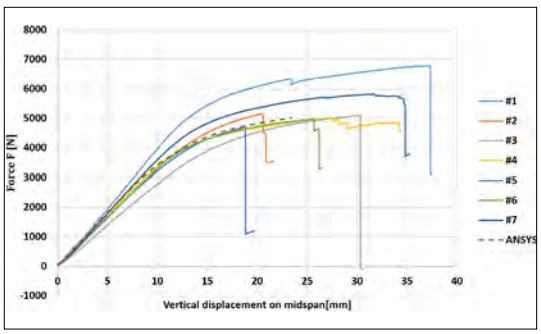


**Fig. 10.** *Force-displacement diagrams of test specimens cracked on one side.*

### 4.3. The resin-restored test specimens

Based on the geometry of the cracked specimens, the resin-restored elements were prepared. **Figure 14** summarizes the force-displacement diagrams of the destructive tests and the theoretical model. The force-displacement function of the finite element model is indicated by the dashed line.

For the repaired specimens, the mean value of the breaking forces obtained during the destructive tests was 5631 N and the mean value of the vertical displacements at midspan was 26.76 mm.

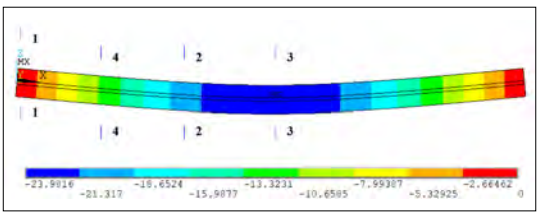

**Fig. 11.** *Vertical displacements of the cracked element.*

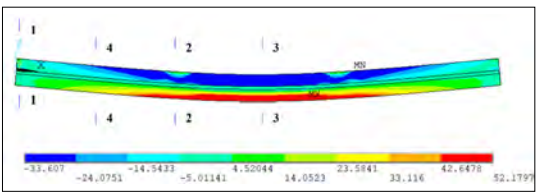

**Fig. 12.** *Distribution of the normal stresses of the cracked element.*

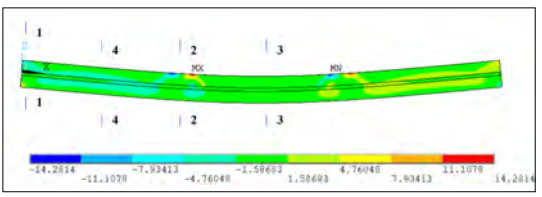

**Fig. 13.** *Distribution of the shear stresses of the cracked element*

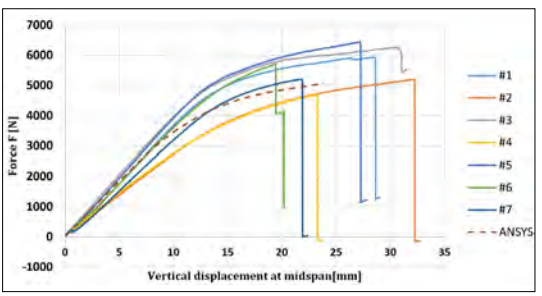


**Fig. 14.** *The force-displacement diagram of the resin-restored test specimens.*

In the theoretical model, the mean value of the breaking forces was 5065.64 N and the mean value of the vertical displacements at midspan was 23.86 mm. Figure 15 shows the vertical displacements in mm of the resin-restored specimen.

Figure 16 illustrates the distribuiton of the normal stresses in N/mm$^2$ of the element restored with epoxy resin. Figure 17 shows the distribution of the shear stresses in N/mm$^2$ of the resin-restored element.

### 4.4. Comparison of cracked and resin-repaired cases

The effect of the resin was analysed by comparing the normal and shear stress diagrams of the sections in the finite element models. Cross sections were taken at midspan (3-3) and 120 mm from the support (4-4). In the section 3-3 there is a maximum normal stress point and in the section 4-4 a maximum shear stress point (Figures 18–27). The cross-sections where stress maxima are found and local effects are not present were investigated. For the sections at the supports and at the force inputs, the stress distribution is not investigated at this time to avoid local effects.

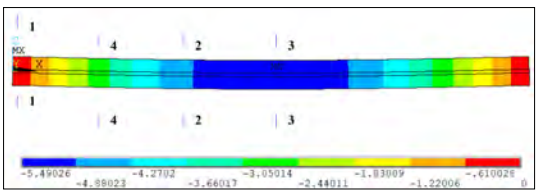

Fig. 15. *Vertical displacements of the resin-restored element.*

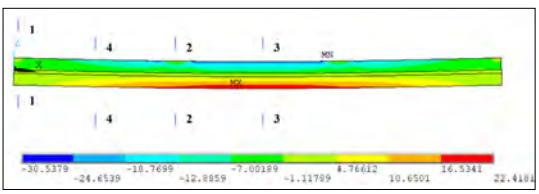

Fig. 16. *Distribution of the normal stresses of the resin-restored element.*

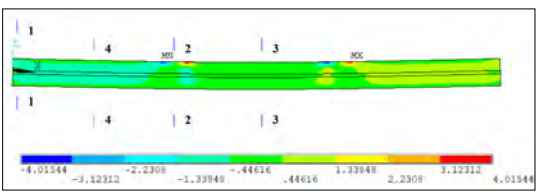

Fig. 17. *Distribution of shear stresses in the resin-restored element.*

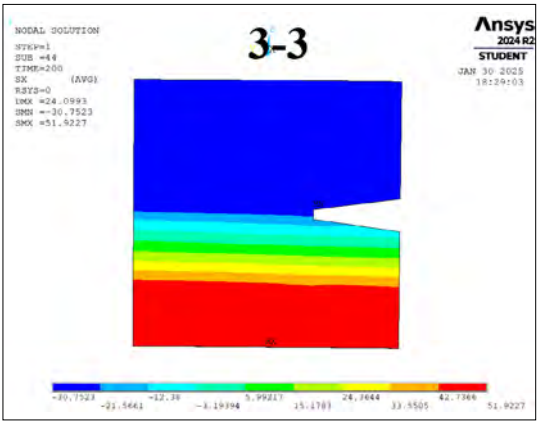


Fig. 18. *Distribution of normal stresses in section 3-3 for the cracked element.*

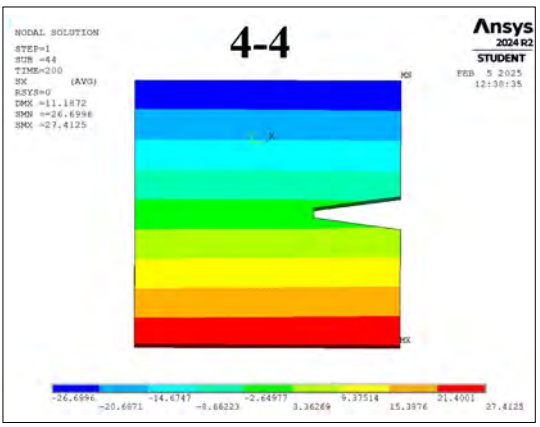


Fig. 19. *Distribution of normal stresses in section 4-4 for the cracked element.*

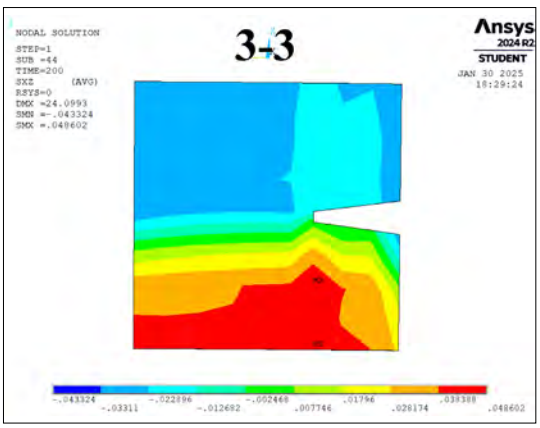


Fig. 20. *Distribution of shear stresses in section 3-3 for the cracked element.*

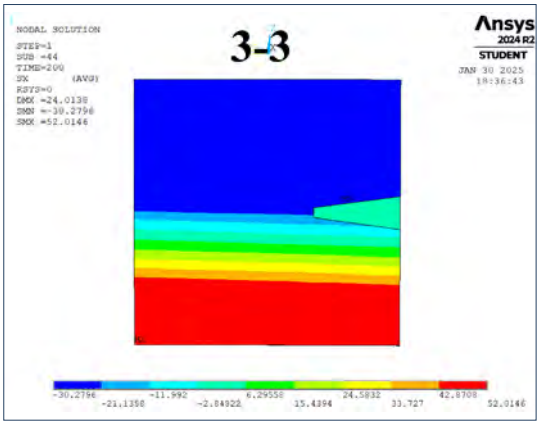


Fig. 21. *Distribution of shear stresses in section 3-3 for the resin-restored element.*

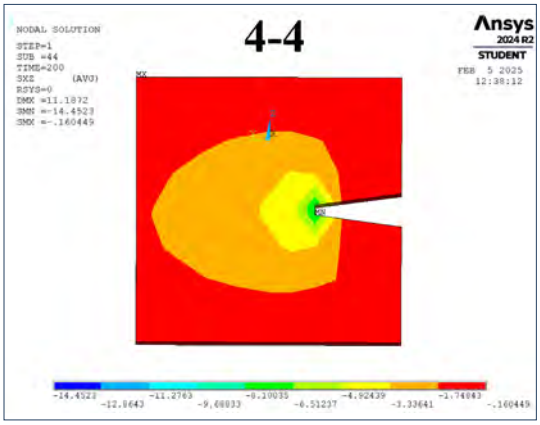


Fig. 24. *Distribution of shear stresses in section 4-4 for the cracked element.*

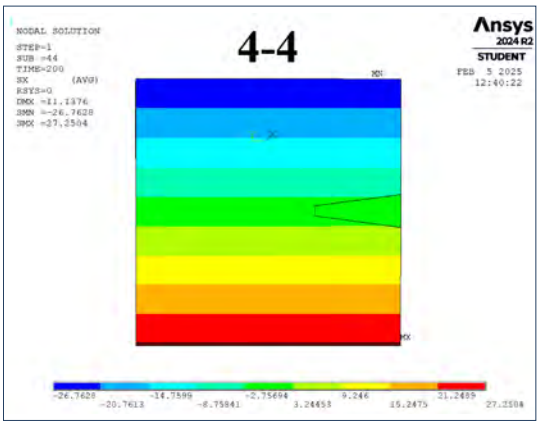


Fig. 22. *Distribution of normal stresses in section 4-4 for the resin-restored element.*

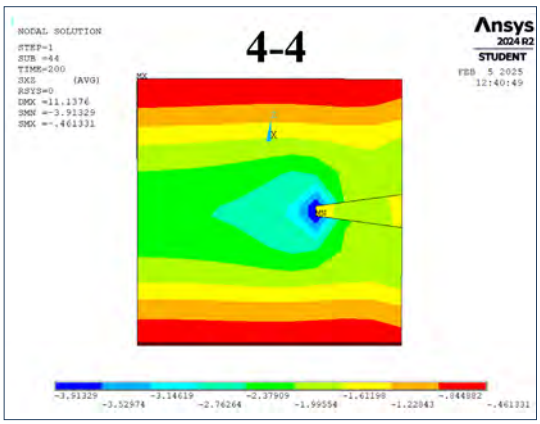


Fig. 25. *Distribution of shear stresses in section 4-4 for the resin-restored element.*

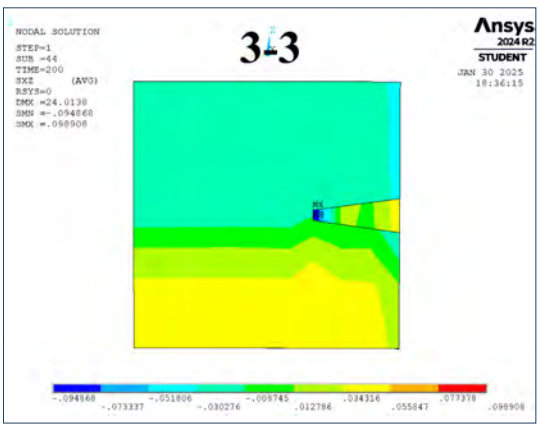


Fig. 23. *Distribution of shear stresses in section 3-3 for the resin-restored element.*

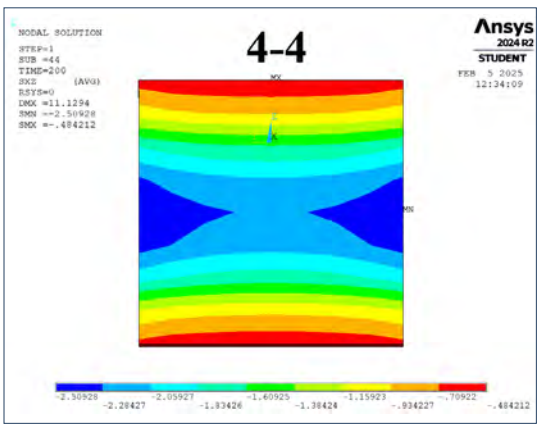


Fig. 26. *Distribution of shear stresses in section 4-4 for the intact element.*

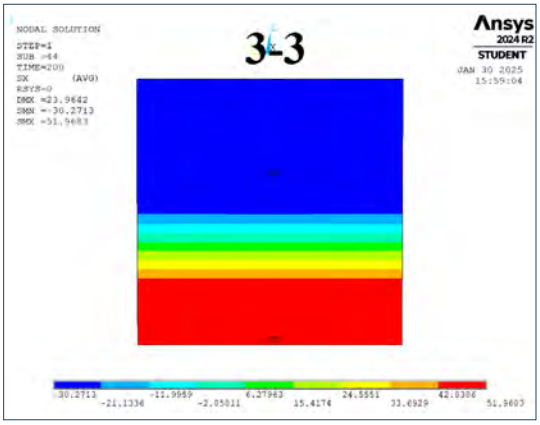


**Fig. 27.** *Distribution of normal stresses in section 3-3 for the intact element.*

## 5. Conclusions

The effect of cracking is not significant for the distribution of normal stresses in either case. This phenomenon can be explained by the position of the crack in the cross section of the element (at the neutral axis). For this reason, the fracture forces do not differ greatly. Fracture occurs due to the exceeding of the limit stress of the normal stresses at this crack depth and position.

Cracking plays a key role in the development of shear stresses. The crack is located at the maximum of the expected shear stress. **Figure 18** illustrates the distribution of shear stresses of intact specimens, where the shear stress XZ peaks at the centre of the cross-section, as expected.

**Figure 16** aillustrates the shear stress diagram of the cracked specimen in cross section 4-4. In the vicinity of the crack, a stress peak is observed with a peak stress value of 8 N/mm$^2$, which is more than three times higher than the corresponding point on the intact specimen.

In **Figure 17** for the resin-restored specimen, the application of resin has a positive effect on the shear stress evolution. The stress peak is found at the peak of the restored crack, but its value is more than 2 times smaller than for the cracked element. By using the epoxy resin, we realized to reduce the stress peaks and to obtain values close to the intact cross-section in terms of shear stress evolution.

In the next steps of the research, we aim to investigate the effect of cracks on both sides of the cross-section and their repair with resin. Subsequently, we also want to investigate cases where the position of the weakening may influence the evolution of the normal stress.

**Acknowledgement**

We are grateful to Dr. Miklós Armuth, Professor (Budapest University of Technology and Economics), Ottó Sebestyén, Technician (Budapest University of Technology and Economics), Dániel Karádi, PhD student in architecture (Budapest University of Technology and Economics) and Miklós Baróthy, Chemical Engineer (Polinvent KFT) who helped and supported us in the appropriate phases of our study.

## References

[1] Márton P.: *A 3PHV60 típusú műgyanta anyagjellemzőinek összehasonlítása a C24 szilárdsági osztályú puhafák anyagjellemzőivel/Determination and Comparison of the Mechanical Properties of Epoxy Resin Type 3PHV60 with C24 Structural Graded Softwood*. Hungarian Technical Scientific Society of Transilvania, Technical Review, 84. (2023) 23–37. https://ojs.emt.ro/muszakiszemle/article/view/1495

[2] Márton P.: *A 3PHV60-típusú műgyanta alkalmazása a faszerkezetek javítására/Application of 3PHV60 Type Epoxy Resin for the Repair of Timber Structures*, Acta Materialia Transylvanica 7/1. (2024) 29–38. https://doi.org/10.33923/amt-2024-01-06

[3] MSZ EN 408:2010+A1:2012 Faszerkezetek. Szerkezeti fa és rétegelt-ragasztott fa. Egyes fizikai és mechanikai tulajdonságok meghatározása

[4] Márton P.: *The Use of Epoxy Resin in the Repair of Cracked Wooden Structural Elements* – The 18th International Conference Interdisciplinarity in Engineering – INTER-ENG, Springer Nature, 2024.

Műszaki Tudományos Közlemények vol. 22. (2025) 72–78.
DOI: Hungarian: https://doi.org/10.33895/mtk-2025.22.12
English: https://doi.org/10.33894/mtk-2025.22.12

# HAZARDS OF LASER BEAM

Balázs Ákos NAGY,[1] Tünde Anna KOVÁCS[2]

[1] *Óbuda University, Bánki Donát Faculty of Mechanical and Safety Engineering, Budapest, Hungary, nagy.balazs@bgk.uni-obuda.hu*

[2] *Óbuda University, Bánki Donát Faculty of Mechanical and Safety Engineering, Budapest, Hungary, kovacs.tunde@bgk.uni-obuda.hu*

**Abstract**

Lasers are now indispensable tools in industry, medicine, communications, and scientific research. Their precision and efficiency have led to widespread adoption. However, their use demands significant caution, as laser radiation poses a serious hazard to the human body, especially the eyes and skin. Due to this reason, most laser sources are isolated from the environment (protective enclosure), however, there are applications where the operator is in the same airspace as the equipment emitting hazardous radiation. In an industrial environment, cutting, welding, and cleaning tasks can be performed with manual laser equipment. In this case, not only does the laser radiation pose a potential risk, but also the smoke gases and aerosols generated during the interaction between the laser light and the material, which can lead to respiratory diseases. To ensure safe operation, the proper use of protective equipment – such as laser safety goggles and specialized clothing – is crucial, along with meticulous workspace design and adherence to international standards. Ensuring radiation safety is not only essential for protecting individual health, but also a fundamental requirement for the sustainable and safe application of laser technology.

**Keywords***: laser beam, scattered radiation, wavelength, handheld laser source, photon-matter interaction.*

## 1. Introduction

Since the first laser-emitting device was developed by Theodore Maiman at the Hughes Research Laboratory, California, in 1960, laser technologies have become indispensable in everyday life [1]. This is due to the unique properties of laser light: compared to conventional light sources, laser beams exhibit low divergence (minimal beam spread), monochromaticity (single-wavelength emission), and coherence, meaning they maintain a constant frequency and phase in their electromagnetic radiation (**Figure 1.**) [2, 3, 4]. The first two properties explain the widespread application of lasers in metrology, medicine, and the entertainment industry. However, in the field of industrial material processing, the energy distribution on the irradiated surface and the ability to achieve high power density are of paramount importance [1]. Due to these characteristics, such lasers are often referred to as high-power lasers, as they are capable of delivering power outputs in the kilowatt range [2, 3].

High-power output can be achieved using gas lasers, particularly $CO_2$ lasers with a gas mixture of C, $N_2$ and $He/H_2O$ vapour in a 1:1:8 ratio, as well as solid-state lasers [2]. Initially, high-power laser systems were primarily developed using $CO_2$ la-

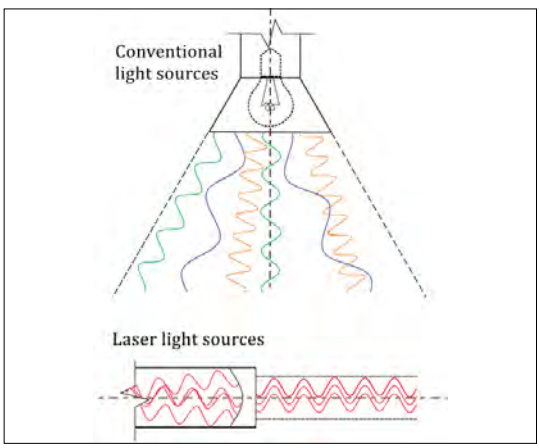


**Fig. 1.** *Schematic diagram of the differences between conventional and laser light sources.*

sers, but due to their complex design, operational difficulties, and high maintenance costs, their use has been declining, though they remain relevant in certain applications [1]. In this type of setup, the laser-active medium (which undergoes excitation) is the $CO_2$ molecule, while the additional gases or vapours are present to sustain a multi-level energy system (Figure 2). Maintaining this system is essential to achieving continuous wave (CW) laser operation, which is indispensable for cutting, surface treatment, and specific welding applications. The emitted radiation has a wavelength of 10,600 nm, which results from the vibrational energy transitions of the $CO_2$ molecule [2, 3].

Over the past 30 years, the development of laser technology has shifted towards solid-state lasers, particularly fiber-based excitation systems [5, 6]. One of the key reasons for this transition is that even the most robust rod lasers (an older approach) cannot compete with the size and efficiency of $CO_2$ laser excitation systems. Additionally, solid-state lasers offer better operational efficiency and lower running costs [7], ], although their maintenance may require specialised components and tools [1]. Furthermore, the beam properties of solid-state lasers significantly expand their range of applications [2, 3].

In these laser systems, the laser medium is an optically transmissive material (crystal) that is doped with laser-active elements. The most common medium is yttrium aluminium garnet (YAG, $Y_3Al_5O_{12}$) doped with neodymium ions ($Nd^{3+}$) though other dopant such as ytterbium, erbium, or holmium are also used [1, 2]. The wavelength of the emitted laser beam depends on the dopant,

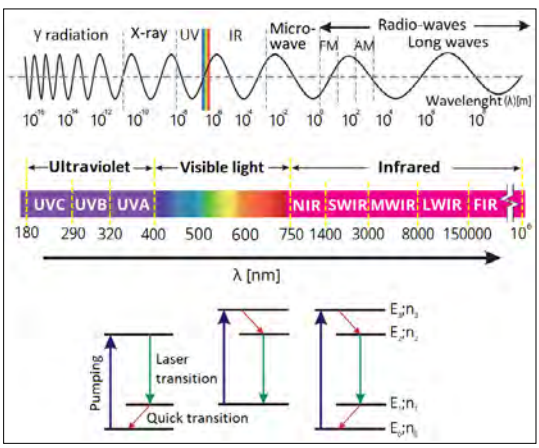


**Fig. 2.** *Wavelengths of radiation and schematic representation of systems with 3 or 4 energy levels*

with neodymium-doped YAG lasers typically operating at 1064 nm (Figure 2). Lasers emitting in this near-infrared (NIR) region enable the processing of materials such as aluminium (Al), copper (Cu), and titanium (Ti), which would be challenging with $CO_2$ lasers [1, 2, 8].

As previously established, fiber laser technology has seen the most significant growth [8, 9], primarily due to its compact excitation system and ease of beam delivery [1, 2]. Maximising these advantages has led to the development of hand-held laser sources [5, 6, 8]. These devices are designed for multiple functions (3-in-1: cutting, welding, and surface cleaning), and upon purchase, they come with interchangeable laser heads tailored to each application. In many cases, a separate wire feeder unit is also included, ensuring a constant welding speed during filler-wire welding, as the process depends on the wire feed rate. Another factor driving the adoption of hand-held laser sources is their easy integration with collaborative robotic arms, which helps maintain a consistent welding speed in autogenous (filler-free) welding processes while improving reproducibility (Figure 3). Additionally, CNC programming enables the definition of a virtual workspace, ensuring that the system prevents laser emission outside the designated area [6].

Nowadays, fourth-generation hand-held laser systems are in production, with manufacturing primarily concentrated in the Middle East. These systems are more cost-effective than CNC-controlled industrial laser systems with fixed workspaces, with an approximate price of €10,000. However, this cost reduction often comes at the expense of compliance with stringent safety standards, as many of these devices only partially adhere to mandatory safety regulations such as EN ISO 11553-2 and CE certification. Consequently, their operation necessitates careful consideration of environmental controls and the implementation of appropriate personal protective measures [5, 6].

**Fig. 3.** *Hand-held laser sources (left) and their integrated system with a cobot (right)* [6]

## 2. Laser Classification

Laser-emitting devices are classified according to their hazard level based on the EN 60825-1 standard, with the 2014 edition currently in effect. The classification is determined by several parameters, including laser power output (*W*, mW), wavelength (nm, µm), exposure duration (s), and emission mode (continuous wave or pulsed operation) [8, 10]. There are four primary laser classes, and within certain classes, additional subcategories denoted by specific letters have been established. The "M" designation originates from the English word "magnification" and, in the context of the standard, indicates that a device originally classified as "harmless" may become hazardous if an optical instrument is placed in front of the source (Class 1M, Class 2M). The "R" designation stands for "reduced", meaning these lasers pose a lower risk compared to standard Class 3 lasers; however, they are still hazardous upon direct exposure (Class 3R). The "B" designation remains from an earlier version of the standard (Class 3B) and has no specific meaning in the current classification (in the 1994 version, Class 3A corresponded to the current Class 3R, while Class 3B remained unchanged) [11, 12, 13].

Class 1 lasers are enclosed systems and pose no risk to human health (e.g., CD players). Class 1M lasers operate at wavelengths between 302.5 and 400 nm, and while they are safe for the naked eye, they can be hazardous when viewed through optical instruments (e.g., laser pointers). Class 2 lasers (400–700 nm, max. 1 mW) rely on the blink reflex to prevent eye damage during brief exposure (e.g., laser pointers). Class 2M lasers share the same characteristics but can be harmful if viewed through optical devices (e.g., marking lasers). Class 3R lasers have an output power between 1–5 mW (400–700 nm). They are not hazardous for short exposure, but prolonged exposure can damage the eye. Warning signs (Figure 4) and protective eyewear are recommended (e.g., laser cutters). Class 3B lasers (5–500 mW) pose a risk of eye damage even from scattered radiation, making protective eyewear mandatory (e.g., industrial and medical lasers). Class 4 lasers present a severe risk of eye and skin injuries, as well as a fire hazard. Protective equipment and strict safety measures are required (e.g., industrial material processing lasers) [10, 11, 13].

Laser machine manufacturers ensure that their products comply with the strictest safety regulations. Therefore, they strive to classify their commercially available equipment within Class 1, ensuring that under normal operating conditions, these devices pose no risk to users [1, 10, 12]. It is important to note that if the safety enclosure of a device initially classified in a higher hazard category is removed (e.g., during maintenance), its actual laser classification increases, thereby posing a significant safety risk to personnel in the vicinity [5, 10].


**Fig. 4.** *Indications of warnings and obligations (according to ISO 7010).*

## 3. Biological Damages and Protection

This article aims to familiarise readers with the effects of scattered laser radiation on biological tissues. The most vulnerable organs are the eye and the skin. In all cases, accredited protective equipment must be provided in compliance with relevant laws and regulations [14].

The eye is the most sensitive organ in the human body concerning radiation exposure, making it imperative to ensure adequate protective measures during laser operations [4, 5, 10]. Figure 5 illustrates the eye's response to different types of radiation exposure.

It can be observed that the infrared radiation (10,600 nm) emitted by $CO_2$ lasers is absorbed by the cornea, potentially altering its structure and the composition of the eyewater. However, under short-term exposure, these effects remain reversible [1, 12]. In the near-infrared (NIR) range, the situation is less favourable: characteristic wavelengths in this spectrum can penetrate through the lens structure, focusing the radiation onto the retina, which can result in localised coagulation [3, 4, 11]. To mitigate these hazards, specialised protective eyewear has been developed, featuring

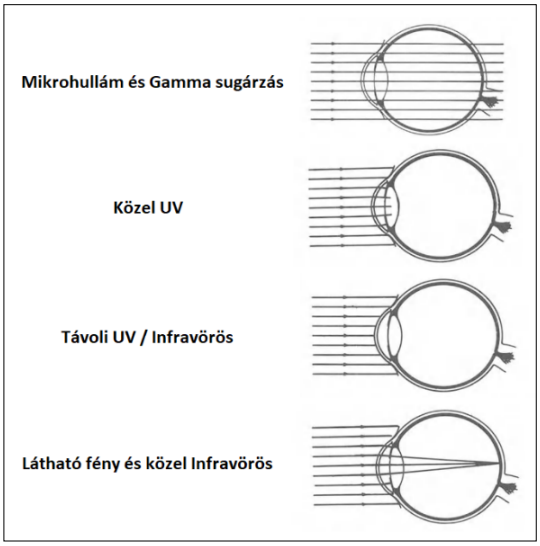


**Fig. 5.** *Schematic diagram of the reaction of the human eye to different radiations.*

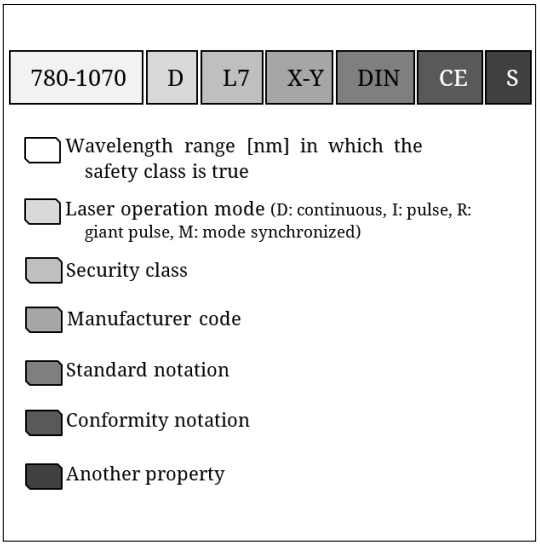


**Fig. 6.** *Illustrates the significant differences in the effects of various laser types.*

lenses with different refractive indices depending on the specific wavelength to be filtered. The most well-known standard for such protective products is EN 207:2020, which imposes stringent requirements, whereas its American counterpart (ANSI Z136.1) focuses solely on defining optical density values [4, 5, 6].

Optical Density (OD) indicates the effectiveness of protection against laser radiation, which is determined through various tests before protective eyewear is released to the market. The *OD* value represents the logarithmic measure of radiation attenuation, expressed as:

$$OD = \log_{10}\left(\frac{M_i}{M_t}\right), \quad (1)$$

where $M_i$ is the power of the incident beam (W), and $M_t$ is the power of the transmitted beam (W) [1, 4, 12]. The higher the *OD* value, the more effective the protection; however, increased OD also correlates with higher costs, making it essential to determine the minimum required protection level [12]. The relationship between OD and the Maximum Permissible Exposure (MPE; J/m$^2$) is given by the following equation:

$$OD = \log_{10}\left(\frac{E}{MPE}\right), \quad (2)$$

where $E$ is the degree of exposure (J/m$^2$). To select the appropriate protective eyewear, it is essential to consider the operating parameters of the laser system, including wavelength, power ($P$; W), beam diameter ($A$; mm$^2$) and operating mode [4, 12]. The EN 207:2020 standard provides a classification table that helps determine the minimum safety rating required for protective eyewear to ensure safe usage. The technical documentation of laser safety glasses includes transmittance and optical density (*OD*) values for specific wavelengths, which should be carefully reviewed when selecting the appropriate protective equipment [5, 6, 12]. To maximise protection, shield-type eyewear should be chosen to protect the facial skin and prevent laser radiation from reaching the eyes from any angle [5, 8, 9]. The marking system for protective eyewear is illustrated in Figure 6 [15].

Laser safety glasses can have lenses made of glass or polycarbonate. Glass lenses offer excellent light transmission properties, providing higher visible light transmission (VLT); however, they tend to be more expensive, heavier, and more fragile. In contrast, polycarbonate lenses are more cost-effective, lighter, and impact-resistant, but they allow less visible light to pass through [4]. For ergonomic considerations, the VLT value is recommended to exceed 35% [4, 5, 8].

Laser safety lenses are coated with thin layers to enhance their filtering performance. One of the most commonly used coating techniques is electron beam evaporation, where the coating material ($SiO_2$, $HfO_2$) is vaporised in a vacuum to form thin films on optical surfaces. This method is often complemented by ion-assisted deposition (IAD), which utilises an ion beam to densify the

coating, reducing its porosity and enhancing laser resistance. Ion beam sputtering (IBS) offers additional advantages by producing extremely dense and low-scatter coatings ($Al_2O_3$, $Ta_2O_5$), improving laser safety glasses' durability and optical performance. Proper material selection is crucial, as optical coatings must shield against laser radiation and maintain optimal light transmission and visual comfort. Multilayer dielectric (MLD) coatings, which combine $SiO_2$ and $HfO_2$ enable protective lenses for solid-state lasers to achieve high optical density with minimal light loss. The thickness of each layer and the refractive index of the materials require precise engineering to ensure that the final coating effectively reduces hazardous reflections and maximises protection [4, 12].

The human skin provides natural protection against environmental influences, but it is less effective against artificial radiation. Laser radiation at different wavelengths penetrates the skin to varying depths, leading to distinct damage mechanisms [4, 10, 11]. Figure 7 illustrates the significant differences in the effects of various laser types.

The $CO_2$ laser (10.6 μm wavelength) radiation penetrates only the uppermost layer of the skin, where it induces damage through thermal conduction. This can lead to tissue overheating and coagulation [12]. In contrast, solid-state lasers, which operate at an order of magnitude shorter wavelength, penetrate deeper into the skin, causing damage through the evaporation of water within the tissues and the over-excitation of haemoglobin ($Fe^{2+}$ and $Fe^{3+}$ ions) in the blood, leading to "blood cell explosion" [4, 9, 11]. This phenomenon can contribute to the formation of blood clots, which, in critical areas such as the capillaries of the eye, may cause blockages [4, 12]. To prevent skin injuries, the entire body must be covered with suitable protective clothing. The material must be capable of absorbing laser radiation without degrading [5, 9, 10]. For $CO_2$ lasers, conventional cowhide welding apparel provides adequate protection. However, for solid-state lasers, specialised composite fabric is required, typically incorporating stainless steel fibers (to reflect radiation) woven with absorptive textiles [12, 16]. The entire human body must be shielded, which is why jackets, pants, and gloves are also manufactured from such materials [8]. In all cases, it is essential to verify that the protective equipment provides adequate shielding for the specific laser type and power level [4, 10].

## 4. Environmental solutions

The principle of ensuring that all laser sources are classified within Class 1 reinforces the prevention of the aforementioned injuries [1, 10, 12]. ]. In industrial applications, high-power lasers are typically controlled by CNC systems, which confine the laser beam within a designated workspace, allowing the system to be easily enclosed and shielded from external exposure [2, 12].

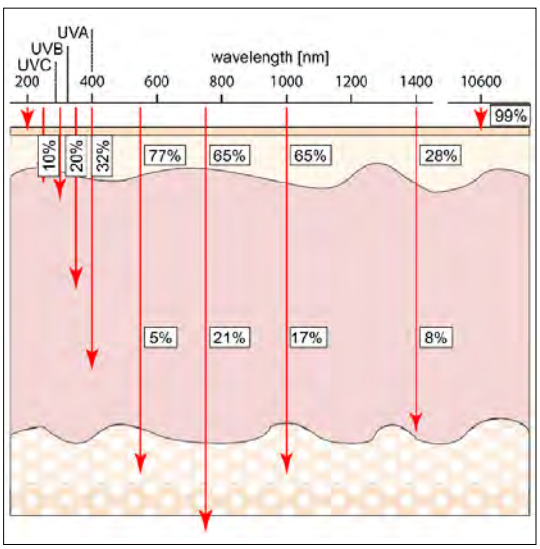


**Fig. 7.** *Depth of penetration of different radiations into human skin* [15]

**Fig. 8.** *Recommended personal protective equipment (internet)*

When hand-held laser sources are used, it is assumed that they are manually operated, thereby exposing the operator to significant scattered radiation [5, 6, 9]. In traditional welding techniques, workspaces are also segregated to prevent injuries caused by UV radiation to individuals outside the working area [3]. Such welding stations are typically enclosed using curtains and screens [3, 10]. However, in my opinion, this level of shielding is insufficient against NIR radiation, as these barriers do not provide hermetic isolation. Nevertheless, specialized welding screens and curtains have been developed specifically to block radiation within this wavelength range. Notably, laser-active systems are available, which are integrated with the laser source and automatically terminate photon emission upon direct radiation exposure [5, 8, 17].

If the laser system is fully enclosed, individuals outside the workspace are protected; however, within the enclosure, various materials with different orientations, absorption coefficients, and surface roughness can increase the level of scattered radiation due to diffuse reflection [4, 5, 9]. To mitigate this effect, VANTA BLACK-type coatings are commonly applied, but other solutions, such as aluminium coatings or sandwich panel structures, have also proven effective [3, 4, 12]. These latter approaches are widely used in the construction of laser welding containers. A fully enclosed welding station must feature at least one observation window, allowing individuals outside the workspace to continuously monitor the operator's health status and detect potential accidents in a timely manner [4, 18]. When selecting such windows, the same criteria applied to laser safety eye-wear must be considered [12].

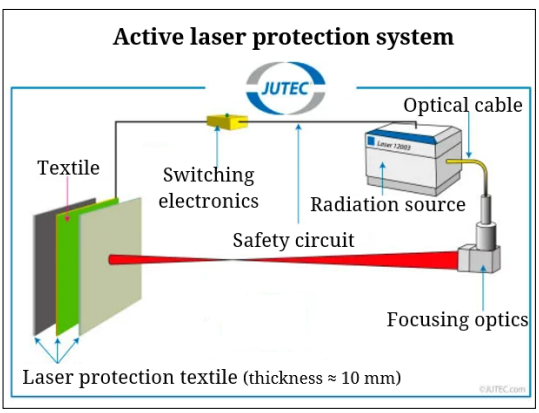


**Fig. 9.** *Schematic diagram of a laser-active system* [17]

Access control is of critical importance in laser work areas, necessitating the installation of clear warning signs (hazard warnings and safety obligations, **Figure 4**) and entry control systems. Measures such as interlocks or locked doors are recommended to prevent unauthorised access [4, 8, 18]. Other essential environmental factors include proper lighting and ventilation. During laser-based metal processing, excessive excitation of the material can generate metal vapours and other fumes, which pose serious respiratory hazards [1, 4, 10]. To mitigate these risks, complete workspace ventilation or localised exhaust systems are recommended [16, 18]. The workspace must be designed in compliance with safety protocols, and beam paths should be arranged to prevent accidental exposure. Furthermore, the operation of high-power laser systems requires the designation of a laser safety officer [4, 10, 18].

## 5. Conclusions

More users have turned to hand-held laser sources in recent years due to their versatile applications and low investment and operating costs. Their compact size and flexible beam delivery make them easy to handle, and they can also be integrated with collaborative robotic arms, enhancing productivity and process automation [2, 5, 6]. Despite their affordability and versatility, hand-held lasers present significant safety challenges, as operators are directly exposed to scattered laser radiation [4, 10, 11]. To ensure adequate protection, the workspace must be enclosed with appropriate materials, and LEAN principles should be considered during its design [1, 12, 16]. The safe use of hand-held lasers requires not only appropriate personal protective equipment—such as specialised eye-wear and protective clothing—but also a well-structured work environment. This includes access control, hazard labelling, warning systems, and adequate ventilation to remove generated fumes and vapours [4, 10, 18].

## References

[1] Elijah Kannatey-Asibu Jr.: *Principles of Laser Materials Processing. Developments and Applications*. 2nd edition, Wiley, Hoboken, NJ, 2023.
[2] Buza Gábor: *Lézesugaras technológiák I.* Edutus Főiskola. Budapest, 2012.
[3] Bitay Enikő: *Lézeres felületkezelés és modellezés*. Erdélyi Múzeum-Egyesület, Kolozsvár, 2007. https://doi.org/10.36242/mtf-04
[4] Ken Barat: *Laser Safety: Tools and Training*. Second Edition, Taylor & Francis LTD, Broken Sound

Parkway, 2017.
[5] Halász Gábor: *A kézi lézeres berendezések biztonságos használata*. Hegesztéstechnika, XXXV/1. (2024) 41–47.
[6] Gáti József, Kovács Tünde, Nagy Balázs: *Gépesített kézi lézeres hegesztés gyakorlati tapasztalatai*. Hegesztéstechnika, XXXIV/4. (2024) 43–47.
[7] https://www.techmonitor.hu/piacmonitor/az-optikai-szalas-lezer-es-a-co2-lezer-osszehasonlitasa-20230310 (accessed on: 2024.12.1.)
[8] Tóth László: *A kézi lézeres hegesztőgépek biztonságtechnikája.* Nagy energiasűrűségű ankét, Magyar Hegesztési Egyesület, Kecskemét, 2023. 10. 26., presentation. https://maheg.hu/wp-content/uploads/2023/11/Lezervedelem_PPT_MDTL-231026-Nagy_energiasurusegu_Anket.pdf
[9] Buza Gábor: *Lézersugaras technológiák tegnap, ma, holnap*. Nagy energiasűrűségű ankét, Magyar Hegesztési Egyesület, Kecskemét, 2023. 10. 26., presentation. https://maheg.hu/wp-content/uploads/2023/11/Buza_Nagy_energiasurusegu.pdf
[10] Bagyinszki Gyula: *Lézerek alkalmazásának technológiai és biztonságtechnikai szempontjai*. XI. Nemzetközi és IV. GTE-MHtE-DVS Hegesztési Konferencia, Budapest, 2004. 08. 23–26., 14–29.
[11] Andraws Andrew, Kovács-Coskun Tünde: *Lézervágás biztonságtechnikai kérdései*. Műszaki Tudományos Közlemények, 5. (2016) 65-68. https://doi.org/10.33895/mtk-2016.05.07
[12] Roy Henderson, Karl Schulmeister: *Laser Safety*. 1st edition, Taylor & Francis Group, Boca Raton, 2003.
[13] EN 60825-1: Safety of Laser Products - Part 1: Equipment Classification and Requirements, 2014.
[14] 2012. évi I. törvény a munka törvénykönyvéről: 51. § és 86. §
[15] EN 207:2017: Personal Eye-Protection Equipment - Filters and Eye-Protectors against Laser Radiation (Laser Eye-Protectors)
[16] Penny J. Smaller: Laser Safety: *Risks, Hazards, and Control Measures*. Laser Therapy, 20/2. (2011) 95–106.
[17] https://www.jutec.com (megtekintve: 2024.11.)
[18] California Institute of Technology: *Laser Safety Manual*, Caltech Environmental Health and Safety Office, California, 2023.

Műszaki Tudományos Közlemények vol. 22. (2025) 79–84.
DOI: Hungarian: https://doi.org/10.33895/mtk-2025.22.13
English: https://doi.org/10.33894/mtk-2025.22.13

# STEEL IN ARCHITECTURAL HERITAGE PROTECTION

Zsolt NAGY,[1] Andrea KELEMEN,[2] Annabella SÁNDULY[3]

[1] *Technical University of Cluj Napoca, CE Faculty, Cluj-Napoca, Romania zsolt.nagy@dst.utcluj.ro*

[2] *Technical University of Cluj Napoca, CE Faculty, Cluj-Napoca, Romania, andrea.kelemen@gordias.ro*

[3] *Lodi University of Technology, Łódź, Poland, annabella.sanduly@dokt.p.lodz.pl*

**Abstract**

The current article presents some steel structural solutions implemented in archaeological and architectural heritage protection applied in Romania using case studies. The paper summarizes also some of the engineering challenges of the project team during the design process.

**Keywords***: steel structure, design challenges, historical monument, ruin protection.*

## 1. Introduction

The preservation of built heritage today increasingly requires an interdisciplinary approach, in which close collaboration between the fields of architecture, archaeology, and engineering is essential. In this context, steel structures offer modern solutions for the protection of buildings and archaeological sites of historical value. The use of steel structures makes it possible to create temporary or permanent reinforcements, to relieve existing building fabric with minimal intervention, and to develop transparent yet durable coverings and structural elements.

Such interventions, however, pose significant engineering and heritage conservation challenges, as contemporary structural solutions must be harmonized with conservation principles and the historical context of the site.

This article presents four case studies in which steel structures were successfully applied during both the design and execution phases.

## 2. Case Studies on the Protection of Monuments and Archaeological Ruins

In the course of unique projects, practical solutions and decisions often emerge that are not found in standard manuals or theoretical curricula. Case studies allow for the structured and reflective dissemination of such experiences. In complex fields such as the protection of built heritage, case studies help to reveal how architecture, engineering, heritage conservation, and archaeology can effectively collaborate.

Moreover, new materials, structural systems, or design methods are often tested for the first time in the context of one-of-a-kind projects.

### 2.1. Castrum in Turda

The first case study presents the architectural intervention aimed at protecting the archaeological remains of the Fifth Macedonica Roman Legion fortress located in Turda, Romania (the ancient Potaissa). It highlights the applied steel structural solutions and the engineering challenges encountered during the design process. The project's objective was to create a large-span covering struc-

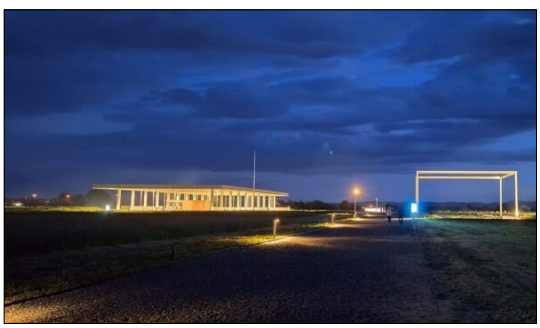

**Fig. 1.** *Castrum Turda in the Spotlight during the Night of Museums. (Source: TurdaNews)*

ture along with a partially suspended steel walkway system, which both protects the uncovered ruins from weathering effects and allows visitors to directly observe the site without causing damage.

The covering measures approximately 40.35 meters in width and 70.35 meters in length and includes a suspended pedestrian system extending roughly 230 meters in four directions — two longitudinal and two transverse — providing safe visitor circulation.

Special attention was given to preserving the historical context, applying minimally invasive solutions (such as steel micro-piles drilled among the ruins for the creation of smaller foundations), and simultaneously ensuring structural stability and visitor safety.

The study provides a detailed analysis of the technical solutions employed by the project team, as well as the complex challenges arising from the integration of heritage conservation principles with contemporary engineering design. For a comprehensive discussion and more detailed description of this work, please refer to our previous publication [1].

The presented project also serves as an excellent example highlighting the roles that a structural engineer assumes within a given construction project [2].

### 2.2. Bolyai street, no. 11

The second case study presents the rehabilitation process of a historic building located in the city center of Târgu Mureș, during which the original Baroque-style roof structure was reconstructed using a modern metal framework. The study primarily focuses on the design of the roof structure and the metal access staircase. The complex, irregularly shaped roof with multiple planes required careful dimensioning and detailing before being installed on the refurbished masonry walls.

The main access staircase, made of steel plates and featuring a special structural system, required advanced computational methods for analysis and verification.

Our article [3] discusses the engineering challenges encountered during the design and execution phases, as well as their solutions: a survey conducted using 3D scanning served as a reference system for the steel structure (Figure 2); discrepancies between the masonry walls and the steel structure had to be addressed; and the irregular geometry was configured taking into account site-specific constraints.

The methods applied during the design and construction phases of the project played a crucial role in addressing the complex geometric and structural challenges. Dimensioning and detailing such a complex structure would have been practically impossible without the use of advanced digital technologies. The precise survey of the existing condition was conducted using laser scanning technology, which provided high-resolution data on the current geometric configuration of the building, as well as deviations arising during construction that significantly influenced the structural design. The resulting three-dimensional point cloud served as the basis for digital modeling and detailed design.

During the project, a BIM (Building Information Modeling) software environment was employed, enabling effective collaboration among various disciplines—such as structural engineers, architects, and mechanical engineers—within a shared

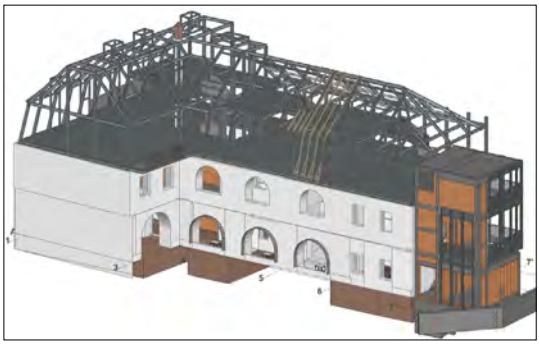

Fig. 2. *Bolyai street 11 building 3D model.*

**Fig. 3.** *Bolyai street 11 roof structure during construction.*

spatial model. This model contained all relevant structural, geometric, and material characteristics, and allowed for real-time coordination and the prevention of potential clashes.

A challenge was posed by the detailing of structural elements with random orientations in the absence of an accurate reference system. To solve this issue, the project team developed a custom coordinate system, to which the three-dimensional connection points of the steel structural elements were aligned. The position, orientation, and shape of the elements were verified in multiple stages using repeated laser scans, thereby ensuring the accuracy of the final model and avoiding manufacturing errors.

One of the key lessons of the methodology is that the objectives of different disciplines can sometimes reflect divergent or even conflicting considerations. The success of the project largely depended on open communication between the parties involved, multidisciplinary collaboration, and the development of compromise solutions.

### 2.3. Restoration of Sebesvár Castle

The third case study presents the design work related to the opening of the medieval Sebesvár castle ruins (known as Bologa in Romanian) to visitors, including the measures required to ensure safety. **Figure 4** shows the structural model prepared by Gordias Engineering Office and the current state of the bastion. During the works, the castle area was cleared of overgrown vegetation, the walls were repaired, landscaping works were carried out, the wall crown was insulated with turf bricks, access ramps were built, and the old tower was made accessible from the inside with the help of steel structural elements. The company responsible for the restoration works partially rebuilt the missing wall sections to such an extent that if we suddenly went back a few hundred years in time and an enemy army approached, the castle in its current state would be ready to withstand a siege **[4]**.

**Fig. 4.** *Designed and executed staircase.*

The role of steel structures in making the medieval Sebesvár castle ruins accessible to visitors is crucial from several perspectives, especially considering the complex challenges of the heritage environment. The following points summarize why steel can be considered the ideal choice in this project:

*Reversibility and Minimal Intervention*:
One of the fundamental principles of heritage conservation is that interventions should be reversible, meaning they should not cause irreversible changes to the original structure. Steel structures fit well with this principle, as they can be fixed point-wise with minimal intervention area and can be easily removed if necessary.

– *High Load-Bearing Capacity with Small Cross-Section*:
In the case of a ruined castle, load capacity is limited—the centuries-old walls cannot bear any arbitrary additional loads. Steel allows for strong yet lightweight and slender structures that do not overly burden the existing masonry.

– *Structural Stability on Difficult Terrain*:
Medieval castles were often built on steep, hard-to-reach locations. Steel structures can be effectively used to create temporary or permanent bridges, stairs, and walkways that minimally load the ground or ruins, while providing safe circulation for visitors.

– *Compatibility with Contemporary Interpretation*:
Modern interventions often aim to visually distinguish themselves from the original structure. The use of steel and its clean design language fit well with contemporary architectural vocabulary while not attempting to imitate the historical appearance—thus respecting the principle of authenticity.

– *Prefabrication and Rapid Assembly*:
Due to the difficult-to-access locations, it is important that structures can be prefabricated and quickly assembled on site. Steel structures perfectly meet this requirement: they can be manufactured in factories and rapidly erected with on-site work.

In summary, although on-site welding was necessary in this project, the fitting of the elements was successfully executed in an aesthetically pleasing manner, providing an enjoyable visual experience for visitors (**Figure 6**).

### 2.4. St. Michael's Church tower stairs

The fourth case study presents a summary of the design work for the steel stairs intended to make the tower of St. Michael's Church in Cluj-Napoca accessible to visitors. **Figure 7** shows a visualization created by the Gordias engineering office, an intermediate phase of the construction work, and the final state of the proposed staircase structure, also reflecting the difficulties encountered during execution due to the confined space and lack of access to the working areas.

During the renovation of the tower, more severe structural problems were revealed than in previous surveys. Due to the significant self-weight resulting from the 19th-century Neo-Gothic tower construction, a 20 cm settlement was observed in the medieval wall sections, which was measurable based on 3D scanning. These issues also influenced the design and construction of the new steel stair structure, as the components had to perfectly adapt to the condition of the existing walls, their irregular planes, and the level differences caused by the settlement. Due to the confined spaces, the stair structure had to be designed in elements that could be installed using only manual two-person handling. The renovation of the Saint Michael Church tower stairs and the opening of the tower to visitors contributed to strengthening the church's cultural and religious role, while ensuring the preservation of the monument and providing an enjoyable experience for visitors. The renovation of Saint Michael Church received the Europa Nostra Award (European Heritage Award) in 2024 in the category of preservation and adaptive reuse.

## 3. Contemporary Structural Interventions in Heritage Environments

The four case studies discussed — related to built heritage elements from different historical periods and with varying functions — showcase common principles, design strategies, and engineering responses. These cases aptly illustrate

**Fig. 5.** *Sebesvár castle before restauration.*

**Fig. 6.** *Sebesvár castle after restauration.*

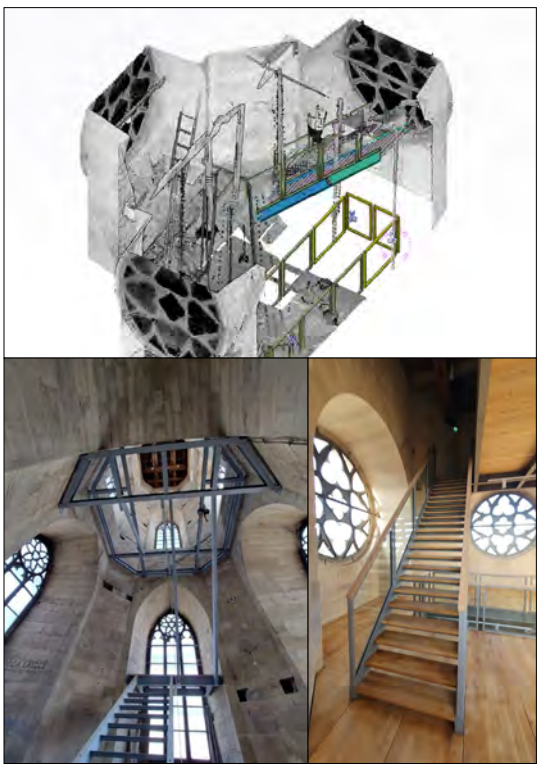

**Fig. 7.** *The structure of the designed and constructed stairs (intermediate and final phases).*

how contemporary structural thinking meets the ethos of heritage conservation in light of 21st-century expectations. The projects at Castrum Turda and the Sebesvár castle ruins primarily aimed at the physical protection of historic structures and making them accessible to tourists. In contrast, the reconstruction of the St. Michael's Church tower stairs and the rebuilding of the Baroque roof structure at Bolyai 11 focused on the functional renewal of existing monuments — reshaping the cultural experience and usability.

In all four projects, steel structures appear not merely as a construction technique choice but as a statement of intent: Through its slenderness and strength, steel allows for minimal intervention in the original structure. Its reversibility and distinctly contemporary appearance ensure a clear differentiation between old and new — avoiding architectural forgery. Thanks to its prefabrication and ease of assembly, steel adapts well to hard-to-reach or historically sensitive sites.

Digital surveying and design tools played a decisive role: Laser scanning and point cloud–based modelling enabled precise documentation of displaced, deformed, or irregular geometries. The use of BIM systems allowed coordination across disciplines and accurate detailed design of geometrically complex connections. In several cases (e.g., St. Michael's Church), hidden structural damages uncovered during construction required ongoing revision of the planned solutions. The detailing of connections between different materials (e.g., stone and steel) and the fine-tuning of structural load transfers demanded significant engineering innovation.

## 4. Conclusions

The conclusions based on the examined case studies can be summarized as follows:

### 4.1. Material Usage Considerations – Advantages of Steel Structures in Heritage Environments

One of the greatest challenges in making the medieval Sebesvár castle ruins accessible was how to provide safety and usability that meet modern standards in a way respectful to the historic structure. The use of steel structures proved justified and advantageous in several respects:

- *Reversibility*: Steel structures allow for removable, non-invasive solutions, thus preserving the integrity of the monument and permitting future modifications if needed.
- *Low weight – high load capacity*: Modern steel profiles enable lightweight yet statically stable constructions that do not overload the historic masonry.
- *Prefabrication and assembly*: Steel elements can be manufactured in controlled factory conditions and quickly assembled on-site with minimal work, especially beneficial in difficult-to-access ruin sites.
- *Contemporary appearance*: Steel is clearly distinguishable from the original stone and brick materials, avoiding architectural forgery and complying with the principle of anastylosis (distinguishable restoration).

### 4.2. Contemporary Structural Solutions in Heritage Conservation – The Role of Steel Structures in the Sebesvár Castle and Turda Castrum Projects

To ensure safe visitor circulation, steel structural interventions were necessary in several locations throughout the projects. These primarily served the following functions:

- Construction of access ramps and walkways to various parts of the castle, designed so as not to overload the existing ruins.
- Placement of viewpoints, railings, and complementary structures that enhance the visitor experience while fulfilling safety functions.
- Application of special fixing and connection techniques enabling the coordinated integration of elements made from different materials (e.g., stone and steel).
- Adaptation to terrain conditions: On sloped, rocky terrain, the flexibility of steel structures allowed for unique fittings and tailored solutions.

## References

[1] Nagy Zs., Kelemen A., Sánduly A., Moldovan P., Moldovan A.: *Acél a műemlékvédelemben: a Tordai Castrum*. XXVIII. Nemzetközi Építéstudományi Konferencia – ÉPKO, Csíksomlyó, Románia, 2024. 120–125. https://ojs.emt.ro/EPKO/article/view/1655

[2] Nagy Zs. (szerk.): *Rolul Inginerului Proiectant de Structuri*, Editura AICPS, 2022. ISBN 978-973-0-36192-6.

[3] Nagy Zs., Nagy Ö., Kelemen A., Kiss Z., Ambrus Á., Calian C.-F.: *Proiectarea unei șarpante de formă barocă folosind structură metalică*. In: "Construiește cu STEEL" Lucrările celei de-a XVIII-a Conferințe Naționale de Construcții Metalice, Kolozsvár, România, 2024. 208-228. https://con-steel-resources.s3.eu-central-1.amazonaws.com/CM18-2024.pdf

[4] Pengő Z.: *Túraajánló karcsú kalandvágyóknak: felújították a sebesvári várat*. Maszol.ro portál https://maszol.ro/belfold/Turaajanlo-karcsu-kalandvagyoknak-felujitottak-a-sebesvari-varat? (accessed on: 2024. 11.15.).

Műszaki Tudományos Közlemények vol. 22. (2025) 85–92.
DOI: Hungarian: https://doi.org/10.33895/mtk-2025.22.14
English: https://doi.org/10.33894/mtk-2025.22.14

# THE ROLE OF COMPUTATIONAL MECHANICS TODAY

István PÁCZELT

*University of Miskolc, Institute of Applied Mechanics, Miskolc, Hungary, istvan.paczelt@uni-miskolc.hu*

**Abstract**

With the proliferation of computers, mechanical problems arising in mechanical engineering practice can be effectively solved. Among the many numerical methods, the present article reports on the development of the finite element method, its development directions, its application possibilities, the importance of error estimation, the requirements supported by the programs and the author'sexperiences, presenting some numerical examples.

**Keywords***: finite element method, approximation, accuracy, variational methods.*

## 1. Introduction

The science of mechanics has a history spanning several centuries and continues to be important today. Moreover, with the expansion of computational capabilities, it is possible to better describe and model real-world conditions.

The way in which the mechanical model defined by the engineer is solved significantly influences the success and the validity of the result obtained. This article draws attention to the 70-year history of the finite element method, one of the most significant approximate calculation methods, the possibilities of approximation methods, the importance of error estimation, and illustrates the versatility of this calculation method through the presentation of author's own experiences and the analysis of practical problems.

### 1.1. The beginning of mechanics

The movement of the planets has for a long time fascinated mankind, what orbits they move in, why we see them in different positions depending on the season, etc.

Significant breakthroughs were achieved by the findings of Nicolaus Copernicus (1473-1543) (the Earth is not the center of the world), Johannes Kepler (1571-1630) with the laws of planetary motion, and Galileo Galilei's (1561-1642) experiments with free fall and movement on a slope, Isaac Newton's (1643-1727) understanding of gravity, the creation of the laws of motion, and Gottfried Wilhelm Leibnitz's (1646-1716) creation of differential calculus, which provided the mathematical basis for the scientific description of motion.

After these, many of the "giants" of the Early New Age, such as Daniel Bernoulli (1700-1782), Leonhard Euler (1707-1783), Jean Le Round d'Alembert (1717-1783), Joseph-Louis Lagrange (1736-1813), Johann Carl Friedrich Gauss (1777-1855), Simeon-Denis Poisson (1781-1841), Claude Louis Marie Henri Navier (1785-1836), Augustin Louis Cauchy (1789-1857), Sir George Biddell Airy (1801-1892), William Rowan Hamilton (1805-1865), Gustav Robert Kirchhoff (1824-1887), and Lord John William Strutt Rayleigh (1842-1919), contributed significantly to the development of what is called classical mechanics.

### 1.2. Mechanics from the 1900s

With the development of industry and the design of modern devices, the ability to perform reliable strength and dynamic calculations became an important requirement. The exact solutions developed for simpler shapes had to be replaced by some approximate method. First, Walter Ritz (1878-1909), then Boris Grigorievich Galerkin (1871-1945) succeeded in treating the differential equation system as an algebraic equation system using the variational method. Eric Reissner (1913-1996) approximated the stress field in addition to the displacement field, thus initiating the research of what is called multi-field variational principles.

In the mechanics of solids, we operate with the following basic quantities: displacement field $\boldsymbol{u}=\boldsymbol{u}(x, y, z, t)$, strain tensor field $\boldsymbol{A}=\boldsymbol{A}(x, y, z, t)$, stress tensor field $\boldsymbol{T}=\boldsymbol{T}(x, y, z, t)$, which represent 3+6+6=15 unknown scalar fields at any point of the body. According to linear theory, they can be defined as the geometric equation $\boldsymbol{A}=0.5(\boldsymbol{u}\circ\nabla+\nabla\circ\boldsymbol{u})$ material law $\boldsymbol{T}=\boldsymbol{T}(\boldsymbol{A}(\boldsymbol{u}))$ and equation of motion $\boldsymbol{T}\cdot\nabla+\boldsymbol{b}=\rho\ddot{\boldsymbol{u}}$ (in the case of time-independent $\nabla\cdot\boldsymbol{T}+\boldsymbol{b}=0$ equilibrium equation). These equations are supplemented by the dynamic $\boldsymbol{T}\cdot\boldsymbol{n}=\boldsymbol{t},\ \boldsymbol{r}\in S_t$ and geometric $\boldsymbol{r}\in S_u$ $\boldsymbol{u}=\boldsymbol{u}_u(x, y, z, t)=\boldsymbol{u}_u(r, t)$, boundary conditions, furthermore, in the dynamic case, the following initial conditions: $\boldsymbol{u}=\boldsymbol{u}_0(x, y, z, t=0)$, $\dot{\boldsymbol{u}}=\dot{\boldsymbol{u}}_0(x, y, z, t=0)$. Here are given $\boldsymbol{u}_u$, $\mathbf{t}$, $\boldsymbol{u}_0(t=0)$, $\dot{\boldsymbol{u}}_0(t=0)$ is the $\nabla$ nabla diff. operator, „$\circ$” is the dyadic, „$\cdot$” is the sign of scalar multiplication, $\boldsymbol{n}$ is the surface normal vector, $S_t$, $S_u$ are the signs of the surface subdomains, $\boldsymbol{r}$ is the location vector. These quantities are illustrated in **Figures 1–3.**

To determine the 15 unknown fields, a system of partial differential equations can be derived for the displacement field and the stress field. In general, their exact solution is only given for a few geometries and special boundary conditions.

It is known that in the case of special geometry, the three-dimensional 3D problem can be reduced to 1D so-called rod, 2D plate or shell problems. For rods, the Jacob Bernoulli and Stephen P. Timoshenko (1878-1972) models were widespread, while for plates, the Raymond David Mindlin (1906-1987) model, which also takes into account shear deformation, and for shells, the Paul M. Naghdi (1924-1994) model. The classical plate and shell models are based on the Gustav Robert Kirchhoff (1824-1887) principle (the normal remains perpendicular to the curved mid-surface during deformation).

These models have successfully solved many problems in engineering practice, and their teaching is still valid in today's higher technical education.

In practical life, an important aspect of design is the prediction of the essential properties of the object to be designed before its implementation, in order to achieve an optimal design. This also requires reliable mechanical calculations, for which a model must be prepared. **Figure 4** shows the possibility of taking various aspects into account.

In the following we outline the history of the finite element method **[1, 2, 3]** related to the approximate solution.

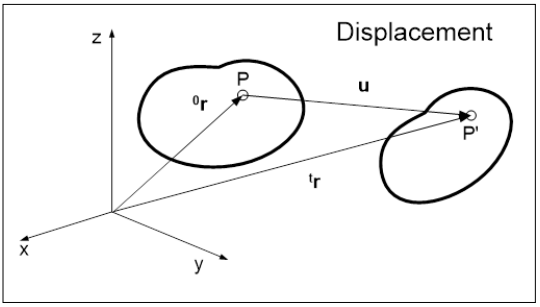


**Fig. 1.** *Displacement vector.*

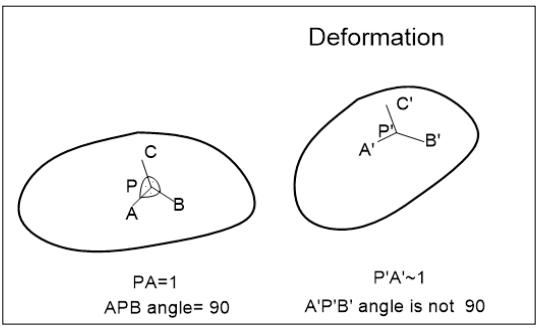


**Fig. 2.** *Deformation detection on the accompanying trider at point P.*

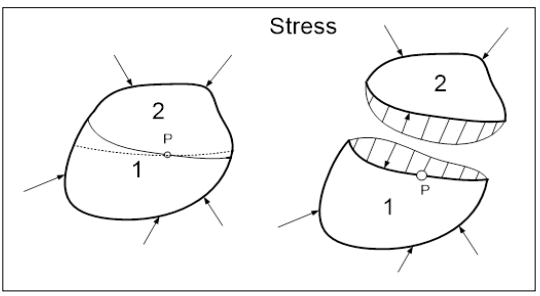


**Fig. 3.** *The internal surface distributed load that ensures equilibrium is the stress.*

## 2. Finite element method

The essence of the method can be easily explained through the example of a stretched rod outlined in **Figure 5.** The rod is divided into elements, the points at the boundary of the elements are called nodes. The displacement at these points is $u_i$, $i=1, ..., 6$. Let us approximate the displacement within the elements with a linear function (dashed line). Obviously, if we include more elements, the dashed linear function within the elements becomes closer to the actual one. Since the solution is not known initially, its approximate function can be obtained from the principle of minimum potential energy, i.e. we will calculate

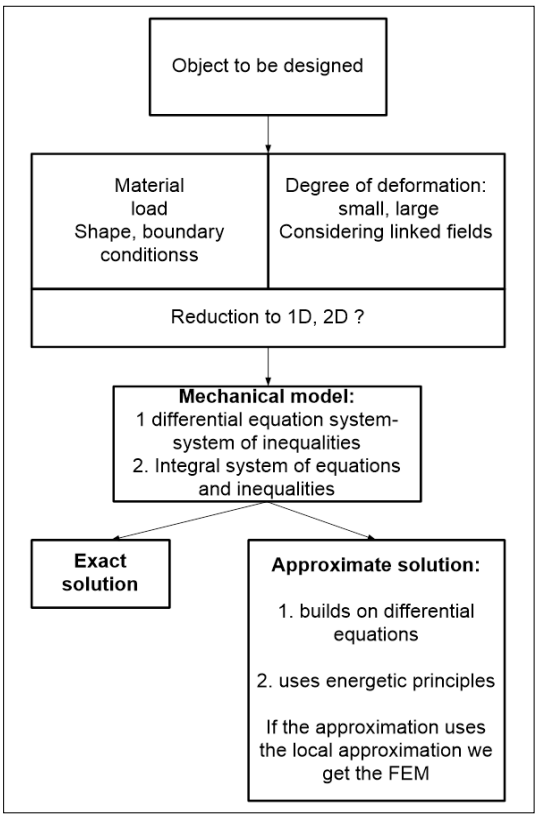


**Fig. 4.** *Main aspects and direction of modeling.*

the displacements at the nodes from an algebraic system of equations. We feel that with more elements we will get a more accurate solution.

Since the length of the elements has been reduced, this approximate solution is called the *h*-version calculation.

Another solution method is also possible. We do not increase the number of elements, but the degree of the approximating polynomial within the element. This was first proposed in the world in 1973 by Barna Szabó (currently an external member of the Hungarian Academy of Sciences, professor emeritus at Washington University in St. Louis). At his suggestion, mathematicians began to deal with this p-version approximation method, examining the degree of convergence of the solution. In the division techniques where the size of the elements in the vicinity of stress singularities is also reduced along with the increase in degree, the procedure is called the hp-version calculation. The log value of the error of deformation energies varies significantly in the log value of the total number of unknowns, according to different functions, which is illustrated in **Figure 6**. The *h*-version technique has the slowest convergence **[1, 2, 3]**. Therefore, it is worth using programs suitable for *p, hp* version calculations when solving specific problems.

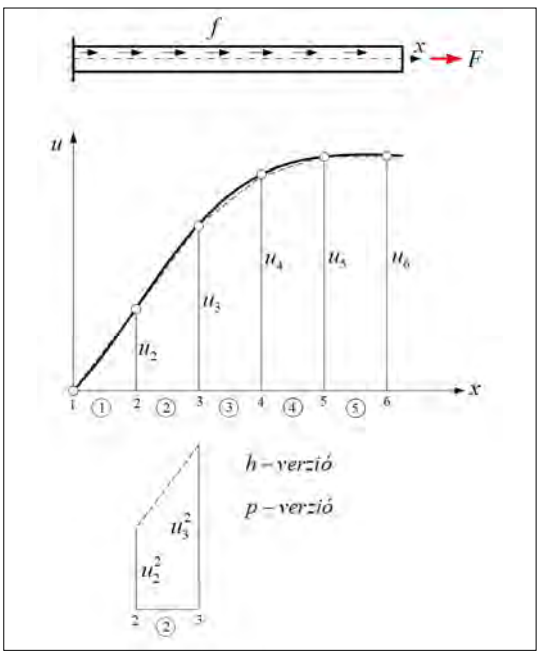


**Fig. 5.** *Displacement field approximation using the finite element method.*

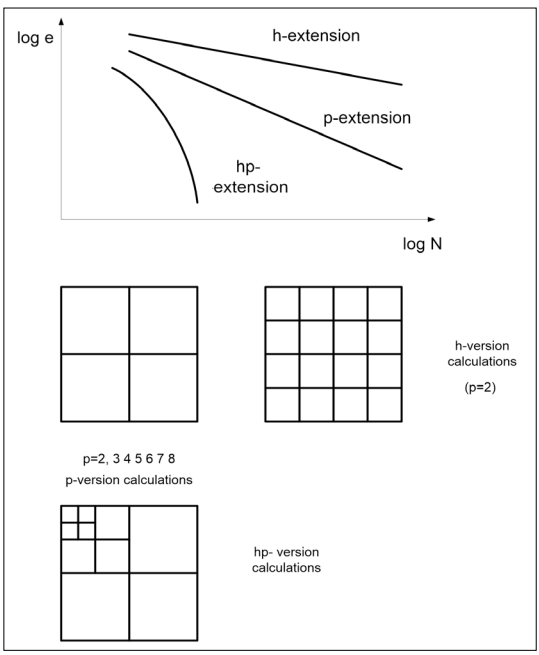


**Fig. 6.** *Convergence of the solution.*

It has been proven [1] that the error can be calculated in terms of $\|e\| \leq kN^{-\lambda}$ where $N$ is the number of unknowns in the problem to be solved.

Since the energy of the exact solution in e is not known, nor are the parameters $k$ and $\lambda$ a minimum of 3 calculations with different orders of approximation must be performed to estimate the error.

Regarding the history of the development of the method, we mention that the article written by M.J. Turner and his colleagues published in 1956 is considered to be the first, and then in 1960 the name finite element became associated with the name of R.W. Clough. Within a short time, several large program systems were developed (1964: ASKA, 1969: SAP, NONSAP, 1969: MARC, ANSYS, NASTRAN).

In 1967, the first book on the finite element method was published, written by O.C. Zienkiewicz and Y.K. Cheung. Further software systems were created: ABAQUS, ADINA in 1972, DYNA in 1976, SYSTUS, COSAR, LSDYNA, PROBE, StressCheck, RASNA, I-DEAS, COSMOS/M, FEAP, FLUENT, SYSWELD, ProCAST, and DEFORM in the 1980s.

On a theoretical level, the convergence of the p version calculation was proven in 1981, and so was the hp version in 1984. In 1991, hierarchical modeling was formulated, in 2006, ASME standardized the conditions for the correct use of the finite element program, and in 2012, the formulation of the reliability of the calculation began.

Conditions formulated against finite element programs:

Expectations of finite element programs:

- convenient description of geometry (using one's own system program or relying on data taken from another system).
- wide range of elements (low and high-degree elements).
- possibility of automatic element division.
- simple definition of constraints and other external effects.
- possibility of special modeling constraints (e.g. substructure technology).
- wide range of material laws.
- possibility of using linear and nonlinear theories.
- wide range of loads.
- fast calculation (multiprocessor algorithm, efficient equation system solvers: with direct solver or iteration).
- error analysis.
- possibility of precision of the calculation.
- combining and graphically illustrating the results.

In the early days, finite element program systems were installed on large central computers, which were accessible via terminals. Starting in the 80s, after the appearance of personal computers, the finite element method has become closer to the user, and even the graphical possibilities have made the method user-friendly. Considering the importance of the topic, special courses were organized in higher education institutions to introduce the method and to access it directly by means of computer rooms. Research has also increased significantly, focusing on the creation of new elements and procedures and their industrial dissemination. Several conferences have been organized for those working with finite elements, to build fruitful relationships.

Several programs were developed at our department to overcome the disadvantages of the embargo at that time: among others, TESZGA was developed for the calculation of shells and tanks, AUTOBUSZVAZ for the calculation of bus frames (also using the support of AUTÓKUT), BANYAV-AG for KBFI, LAPÁT for GANZ-MÁVAG, ROBOT and SIK for VIDEOTON, ABRONCS 1, 2, 3 commissioned by TAURUS, and FEM3D, a finite element program system for solving strength and dynamic problems of complex flexible structures.

It is worth comparing the shape functions of rectangular elements used in the h-version calculations operating with classical Lagrange shape functions with the Legendre functions used for p-version calculations, and also analyzing the computational advantages and disadvantages that can be deduced from these.

On the left side of **Figure 7** the shape functions applied to the first side of the element in the $p$ version can be seen, similarly, on the right side, the $h$ version element using Lagrange functions [3].

We see that with the $p$ version, as $p$ increases, the top two figures belong to $p=1$ at $p=2$ a new quadratic function enters, and then so does the cubic function below in sub-**Figure 7.** So if the approximation is $p=2$ only the functions belonging to $p=1$ and $p=2$ work on the element, if $p=3$, then new functions enter, without spoiling the previous ones. This is no longer the case in the $h$-version case outlined on the right. In the quadratic approximation, in addition to the corner points, the side midpoints appear, i.e., a total of eight points, while in the cubic approximation, we have another 1-1 on the sides, i.e., a total of 12 nodes, but the assumed shape functions are no

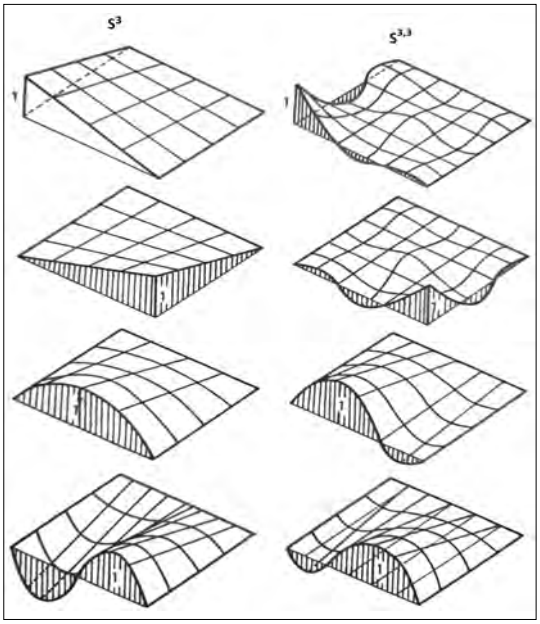

**Fig. 7.** *Shape functions for p and h version elements.*

longer the same as the previous ones, since the Lagrange functions must be zero at the nodes except for one point. This means that the stiffness matrix calculated in the lower-order approximation will no longer be usable, while in the *p*-version the previous one will correspond to a part of the new one. The requirement to perform a minimum of 3 calculations is very well programmable in the *p*-version (see e.g. StressCheck program [4]).

Formally, after discretization

$$\mathbf{M}\ddot{\mathbf{q}} + \mathbf{C}\dot{\mathbf{q}} + \mathbf{K}\mathbf{q} = \mathbf{f} \qquad (1)$$

we obtain a differential equation, where **M** is the mass, **C** is the damping matrix, **K** is the stiffness matrix, **f** is the load vector, **q** is the nodal displacement vector (unknown).

In the nonlinear (static) case, the equation for the increments can be written as

$$\mathbf{K}_T \Delta\mathbf{q} = \mathbf{f}_n - \mathbf{f}_{\sigma_n}. \qquad (2)$$

Due to the location of the nodes, the above matrices have a band structure. Reducing the band width reduces the calculation time, which is why sophisticated finite element software systems also include band reduction procedures.

Automatic re-meshing strategies have also been developed to reduce the errors that occur during the calculation.

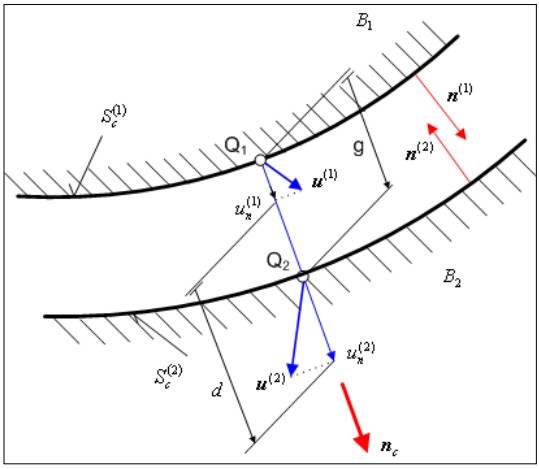


**Fig. 8.** *Contact displacements and the initial gap g.*

A separate class of nonlinear problems is the clarification of the contact relations between bodies. In this case, inequalities can be written for on the contact surfaces [5]. So, a system of inequalities must be solved!

To solve these, mathematical programming procedures or special iteration methods can be used to create contact finite elements.

The gap between the bodies after deformation in the relevant contact region: (see Figure 8):

$$d = u_n^{(2)} - u_n^{(1)} + g \quad \boldsymbol{r} \in S_c = S_0 \cup S_p \qquad (3)$$

If

$$d \geq 0, p_n = 0 \quad \boldsymbol{r} \in S_0 \quad \text{gap},$$
$$d = 0 \quad p_n \geq 0 \quad \boldsymbol{r} \in S_p \quad \textit{contact}, \qquad (4)$$

but $d\, p_{n=0} \quad \boldsymbol{r} \in S_c$

## 3. Examples

Here we present only two simpler tasks.

### 3.1. Contact of cylindrical bodies

Let us examine the contact problem of two cylindrical bodies made of the same material. The radius of the inner holes is $r_i = 20$ mm, the outer ones are $r_e^{(1)} = 120$ mm, $r_e^{(2)} = 140$ mm, respectively, while their heights are $b = b^{(1)} = b^{(2)} = 100$ mm (Figure 9). The lower meridian of the upper cylinder $B_1$ is characterized by the following function:

$$g = 0{,}0035\,(r-20)^2, \qquad (5)$$

which also corresponds to the initial gap between the bodies. The Young's modulus of the material of the bodies is $E = 2 \cdot 10^5$ MPa and the Poisson's ra-

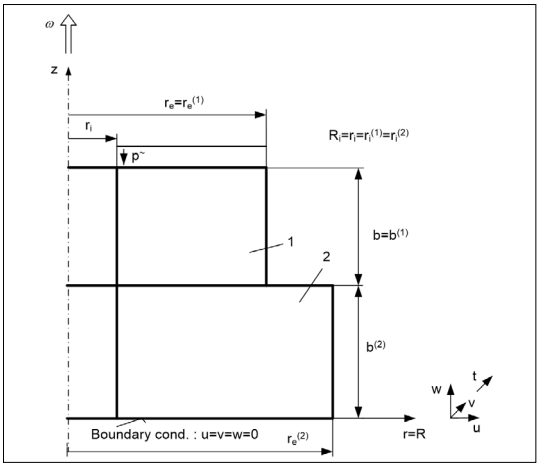


Fig. 9. *KContact of two cylindrical bodies.*

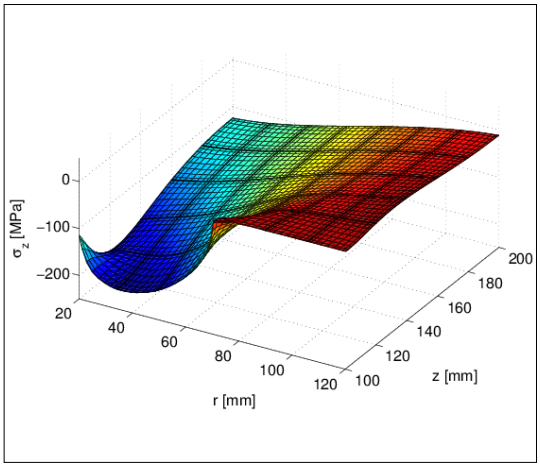


Fig. 12. $\sigma_z$ *normal stress distribution.*

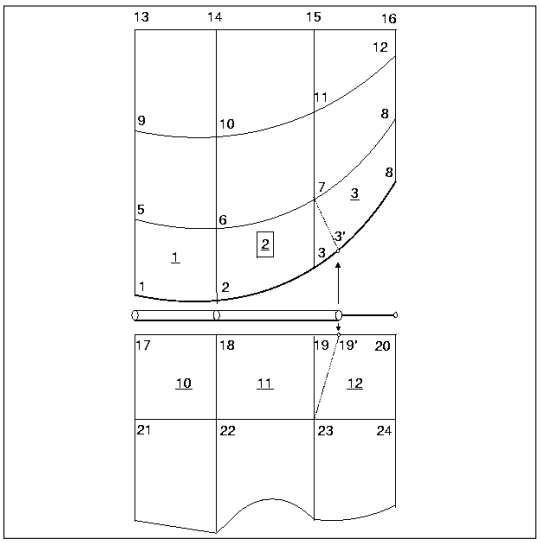


Fig. 10. *Moving the nodes 3→3', 19→19'.*

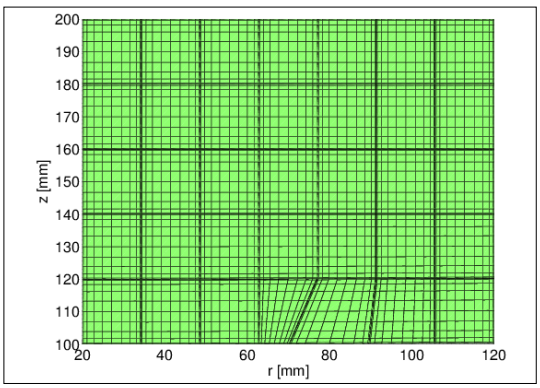


Fig. 11. *Modified 7×5 mesh, radius of the edge of the contact area* $r_p = 70.37$ *mm.*

tio is $\nu = 0{,}3$. The vertical displacement of the upper edge of the body $B_1$ is given byt: $w_0 = 0.15$ mm.

The solution is modeled with finite elements of degree $p = 8$. The initial mesh is modified using the so-called positioning technique in such a way that the node of the finite element coincides with the boundary of the contact area **[6]**. This allows us to achieve freedom from oscillation of the stresses. In **Figure 10,** the end of the contact region does not coincide with the right-hand ends of elements 2 and 11, so the nodes 3 and 19 must be moved. **Figure 11** shows this for a 7×5 mesh, and the distribution of the normal stress $\sigma_z$ can be seen in **Figure 12**.

For further refinement solution techniques, see the paper under **[7]**.

### 3.2. Roller rounding

We now examine a type of problem completely different from those described above. The rounding of a cylindrical roller must be determined in such a way that the pressure in the meridian plane follows a course specified by us. This can be achieved by partially controlling the contact pressure **[5, 8]**.

The basic idea of the method is clearly shown in **Figure 13.**

We have a “roof” under which the pressure must be located. Since the highest value occurs in the meridian plane, here the pressure touches the roof, and in other places it is below it. The course of the pressure in the meridian plane can be prescribed using spline (Hermite) functions.

The figure shows half of the roller. Depending on the length of the constant section, we will get pressures of different heights and slopes. The de-

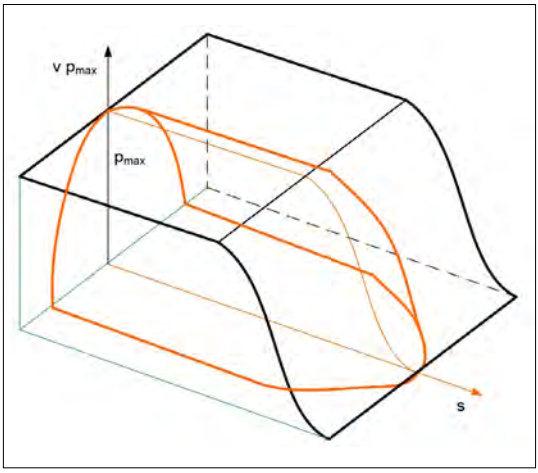


Fig. 13. *Function prescribing partial pressure control.*

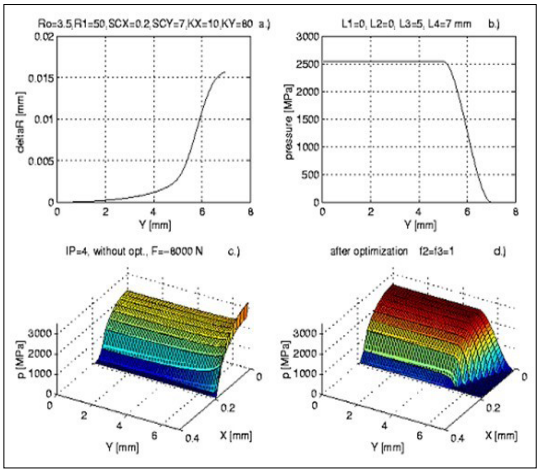


Fig. 14. *Result of the roller rounding.*

signer has to decide which variant he considers the best. For example, the fatigue limit specification criterion for roller bearings can be decisive.

**Figure 14** shows the change in radius obtained from the solution of the optimization problem, the pressure falling into the meridian, the pressure rising high at the end obtained for the original constant radius roller, and the pressure of the optimal rounded roller, looking at a quarter of the solution.

The control function ensures that the pressure at the end of the roller and its derivative with respect to s are also zero. When setting up the problem, the elastic bodies were taken into account by means of the influence function obtained from the Boussinesq solution for the elastic half-space **[5]**. The number of surface elements taken is 10×40. The load is 8000 N, the roller radius is 3.5 mm, and the contact area tested is 0.2×7 mm.

## 4. The future of the finite element method

It is a fact that while in the 1950s, measurement represented 95% of linear stress analysis, in the 1970s it represented 50%, and in the 1990s it represented only 1%, compared to 99% computer simulation. The possibilities of numerical mechanics are increasing in everyday practice, and their practical benefits are clear.

We also experience that the domestic and international conferences organized focus on numerical research in many cases, presenting the diversity of design engineering tasks. For example, at the USACM (USA Congress on Computational Mechanics) held in San Francisco in 1997, 450 presentations were given in 96 sections.

In Europe, ECCOMAS organizes similar conferences every 4 years.

The large number of participants also indicates the importance of the research, and the fact that serious forces are at work, conquering newer and newer areas in the field of mechanics.

The large number of journals dealing with finite elements, and the quality of the books published underline the importance of this scientific field, its will to live, and the urgent need to educate the next generation.

## 5. Conclusions

We can state that a new profession has emerged, which deals with

- the analysis and optimization of mechanical problems,
- the development of specialist software,
- the identification of models,
- the training and installation of computer systems,
- the development and teaching of mechanical numerical methods.

In connection with all this, we can also state that the role of mechanics is being valued and strengthened, since

- more precise models can be built,
- the static and dynamic examinations of complex systems (solid-body-liquid/gas systems, intelligent structures containing piezoelectric elements) become feasible possible.
- When designing new machines and structures, and examining machine manufacturing pro-

cesses, the problems to be solved have become conveniently manageable with numerical techniques based on the high-degree-of-freedom finite element/boundary element method for simulating mechanical states.
– Error estimation and automatic refinement of results are services expected and required from the program.
– Complex design systems are available, to which computer programs suitable for analyzing mechanical models can be easily connected.
– In the fierce market competition related to the development of new products and technologies, modern strength, dynamics, and multidisciplinary knowledge are of strategic importance, which greatly increases the value of engineers in possession of this knowledge.

## References

[1] Szabó B., Babuska I.: *Finite Element Analysis.* New York, Wiley-Intersience, 1991.
[2] Szabó B, Babuska I.: *Introduction to Finite Element Analysis, Formulation, Verification and Validation.* A John Wiley and Sons, Ltd., Chichester, UK, 2011.
[3] Páczelt I.: *Végeselem-módszer a mérnöki gyakorlatban.* I. és II. kötet. Miskolci Egyetemi Kiadó, Miskolc, 1999, 2025.
[4] Engineering Software Research and Development, Inc. (ESRD): StressCheck program https://www.esrd.com/
[5] Páczelt I.: *Iterative Methods for Solution of Contact Optimization Problems.* Archives of Mechanics, 52. (2000) 685–711.
[6] Páczelt I., Szabó B., Szabó T.: *Solution of Contact Problem Using the Hp-Version of the Finite Element Method.* Computers and Mathematics with Applications, 38. (1999) 49–69. https://doi.org/10.1016/S0898-1221(99)00261-8
[7] Páczelt I., Baksa A., Szabó T.: *Formulation of the P-Extension Finite Elements for the Solution of Normal Contact Problems.* Journal of Computational and Applied Mechanics, 15/2. (2020) 135–172. https://doi.org/10.32973/jcam.2020.009
[8] Páczelt I., Baksa A. Szabó T.: *Product Design Using a Contact-Optimization Technique.* Strojniski Vestnik-Journal of Mechanical Engineering, 53/7-8. (2007) 442–461.

Műszaki Tudományos Közlemények vol. 22. (2025) 93–97.
DOI: Hungarian: https://doi.org/10.33895/mtk-2025.22.15
English: https://doi.org/10.33894/mtk-2025.22.15

# HIGH PRECISION MODELLING AND STRENGTH ANALYSIS OF TOOTH IMPLANTS

Klaudia PAPP,[1] István Attila PIROS,[1] Bálint DEÁK[2]

[1] *John von Neumann University, Department of Innovative of Vehicles and Materials, Kecskemét, Hungary, papp.klaudia@nje.hu*

[2] *University of Szeged, Faculty of Dentistry, Szeged, Hungary, deakbalint7@gmail.com*

**Abstract**

The design and mechanical analysis of patient-specific dental prostheses play a crucial role in modern dentistry and biomechanical research. With the advancement of digital design and simulation tools, it has become possible to create customized dental prostheses tailored to individual patients, ensuring not only anatomical compatibility but also optimal mechanical stability.

In our study, we present the design and finite element analysis of a bridge-type dental prosthesis, which was created based on the reconstruction of a real mandible. Our goal was to examine the behavior of the dental prosthesis and mandible under load, with a particular focus on stress distribution and deformations.

**Keywords***: Tooth implants, NURBS modeling, Finite element analysis, von Mises stress distribution.*

## 1. Reconstruction of the teeth and mandible

The aim of our research was to create a high-quality, detailed geometric reconstruction of the mandible and teeth based on CT images. The resulting model provided the basis for further biomechanical and strength studies, which will help to design optimal prostheses and to better understand the mechanical behaviour of the tooth-mandible system.

The first step was to reconstruct the mandible. For this purpose, CT images were segmented in three main planes – axial, sagittal and cortical – using 3D Slicer [1]. This process allowed for a better separation of bony and soft tissues, which facilitated a more accurate modeling [2]. The segmented sections were then imported into the PTC Creo 11 design software, where NURBS curves were created during reconstruction and NURBS surfaces were then spanned onto them. Particular attention was paid to the tangential contact between the curves and to keep the number of surfaces as small as possible, as overly complex geometry may complicate subsequent simulation studies [3]. After reconstruction of the mandible, its structure was divided into two layers: spongiosa and cortical bone layers, to better model their different mechanical properties [4].

The next step was to reconstruct the teeth, following similar principles as for the mandible. The teeth were individually reconstructed from the CT images, initially as a solid structure. Our primary goal in this phase was to accurately reconstruct the geometry of the teeth and to correct errors and inaccuracies that may have occurred in the original CT data. These included, for example, undue cavities, minor topological irregularities or noisy surfaces [5]. In this initial phase, the teeth were not yet stratified, as the focus was first on accurately restoring their external shape.

The completed remodeled mandible is shown in **Figure 1.**

The creation of a complete model provided the opportunity to analyse the mechanical stress capacity of the tooth-mandible system and the behaviour of prostheses and implants under different loading conditions by subsequent biomechanical and strength studies. The reconstruction methods used ensured high resolution and smooth topology of the model, which are essential for accurate simulation studies and medical applications.

## 2. Tooth implants design and modelling

### 2.1. High quality modelling of tooth implants

In our research, we aimed to create a patient-specific prosthesis that precisely matches the original anatomical structure of the patient's mandible and teeth, following precise modeling of the mandible and teeth. The prosthesis is a bridge-type restoration designed for two ground teeth. The bridge is bonded to the ground teeth. This solution is considered a fixed tooth implant, which acts as a bridge to remedy the tooth deficiency and provides the patient with a durable, functionally load-bearing restoration.

The bridge designed for existing teeth is shown in **Figure 2.**

The geometry of the bridge was created by geometrically offsetting the surfaces of the original teeth, thus ensuring a proper fit of the prosthesis on the surface of the extracted teeth **[6]**.

The fit of the restoration on the ground teeth is shown in **Figure 3.**

In the picture, the area marked in pink is the spongiosa layer of the mandible, which forms part of the supporting structure of the teeth, and the two ground teeth on which the bridge rests. These parts are connected to each other in a bonded way to prevent displacement **[7]**.

The geometry of the implant closely follows the patient's individual anatomy to ensure proper fit and stability. The structural design of the bridge is such that the bite forces are properly distributed over the cantilever teeth, minimising the risk of overloading.

The bridge-type implant thus created provides an opportunity for further mechanical analyses that can help optimise the final design and facilitate preparation for clinical application.

### 2.2. Strength analysis of tooth implant

Following the design of a patient-specific bridge-type implant, a strength analysis was performed in PTC Creo 11 software using the integrated Ansys simulation module. Our goal was to investigate the mechanical behaviour and resistance of the implant in a static loading environment.

The following boundary conditions and loads were applied in the finite element analysis:

- Boundary conditions: the arthroplasty and crown protrusion of the mandible were fixed in order to investigate the loading behaviour of the implant under realistic conditions, and, in addition, since only the half of the mandible was investigated in order to run the simulations faster, a symmetry condition was added to the mandible where this mandible was cut, so that displacement was only allowed along the axis of the cut surface.
- Load: a static force of 100 N in the vertical direction was applied to the bite surface of the middle tooth of the bridge, corresponding to an average bite force **[8]**.

The applied boundary conditions and loads are shown in **Figure 4.**

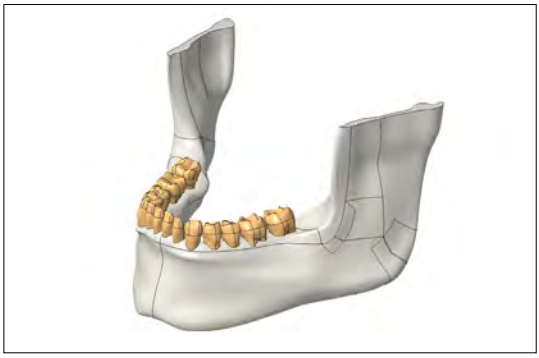

**Fig. 1.** *Mandible modelled from CT images.*

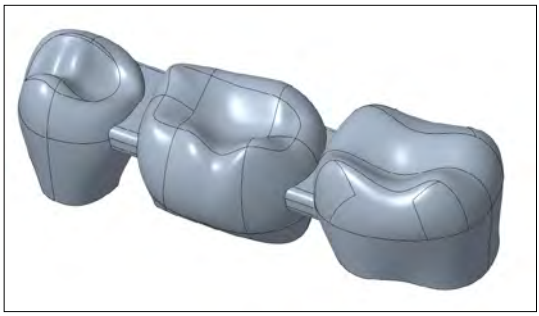

**Fig. 2.** *The bridge type of implant*

**Fig. 3.** *The fit and connection of the implant to the ground teeth.*

During the modeling of the implant, care was taken to define the bite surfaces as separate, well-defined surfaces [9]. As shown in Figure 5 this allowed for accurate load assignment and precise determination of the actual mechanical stresses on the implant.

Before starting the strength analysis, the whole model was meshed with finite element meshing to ensure the accuracy of the numerical calculations [10]. This meshing is shown in Figure 6.

For meshing, a tetrahedral finite element mesh was used, which is particularly suitable for accurately mapping complex organic geometries such as the shape of the mandible and the dentition [11].

The tetrahedral mesh is an excellent fit for the curved, complex shape of the mandible and tooth implant, as tetrahedral elements fill the available volume more efficiently than conventional hexahedral elements. Another significant advantage is that it can be generated automatically, requiring less manual intervention, which makes it faster and easier to apply to organic shaped models. In addition, to achieve accurate stress distribution results, it is possible to vary the element size to create a denser mesh in critical areas, improving the accuracy and reliability of the analysis. The tetrahedral elements are able to handle more complex boundary conditions and loading situations, which was a particularly important consideration in the modeling of implant.

By constructing the meshing, we ensured that the mandible, the implant and the fixed teeth were represented at the appropriate resolution in the finite element analysis, thus obtaining more accurate and detailed results on their loading behaviour.

The first step in the finite element simulations was to investigate the total deformation, which shows the extent to which static loading causes parts of the model to move from their original position. The results are shown in Figure 7, which shows that the largest deformation was at the lower part of the mandible, at the mandible tip, where the maximum displacement was 0.1706 mm.

This result suggests that the mandible undergoes minimal elastic deformation under the applied 100 N bite load, which is a natural phenomenon. The greater displacement in the mandible is explained by the fact that this area is furthest from one of the fixed boundary conditions (mandibular arthroplasty and crown protrusion) and therefore has a greater degree of freedom to move [12].

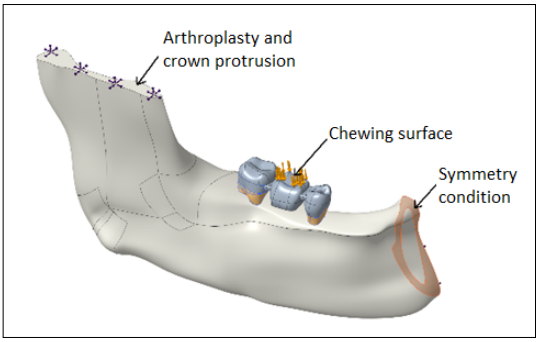


**Fig. 4.** *Loads and boundary conditions.*

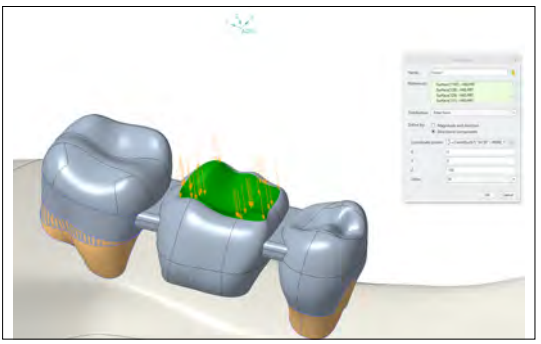

**Fig. 5.** *Application of the load to the bite surface.*

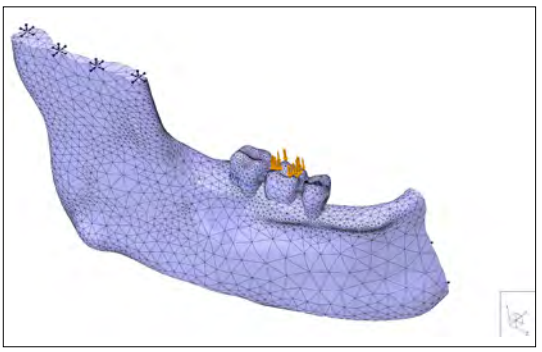

**Fig. 6.** *Meshing on the mandible.*

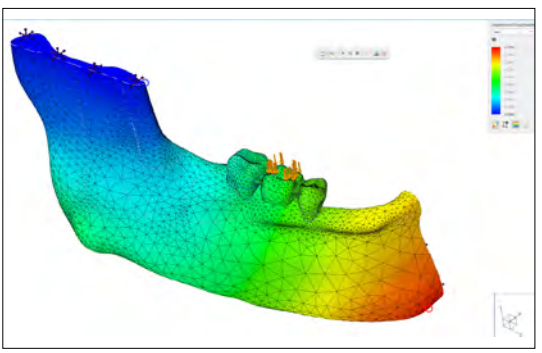

**Fig. 7.** *Total deformation.*

As a next step in the finite element simulation, a von Mises stress test was performed to analyse the stress distribution in the implant and mandible material under static loading. The result of the stress test is shown in **Figure 8.**

In the case of the mandible, the highest stress was in the ramus region, where the maximum value exceeded 10 MPa. This result is in agreement with the fact that the ramus plays a key role in the load transmission due to the masticatory force, and therefore the greatest mechanical stress is concentrated in this area **[13]**.

In the case of implant, the highest stresses were found on the bridge structure, which is located between the two grinded teeth. Here, the principal stress reached 33.9 MPa, indicating that this part of the implant is a highly stressed zone. This value is also significant because the main loading point of bridges is the middle part, where bending and shear stresses are generated due to the bite force **[13]**.

The maximum stresses on the bridge are shown in **Figure 9** and **10.**

The results show that both the mandible and the implant structure exhibit suitable mechanical resistance, as the applied stresses are within the expected range **[14]**. Further fine-optimization of the implant geometry can help to reduce the maximum stress values and to distribute the forces more evenly.

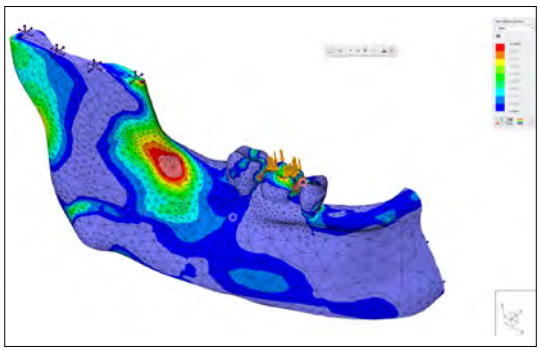

**Fig. 8.** *Von Mises stress analysis.*

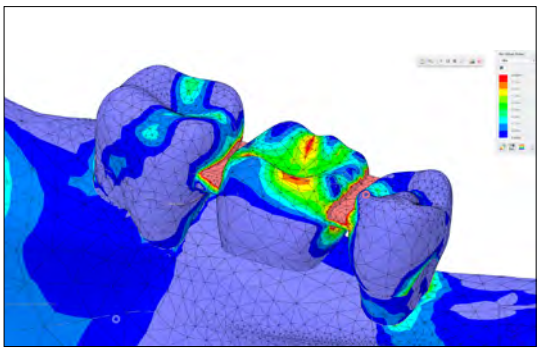

**Fig. 9.** *Maximum stress on the bridge, top view.*

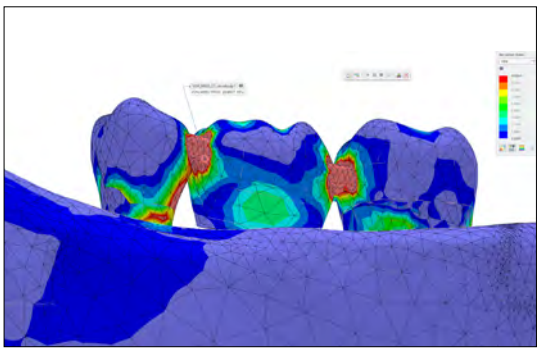

**Fig. 10.** *Maximum stress on the bridge, bottom view.*

## 3. Conclusions

The aim of our research was the design and mechanical testing of a patient-specific implant based on the geometric reconstruction of a real mandible. The planned implant is a bridge-type restoration that was fitted on two ground teeth. The complete model was created and simulation studies were performed in PTC Creo 11 software using the Ansys finite element module.

As a first step in the simulation process, the entire structure was fitted with a tetrahedral finite element mesh, which is an excellent tool for tracing the complex geometry more accurately. Subsequently, mechanical analyses were carried out, treating the mandibular arthroplasty and crown protrusion as boundary conditions and the mandible cut surface as a symmetry condition, while the loading of the implant was modelled by a static force of 100 N in the vertical direction applied to the bite surface of the central tooth of the bridge.

The results showed that the maximum value of the total deformation was 0.1706 mm, which occurred at the lower part of the mandible. When the stress distribution was examined, the highest von Mises stress was developed in the ramus part of the mandible, exceeding 10 MPa. In the case of the implant, the most stressed zone was the central part of the bridge, where the stress increased to 33.9 MPa.

## References


[1] Wang C.-S., Lin M.-C., Wang C.-C., Chen C.-F., Hsieh J.-C.: *Feature Reconstruction for 3D Medical Images Processing*. In: Gao J.X., Xu D., Sun X., Wu Y. (eds.) *Proceedings of the 2013 6th International Conference on Biomedical Engineering and Informatics* (BMEI 2013), Vol. 1 and 2, 69–74. IEEE, New York (2013). https://doi.org/10.1109/BMEI.2013.6746909

[2] Nguyen, V.S., Tran, M.H., Le, S.T.: *Visualization of Medical Images Data Based on Geometric Modeling*. In: Dang, T.K., Kng, J., Ta-kizawa, M., Bui, S.H. (eds.) *Future Data and Security Engineering*. Lecture Notes in Computer Science, pp. 560–576. Springer, Cham (2019). https://doi.org/10.1007/978-3-030-35653-8 36

[3] Aubin, C.-, Dansereau, J., Parent, F., Labelle, H., Guise, J.A.: *Morphometric Evaluations of Personalised 3D Reconstructions and Geometric Models of the Human Spine.* Medical and Biological Engineering and Computing, 35/6. (1997) 611–618. https://doi.org/10.1007/BF02510968

[4] AlZubi, S., Jararweh, Y., Al-Zoubi, H., Elbes, M., Kanan, T., Gupta, B.: *Multiorientation Geometric Medical Volumes Segmentation Using 3D Multiresolution Analysis.* Multimedia Tools and Applications, 78/17. 24223–24248 (2019) https://doi.org/10.1007/s11042-018-7003-4

[5] He, J., Chen, S., Zhang, H., Tao, X., Lin, W., Zhang, S., Zeng, D., Ma, J.: *Downsampled Imaging Geometric Modeling for Accurate CT Reconstruction via Deep Learning*. IEEE Transactions on Medical Imaging, 40/11. (2021) 2976–2985 https://doi.org/10.1109/TMI.2021.3074783

[6] Liu, C.-C., Hsu, C.-H., Hsiao, I.-T., Lin, K.M.: *Effect of Geometric Models on Convergence Rate in Iterative PET Image Reconstructions.* Journal of Instrumentation, 4(05), 05010 (2009) https://doi.org/10.1088/1748-0221/4/05/P05010

[7] Garrido, A.H., Cerra, P.P., Zapico, A.O., Lopez, M.D.G.: *Geometric Data Collection in Medical Imaging*. DYNA, 86/2. (2011) 222–231. https://doi.org/10.6036/3868

[8] Pemmada, R., Telang, V.S., Tandon, P., Thomas, V.: *Patient-Specific Mechanical Analysis of PCL Periodontal Membrane: Modeling and Simulation.* Journal of the Mechanical Behavior of Biomedical Materials, 151. (2024) 106397 https://doi.org/10.1016/j.jmbbm.2024.106397

[9] Franchini, S., Gentile, A., Vassallo, G., Vitabile, S.: *Implementation and Evaluation of Medical Imaging Techniques Based on Conformal Geometric Algebra*. International Journal of Applied Mathematics and Computer Science, 30/3. (2020) 415–433.

[10] Abdel-Aziz, H.S., Zanaty, E.A., Ali, H.A., Saad, M.K.: *Generating Bezier Curves for Medical Image Reconstruction.* Results in Physics, 23. (2021) 103996 https://doi.org/10.1016/j.rinp.2021.103996

[11] Majeed, A., Mt Piah, A.R., Rafique, M., Ab-dullah, J.Y., Rajion, Z.A.: *NURBS Curves with the Application of Multiple Bones Fracture Reconstruction.* Applied Mathematics and Computation, 315. (2017) 70–84. https://doi.org/10.1016/j.amc. 2017.05.061

[12] Lv, X., Fu, D.: *Research on Rapid Imitation of Human Tibia and Five-Axis CNC Machining Based on Computer-aided.* Journal of Physics: Conference Series, 1648(3), 032130 (2020) https://doi.org/10.1088/17426596/1648/3/032130

[13] Yao, Q., Zhuang, Y., Aji, Y., Zhang, Q., Luo, Y., Li, S.: *Biomechanical Impact of Different Isthmus Positions in Mandibular First Molar Root Canals: a Finite Element Analysis.* Clinical Oral Investigations, 28/6. (2024) 311 https://doi.org/10.1007/s00784-024-05715-1

[14] Demir, O., Uslan, I., Buyuk, M., Salamci, M.U.: *Development and Validation of a Digital Twin of the Human Lower Jaw under Impact Loading by Using Non-Linear Finite Element Analyses.* Journal of the Mechanical Behavior of Biomedical Materials, 148, (2023) 106207. https://doi.org/10.1016/j.jmbbm.2023.106207

Műszaki Tudományos Közlemények vol. 22. (2025) 98–101.
DOI: Hungarian: https://doi.org/10.33895/mtk-2025.22.16
English: https://doi.org/10.33894/mtk-2025.22.16

# COMPUTER SIMULATION TO VISUALIZE THE RESULTS OF SOIL TILLAGE WITH DISC HARROW

Judit PÁSZTOR,[1] Ferenc TOLVALY-ROȘCA[2]

*Sapientia Hungarian University of Transylvania, Faculty of Technical and Human Sciences, Târgu Mureş, Department of Mechanical Engineering, Romania*

[1] *pjudit@ms.sapientia.ro*

[2] *tferi@ms.sapientia.ro*

**Abstract**

The disc harrow is the basic machine for shredding soil. It loosens, smooths and mixes the top layer of soil during shredding. It also chops and incorporates weeds and stalk residues into the soil. In this paper, we will explore the factors that influence the operation process of the disc harrow and apply them to the Bomet BTP 4×6 disc harrow. A body model of the Bomet BTP 4×6 disc harrow is prepared and the results of its operation process are simulated in three different operating situations.

**Keywords***: disc harrow, computer simulation, operation process.*

## 1. Introduction: Overview of the Disc Harrow

The disc harrow is a widely used implement in soil shredding and tillage operations. In addition to shredding the soil, it also loosens, levels, and partially mixes the upper soil layer, making it a viable alternative to traditional ploughing in certain cases **[1]**.

The main working elements of the disc harrow (**Figure 1**) are the disc blades, which can feature either smooth or cutout edges. These disc blades are mounted on a common axle, separated by spacer sleeves to maintain consistent spacing. A set of disc blades mounted on the same axle forms a disc battery, which is attached to the frame of the implement.

**Fig. 1.** *Construction of the Bomet BTP 4×6 Disc Harrow.*

Based on the configuration of these disc batteries, disc harrows can be categorized into V-shaped or X-shaped configurations.

The disc harrow is considered a semi-active tillage implement: during operation, the disc blades rotate relative to the frame during the work machine is towed. The axis of the disc battery is typically set at an angle of attack γ relative to the direction of travel **Figure 2.a**. As the machine is towed, the disc blades mounted on the axle rotate and continuously cut into the soil **Figure 2.b**. The soil clods are lifted along the inner surface of the disc blades and subsequently fall back to the ground. This process results in the fragmentation, loosening, mixing, and slight turning of the soil. The worked soil is also displaced laterally.

As a consequence of the disc harrow's operation, the bottom of the tilled soil is not uniform; a ridge forms between the disc blades, which may even be detectable at the surface (**Figures 2.b**, **2.c**).

Requirements for the disc harrow's working process:

– The worked soil surface should be even, with no untilled strips remaining [2];
– The furrow bottom should be as smooth as possible, and the height of the formed ridge should be minimized [2, 3];
– The disc blades should effectively chop and incorporate crop residues and stubble into the soil [4].

To meet these requirements, the second disc battery is offset relative to the first, so the rear disc blades work between the areas already cultivated by the front battery, Figure 2.

The disc blades mounted on the second battery return the soil displaced to the sides.

Effective fragmentation is achieved by cut-out-edge disc blades, typically mounted on the front battery.

The working process of the machine is rapid, making field observation and evaluation challenging.

To better understand the disc harrow's operation, we aim to visualize the process through computer simulation in this paper.

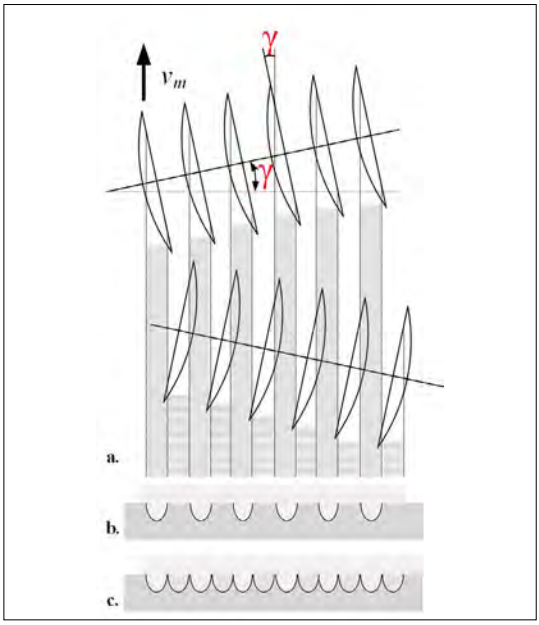


Fig. 2. *Operation process of disc harrows: a – on the soil surface; b – at the furrow bottom after the first disc battery; c – along the furrow bottom after the disc blades operating in staggered alignment.*

## 2. Computer Simulation of the Operation Process of the Disc Harrow

Methodology:

– A solid model of the Bomet BTP 4x6 disc harrow, located at the machine yard of Sapientia Hungarian University of Transylvania, Faculty of Târgu Mureș, is created.
– The key factors that characterize the working process of the disc harrow are identified.
– The working process is simulated using real operational data.
– The relationships between the key characteristics and the working process are analyzed.

### 2.1. Solid Model of the Bomet BTP 4×6 Disc Harrow

The Bomet BTP 4×6 2,2m disc harrow is equipped with four batteries Figure 1. These batteries are arranged in an X-configuration, with each battery consisting of six disc blades.

The diameter of the disc blades is Φ 460 mm, and the spacing between the blades is 172 mm. The working width of the machine is 2200 mm, and its total mass is 615 kg [5].

Figure 3 shows the solid model of two consecutive disc batteries, both depicted with smooth-edged disc blades.

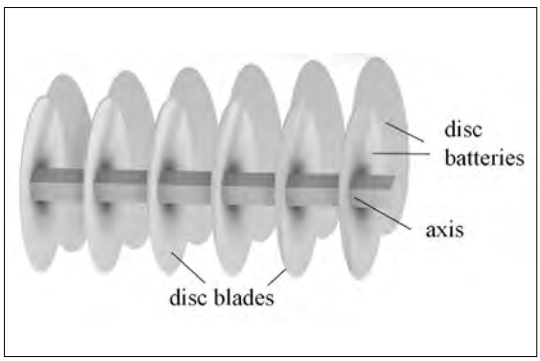


Fig. 3. *Solid Model of the Disc Harrow Batteries.*

### 2.2. Factors Characterizing the Operation Process of the Disc Harrow

Figure 4 illustrates the cross-sectional profile of the soil worked by two adjacent disc blades, along with the corresponding geometrical parameters of the blades.

The working process requirements of the disc harrow, such as the absence of untilled strips, uniformity of the furrow bottom, the cross- section of the cultivated soil and the ridge height, can be assessed based on these factors.

The relationship for the cultivated soil cross-section $S_d$ is described in [3]:

$$S_d = 2(a-c)\sin\gamma\sqrt{c(D-c)} + \frac{1}{8}D^2(\varphi_c - \sin\varphi_c)\sin\gamma \ [mm^2]' \quad (1)$$

where: $a$ is the working depth [mm]; $c$ is the height of the unworked soil ridge [mm]; $\gamma$ is the attack angle of the disc battery [°]; $\varphi_c$ is the theoretical central angle corresponding to the disc blade ridge height [°].

The relationship for the theoretical central angle corresponding to the ridge height on the disc blade is given in [3]:

$$\varphi_c = 2\,acos\left(1-\frac{2c}{D}\right). \quad (2)$$

The relationship between the ridge height and the geometrical characteristics of the disc harrow is given in [4]:

$$b = 2\tan\gamma\sqrt{c(D-c)}, \quad (3)$$

where: $b$ is the distance between adjacent disc blades working side by side [mm].

Based on the (1), (2), and (3) relationships, the working process of the disc harrow is influenced by:

– the working depth;
– the attack angle γ of the disc blades.

### 2.3. Simulation of the Operation Process of the Disc Batteries

The four batteries of the Bomet BTP 4×6 2,2m disc harrow are symmetrically arranged, so the simulation is performed only for two consecutive disc batteries.

The disc batteries of the Bomet BTP 4×6 2,2 m disc harrow can be set to attack angles of γ = 12°/15°/17° [5].

The working depth of the disc blades depends on the weight force applied to the blades, which can be adjusted by adding supplementary weight. The simulations are carried out for working depths of a=60 mm, a=90 mm, and a=120 mm.

Three simulations were performed, based on the data in Table 1. Nine isometric views were prepared for illustration, six of which are shown in the paper.

**Table 1.** *Operational Parameters of the Simulations*

| Simulation | γ [°] | a [mm] |
|---|---|---|
| First | 12 | 60 |
| Second | 15 | 90 |
| Third | 17 | 120 |

The computer simulations were performed using the continuous remeshing extraction method [6]. The removed soil is not returned to the surface, allowing for the observation of the unworked ridge peaks and the furrow bottom. The simulation can also be recorded as a moving image.

During the simulations, the effects of the disc battery 's attack angle and working depth on the cross-section of the cultivated soil and the uniformity of the furrow bottom are observed.

The first simulation is shown in Figure 5.

In Figure 5 it is clearly visible that there are unworked areas and strips on the soil surface.

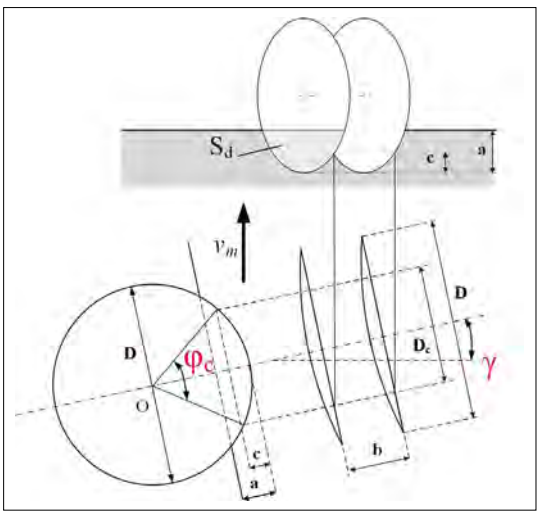


**Fig. 4.** *Geometry and Kinematics of the Disc Blades.*

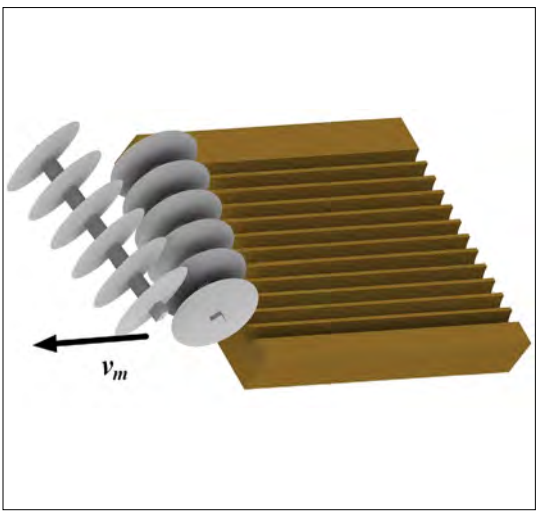


**Fig. 5.** *The First simulation, γ = 12°, a = 60 mm.*

The second simulation is shown in **Figure 6**. This simulation was performed with a larger attack angle and working depth, improving the soil processing. There are no unworked strips on the surface, but the furrow bottom is still quite uneven.

The third simulation is shown in **Figure 7.**

The third simulation was performed with the largest attack angle and working depth. The ridge height is smaller than the working depth, meaning the formed ridge peaks are not visible on the surface.

The results of the working process with the three different angle settings and working depths are illustrated in **Figure 8.**

The computer simulations clearly show that increasing the attack angle of the disc battery and the working depth results in a larger cultivated soil cross-section, as expected from the (1) relationship.

A larger attack angle leads to a more uniform formation of the furrow bottom.

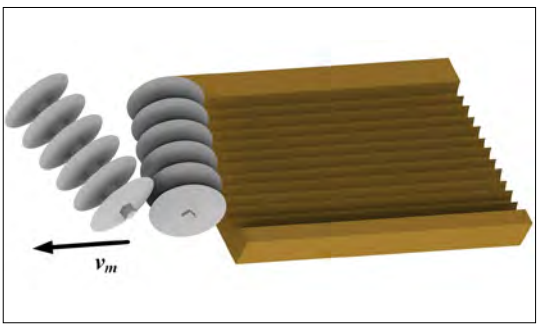


**Fig. 6.** *The Second simulation, γ = 15°, a = 90 mm.*

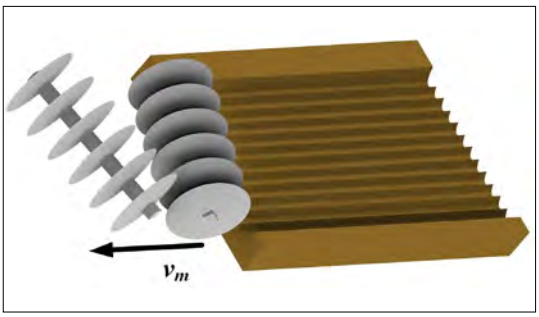


**Fig. 7.** *The Third simulation, γ = 17°, a = 120 mm.*

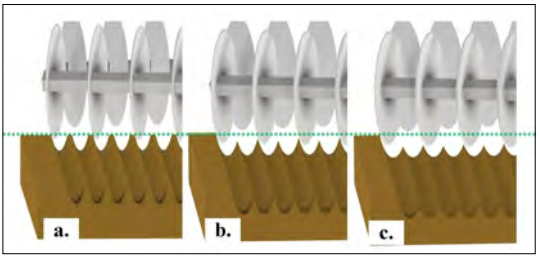


**Fig. 8.** *Illustration of the Cross-Section of the Worked Soil and the Ridge Peak Height: a) γ = 12°, a = 60 mm; b) γ = 15°, a = 90 mm; c) γ = 17°, a = 120 mm*

## 3. Conclusion

The simulation of the disc harrow's working process, implemented with real operational data, clearly illustrates the phenomenon and confirms that adding counterweights to the disc harrow or increasing the attack angle of the disc batteries is necessary to achieve a uniformly cultivated seedbed.

## References

[1] Vlăduț N.-V., Atanasov A., Ungureanu N., Ivașcu L.V., Cioca L.-I., Popa L.-D., Matei Gh., Boruz S., Cerempei V., Țîței V., Nenciu F., Milea O.-E., Dumitru Ș., Caba I.: *Trends in the Development of Conservation. Ecological Agriculture in the Context of Current Climate Change – A Review*. INMATEH - Agricultural Engineering, 74/3. (2024) 980–1032. https://doi.org/10.35633/inmateh-74-86

[2] Qiu Y., Chen Z., Hou Z., Liu H., Gu F., Dai N.: *Investigation on Data Collection and Fractal Characteristics of Soil Surface Roughness.* INMATEH - Agricultural Engineering, 61/2. (2020) 135–142. https://doi.org/10.35633/inmateh-61-15

[3] Căproiu Ș., Scripnic V., Ros V., Babiciu P., Ciubotaru C.: *Mașini agricole de lucrat solul, semănat și întreținere a culturilor*. Ed. Didactică și Pedagogică, București, 1982, 202–209.

[4] Naghiu A., Baraldi G., Naghiu L.: *Mașini și instalații agricole.* Risoprint Kiadó, Kolozsvár, 2004, 150,168.

[5] https://www.dianatrans.ro/utilaje-agricole-noi/discuri-trase--65/disc-btp--724.htm (letöltve 2025.02.28.)

[6] Tolvaly-Roșca F., Pásztor J.: *Work Process Analysis of the Machines with Working Parts Entrained in Seedbed Preparation Works*. INMATEH-Agricultural Engineering, 58/2. (2019) 2068–2239. https://doi.org/10.35633/INMATEH-58-01

Műszaki Tudományos Közlemények vol. 22. (2025) 102–105.
DOI: Hungarian: https://doi.org/10.33895/mtk-2025.22.17
English: https://doi.org/10.33894/mtk-2025.22.17

# DESIGN AND VALIDATION OF EQUIPMENT FOR TESTING THE LOAD CAPACITY OF LUBRICANTS

Popa-Müller Izolda,[1] Lőrincz Norbert[2]

[1] *Sapientia Hungarian University of Transylvania, Faculty of Technical and Human Sciences, Târgu Mureș,- Department of Mechanical Engineering, Romania, ipmuller@ms.sapientia.ro*

[2] *Hamorform Industry, Vlahita, Romania, lorincz.norbert@yahoo.com*

**Abstract**

To test the load carrying capacity of lubricating oils, we designed a device based on a modelling model of a tribological system in line contact. Under different loads and in contact with different materials, the wear rate is monitored. We investigate at what force load and over what time the wear occurs. It is an important tool in tribological laboratory practice because it can be used to determine the load capacity of a lubricating oil under test conditions and to determine the maximum load at which no wear will occur.

**Keywords***: lubricating oil, wear mark, force, time.*

## 1. Introduction

The most important role of lubricant is to reduce friction, which prevents wear on surfaces.

The use of lubricants according to their state of aggregation [1]:

– liquid lubricants (lubricating oils);
– plastic lubricants (greases);
– solid lubricants (graphite, molybdenum disulphide, etc.);
– gaseous lubricants (air, any inert gas).

In technical practice, liquid lubricants, lubricating oils, are most commonly used.

The parameters describing the most important properties of lubricants are [2]:

– viscosity, used to measure the fluid's ability to flow;
– consistency: a measure of the stiffness of grease;
– film-forming ability, a film of lubricant separating moving parts.

Lubricants should ensure that the optimum lubrication condition is maintained for as long as possible.

Causes of fatigue:

– internal changes in the lubricants;
– external contamination of lubricants;
– loss of efficiency of additives.

A kenőolaj összetétele alapolajból és a hozzáadott adalékokból áll.

The composition of a lubricating oil consists of a base oil and added additives.

The additives greatly alter the properties of the lubricating oil, improving its wear, friction, oxidation, foaming and corrosion properties.

Classification of lubricating oils:

– Vegetable and animal oils
– naphthenic and mixed base oils
– Synthetic lubricating oils, used in special cases, mainly at temperatures above 90°C or at very low temperatures. The most common synthetic oils are ester, poly-alpha-olefin, silicone and fluorinated oils and polyglycols.

## 2. Tribological studies

### 2.1. Design of equipment for testing the load carrying capacity of lubricants

The tribological tests are designed as follows: [3–7]

– to design a structure optimised for long life;
– design of an optimum structure in terms of operation
– to determine the data needed to establish maintenance and overhaul periods;
– monitoring the machine's operating condition;
– to simulate the wear of components by means of model tests;

– determining the factors influencing the behaviour of the tribological system;
– selection of the pair of materials and lubricants required for the construction and operation of a given friction structure;
– checking the quality of materials and lubricants.

For our application, we used the slotted disc tribological model, **Figure 1.**

One part of our system provides the rotary motion of the ring, while the other part is made up of a mechanism that provides a gradual load on the test piece.

The ring is locked at one end of the shaft and rotates in line contact with the test piece. The ring rotates at a constant speed of 800 [r/pm]. A lubricant is applied to the lubricant reservoir below the ring, forming a lubricating film between the two contact surfaces.

At the other end is a belt pulley **[1, 8]**, attached by a latch, to which an electric motor is connected by a belt drive. From the point of view of speed adjustment and transmission, a belt drive is required **[9]**. During operation, the minimum load at which the lubricant film breaks and fatigue starts is determined by gradually increasing the load, **Figure 2.**

The test impactor is loaded by a pair of force arms. One of the two levers locks the impactor in position, while the other lever presses the impactor against the ring. The progressive loading provided by the force arms is achieved by weights of different masses, **Figure 3.**

During operation, the minimum load at which the lubricant film breaks and starts to crack is determined by gradually increasing the load.

Both parts are fixed on a structure made of a lock section welded together, **Figure 4.**

The implemented device can be observed in **Figure 5.**

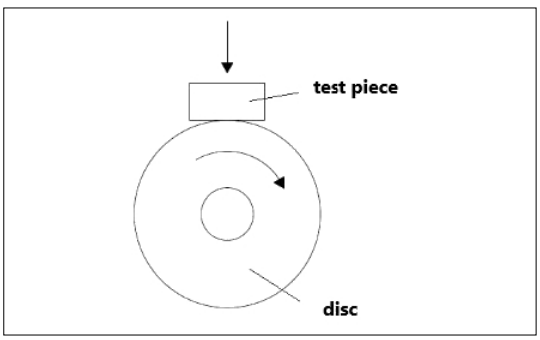


**Fig. 1.** *Bloc-disc model.*

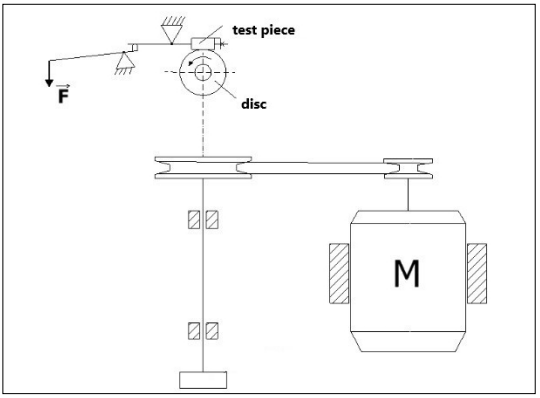


**Fig. 2.** *Kinematic sketch of the equipment.*

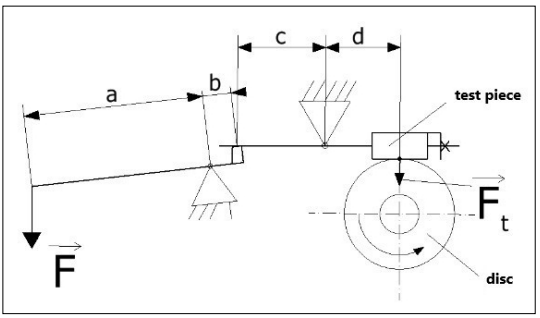


**Fig. 3.** *Kinematics of the power arm of the equipment.*

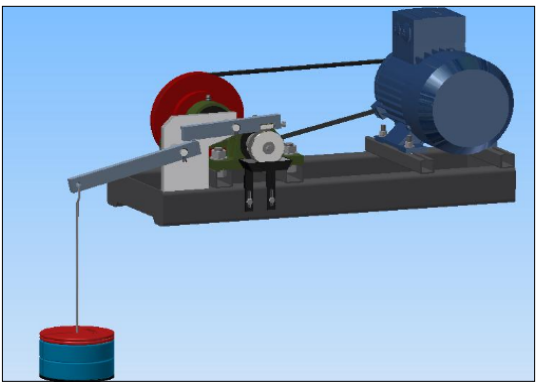

**Fig. 4.** *Spatial model of equipment.*

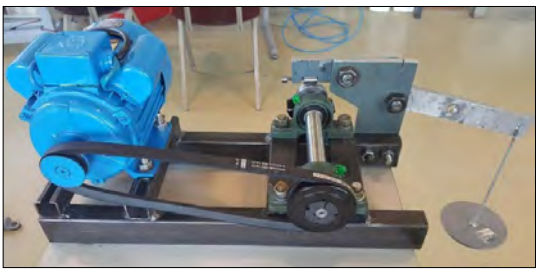

**Fig. 5.** *Completed equipment*

### 2.2. Subject of the study

The aim of the test is to study the load carrying capacity of lubricating oil on different contact surfaces. This is done by investigating the force load and the time after which wear occurs.

To determine, under given test conditions, the maximum load at which the burr does not yet appear.

The tests were carried out on specimens of Cu, CuZn, C45 using a steel ring. T90 type oil was used in the tests. This is a transmission oil used in low speed industrial gears with a viscosity index of 90.

Properties of lubricating oil:

– kinematic viscosity 40°C, $\nu = 160 mm^2/s$;

– kinematic viscosity 100°C, $\nu = 16.5–18 mm^2/s$;

– density 15°C, $\varrho = 0.91 g/cm^3$.

Test procedure: the load is gradually increased every minute until a crack appears on the test specimen, indicated by a characteristic sound.

The wear marks on the surfaces of Cu, CuZn, C45 specimens are observed in **Figure 6.**

### 2.3. Measurement results

**Table 1** shows the measurement results obtained during the study.

The equipment allowed precise monitoring of the wear process, while providing reproducible and reliable data for a specific lubricating oil on two different contacting materials.

The maximum load capacity of the lubricant is the highest for steel-steel. Here, an average load of 2350 grams and an average load time of 320 s result in a wear width of 0.5 mm.

During lubrication, the wear marks for steel-steel contact of the same materials occur at higher loads than for steel-red brass or steel-brass.

### 2.4. Data processing

Load force and load duration affect the size of the indentation mark, **Table 1.**

For data processing, a variable including both the load force and the load time was introduced. The variable is the ratio of load force to load time, $F/t$ ratio, where: $F$ is load force [N]; $t$ is load time [s].

As a function of the variable, the wear rate of different materials Cu, CuZn, C45 in the presence of the lubricant can be monitored.

The data are given in **Table 2**.

**Figure 7** shows the measured wear widths as a function of the F/t ratio.

The effect of the hardness of the material on the wear width is shown in **Figure 8**. The correlation

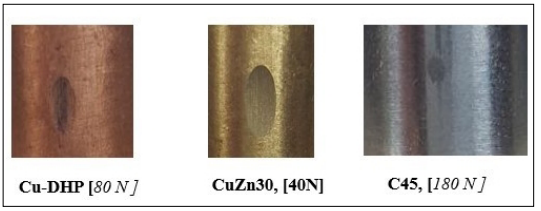


**Fig. 6.** *Abrasions on the surfaces of Cu, CuZn, C45 test pieces.*

**Table 1.** *Measurement data values*

| | | Load mass [g] | Load force [N] | Duration, [s] | Wear width |
|---|---|---|---|---|---|
| **Steel** | **Cooper** | 1000 | 80 | 240 | 1 |
| | | 1250 | 100 | 270 | 1.5 |
| | | 1250 | 100 | 270 | 1.5 |
| average | | 1166.(6) | 93.(3) | 260 | 1.(3) |
| **Steel** | **Brass** | 500 | 40 | 120 | 1 |
| | | 500 | 40 | 180 | 1.75 |
| | | 500 | 40 | 180 | 1.75 |
| average | | 500 | 40 | 160 | 1.5 |
| **Steel** | **Steel** | 2300 | 200 | 330 | 0.5 |
| | | 2250 | 180 | 300 | 0.5 |
| | | 2300 | 184 | 330 | 0.5 |
| average | | 2283.(3) | 188 | 320 | 0.5 |

**Table 2.** *Data processing values*

| HB | Load force [N] | Appearance of wear sound t[s] | Force/ time | Wear width [mm] |
|---|---|---|---|---|
| 60 | 93.(3) | 260 | 0.358974 | 1.33 |
| 95 | 40 | 160 | 0.25 | 1.50 |
| 250 | 188 | 520 | 0.5875 | 0.50 |

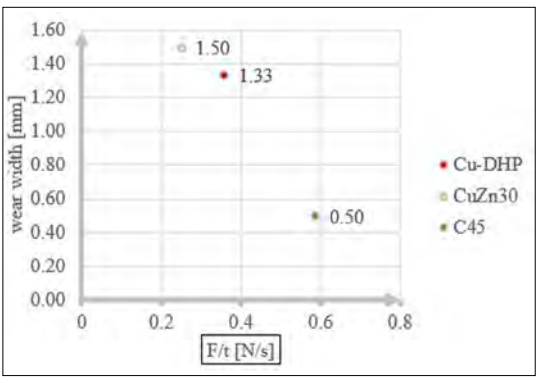


**Fig. 7.** *Variable influence of load-time on wear width.*

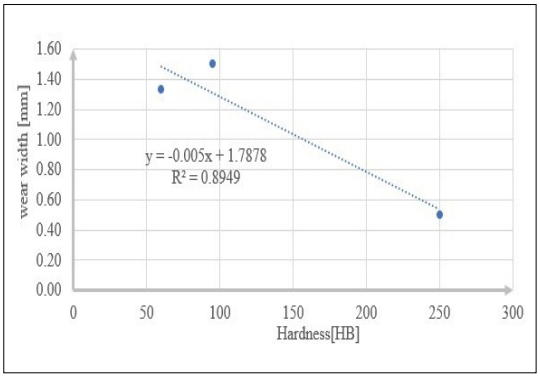


**Fig. 8.** *The effect of material hardness on wear width.*

in his figure, $R_2 = 0.89$, shows a strong relationship between the hardness of Cu, CuZn, C45 materials and the wear widths.

The regression line shows that the higher the hardness of the materials the lower the wear width.

## 3. Conclusions

It has been shown that the wear trace when using a lubricant depends on the material of the contact surfaces.

The validation experiments carried out have demonstrated that this tribological laboratory apparatus is suitable for testing the load carrying capacity of lubricants, supporting the selection and optimisation of the appropriate lubricant for different industrial applications.

## References

[1] Kozma M.: *Gépelemek 9*. Budapesti Műszaki Egyetem Gépészmérnöki Kar, Műegyetemi Kiadó, 1995.
[2] Műszeroldal: *A kenőanyagok vizsgálata.* http://www.muszeroldal.hu/measurenotes/kenoanyagokvizsg.pdf
[3] Burschik E., Csop Á. et.al.: *Kenéstechnikai kézikönyv*. Műszaki könyvkiadó, Budapest, 1961.
[4] Kozma M.: *Tribológia.* Műegyetemi Kiadó, Budapest, 2001.
[5] Matieșan D., Antal A., et.al.: *Elemente de proiectare pentru mecanismele cu șurub și piuliță.* Institutul politehnic Cluj-Napoca, 1985.
[6] Valasek I.: *Tribológiai kézikönyv*. Tribotechnik Kft. Budapest, 1996.
[7] Pavelescu D., Mușat M., Tudor A.: *Tribologie*. Editura Didactică și Pedagogică, București, 1977.
[8] Kozma M.: *Tribológia alapjai.* Veszprémi Egyetem Szakmérnöki Jegyzet, Kézirat, Bp. 1997.
[9] Horváth M., Márkos S.: *Gépgyártástechnológia,* Műegyetem, 1995.

Műszaki Tudományos Közlemények vol. 22. (2025) 106–109.
DOI: Hungarian: https://doi.org/10.33895/mtk-2025.22.18
English: https://doi.org/10.33894/mtk-2025.22.18

# ANALYTICAL AND NUMERICAL STUDY ON THE BEHAVIOR OF STEEL FLUSH END PLATE (FEP) CONNECTIONS

Abigail-Bethsabé SÜTŐ,[1] Nóra URSZULY,[2] Barnabás-Attila LŐRINCZ,[3] Zsolt NAGY,[4] Marius-Ștefan BURU[5]

*Technical University of Cluj-Napoca, Faculty of Civil Engineering, Cluj-Napoca, Romani.*

[1] *suto.at.abigail@student.utcluj.ro*

[2] *urszuly.sz.nora@student.utcluj.ro*

[3] *barnabas.lorincz@campus.utcluj.ro*

[4] *zsolt.nagy@dst.utcluj.ro*

[5] *marius.buru@mecon.utcluj.ro*

**Abstract**

This study evaluates the behavior of the steel flush end plate (FEP) beam-to-column external joint, presented in reference [1]. The investigations involve both analytical and numerical approaches to assess the performance of this typical connection. The analytical method, described in reference [2], represents the Component Method and the numerical analyses involved two finite element method-based software, Consteel and IDEA StatiCa. These two software tools adopt two distinct methodologies - one utilizing the Component Method, while the other implements the Component-Based Finite Element Method. A comparative analysis of the results was performed to evaluate the reliability of the analytical and numerical methods and to analyse the differences between these procedures. The results of the investigations indicate that the end plate is the weakest component of the examined connection. Therefore, a numerical parametric study was conducted to analyse the influence of the end-plate thickness on the overall behavior of the steel flush end-plate beam-to-column external joint.

**Keywords***: steel structures, flush end-plate (FEP) connections, component method, component-based finite element method (CBFEM), semi-rigid joint.*

## 1. Introduction

Connections are critical components of steel or composite structures, significantly influencing their overall behaviour in terms of internal stress distribution and deformations. This paper presents the results of a preliminary study on the behaviour of a beam-to-column external steel connection, isolated from the tested specimens presented in reference **[1]**. Through analytical and numerical methods, this study provides a comprehensive evaluation of how variations in end plate thickness affect the initial stiffness and load bearing capacity of the examined connection.

The analytical evaluation of the steel joints with different end plate thicknesses was carried out using the Component Method, in accordance with the SR EN 1993-1-8:2005 **[2]** standard. Furthermore, the numerical analysis of these joints was performed using Consteel and Idea StatiCa software, which apply different methods: the Component Method and Component-Based Finite Element Method (CBFEM).

The specimens presented in **[1]** were designed to represent typical flush end plate connections within a structural frame with a span of 8.00 m. One test was conducted on an internal joint (T1), while two tests were performed on external joints (T2, T3). In all three cases, the joints were made of steel columns and composite beams with a 10 cm thick and one meter wide reinforced concrete slab. The slab was connected to the steel beam using a single row of 11 pcs. shear studs, welded to the upper flange of the beam and spaced at 10 cm intervals. The column sections consisted of HEB240 profiles, while the beams were made of IPE270 profiles. At the load point, located at the

free end of the IPE cantilever, 10 mm thick stiffening plates were added.

The end plate, with a thickness of 10 mm, was welded to the IPE270 beam and fastened to the column with four M16 bolts. The HEB240 and IPE270 profiles were fabricated from S275 steel grade, while the bolts were of class 10.9.

The tested specimens are illustrated in **Figure 1.** and the results obtained for the initial stiffness ($S_{j.ini}$) and moment resistance ($M_{j.Rd}$) of the external composite connections are presented in **Table 1.**

## 2. Analytical Evaluation

The analytical investigation was conducted using the Component Method, where each component is identified as a spring with a nonlinear force-deformation curve, as mentioned by J. Jaspart **[3]**. Therefore, each component is considered as a semi-rigid component. The method requires the following steps:

- identifying the active components within the joint;
- determining the stiffness and/or the capacity of each individual component, including key parameters such as initial stiffness, design bending resistance and shear resistance;
- identifying the weakest component which determines the final capacity of the joint.

Analytical results indicate that, in the case of the examined flush end plate connection composed entirely of steel parts, the end plate is the weakest component of the joint. The results demonstrate a significant increase in moment resistance and initial stiffness as the thickness increases. However, beyond a thickness of 16 mm, this effect diminishes, as the column flange becomes the most sensitive component.

**Table 2** presents the analytically determined initial stiffness ($S_{j.ini}$) and moment resistance ($M_{j.Rd}$) of the assessed joint with varying end plate thicknesses, showing the percentage differences ($S_{j.ini}^{10+}$) in initial stiffness between the joint with a 10 mm thick end plate and those with greater thicknesses.

## 3. Numerical Analysis

In reference**[1]**, the weld size between the beam and the end plate was not specified. Therefore, 3 mm weld was used throughout the evaluations to match the end plate dimensions. Furthermore, it should be noted that the mechanical properties obtained through tensile testing of the steel components were not provided in reference **[1]**. As a result, the numerical analyses were conducted using theoretical mechanical properties, specifically a yield strength of 275 N/mm² and a Young's modulus of 210 GPa.

Consteel and Idea StatiCa software were used to numerically evaluate the flush end plate external joint. Consteel adopts the Component Method, while Idea StatiCa utilizes the Component Based Finite Element Method (CBFEM) for the evaluation of steel connections.

As previously mentioned, the Component Method considers each joint component as a spring.

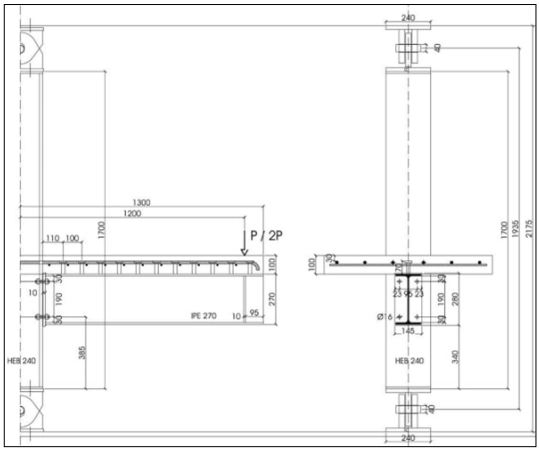


**Fig. 1.** *The T2 and T3 specimens, tested as part of the experimental program* **[1]**

**Table 1.** *Results from reference* **[1]** *for the composite joint*

| Connection | $S_{j.ini}$ [kNm/rad] | $M_{j.Rd}$ [kNm] |
|---|---|---|
| T2 | 13700 | 147.4 |
| T3 | 15800 | 163.1 |

**Table 2.** *Analytical results of the investigated joint*

| Connection | $S_{j.ini}$ [kNm/rad] | $M_{j.Rd}$ [kNm] | $S_{j.ini}^{10+}$ (%) |
|---|---|---|---|
| A-p10mm | 10034.49 | 34.28 | 0 |
| A-p12mm | 11466.35 | 39.54 | 14.26 |
| A-p14mm | 12312.10 | 45.77 | 22.70 |
| A-p16mm | 12796.50 | 52.94 | 27.53 |
| A-p18mm | 13064.54 | 57.64 | 30.19 |
| A-p20mm | 13201.75 | 57.82 | 31.56 |

In contrast, CBFEM integrates the advantages of the Component Method and the Finite Element Method by decomposing the joint into its individual components. It then applies nonlinear material analysis to evaluate each component independently, as well as the joint as a whole, considering component interactions that ultimately determine the overall capacity of the joint, as described by Lubomír Šabatka [4].

A numerical analysis was performed to compare both methods and to validate the analytical results. The results obtained from Consteel and the analytical method showed strong agreement, with differences in initial stiffness and moment resistance remaining below 10%.

The finite element model of the examined flush end plate connection is shown in Figure 2 and the results of the analysis are presented in Table 3 and 4. Additionally, a parametric study was performed by increasing the thickness of the end plate.

## 4. Discussions and Results

In the ArcelorMittal design guide [5] for multi-storey buildings, it is specified that flush end plate connections with relatively thin end plates (10 mm in S275 steel grade) are generally assumed to be pinned. However, the developed numerical models demonstrated that the investigated configuration exhibits semi-rigid behaviour. Figures 3 and 4 illustrate the differences in bending moment distributions for a frame structure with a span of 8 m. The first illustrates the effect of the tested joint on the bending moment distribution within the structure, while the second uses pinned connection as a reference to compare the effect of different joint types on the structural behaviour.

Furthermore, the analytical and numerical evaluations provide valuable insights into how the choice of calculation method can lead to variations in the results. For the examined joint, tested in reference [1], featuring a 10 mm thick end

**Table 3.** *Numerical results of the investigated joint in Consteel*

| Connection | $S_{j.ini}$ [kNm/rad] | $M_{j.Rd}$ [kNm] |
|---|---|---|
| NC-p10mm | 9216.41 | 34 |
| NC-p12mm | 10929.6 | 39.14 |
| NC-p14mm | 12026.5 | 45.22 |
| NC-p16mm | 12700.32 | 52.23 |
| NC-p18mm | 13102.63 | 52.07 |
| NC-p20mm | 13333.14 | 52.07 |

**Table 4.** *Numerical results of the investigated joint in Idea StatiCa*

| Connection | $S_{j.ini}$ [kNm/rad] | $M_{j.Rd}$ [kNm] |
|---|---|---|
| NI-p10mm | 9319.441 | 31.022 |
| NI-p12mm | 11359.719 | 38.301 |
| NI-p14mm | 11818.897 | 45.233 |
| NI-p16mm | 12629.169 | 52.165 |
| NI-p18mm | 13351.153 | 53.032 |
| NI-p20mm | 13860.144 | 53.205 |

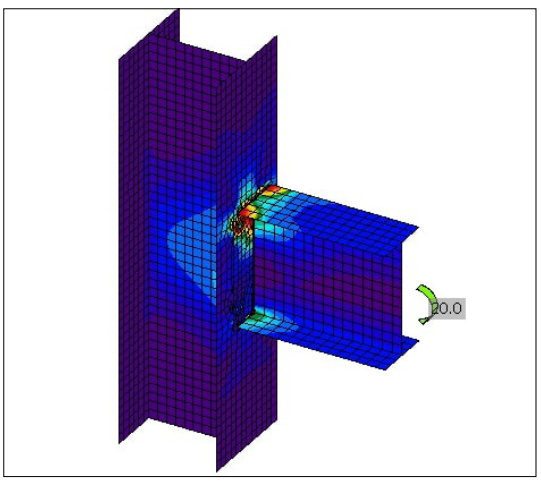


**Fig. 2.** *Finite element model of the investigated joint.*

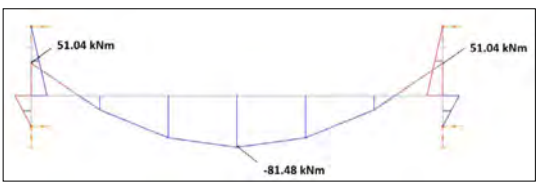


**Fig. 3.** *Bending moment diagram for the studied joints.*

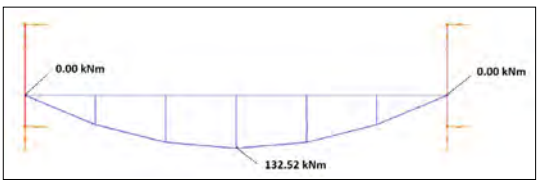


**Fig. 4.** *Bending moment diagram for pinned connections.*

plate, the results show a high degree of similarity, with differences below 10%. Both the analytical evaluation and Consteel software utilize the Component Method, leading to comparable moment resistance and initial stiffness values. Although Idea StatiCa employs CBFEM, its results do not differ significantly from those obtained using Component Method.

Based on the results of the analytical and numerical analyses, it has been demonstrated that the end plate is the weakest element of the examined connection. The results indicate a significant increase in moment resistance and initial stiffness as the end plate thickness increases. However, beyond a thickness of 16 mm this effect becomes less pronounced, as the column flange then becomes the most critical component of the connection.

## 5. Conclusion

The evaluation of the connection was made using analytical and numerical methods, revealing its semi-rigid behaviour and its ability to transfer bending moments. The results indicate that the Component Method and CBFEM procedure yield comparable moment resistance and stiffness values, with differences remaining within an acceptable range for the examined joint.

Further aims of the study include an experimental program involving the testing of two types of connections: joints connecting exclusively steel parts and joints connecting steel columns and composite beams.

## References

[1] Gil B., Bayo E.: *An Alternative Design for Internal and External Semi-Rigid Composite Joints. Part I: Experimental research.* Engineering Structures, 30, 2008. https://doi.org/10.1016/j.engstruct.2007.03.009

[2] Eurocode 3: Design of Steel Structures-Part 1-8: Design of Joints, European Standard, 2005.

[3] Jaspart J.-P., Weynand K.: *Design of Joints in Steel and Composite Structures*. ECCS-European Convention for Constructional Steelwork, Berlin 2016. 401.

[4] Šabatka L., Wald F., Kabeláč J., Kolaja D., Pospíšil M.: *Structural Analysis and Design of Steel Connections Using Component-Based Finite Element Model.* Journal of Civil Engineering and Architecture 9/8. (2015). https://doi.org/10.17265/1934-7359/2015.08.002

[5] ArcelorMittal: Multi-Storey Steel Buildings – Part 2: Concept Design, 2008.

Műszaki Tudományos Közlemények vol. 22. (2025) 110–115.
DOI: Hungarian: https://doi.org/10.33895/mtk-2025.22.19
English: https://doi.org/10.33894/mtk-2025.22.19

# DESIGN AND EXAMINATION OF A REAR SPOILER FOR AN ELECTRIC RACE CAR

Dániel TASKÓ,[1] Attila SZÁNTÓ,[2] Dávid PETTENDI,[3] Szabolcs Sándor DIÓS,[4] Géza HUSI[5]

[1] *Debrecen University, Faculty of Engineering, Department of Vehicles Engineering, Debrecen, Hungary, dtasko2001@gmail.com*

[2] *Debrecen University, Faculty of Engineering, Department of Basic Technical Studies, Debrecen, Hungary, szanto.attila@eng.unideb.hu*

[3] *Debrecen University, Faculty of Engineering, Department of Mechanical Engineering, Debrecen Hungary, pettendid4@gmail.com*

[4] *Debrecen University, Faculty of Informatics, Debrecen, Hungary, dios.szabolcs@eng.unideb.hu*

[5] *Debrecen University, Faculty of Engineering, Department of Vehicles Engineering, Debrecen, Hungary, husigeza@eng.unideb.hu*

**Abstract**

The task of the project was the design and CFD simulation of a Toyota MR2 component. The design took into account that the vehicle will be modified for racing purposes. Accordingly, a wing profile was chosen and a 3D CAD model of the profile was created. The wing was designed considering the aerodynamic characteristics of the car, and the brackets to attach the wing to the vehicle were also made. During the testing process, the optimum entry angle of the wing was found.

**Keywords***: electric race car, aerodynamics, rear wing, wing profile, CFD simulation.*

## 1. Introduction

The University of Debrecen, Faculty of Technology has launched new developments in the field of trains for the automotive industry. Artificial intelligence is becoming more and more prevalent in IT and we have started to integrate it into the development and teaching of the Vehicle Engineering Laboratory. The lab has a number of older robot units that are currently undergoing functional upgrades so that they will be able to use AI [1].

A Digital-Twin model of the lab has been created, so it is possible to perform measurements in the virtual lab [2]. Furthermore, it is possible to program virtual 3D robots without actually being in the lab [3]. Measurements in the field of robotics have also been performed in the lab, mainly in the area of singularity measurements [4].

For vehicle navigation, we implemented AGV trajectory planning using augmented reality techniques [5].

Our goal is to develop an Industry 5.0 pattern making system within the lab, where each robot unit can make decisions in workflows based on AI learning from its own dataset. Primarily in sorting tasks and path planning [6].

As the region relies heavily on the automotive industry, a number of simulation models have been designed for forklift trucks [7]. The necessary telemetric data were measured during our previous competitions and analysed later [8].

In keeping with the spirit of the times, sustainability is also a priority in our developments [9]. Innovation is a dominant feature of the engineering profession, which is also present in vehicle development.

Aerodynamic elements are playing an increasingly important role in motor racing, allowing cars to become faster and achieve better lap times. Aerodynamic elements help to efficiently dissipate the air around the car and create downforce, which gives the car more grip, resulting in higher cornering speeds, shorter braking distances and better

acceleration. As well as downforce, these devices also increase drag, so it is important to find the most effective solution for the application, which is the happy medium between downforce and drag. The project aims to design the rear wing of a Toyota MR2 electric race car.

## 2. Rear wing operation

The rear wings are an aerodynamic element on the vehicle's undercarriage, designed to create more grip and to make the vehicle more stable at high speeds [11].

The wings work by using Bernoulli's principle and Newton's 3rd law to form their lift. On the convex surface of the wing, the Bernoulli principle causes the air to accelerate and its pressure to decrease [12]. The higher pressure of the air on the other side of the wing pushes the wing towards the lower pressure, according to Newton's 3rd law [13].

The efficiency of the wing is influenced by five characteristics: lift and drag coefficients, angle of entry, aspect ratio and airfoil design [14]. These characteristics should be chosen with the airfoil's purpose in mind [15].

The wings mounted on motor vehicles work "quasi" in the same way as the wings on aircraft, the difference being that the rear wings of motor vehicles are upside down so that their lift is in the opposite direction. The force exerted by the wing results in greater traction [16].

It is important to mention the wing tips, which reduce the turbulence on the wing tips that is created when the pressure differences are equalized [17].

The drag of a car is calculated using the following formula:

$$F_D = \frac{1}{2} \cdot \rho \cdot v^2 \cdot C_D \cdot A \qquad (1)$$

Turbulence degrades wing efficiency, increasing drag and reducing lift. End flaps minimize these adverse effects, improving the aerodynamic performance of the wing [18]. The lift force on a car can be calculated using the following formula:

$$F_L = \frac{1}{2} \cdot \rho \cdot v^2 \cdot C_L \cdot A \qquad (2)$$

## 3. Designing the rear wing

The vehicle in question, which is owned by the University of Debrecen, Faculty of Engineering, is a Toyota MR2. The official data available were used for the study [19].

The main design considerations for the wing were determined according to the vehicle's aerodynamic sign-plates and the specific needs of slalom racing. The basic criterion for sizing the wing was that it should not exceed the width of the car, which is 1700 mm. This is important because elements protruding from the plane of the bodywork during obstacle avoidance on slalom tracks could hinder maneuvering [20]. Accordingly, the wing span was set at 1700 mm, while the length of the wing profile was set at 300 mm.

A key consideration in the choice of aerodynamic characteristics was to achieve adequate downforce with relatively low drag. On slalom slopes, where lower speeds are generally dominant, higher downforce is of paramount importance as it increases the grip of the vehicle. Minimizing drag was a secondary consideration, but still an advantage for such a high performance vehicle.

When designing the wing, attention was also paid to ensuring adjustability. Slalom races are held on different types of tracks, which have different aerodynamic requirements. The adjustable angle of entry allows the wing to always adapt to the specific needs of the track, thus providing optimum performance.

For the choice of the airfoil, a model with a high forward pitch, a smooth lift and a relatively low drag was chosen based on literature [21]. To design the airfoil, I used an airfoil generator developed by the NACA (National Advisory Committee for Aeronautics) [22] This tool allowed the accurate creation of the desired geometry profile, which is the basis for the aerodynamic performance of the wing.

The NACA generator was used to produce a 5-digit air foil that meets the requirements for high lift. During the generation process, the lift coefficient was set to 1.0, the maximum forward deflection was set at 25% of the air foil length, and the thickness was set to 6% of the chord length. The resulting air foil profile was used as the basis for the design and simulation processes, ensuring optimal performance of the air foil [22]. The air foil profile generator is shown in Figure 1.

Then, from the completed air foil, we designed the 3D CAD model represented in Figure 2.

### 3.1. Wing rib design

An important aspect in the design of the wing rib was the applicability of additive manufacturing technology. To this end, the rib is 300 mm long, 6 mm thick and designed with a wall thickness of 4 mm, which provides sufficient stiffness to with-

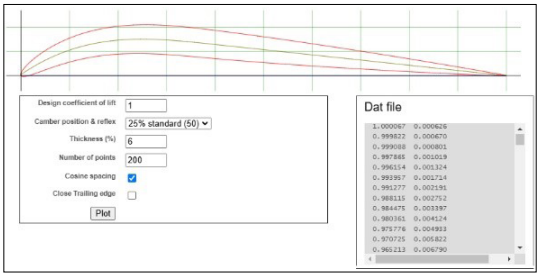


**Fig. 1.** *NACA air foil generator* **[22]**

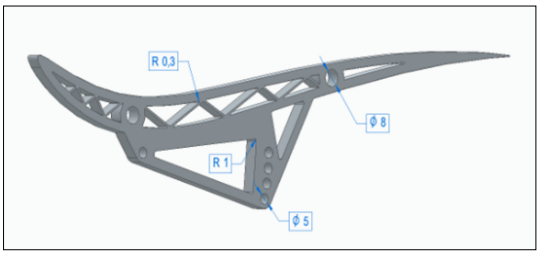


**Fig. 2.** *Air foil 3D CAD model*

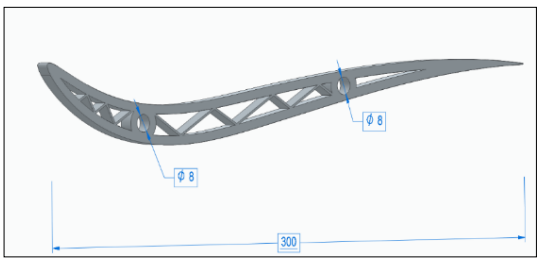


**Fig. 3.** *Wing ribs*

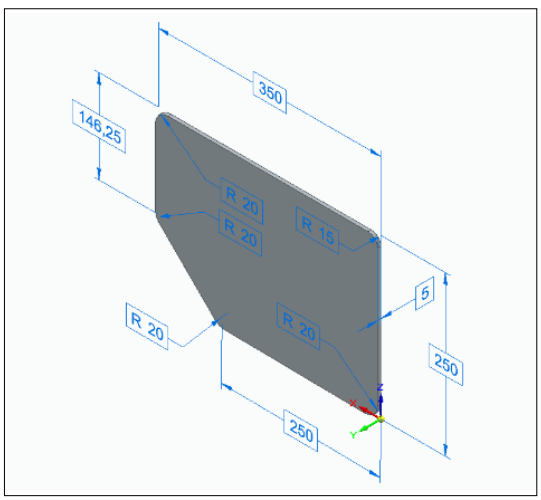


**Fig. 4.** *Windshield*

stand the forces applied. The internal stiffeners are 1 mm thick, and there are 0,3 mm rounded edges at the joints. Two 8 mm diameter holes allow easy and stable assembly of the wing frame on aluminium rods. The design is light, rigid and economical to manufacture (**Figure 3**).

In order to minimise the impact of turbulent air currents on the wing's efficiency, the wing's end plate is designed with a large surface area. 250 millimetres high and 350 millimetres long, the lower side is oriented upwards at an angle of 45 degrees at 250 millimetres. It is 5 millimetres thick.

Various roundings are visible on the model (**Figure 4**), which are also responsible for improving flow and reducing turbulence.

The purpose of the mounting brackets is to secure the wing structure to the vehicle body in a stable and secure manner, ensuring the correct position and angle of the wing under the effects of acceleration, braking and downforce. It is important that the design and material of the brackets guarantee the deformation resistance and aerodynamic performance of the structure. Solid Edge **[23]** was used to design the cantilevers. The base was designed to be 250 mm long, 80 mm wide and 10 mm thick. The attachment to the car boot lid is provided by four holes with a diameter of 5 mm located in the four corners of the base (**Figure 5**).

The wing can be attached to the wing brackets by means of a modified wing rib, which also provides adjustability.

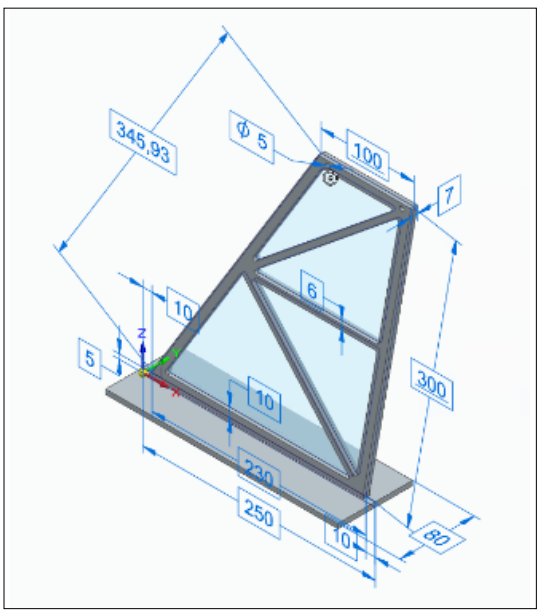


**Fig. 5.** *Fixing bracket.*

### 3.2. Wing assembly

The assembly model was created using Solid Edge Assembly.

On the base, the holes were drilled and the wing brackets were attached to these holes.

The wing ribs were attached to the brackets and fastened together with M5 screws selected from the Solid Edge model book. The wing model was then glued on and the elements joined.

We also made two types of wing models, one without wing tips and one with wing tips, as shown in **Figure 6.**

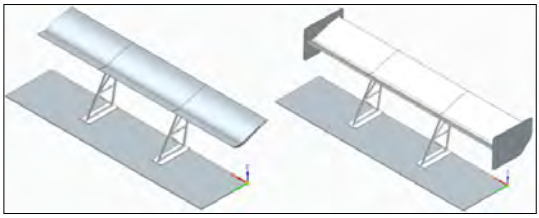

**Fig. 6.** *Assembly models without and with wingtip.*

## 4. CFD simulation study

The models were placed into the CFD simulation program Simscale **[24]** and the current-latency simulations were performed. The program determined the direction and magnitude of the forces acting on the model based on the given current-phase values.

In the simulations, the flow velocity was set to 50 km/h, since our own experience has shown that slalom races do not usually have a bend capable of achieving higher speeds.

Simulations were used to determine the most suitable entry angle for the speed determined (**Figure 7**).

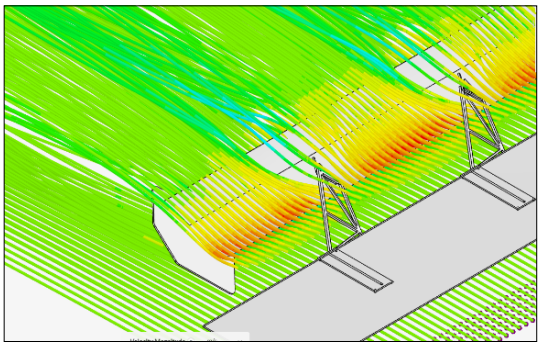

**Fig. 7.** *CFD simulation of a wing model with 10° angle of attack.*

The values obtained from the simulations were sorted into a table and used to select the 10° angle of entry (see **Table 1**).

**Table 1.** *CFD simulation values for wing profiles*

| Angle of entry | Downforce | Air resistance |
|---|---|---|
| 0° | 17-20N | 3-3.5N |
| 5° | 47-49N | 4-4.5N |
| 10° | 72-73N | 5-6.5N |
| 15° | 82-85N | 14-16N |

With this setup, CFD simulations were carried out on both the wing without an endplate and the wing with an endplate.

### 4.1. Simulation of a wing without wingtip

The results of the CFD simulation show that the assembled model achieves a downforce of 41-42N, which is far below the values of the simple wing model. This performance degradation is not surprising, as the cantilevers significantly break the flow under the wing and induce vortices.

Obviously, the drag of the assembled model is higher than that of the simple wing model. 12-13N is the drag of the complete model.

### 4.2. Simulation of the air foil wing

The simulation showed that the wing with end plates produced a down-tension force of 52-53N. The end flaps reduced the turbulence on the wing tips, thus increasing the downforce. The drag was also reduced compared to the wing model without wingtips, although not by much, but improved in this aspect as well. It can be clearly seen that, thanks to the air foil, lower and higher pressure air cannot create turbulent airflow on the wingtip.

**Table 2.** *Without wingtip and with wingtip*

| Considerations | Wing-wing-wing without wing-tip | Wing-fin wing | Difference |
|---|---|---|---|
| Downforce | 42N | 53N | 21% |
| Air resistance | 13N | 12N | 8% |

The simulations showed significant differences between the two wings, which are summarised in **Table 2.** Based on the data, the wingtip solution is more efficient and will be the best solution for the race car.

## 5. Conclusion

The aim of the project was to design and simulation test a rear wing that could improve the driving dynamics of the Toyota MR2 for slalom racing. The design of the wing was based on the literature to determine the optimal wing profile and the geometric parameters required for the simulations. In the analysis of the 3D model created with Solid Edge software, we also investigated the effectiveness of the wing tips in reducing tip vorticity, increasing downforce and reducing drag. CFD simulations at 50 km/h showed that the configuration with wing tips resulted in 21% higher downforce and 8% lower drag than the version without tips. These benefits significantly improve the vehicle's cornering capabilities and acceleration, which is a key priority in competition.

Since we also use DAQ data acquisition systems in the Faculty of Engineering, Vehicle Manufacturing Laboratory **[25]**, we will be able to compare the data with future modifications to the vehicle **[26]**.

### Acknowledgements

We would like to express our sincere gratitude to Timotei Erdei, lecturer at the Department of Vehicles Engineering and head of the Vehicle Engineering Laboratory. Also to the University of Debrecen, Faculty of Engineering.

„SUPPORTED BY THE EKÖP-24-4 UNIVERSITY RESEARCH SCHOLARSHIP PROGRAM OF THE MINISTRY FOR CULTURE AND INNOVATION FROM THE SOURCE OF THE NATIONAL RESEARCH, DEVELOPMENT AND INNOVATION FUND"

### References

**[1]** Kapusi T. P., Erdei T. I., Husi G., Hajdu A.: *Application of Deep Learning in the Deployment of an Industrial SCARA Machine for Real-Time Object Detection*. Robotics, 11. (2022) 69. **https://doi.org/10.3390/robotics11040069**

**[2]** Erdei T. I., Krakó R., Husi G.: *Design of a Digital Twin Training Centre for an Industrial Robot Arm*. Appl. Sci. 12. (2022) 8862. **https://doi.org/10.3390/app12178862**

**[3]** Erdei T. I., Nusser D. P., Husi G.: *Cyber-Physical Recreation of Six DOF Industrial Robot Arm*. International Review of Applied Sciences and Engineering, 15/2. (2024) 147–160. **https://doi.org/10.1556/1848.2023.00660**

**[4]** Erdei T. I., Husi G.: *Singularity Measurement in the Cyber-Physical and Intelligent Robot Systems Laboratory*. International Review of Applied Sciences and Engineering IRASE, 11/2. (2020) 82–87. **https://doi.org/10.1556/1848.2020.20001**

**[5]** Erdei T. I., Molnár Zs., Obinna Nwachukwu C., Husi G.: *A Novel Design of an Augmented Reality Based Navigation System & its Industrial Applications*. ACTA IMEKO, 7/1 (2018) 57–62. **https://doi.org/10.21014/acta_imeko.v7i1.528**

**[6]** Erdei T. I., Kapusi T. P., Hajdu A., Husi G.: *Image-to-Image Translation-Based Deep Learning Application for Object Identification in Industrial Robot Systems*. Robotics, 13. (2024) 88. **https://doi.org/10.3390/robotics13060088**

**[7]** Szántó A., Ádámkó É., Juhász G., Sziki G. Á.: *Simultaneous Measurement of the Moment of Inertia and Braking Torque of Electric Motors Applying Additional Inertia.* Measurement, 204.(2022) 112135.

**[8]** Sziki G. Á., Szántó,A., Kiss J., Juhász G., Ádámkó É.: *Measurement System for the Experimental Study and Testing of Electric Motors at the Faculty of Engineering, University of Debrecen*. Applied Sciences, 12/19. (2022) 10095.

**[9]** Mollah M. A., Amin M. Bin, Debnath G. C., Hosain M. S., Rahaman M. A., Abdullah M.: *Nexus among Digital Leadership, Digital Transformation, and Digital Innovation for Sustainable Financial Performance: Revealing the Influence of Environmental Dynamism*. Sustainability (Switzerland), 16/18. (2024) 8023. **https://doi.org/10.3390/su16188023**

[10] Mollah M. A., Pal D., Amin M. Bin, Rahaman M. A., Abdullah M.: *Effect of Technological Culture and Knowledge Sharing on Organizational Performance: The Mediating Role of Digital Innovation and Self-Efficacy as Moderation*. Journal of Infrastructure, Policy and Development, 8/12. (2024) 7594. **https://doi.org/10.24294/jipd.v8i12.7594**

**[11]** Build Your Own Race Car: Car Aero-dynamics Basics and How-to Design Tips Cont [Oline], **https://www.buildyourownracecar.com/race-car-aerodynamics-basics-and-design/4/#google_vignette**

**[12]** Filipovic M., Vukobratovic M.: *New Interpretation of the Euler-Bernoulli Equation*. 6th International Symposium on Intelligent Systems and Informatics, Subotica, Serbia, 2008, 1–6. **https://doi.org/10.1109/SISY.2008.4664967**

**[13]** Bloch A. M., Crouch P. E.: *Newton's Law and Nonholonomic Systems.* Proceedings of the 37th IEEE Conference on Decision and Control (Cat. No.98CH36171), Tampa, FL, USA, vol.4 (1998) 3569–3574,. **https://doi.org/10.1109/CDC.1998.761733**.

**[14]** Mechanical Engineering Assignment Help [Online], **https://www.mechanicalengineeringassignment-help.com/blog/optimizing-aerodynamics-race-car-rear-wing/**

**[15]** Racing Car Dynamics: How Air Improves Lap Times [Online],

**https://racingcardynamics.com/race-car-aerodynamics-air-lap-times/**

**[16]** Technical: Rear Wing Endplates in F1: An Extensive Analysis, [Online], **https://www.f1technical.net/features/20279**

**[17]** Happian-Smith J.: *5. Body Design: Aerodinamics*. In: *An Introduction to Modern Vehicle Design*. Publisher Butterworth Heinemann, 2000. ISBN: 0-7506-5044-3.

**[18]** Zomotor Á.: *2. Járműre ható erők*. In: *Gépjármű menetdinamika*, Széchenyi István Egyetem és IbB Hungary Járműakadémia, Kiadó: Maróti Könyvkereskedés és Könyvkiadó, 2006.

**[19]** Toyota MR2 Datasheet [Online]; **https://media.toyota.co.uk/wp-content/uploads/sites/5/pdf/MR2-Gen2-UK-launch-pack-1990.pdf**

**[20]** McBeath S.: *Competition Car Downforce: A Practical Handbook*. Haynes 2000.

**[21]** Toyota Motor Corporation, Toyota Completely Renews its MR2, Toyota Global Newsroom. **https://global.toyota/en/detail/7838423**

**[22]** Airfoil Tools: NACA 5 Digit Airfoils [Online]; **http://www.airfoiltools.com/airfoil/naca5digit**

**[23]** Gongzhang, Hanlin & Axtelius, Eric. (2020). Aircraft Winglet Design. **https://doi.org/10.13140/RG.2.2.34449.92001**.

**[24]** Murad, Jousef: *Harnessing the Power of the Cloud -Computational Fluid Dynamics With SimScale*. (2021). 10.1115/FEDSM2021-66406.

**[25]** Dave G. S., Pandhare A. P., Kulkarni A. P., Khankal D. V., Abdullah M.: *Experimental Investigation of Centrifugal Pump Machine and Its Faults through Different Type of DAQ System and Selecting One Based on Statistical Approach*. Cogent Engineering, 11/1. (2024). **https://doi.org/10.1080/23311916.2024.2417683**

**[26]** Masuk A., Diós S. S., Dinya T., Szántó A., Husi G.: *Labor Developments and Methods for Supporting Education in the Cyber-Physical and Intelligent Robot Systems Laboratory*. Műszaki Tudományos Közlemények, 20. (2024) 36–41. **https://doi.org/10.33894/mtk-2024.20.07**

Műszaki Tudományos Közlemények vol. 22. (2025) 116–122.
DOI: Hungarian: https://doi.org/10.33895/mtk-2025.22.20
English: https://doi.org/10.33894/mtk-2025.22.20

# DESIGN AND FINITE ELEMENT SIMULATION OF ZETOR 10245 TYPE AGRICULTURAL TRACTOR BALANCER AXLE TURNING TECHNOLOGY

Csaba VARGA,[1] Attila SZÁNTÓ,[2] Tamás Gergő ASZTALOS,[3] Szabolcs Sándor DIÓS,[4] Géza HUSI[5]

[1] *Debrecen University, Faculty of Engineering, Department of Vehicles Engineering, Debrecen, Hungary, csabavarga.t@gmail.com*

[2] *Debrecen University, Faculty of Engineering, Department of Basic Technical Studies, Debrecen, Hungary, szanto.attila@eng.unideb.hu*

[3] *Debrecen University, Faculty of Engineering, Hungary, gergoasztalos.28@gmail.com*

[4] *Debrecen University, Faculty of Informatics, Debrecen, Hungary, dios.szabolcs@eng.unideb.hu*

[5] *Debrecen University, Faculty of Engineering, Department of Vehicles Engineering, Debrecen, Hungary, husigeza@eng.unideb.hu*

**Abstract**

The project is investigating the production of a balancer shaft for the Zetor 10245 tractor, focusing on vibration reduction for in-line four-cylinder engines. Using 100Cr6 high-carbon bearing steel, advanced meg-machining techniques and finite element simulations were applied to optimize performance and life. Stress analysis, toolpath optimization and precision machining on a DMG MORI NT 4250 DCG machine ensured structural integrity and high-quality output. Surface roughness and performance measurements validated the design, demonstrating the effective integration of material selection, machining and simulation to increase engine reliability.

**Keywords***: balance shaft, 100Cr6 steel, finite element simulation, machining optimization.*

## 1. Introduction

The Debrecen region is not only important for the automotive industry, but also for agriculture. That is why, in addition to the low-tech vehicles, tractor-related developments and maintenance are also important.

The balancer axle plays a critical role in reducing vibration in in-line four-cylinder engines by counteracting first- and second-order forces. Using 100Cr6 high-carbon steel, advanced machining processes such as turning, milling and grooving were applied to achieve accuracy and durability. Finite element simulations were carried out to evaluate stress distribution, deformations and performance under realistic conditions. This integrated approach ensures the production of a reliable component that increases the efficiency and lifetime of the motor. The Zetor 10245 tractor is shown in **Figure 1.**

### 1.1. Analysis of the balancing axis

Several wear patterns were evident at the bearing location, including diameter reduction and ovality due to the geometry of the shaft, and indentations outside the bearing contact surfaces probably occurred after the gear slipped, as the shaft continued to rotate to maintain momentum

**Fig. 1**. *Zetor 10245 at work in spring.*

from its mass. The shaft itself can be seen in Figure 2.

The various instances of wear all point in the same direction, even when achieving material-side design life in bearing and shaft terms, so the following case was inevitable [1, 2].

### 1.2. Material choice

The Sauter HO ultrasonic hardness tester was an extremely valuable tool in this project to evaluate the material hardness and surface roughness of the balancer shaft. The measuring instrument used is shown in Figure 3.

The results of the tests showed that it has almost uniform hardness parameters on both sides, except for the bearing surfaces of the component, which exhibit extremely high strength and wear resistance for longer shaft life. The hardness measurement results are summarized in Table 1.

### 1.3. Selected material

For the balancer shaft, We chose 100Cr6, a steel with excellent strength, toughness and wear resistance, making it an optimal choice for sub-assemblies that are subjected to dynamic loads and stresses during operation (Figure 4).

## 2. 3D model design

The following measurement tools were used in the design:

- Digital caliper: for measuring the outside diameter, length and distance between critical surfaces of the shaft.
- Stirrup micrometer: used to measure the diameter of the shaft, ensuring a fine tolerance within the Mechani-Kai limits.
- Radius template set: with the help of this tool the curves and the radius on the balancing shaft were measured.

In the initial phase of the 3D modelling process, 2D sketches of the shaft were created in SolidEdge [5]. ]. Using the data obtained from the measurements, two-dimensional profiles were created for the most important cross-sections, namely the shaft diameter, the gear positions and the grooves for the curved latch nest.

In addition to refining the 3D model, Fusion 360 was used to design and simulate the machining process. The first step in the process is the set-up of the stock, which involves defining the dimensions of the cylindrical stock. A solid bar with a diameter of 55mm and a length of 700mm was used as the basis for the part, and the stock was positioned for the machining operations.

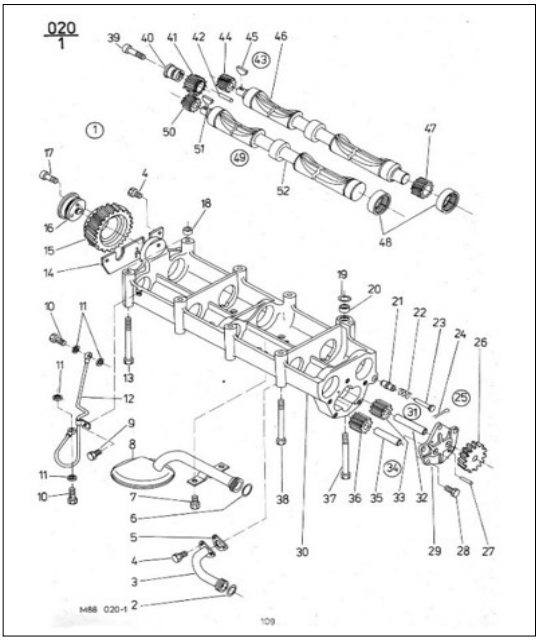


Fig. 2. *Exploded view of the balancing unit.* [3]


Fig. 3. *The Sauter HO hardness tester.*

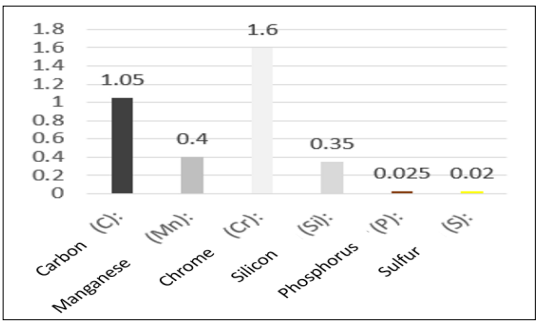


Fig. 4. *Chemical composition diagram of 100Cr6.* [4]

Table 1. *Results of the hardness measurement*

| 1. | 2. | 3. | 4. | 5. | 6. | 7. |
|---|---|---|---|---|---|---|
| 21.6 HRC | 56.7 HRC | 31.1 HRC | 58.9 HRC | 30.8 HRC | 56.9 HRC | 22.1 HRC |
| 22.2 HRC | 48.1 HRC | 27.9 HRC | 55.9 HRC | 29.2 HRC | 57.7 HRC | 28.3 HRC |

## 3. Turning processes

During turning, each operation serves a specific purpose in shaping and machining the workpiece to meet the desired machining properties. In this section, We discuss the characteristics and parameters of each operation, including homo-locating, longitudinal turning roughing, longitudinal turning smoothing, external recess roughing, external recess smoothing, drilling and profile finishing [6]. The imported model is shown in Figure 5.

The tools used in the process, i.e. those recommended by Sandvik Hungary Ltd., were carefully selected to achieve the required accuracy, optimum surface quality and efficient material removal (Figure 6) [7].

To ensure that the end points of the shaft are perfectly flat and accurately dimensioned, face machining was used. During this turning process, the tool is moved radially towards the centre line at the workpiece end.

The values used for the frontal stiffening are summarised in Table 2.

Longitudinal turning, or straight turning, is a machining operation in which the cutting tool moves in a direction parallel to the axis of the rotating workpiece, thereby reducing the diameter in the longitudinal direction. External grooving is a turning operation in which the cutting tool creates a groove or recess along the external diameter of the cylindrical workpiece. In external grooving, the tool is inserted directly into the workpiece at the desired location and moves radially in the material to achieve the desired depth. Chamfering, also important, is a turning operation used to separate the finished part from the rest of the workpiece or bar stock (Figure 7).

In the parting operation, the cutting tool is inserted indirectly into the rotating workpiece until it reaches the centre, effectively cutting through the diameter and creating a separate sub-part.

The catch values are summarised in Table 3.

## 4. Turning processes

Each process has specific characteristics, applications and operating parameters that affect efficiency, accuracy and surface quality [10]. Milling operations are a type of operation in which a flat-end milling cutter is used to create precise, flat-bottomed pockets and other complex profiles on the workpiece. In the case of a balancing spindle, for example, the pockets are machined to achieve the desired mass distribution, which is essential for vibration reduction and proper op-

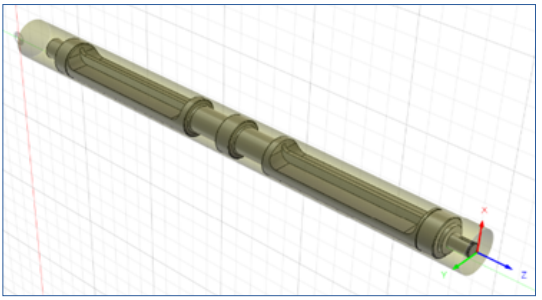

Fig. 5. *Model designed in Fusion 360.*

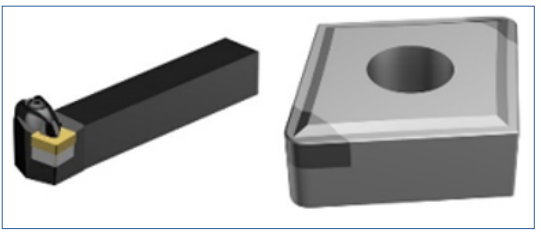

Fig. 6. *DCKNR 2020K 12 turning lathe blade holder and CNGM12041 2F-HGR 7125 blade.* [8, 9]

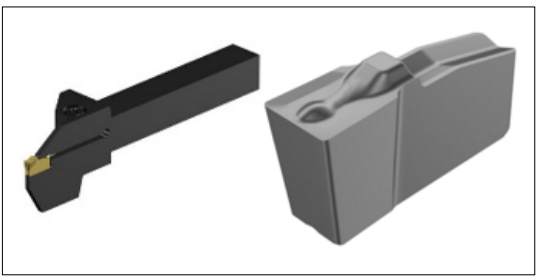

Fig. 7. *RF151.23-08-25 lathe insert holder and 25-4G 525 lathe insert.* [12]

Table 2. *Catches and their characteristics during frontal lobing*

| | Roughing | Smoothing |
|---|---|---|
| Number of passes | 8 | 1 |
| Cutting speed $v_c$ | 145 m/min | 145 m/min |
| Speed feed per revolution $f_n$ | 0.177 mm | 0.19 mm |
| Depth of grip $a_p$ | 0.567 mm | 0.465 mm |

Table 3. *Catches and their characteristics during external stabbings*

| | |
|---|---|
| Number of passes | 1 |
| Cutting speed $v_c$ | 124 m/min |
| Speed feed per revolution $f_n$ | 0.2 mm |
| Maximum rotation speed | 4000 rpm |

**Table 4.** *Catches and their characteristics during flat-end milling*

| | |
|---|---|
| Cutting speed $v_c$ | 236 m/min |
| Feed per tooth $f_z$ | 0.0901mm |
| Maximum grip depth | 25 mm |

**Fig. 8.** *930-B30-S-20-088 tool holder and 1P330-2000-XA 1620 solid carbide shank grinder for medium roughing.* **[14, 15]**

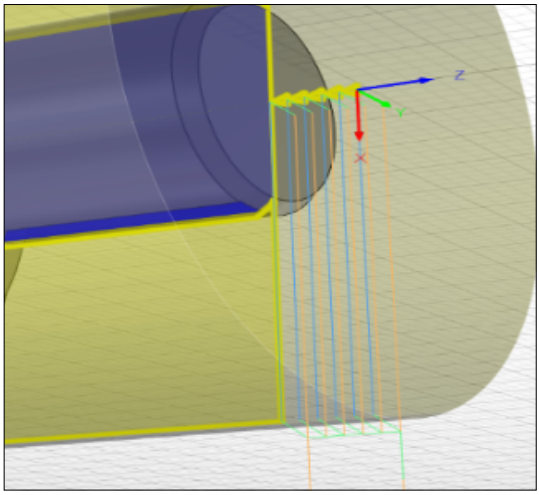

**Fig. 9.** *Toolpath for the frontal machining process.*

eration **[11].** The toolholder and the shank milling cutter can be seen in **Figure 8.**

The values for flat-end milling are summarised in **Table 4.**

## 5. Generating the toolpath

We designed the toolpaths for the machining process using the integrated CAM tools provided by Fusion 360 **[13]** using the different tools we found suitable during my research: depth of cut, cutting speed, radial depth of cut, feed per tooth (**Figure 9**).

For each section of the shaft, specific operations were selected and the corresponding parameters were set, such as main spindle speed, feed per revolution (**Figure 10**).

A series of simulations were carried out to gain insight into how each cutting tool interacts with the material. Ansys was also used to perform the simulations **[16]**.

The simulations showed in real time the manufacturing process from material removal to the final shape of the finished balance shaft (**Figure 11**).

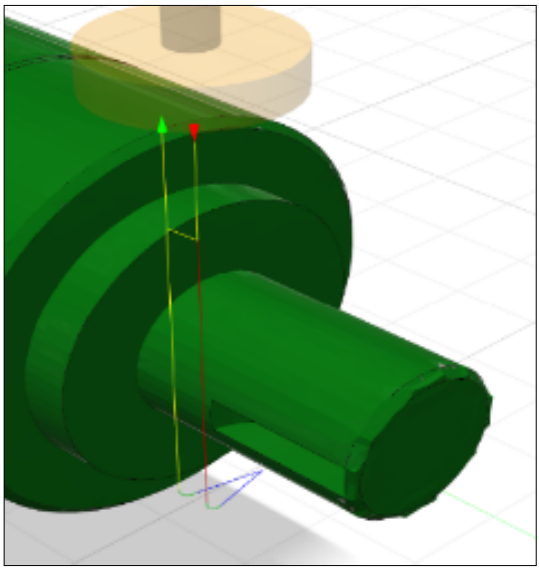

**Fig. 10.** *Curved bolt grooving, milling process tool path.*

## 6. Component handling method

When machining the balancer shaft, six-part machining was critical to ensure accuracy and efficiency. The use of primary and secondary spindles ensured safe retention and through-feed of the workpiece during the various machining stages. The main spindle initially held the workpiece, ensuring stability during operations such

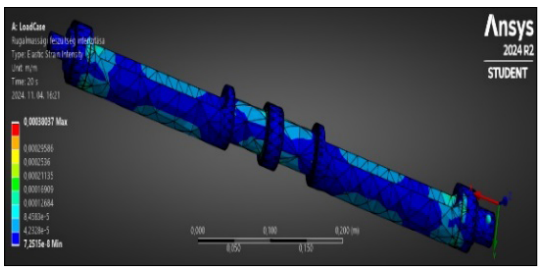


**Fig. 11.** *Elastic tension intensity test result.*

as longitudinal turning, face turning and grooving (Figure 12).

Once the primary operations were complete, the spindle engaged to hold the opposite end of the spindle, facilitating a smooth transfer of the part without the need for manual repositioning.

## 7. Finite element simulation

We performed a comprehensive finite element simulation to analyse the performance of the flywheel shaft under different operating conditions. The aim of the simulation was to create a realistic model that accurately represents the physical behaviour of the balancer shaft when subjected to different forces and conditions.

The simulation has highlighted the axial deformation along the length of the shaft due to the axle load and bearing forces. The axial deformation can cause the shaft to elongate slightly under high loads, leading to possible displacement of critical surfaces. Such deflections can lead to uneven load distribution on bearings and coupling components, which can result in increased wear or even mechanical failure [4].

The radial deflection, i.e. the deflection when the axle is subjected to bending stresses, has also been understood, especially in areas subject to geometric deformation, such as grooves or reduced cross-sections.

The application of elastic strain intensity analysis allowed the safe operating parameters of 100Cr6 to be determined, ensuring that the elastic properties of the material are capable of accommodating the expected loading conditions of the tensile field. The deformation values can be seen in Figure 13.

The methods and technologies used in the design and manufacture of the balancer shaft have demonstrated that the combination of appropriate material selection, precision machining and simulation is key to producing reliable and durable components. The use of 100Cr6 material, the state-of-the-art DMG MORI NT 4250 DCG machine and optimised machining parameters contributed to the high quality of the final product. The tests carried out, such as surface roughness and hardness measurements, confirmed that the shaft meets the stringent requirements of agricultural machinery. This project provided an effective solution to increase the reliability and lifetime of the Zetor 10245 tractor.

## 9. Research infrastructure

The University of Debrecen, Faculty of Technology has implemented a number of improvements in the laboratories, which will be decisive in the coming period. The established automotive lab provides the opportunity to start new developments in the field of robotics [17]. The field of artificial intelligence is gaining significant ground in the industry, therefore we started to complement the basic robot functions in the automotive lab based on our own dataset [18]. For the preliminary teaching we used Digital-Twin techniques in the lab [19]. The automotive engineering lab is also significant for the Faculty of Engineering, as the region is now mainly defined by the automotive industry, so that optimizations [20] and machine learning solutions can open new innovative avenues [21]. Simulations on vehicle dynamics were also performed in the lab, on the topic of electric motors [22], based on previous telemetry data [23]. DAQ data acquisition systems have been used for these [24], which have also been used in our aircraft development [25].

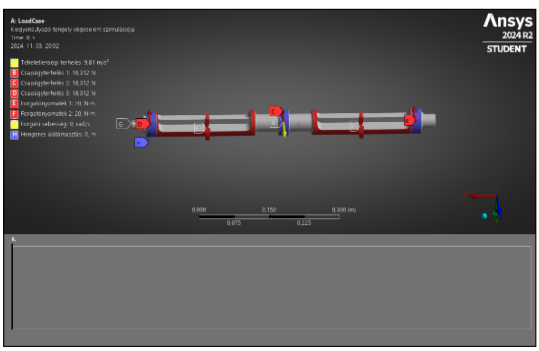


Fig. 12. *Ansys 2024 R2 model created in student-licence software.*

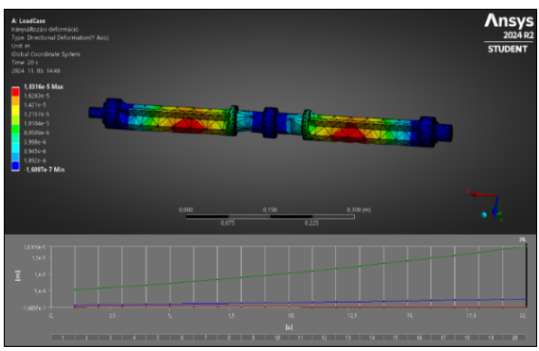


Fig. 13. *Result of the deformation marker test.*

**Acknowledgements**

We would like to express our sincere gratitude to Timotei Erdei, the head of the Vehicles Engineering Department and the head of the Vehicle Manufacturing Laboratory, and Gábor Balogh, a master's student in mechanical engineering. Also to the University of Debrecen, Faculty of Engineering.

## References

[1] *Bearing Damage Evaluation Guide*. SKF Group, Gothen-burg, Sweden, 2017.

[2] *Bearing Damage and Failure Analysis*. SKF Group, Gothenburg, Sweden, 2014.

[3] *Zetor Spare Parts Catalog 8211-16245*. Zetor Tractors a.s., Brno, Czech Republic, Jan. 1990.

[4] 100Cr6, Magas széntartalmú csapágyacél technikai adatlap,inoxservice.hu [Online] https://www.inoxservice.hu/upload/inline/adatlapok/kovacsolttombok/1.3505%20-%20ADATLAP.pdf

[5] Goanta A., Haraga G.: *Aspects of Modelling Classical or Synchronous Modelling with Solid Edge ST. 9.* MATEC Web Conferences, 112. (2017) 06024. https://doi.org/10.1051/matecconf/201711206024

[6] *Handbook of Cutting Data & Parameters – Milling and Drilling*. Ingersoll Werkzeuge GmbH, Haiger, Germany, 2023.

[7] Kalpakjian S., Schmid S. R.: *Manufacturing Engineering and Technology*, 8th ed., Pearson, 2019. https://doi.org/10.1016/B978-0-12-814104-6.00012-3

[8] *Sandvik Coromant Turning Tools*. Sandvik Coromant, Hungary, 2020. p. 206.

[9] *Sandvik Coromant Turning Tools*. Sandvik Coromant, Hungary, 2020. p. 163.

[10] *Sokoldalúan felhasználható tömör keményfém szármarók.* CoroMill Dura [Online] https://www.sandvik.coromant.com/hu-hu/tools/milling-tools-old/solid-carbide-end-mills/coromill-dura/coromill-dura-multimaterial

[11] *Sandvik Coromant Turning Tools*. Sandvik Coromant, Hungary, 2020. p. 409.

[12] *Sandvik Coromant Turning Tools.* Sandvik Coromant, Hungary, 2020. p. 208.

[13] Hassan I., Al-Mashhadi H., Radi K., Jawad H.: *IoT Based Multitasking Games and Entertainment Arcade Station Using Raspberry-Pi.* Journal of Southwest Jiaotong University. 54. https://doi.org/10.35741/issn.0258-2724.54.3.4

[14] Sandvik Coromant Turning Tools, Sandvik Coromant, Hungary, 2020. p. 407.

[15] CoroChuck 930 Nagy pontosságú hidraulikus tokmány, C-1040:266 hu-HU, AB Sandvik Coromant, 2019. p. 2

[16] B. Zheng, J. Zhang, Y. Yao: *Finite Element Analysis of the Piston Based on ANSYS.* IEEE 3rd Information Technology, Networking, Electronic and Automation Control Conference (ITNEC), Chengdu, China, 2019, 1908–1911. https://doi.org/10.1109/ITNEC.2019.8729409

[17] Kapusi T. P., Erdei T. I., Husi G., Hajdu A:. *Application of Deep Learning in the Deployment of an Industrial SCARA Machine for Real-Time Object Detection.* Robotics 11. (2022) 69. https://doi.org/10.3390/robotics11040069

[18] Erdei T. I., Nusser D. P., Husi G.: *Cyber-Physical Recreation of Six DOF Industrial Robot Arm.* International Review of Applied Sciences and Engineering, 15/2. (2024) 147–160. https://doi.org/10.1556/1848.2023.00660

[19] Erdei T. I., Krakó R., Husi G.: *Design of a Digital Twin Training Centre for an Industrial Robot Arm*. Applied Sci.ences, 12/17. (2022) 8862. https://doi.org/10.3390/app12178862

[20] Ahmed M., Sulaiman M. H., Hassan M. M., Rahaman M. A., Abdullah M.: *Selective Opposition Based Constrained Barnacle Mating Optimization: Theory and Applications*. Results in Control and Optimization, 17. (2024) 100487. https://doi.org/10.1016/j.rico.2024.100487

[21] Deshpande A. R., Kulkarni A. P., Wasatkar N., Gajalkar V., Abdullah M.: *Prediction of Wear Rate of Glass-Filled PTFE Composites Based on Machine Learning Approaches*. Polymers, 16/18. (2024) 2666. https://doi.org/10.3390/polym16182666

[22] Szántó A., Ádámkó É., Juhász G., Sziki G. Á.: *Simultaneous Measurement of the Moment of Inertia and Braking Torque of Electric Motors Applying Additional Inertia.* Measurement, 204. (2022) 112135. https://doi.org/10.1016/j.measurement.2022.112135

[23] Sziki G. Á., Szántó A., Kiss J., Juhász G., Ádámkó É.: *Measurement System for the Experimental Study and Testing of Electric Motors at the Faculty of Engineering*. University of Debrecen. Applied Sciences, 12/19. (2022) 10095. https://doi.org/10.3390/app121910095

[24] Dave G. S., Pandhare A. P., Kulkarni A. P., Khanka, D. V., Abdullah M.: *Experimental Investigation of Centrifugal Pump Machine and Its Faults through Different Type of DAQ System and Selecting One Based on Statistical Approach.* Cogent Engineering, 11/1. (2024). https://doi.org/10.1080/23311916.2024.2417683

[25] Abdullah M., Husi G.: *Aero Graphene in Modern Aircraft & UAV*. Recent Innovations in Mechatronics, 9/1. (2022). https://doi.org/10.17667/riim.2022.1/4

# SZERZŐK JEGYZÉKE
# LIST OF AUTHORS